LOFAR Observations of Shocks in the Solar Corona

Ciara A. Maguire

A thesis submitted for the degree of
Doctor of Philosophy

School of Physics
Trinity College Dublin
The University of Dublin

2022

Declaration

I, Ciara Maguire, declare that this thesis has not been submitted as an exercise for a degree at this or any other university and it is entirely my own work.

I agree to deposit this thesis in the University's open access institutional repository or allow the library to do so on my behalf, subject to Irish Copyright Legislation and Trinity College Library conditions of use and acknowledgement.

Ciara Maguire
October 19, 2021

Glossary

AIA Atmospheric Imager Assembly

AR Active Regions

CH Coronal holes

CME Coronal Mass Ejection

CPS Central Processing System

ESA European Space Agency

EUV Extreme Ultraviolet

GOES Geostationary Operational Environmental Satellite

ILT International LOFAR Telescope

KSP Key Science Project

LASCO Large Angle and Spectrometric Coronagraph

LOFAR LOw Frequency ARay

NOAA National Oceanic and Atmospheric Administration

MWA Murchison Widefield Array

NASA National Aeronautics and Space Administration

PSF Point Spread Function

PFSS Potential Field Source Surface

QS Quiet Sun

RFI Radio Frequency Interference

SDA Shock Drift Acceleration

SDO Solar Dynamics Observatory

SKA Square Kilometer Array

SUVI Solar Ultraviolet Imager

Summary

The Sun produces a variety of highly dynamic and energetic explosive events including the emission of intense bursts of electromagnetic radiation (such as a solar flare) and the large-scale eruption of magnetised plasma, known as a coronal mass ejection (CME). Flares and CMEs can drive shocks that propagate through the solar atmosphere, known as the corona, with velocities of hundreds of kilometres per second. These shocks are often associated with intense radio emissions known as type II radio bursts. Despite several decades of observations, many questions remain concerning the nature of shock formation and propagation, and how electron acceleration and radio emission are generated during these processes. In this thesis, I aim to further our current understanding of the fundamental properties of shocks in the low corona and how they evolve with time and distance. I also investigate the origin of a coronal shock and carry out a detailed study of shock formation associated with a complex solar eruption.

Coronal shocks can have a variety of observational manifestations that can be exploited to derive shock properties. One property of interest is the shock Alfvén Mach number, which is a proxy for the shock strength. The first aim of this thesis was to study the evolution of a CME-driven shock that occurred on 2 September 2017 and investigate three commonly used methods of calculating the Alfvén Mach number. This allowed us to test the consistency of the methods and derive more detailed shock characteristics than would normally be possible using just one method. I found that the three different methods of estimating shock Alfvén Mach number yield consistent results. Namely, the Alfvén Mach number was initially $\sim$1.5 and increased up to 4 as the shock propagated from a heliocentric distance of 1.4 to 3 $R_\odot$ over $\sim$17 min. This means the shock became progressively stronger over this time frame. This then led to an investigation into the conditions necessary for shocks to efficiently accelerate electrons and generate radio emission. I found that the change in the angle between the local shock norm and coronal magnetic field direction, from predominantly quasi-perpendicular to quasi-parallel, was related to the onset and ceasing of the type II radio emission.

In addition to an investigation on the optimal environments for shock electron acceleration, I investigated the origin of a coronal shock that occurred on 16 October 2015. Radio interferometric observations were used to determine the location of the associated type II burst. The images revealed a clear separation of 0.3-0.5 $R_\odot$ between the type II fundamental and harmonic components, which contradicts the underlying plasma emission mechanism. Such behaviour was attributed to radio wave scattering

in the corona. I accounted for scattering effects using an analytical approach and determined the true propagation path of the shock. I found that the type II burst was located at a much higher altitude than a plasma jet and had a significantly larger velocity. That is, the jet speed was $\sim$200 km s^{-1} while the type II burst propagated at $\sim$1000 km s^{-1}. This allowed us to infer that the type II burst was generated by a particular type of shock, called a piston shock, which was driven by the jet in the low corona. This work highlighted the importance of accounting for radio wave scattering effects in radio imaging to accurately determine type II burst kinematics and thus the shock origin.

Type II bursts can often exhibit variations in morphology and fine structure, which can give us insight into the behaviour of shocks in the low corona. The final aim of this thesis was to investigate the complex radio emission associated with a solar eruption that occurred on 16 October 2015. Radio interferometric images revealed that the shock associated type II burst was composed of multiple short lanes of emission that were generated in different regions of the shock, where the local plasma conditions were favourable for plasma emission. The high-resolution radio observations enabled us to identify and precisely locate the short lanes, which would not be evident in lower-resolution observations. The shock was generated by a plasma spray that propagated in multiple directions, at speeds ranging from 50 to 200 kms^{-1}. In conjunction with this, I also imaged an intriguing type II feature called band-splitting, the origin of which is subject to debate. I found that the upper and lower split-bands were co-spatial, which indicates that the emission comes from ahead and behind the shock front simultaneously. From the band-splitting, the Alfvén Mach number was found to be in the range 1.52 to 1.62, which is consistent with shocks in the low corona. These unique observations shed light on the nature of radio emission generated by shocks in the low corona. This study also highlights the importance of high-resolution radio imaging and how imaging is needed to correctly interpret type II spectroscopic data.

The work in this thesis has provided new insight into shock formation and propagation and how electron acceleration and radio emission are generated during these processes.

To my family

Acknowledgements

I have been fortunate to meet some wonderful people over the past four years. Many of whom have helped me get to this point.

Firstly, I would like to thank my supervisor, Peter Gallagher, and co-supervisor, Eoin Carley for their invaluable support and advice during my PhD study. Thank you both for guiding my research and providing so many learning opportunities.

Many thanks to all of the colleagues I have worked with at TCD and DIAS, especially those in the solar physics group. To Sophie Murray, thank you for your support, especially over the thesis process. Also a big thank you to Pearse Murphy, for being a great office buddy and sounding board when I needed it.

I would like to express my sincere gratitude to my mentor Claire Raftery. Thank you for all the encouragement, compassion and input you have given me, particularly over the past few months. You have been a great role model and friend. It has truly been an honour to receive your mentorship. I also wish to thank Nicole Vilmer for providing me with the opportunity to work in Observatoire de Paris. Although my time in Paris was cut short it was a privilege to work under your guidance.

To all my friends and family, thank you for the moral support over the years. To my Mum and Dad, thank you for your unconditional, unequivocal, and loving support. You have my utmost thanks, love, and respect. I owe everything to you both. To my brother, thank you for always keeping me grounded, reminding me of what is important in life, and always being supportive of my adventures. To John, thank you for being there for me and for telling me that I am doing great even when I didn't feel that way. To Taz, thank you for always cheering me up. Last, but certainly not least, a special thank you to my PhD sister, Aoife Maria Ryan. I am forever grateful for the support, encouragement and love you have given me over the past four years. I couldn't have done this without you.

List of Publications

1. **Maguire, C.A.**, Carley, E. P., McCauley, J. & Gallagher, P.T.
   "Evolution of the Alfvén Mach number associated with a coronal mass ejection shock", *Astronomy and Astrophysics*, 633, A56, (2020)

2. **Maguire, C.A.**, Carley, E. P., Zucca, P., Vilmer, N. & Gallagher, P.T.
   "LOFAR Observations of a Jet-driven Piston Shock in the Low Solar Corona", *The Astrophysical Journal*, 909, 2 (2021)

3. **Maguire, C.A.**, Ryan, A. M., Carley, E.P., Zucca, P., Murphy, P. C., & Gallagher, P.T. "LOFAR observations of multiple shocks driven by complex flare spray", *The Astrophysical Journal*, in prep.

4. Murphy, P. C., Callanan, P., McCauley, J., Redman, M. P., McKenna, D, Ó Fionnagáin, D., Louis, C. K., Redman, M. P., Cañizares, L. A., Carley, E. P., Maloney, S. A., Coghlan, B., Daly, M., Scully, J., Dooley, J., Gajjar, V., Giese, C., Brennan, A., Keane, E. F., **Maguire, C. A.**, Quinn, J., Mooney, S., Ryan, A. M., Walsh, J., Jackman, C. M., Golden, A., Ray, T. P., Doyle, J. G., Rigney, J., Burton, M. & Gallagher, P. T.
   "First Results from the REALtime Transient Acquisition (REALTA) backend at the Irish LOFAR station", *Astronomy and Astrophysics*, 909, 2 (2021)

5. Ryan, A. M., **Maguire, C. A.**, Murphy, P. C., Carley, E. P., Sharma, R., & Gallagher, P. T. "LOFAR imaging of microflares in the Quiet Sun at <70 MHz", *The Astrophysical Journal*, in prep.

6. Murphy, P.C., Ryan, A. M., Carley, E. P., **Maguire, C. A.**, & Gallagher, P. T. "The intrinsic sizes of Type III radio bursts and comparison to numerical simulations", *Astronomy & Astrophysics*, in prep.

Contents

List of Figures

List of Tables

1 Introduction

The Sun produces a variety of dynamic and energetic explosive events including the emission of intense bursts of electromagnetic radiation (solar flare) and the large-scale eruption of magnetised plasma, known as a coronal mass ejection (CME). Flares and CMEs can drive shocks that propagate through the solar atmosphere, known as the corona, with speeds of hundreds of kilometres per second (Vršnak and Cliver, 2008). If directed towards Earth, these events are a potential threat to both space and ground-based technologies including satellite telecommunications, GPS networks and electrical power grid systems (Schrijver et al., 2015). Hence there is a need to study and understand the physics associated with for shock initiation and propagation in the solar atmosphere.

Shocks in the solar atmosphere are a complex phenomenon and they can have a variety of observational manifestations such as enhancements at extreme ultraviolet (EUV) and visible wavelengths, and intense bursts of radio emission. Using EUV and visible images from space-based instruments we can study the source of energy or eruptive event, driver and large-scale dynamics of shocks. While radio imaging and spectroscopy provided by ground-based instruments allow us to determine the precise

location of shocks and reveal details about shock acceleration processes. The benefit of radio observations is that radio sources in the corona are predominately generated at the local plasma frequency. As a result, radio observations provide powerful diagnostics on the solar atmosphere and a large variety of dynamic phenomena. In this thesis, I use the latest observational by ground and space-based instruments to understand the nature of shock formation and propagation and how electron acceleration and radio emission are generated during these processes. In this chapter, an introduction to the solar corona and the main coronal phenomena relevant to this thesis are presented. The corona is described in a historical context and then discussed in relation to the other layers of the solar atmosphere. The all important Sun's magnetic field is briefly discussed as it is both the scaffolding for structures in the corona and the energy reservoir that powers solar eruptions. The main solar features and eruptive activities that are associated with coronal shocks are then described and the different types of radio bursts are outlined. This is followed by a more detailed discussion on the radio signature of solar shocks, type II radio bursts.

1.1 Solar Atmosphere and Activity

1.1.1 The Solar Corona

The Sun produces large-scale eruptive events that can drive shocks through the solar corona. The solar corona, the outermost layer of the Sun, is a hot, tenuous part of the solar atmosphere. It begins ∼2500 km above the solar surface and extends out into interplanetary space. The corona can only be observed by the naked eye during total solar eclipses when the Moon blocks out the intense light from the Sun's visible surface and the faint scattered light reveals the corona's tenuous structure. Figure 1.1 shows an ancient stone monument in Loughcrew, County Meath, Ireland, which may be the world's oldest surviving depictions of an eclipse. The spiral petroglyphs are believed to

Figure 1.1: Ancient carvings in Loughcrew, County Meath, Ireland that is believed to depict the Moon partially occulting the Sun during an eclipse over 5,000 years ago. Credit: Michael Fox, Boynevalleytours.com.

illustrate the alignments of the Sun, Moon and horizon during the solar eclipse on 30 November 3340 B.C.[1]. Many historians believe that the ancient Irish Celts predicted solar eclipses and celebrated a "festival of light" to welcome the solar phenomenon. Numerous ancient texts describe the "ethereal glow" surrounding the eclipsed Sun (Stephenson, 1997; de Jong and van Soldt, 1989; Pasachoff and Olson, 2014) but it is believed that the Italian-born French astronomer, Giovanni Cassini was the first to coin the term *corona* (meaning a wreath, garland, or crown in ancient Greek) after the May 1706 solar eclipse. He described the corona as "une couronne d'une lumière pâle" or a crown of pale light. Perhaps the first scientist to report on the corona was the German astronomer Johannes Kepler. In his 1604 book Astronomiae Pars Optica ("The Optical Part of Astronomy"), he expressed his belief that the corona was a

[1] https://eclipse2017.nasa.gov/eclipse-history

feature of the Moon. Later others suggested it was due to interaction between the Sun and Earths's atmosphere (Westfall and Sheehan, 2015). Thanks to the development of photography and spectroscopy in the latter half of the nineteenth century significant progress was made in understanding the origin, composition, and structure of the corona. In 1868, the first spectroscopic measurements of the Sun were made, which led to the discovery of a new chemical element (helium) at the solar limb from the detection of a bright 587.6 nm emission line and the identification of the characteristic solar Fraunhofer lines in the coronal spectrum (Lockyer and N., 1869). During the solar eclipse of August 1869, Harkness and Young (1986) observed a mysterious new spectral line that did not correspond to any known element. It was speculated that this line alluded to the existence of another new element, which they called "coronium". Subsequent laboratory experiments in the 1930-40s demonstrated that the emission line was in fact associated with unusually high ionization states of known elements such as iron, calcium, and nickel (Grotrian, 1939; Edlén, 1943). This discovery was puzzling since the temperatures necessary to produce these high ionisation's states are several orders of magnitude larger than the temperature at the Sun's surface. This rapid increase in temperature, termed *the coronal heating problem*, remains one of the longest-standing questions in solar physics (Klimchuk et al., 2006).

The Solar Atmosphere

Temperature, as well as density, are considered to be the main parameters that characterise the layers of the Sun's atmosphere. There are three distinct regions as shown in Figure 1.2. The figure describes temperature and mass density in terms of height above the solar surface as per the standard VAL model, a 1D model named after the scientists behind its development (Vernazza et al., 1981). The first layer of the solar atmosphere is called the *photosphere*, which comes from the Greek word "photos" meaning light. This is in reference to the fact that the photosphere is the only layer of the Sun's atmosphere visible to the naked eye when observed from Earth. It is the layer used to

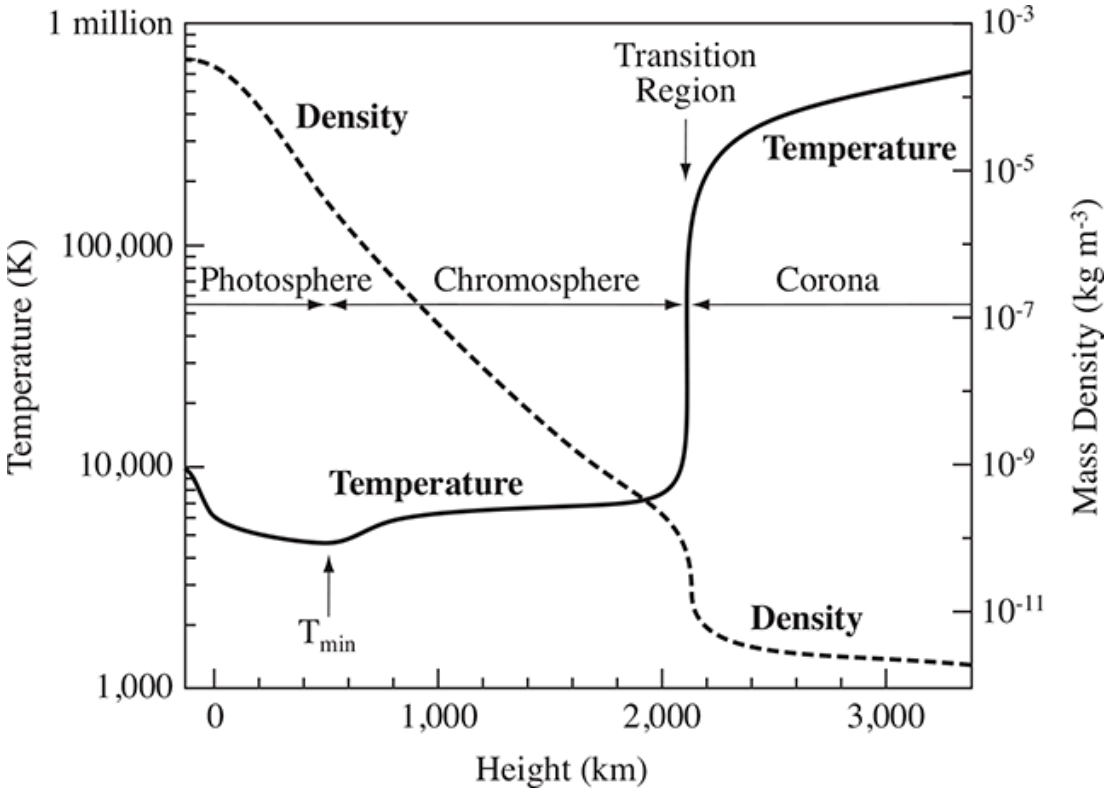

Figure 1.2: Variation in temperature and mass density as a function of height in the solar atmosphere. The photosphere and chromosphere are comprised of neutral atoms but the corona is an ionised plasma due to the higher temperature. Note the abrupt jump in the values along the transition region. Credit: Lang (2001).

determine the radius of the Sun, given as $R \approx 6.96 \times 10^5$ km. The temperature decreases from 6,400 K to 4,400 K over the depth of the photosphere, which is ∼500 km.

Above the photosphere lies the *chromosphere*, which is around 2000 km thick. The temperature increases to 20,000 K with increasing height while the density rapidly decreases from $\sim 10^{16}\,\mathrm{cm}^{-3}$ to $\sim 10^{11}\mathrm{cm}^{-3}$. The increasing temperature means the level of hydrogen and helium ionisation increases closer to the chromospheric surface. Between the chromosphere and the corona lies the transition region. Here in this very thin region, the temperature dramatically increases to above 1 MK over a distance of 100 km (see Figure 1.2). The magnetic field dominates at altitudes above the transition region therefore the morphology and dynamics of coronal structures is determined by the magnetic field. In the outermost layers of the corona, the pressure of the material is much greater than the pressure of the local interstellar medium resulting in a

persistent yet variable plasma flow referred to as the solar wind (Parker, 1958). However, the boundary between the corona and solar wind is somewhat ambiguous. The term corona most commonly refers to the region within $1.1-10\,R_\odot$ while the terms solar wind and/or interplanetary medium are used for regions of larger heliocentric distances.

Ultraviolet wavelengths allow observations of the corona up to heights of $\sim 0.5\,R_\odot$ above the solar surface. More extensive observations of the corona, sampling larger heights are carried out at visible wavelengths, colloquially known as the "white-light" corona. The corona's white-light radiation is primarily due to the scattering of photospheric light by particles and dust. The visible coronal radiation is primarily divided into two different layers: the K corona and the F corona. The K corona (K for kontinuierlich meaning "continuous" in German) is produced by Thomson scattering of photospheric light by coronal electrons. The spectrum of the K-corona is that of the photosphere, however the high temperatures means the electrons have high thermal velocities which wash out (due to thermal broadening) the Fraunhofer lines. The K corona dominates from the low solar atmosphere up to $\sim 4\,R_\odot$. Beyond this height, photospheric radiation is primarily scattered off dust particles via Rayleigh scattering. This layer is known as F-corona (F for Fraunhofer as the absorption lines are visible) and this extends into interplanetary space, beyond Earth (Kimura and Mann, 1998).

Ultraviolet and white-light observations are the main method of imaging the low and extended corona, respectively. However, the corona is also a strong emitter at radio wavelengths, from microwave to kilo-metric wavelengths. These radio observations mimic some of the characteristics seen in EUV and white-light in the low corona (albeit at lower spatial resolution) and sometimes dynamical phenomena seen in the outer corona. Today, there are a number of space and ground-based instruments, providing multi-wavelength observations of the solar corona and solar activity. These observations reveal numerous coronal features and dynamic phenomena (see Section 1.1.3), some of which drive shocks in the corona, accelerate electrons and generate radio emission.

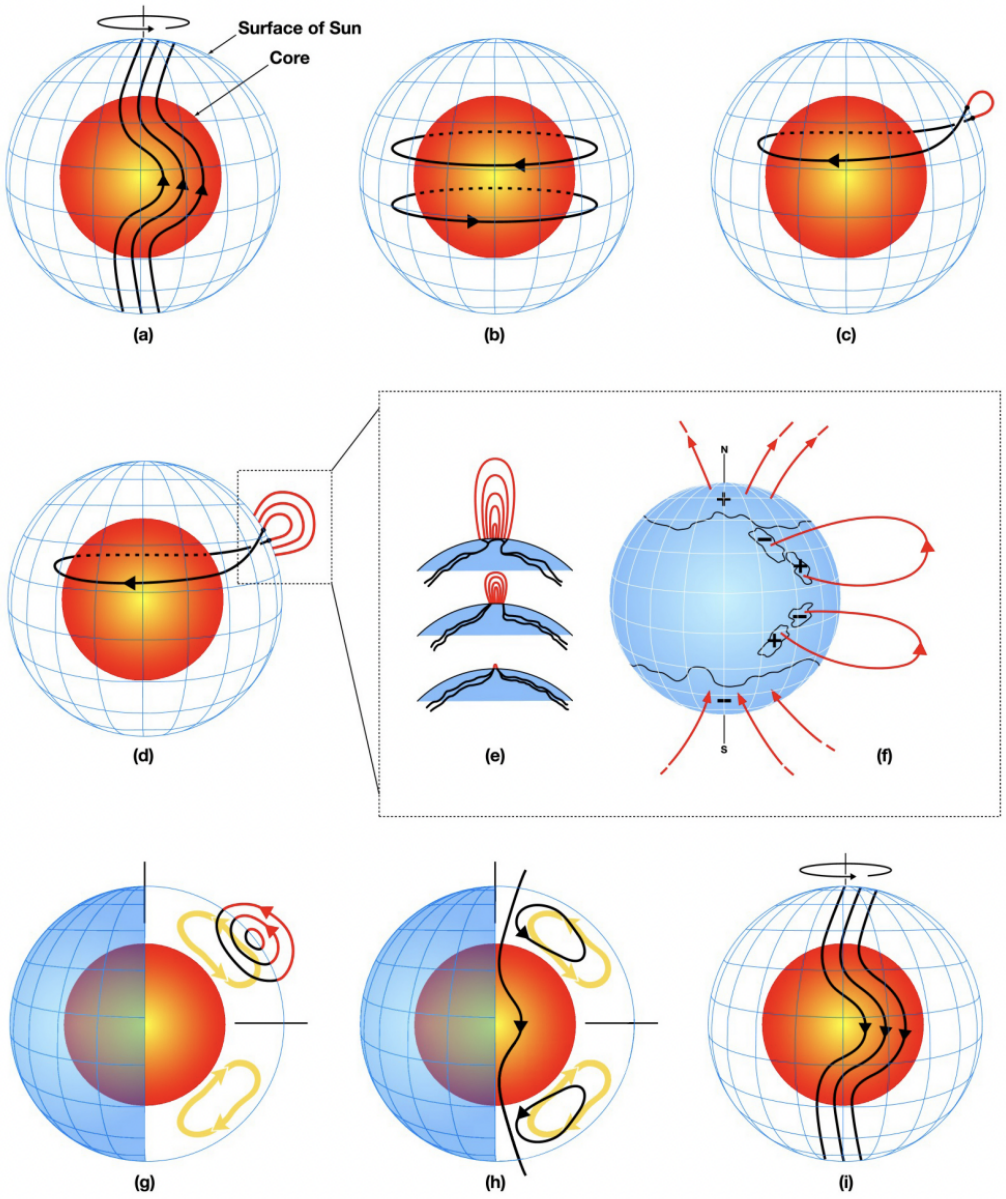

Figure 1.3: 11-year solar magnetic field cycle. The Sun's radiative core is represented by the red inner sphere and the solar surface is represented by the blue mesh. (a) Shearing of poloidal field due to differential rotation at the convection zone. (b) Magnetic field lines get dragged around in a toroidal direction, an action known as the Ω effect. (c) Concentrations of strong toroidal field rise to the surface, forming a bipolar sunspot with a magnetic field extending into the corona. (d,e) Additional flux ropes emerge and spread (f) sunspots and coronal loops form. (g) Due to solar rotation, the Coriolis effect twists these loop back towards north-south orientation reinforcing the original poloidal field, this is known as the α-effect. (h-i) Magnetic field configuration returns to poloidal state. These poloidal fields have a sign opposite to those at the beginning of the sequence, in frame (a). Credit: Dikpati and Gilman (2009)

1.1.2 Solar Magnetic Field

To understand coronal features and activities, we must first discuss the Sun's magnetic field, which is both the scaffolding for structures in the corona and the energy reservoir that powers eruptions. The Sun's magnetic field is created via a dynamo process (see Charbonneau and Paul (2010) for a comprehensive review). This process involves generating a magnetic field through induction by the rotation of a convecting, turbulent, and electrically-conductive fluid. To fully understand how a dynamo is created in the solar context, it is helpful to first outline the solar interior, namely, the *core*, the *radiative zone* and the *convection zone*. The core is the innermost region where mass is converted into energy by the nuclear fusion of hydrogen into helium. The intense energy from the core is transported via thermal radiation in the form of high energy photons in the so-called radiative zone, which extends from 0.25-0.7 $R_\odot$. The temperature drops from $\sim 7\times10^6$ K at the bottom of the radiative zone to 2×10^6 K just below the next layer, the convection zone. Here at the convection zone the solar plasma is cool enough to form highly ionised atoms and becomes optically thick. As a result, this region is convectively unstable and energy is transported through mass motions. The boundary between the co-rotating radiative zone and the differentially rotating convective zone is called the *tachocline*. The onset of differential rotation in the tachocline causes a strong shear, which is regarded to be a major factor in the solar dynamo's cyclic nature.

The Sun's magnetic field configuration is known to vary over an 11-year cycle as shown in Figure 1.3 (Babcock et al., 1961; Parker, 1975; Fan et al., 1993). This cycle describes how the solar magnetic field goes from a poloidal configuration associated with solar minimum to a toroidally stressed state associated with solar maximum. At the beginning of the solar cycle, the solar magnetic field is largely dipolar and aligned to the solar rotation axis, thus each hemisphere has opposite dominant polarity. As the cycle progresses, the differential rotation of the convection zone winds the field

around the solar axis into a stressed state. The process of the large scale twisting transforming the poloidal field to toroidal field is known as the Ω-effect (Figure 1.3a-b). The stored field eventually gets wound into twisted magnetic structures known as flux-ropes (Figure 1.3c). A continuous build-up of magnetic field strength in these flux ropes increases their magnetic pressure and they become unstable and rise up in the form of loops (Figure 1.3d-f). When the field eventually surfaces it creates sunspots in the photosphere and a complex magnetic structure in the solar atmosphere known as an active region (see further details in Section 1.1.3.1). To complete the cycle, the flux ropes experience a Coriolis force that twists the loops back towards north-south orientation reinforcing the original poloidal field, referred to as the α-effect (Figure 1.3g). This results in an overall flip in polarity of the solar magnetic field as seen in Figure 1.3(h-i). This occurs every 11 years, thus a complete cycle to return back to its original state takes 22 years. The constant evolution of the solar magnetic field gives rise to both the observed structure of the corona and energetic events such as solar flares and coronal mass ejections.

1.1.3 Coronal Features and Activities

1.1.3.1 Active Regions

Active regions (AR) are the most prominent feature of the corona. As the name suggests ARs are sites of enhanced activity, where energetic events like flares and coronal mass ejections are likely to originate. ARs are the coronal counterpart to sunspot groups which are seen in the photosphere. Sunspot groups are best observed in magnetograms and at visible wavelengths, as seen in Figure 1.4 (a) and (b), respectively. The AR associated with this sunspot group is observed as bright features in both the chromosphere and corona as seen in (c) and (d), respectively.

Sunspot groups are typically bipolar in nature, with a strongly concentrated leading magnetic polarity, which is followed by a more fragmented trailing group of opposite

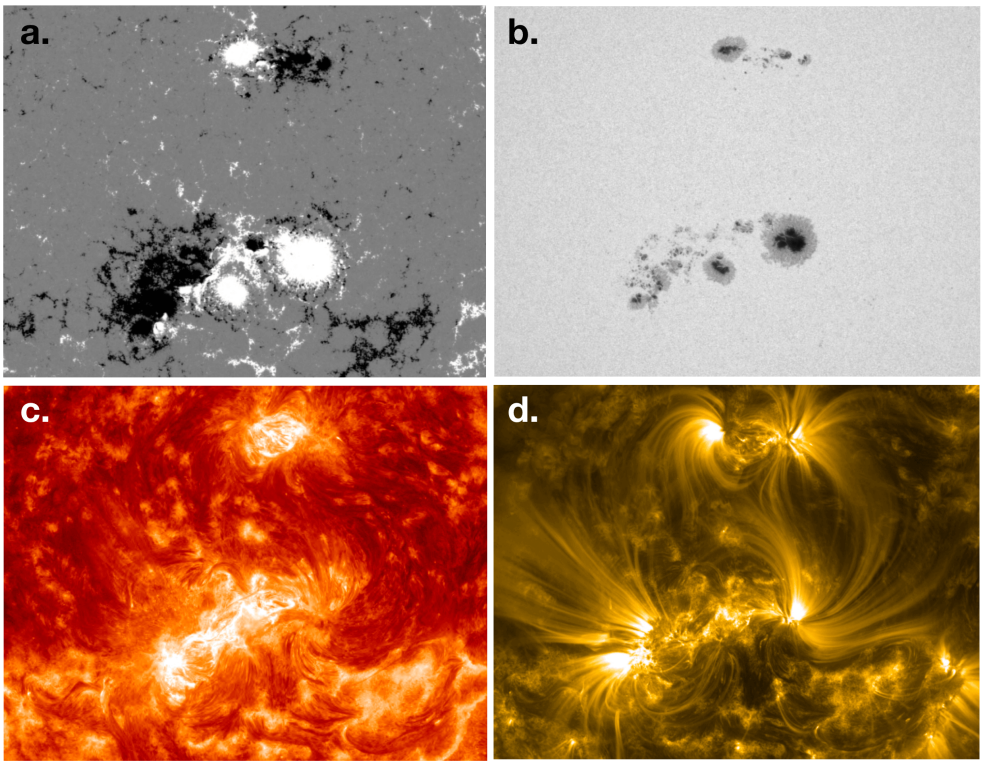

Figure 1.4: Solar Dynamics Observatory observations from Helioseismic and Magnetic Imager (HMI) and Atmospheric Imaging Assembly (AIA) on 7 January 2014. (a) Magnetogram taken by HMI of a sunspot group. The black and white indicating different polarity (b) Continuum intensity map of the sunspot group. The dark central region is the *umbra* and an outer filament structure is known as the *penumbra*. (c) The chromospheric counterpart as seen in the EUV 304 Å passband of AIA. (d) The coronal active region as seen in the EUV 171 Å passband of AIA.

polarity. At the surface, these regions of opposite polarity are often visibly linked by closed magnetic field loops, which can be observed in X-ray and EUV when populated with sufficient plasma. The sunspots on the photosphere typically have magnetic field strengths of ∼1000 G while the magnetic loops in the corona have field strengths of 100-300 G. As a consequence of the strong magnetic field, ARs have a higher average temperature (2-6 MK) compared to the quiet Sun (lower than 1 MK). It should also be noted that more complicated configurations (other than the aforementioned bipolar field configuration) are possible either intrinsically or through additional flux emergence and interactions with preexisting structures (McIntosh, 1990; Jaeggli et al., 2016; Guerra et al., 2018). The constant motion of the photospheric plasma, to which

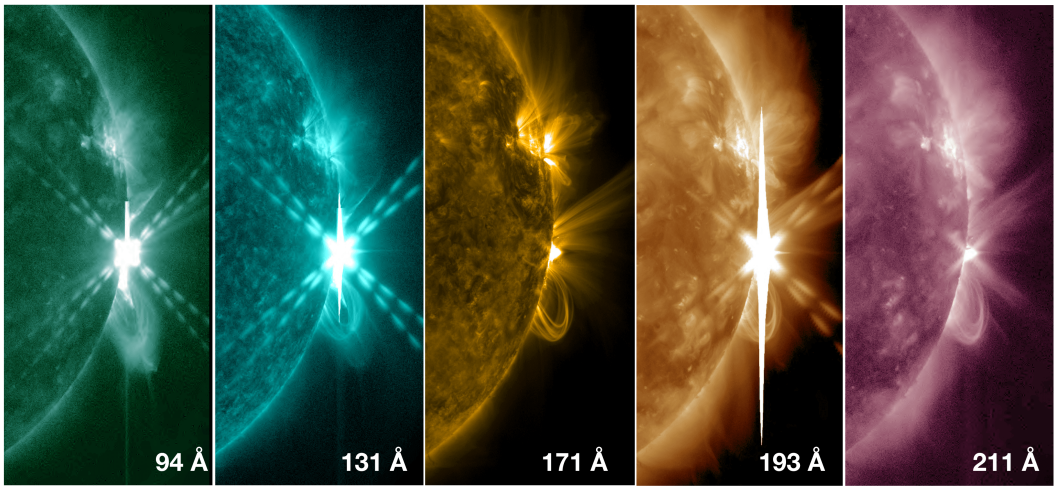

Figure 1.5: X8.2-class flare observed in EUV by NASA's Solar Dynamic Observatory on 10 September 2017 in five different channels; 94, 131, 171, 193 and 211 Å. Credit: NASA/SDO

the coronal loops are connected, causes shearing and twisting in the overlying magnetic loops. This creates an increasingly unstable magnetic configuration until reconfiguration of the magnetic fields occurs.

1.1.3.2 Solar Flares

A solar flare is an intense, localized brightening across the entire electromagnetic spectrum caused by the sudden reconnection of magnetic field lines on the Sun. The process can release up to 10^{32} ergs (10^{25} J) over periods of less than an hour (Emslie et al., 2004) making them the most energetic phenomena in our solar system. The first detailed observations of a flare were documented in 1859 by R. C. Carrington and R. Hodgson, independently (Carrington, 1859; Hodgson, 1859). During routine surveys of a sunspot group, they observed a sudden, intense white-light brightening that lasted for approximately five minutes. Over the next 24 hours, magnetic disturbances were observed at Earth including spectacular aurora at mid-latitudes. The flare that Carrington and Hodgson had witnessed was what we know now to be a white-light flare. Whilst flares are associated with enhanced radiation levels across the majority of the electromagnetic spectrum, only the strongest flares are detectable in white-light

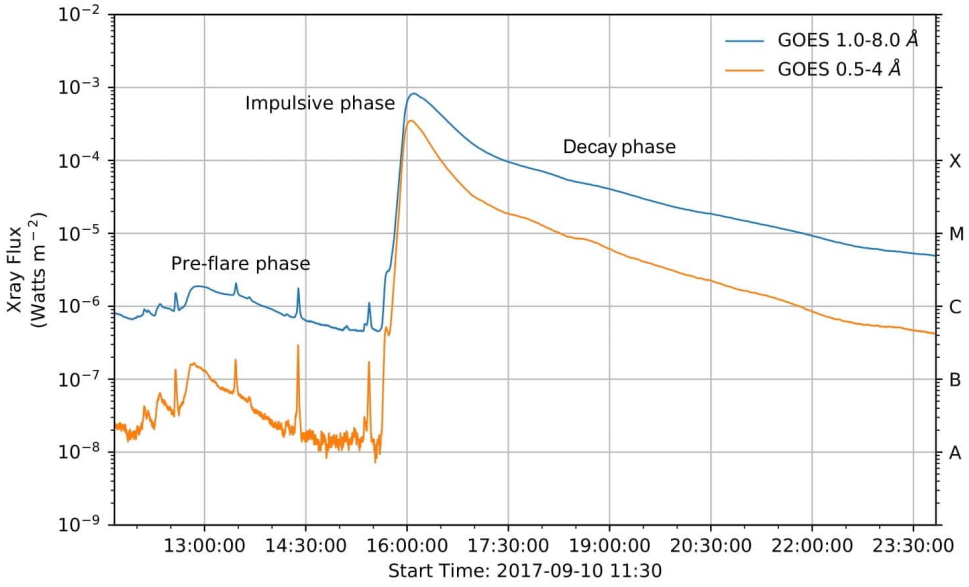

Figure 1.6: X-rays level emission measured by GOES on 10 September 2017. The pre-flare phase, the impulsive phase and the decay phase are labelled.

(Hudson et al., 1992). Despite several decades of observations, the exact nature and underlying physical mechanism that generates solar flares are still being actively debated (See Fletcher et al. (2011); Shibata and Magara (2011) for review on current flare models).

Since the primary flare response is X-ray emission, the magnitude of flares is often characterised according to their peak soft X-ray (SXR) flux in the 1-8 Å channel of the X-ray sensor on-board the Geostationary Operational Environmental Satellite (GOES). Flares are designated a magnitude class, namely A, B, C, M and X. This classification system is base-ten scaled, meaning that each class achieves ten times more in peak SXR flux than the previous, with the X class flares having the highest flux value. Furthermore, each flare classification is given a two-digit designation corresponding to their peak flux value, for example, a flare with peak flux $2.7\times10^{-4}\,\mathrm{Wm}^{-2}$ has a X2.7 classification. An example of an X class flare is shown in Figure 1.5 as imaged by the Atmospheric Imaging Assembly (AIA; Lemen, 2012) instrument onboard the Solar Dynamics Observatory (SDO; Pesnell, 2015) in multiple EUV channels. The

different channels detect EUV emission at different temperatures (see Section 4.2). The intense burst of radiation saturates the instrument's detectors, particularly in the 193 Å channel. Figure 1.6 shows the corresponding GOES X-ray light curve in two passbands (1-8 Å & 0.5-4 Å) for the same flare event.

While the precise physical processes that drive solar flares are not fully understood, the general consensus is that sheared and stressed magnetic field lines in the AR re-organize themselves into a lower energy configuration in a process called magnetic reconnection. This causes the rapid release of magnetic energy, which is converted into both thermal and kinetic energy. The evolution of a flare generally exhibits three distinct phases namely, (1) the pre-flare, (2) the impulsive and (3) decay (or gradual) phase, during which different physical processes dominate (Fletcher et al., 2011; Benz, 2016). In the pre-flare phase (also referred to as the flare precursor), minor activity at EUV and X-ray wavelengths are observed as the flaring region slowly heats up. Eventually, magnetic reconnection between oppositely directed magnetic field lines occurs and there is an abrupt release of stored magnetic energy. The impulsive phase follows. This phase is characterised by the sudden accelerating particles to relativistic, non-thermal energies, transfer of magnetic energy into local plasma heating, bulk plasma flow and generation of waves. Charged particles undergo rapid acceleration from the site of magnetic reconnection, with the majority of particles spiralling down along the newly reconnected closed magnetic field lines towards the chromosphere (Litvinenko, 2003). The accelerated electrons collide with the denser chromospheric plasma that results in non-thermal bremsstrahlung emission, observed as hard X-ray foot-points. Particles that are accelerated upwards, can escape along open magnetic field lines and on occasion produce radio emission in the form of type III radio bursts (see Section 1.2). Plasma and magnetic field structures that are suspended above the flare site may be ejected outwards in what is known as a coronal mass ejection (see Section 1.1.3.5). The impulsive phase of the flare lasts only a few minutes and is followed by a decay phase. During this phase, the bulk energy of the flare is transported in the form of heating

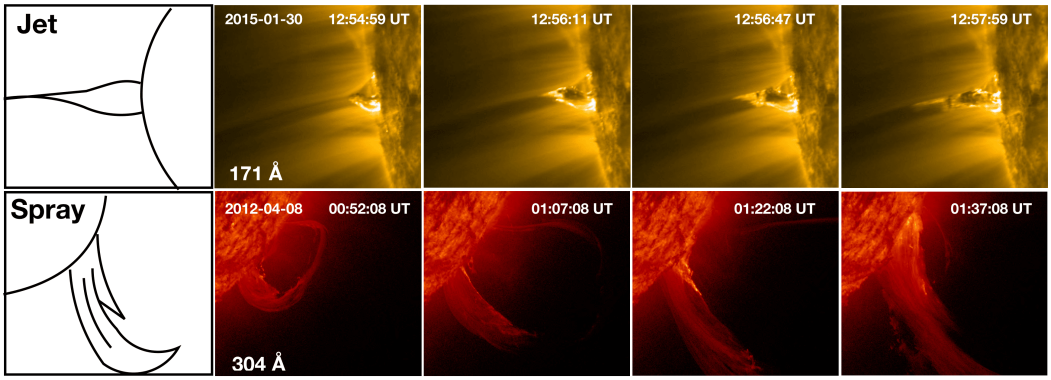

Figure 1.7: Solar eruptions observed by SDO/AIA. The top and bottom panels show the evolution of a coronal jet at 171 Å and spray at 304 Å, respectively.

(Birn et al., 2009). The heating of the chromosphere causes the plasma to expand into the coronal loops above, a process called chromospheric evaporation (Antiochos et al., 1978; Milligan et al., 2006; Milligan and Dennis, 2009). The heated plasma in the loops reaches temperatures on the order of 10^7 K and subsequently emits intense EUV and soft X-ray radiation. As the loops begin to cool and they become detectable in other lower energy wavelength ranges such as H-α. The loops can remain visible for hours after some larger flares until they return to a pre-flare state.

1.1.3.3 Jets and Sprays

Aside from flares, other transient events are observed in the solar corona such as coronal jets and sprays. Figure 1.7 shows the evolution of a coronal jet (top panel) and spray (bottom panel) as seen by the 171 Å and 304 Å EUV channels of SDO/AIA, respectively. A jet most commonly refers to an impulsive, sharp-edged, collimated plasma flow that emerges from the footpoint of an AR. They are observed throughout the solar atmosphere across multiple wavelengths, from UV to X-rays (Mulay et al., 2016; Raouafi et al., 2016). Sprays are similar to jets but they tend to be more fan-like in structure (Gallagher et al., 2000; Li et al., 2002). Currently, the precise mechanism that generates jets and sprays are not fully understood. However, they are most likely the result of magnetic reconnection between the pre-existing overlying coronal field

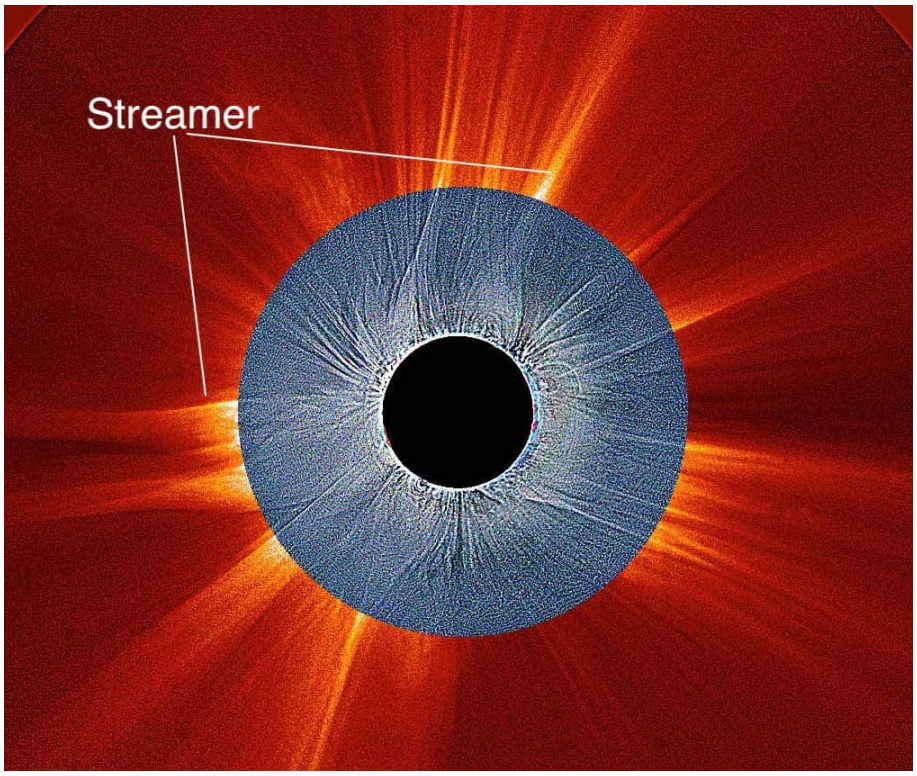

Figure 1.8: A composite image of the corona during the 1999 total eclipse in Iran. The streamers are seen to extend from the solar surface to several solar radii. Credit: Koutchmy et al. (2004).

lines and the newly emerged field lines. Consequently, jets and sprays can manifest in several different solar environments. In Chapters 6 and 7, we return to discussions on jets and sprays in the context of coronal shocks.

1.1.3.4 Streamers

The most prominent and bright features observed in white-light images are coronal streamers. They are high density, cusp-shaped structures that usually observed in the vicinity of ARs and extend radially from the solar surface to several solar radii, as illustrated in Figure 1.8. They are considered to be long-lived coronal structures as they can persist for several days or even much longer. The streamer's morphology reflects the underlying magnetic field configuration, which consists of a region of large-scale closed field lines adjacent to open-field regions (Aschwanden, 2004; Antonucci et al., 2020). A subclass of streamers known as helmet streamers, refer to particularly large

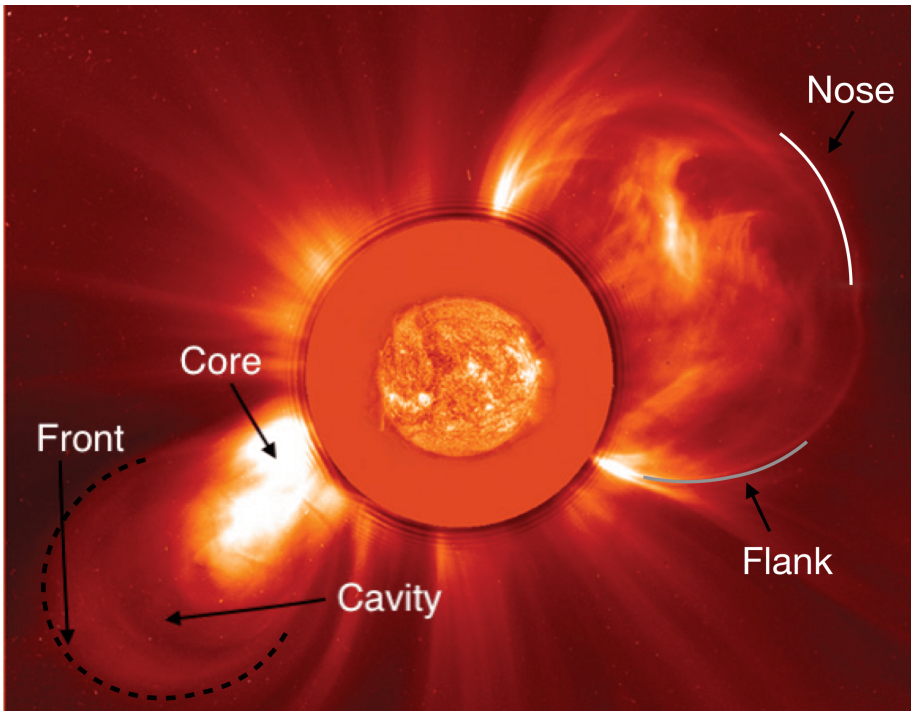

Figure 1.9: A double set of CMEs observed by LASCO C2 onboard SOHO on 8 November 2000. It appears that the two CMEs are propagating in symmetrically opposite directions away from the Sun. The bright core, dark cavity and bright front (indicated by a dashed line) are labelled on one CME. Regions that are considered to be the nose and flank are indicated on the other CME. For reference an image from the Extreme ultraviolet Imaging Telescope (EIT) also onboard SOHO in the 304 Å channel has been superimposed over the occulted Sun. Credit SOHO/ESA/NASA.

and symmetric streamers that connect oppositely polarised active regions. Streamers tend to constrain the outflow of material but dynamical interactions with neighbouring coronal structures can lead to different types of white light features such as coronal mass ejections and streamer puffs (Bemporad et al., 2005; Jiang et al., 2009).

1.1.3.5 Coronal Mass Ejections

Coronal mass ejections (CMEs) are large scale eruptions of plasma and magnetic fields that can propagate from the low corona out into interplanetary space. With kinetic energies of 10^{29} to 10^{32} ergs (Vourlidas et al., 2010), they are the most energetic eruptive phenomena in the solar system and can potentially drive adverse space-weather effects at Earth and the near-Earth environment (Howard, 2014). CMEs are most of-

ten observed by a special white-light instrument called a coronagraph. Either space and ground-based, coronagraphs are specifically designed to obscure emission from the bright solar disk so that the much fainter coronal emission can be imaged. The mass of plasma expelled by a CME can range between 10^{10}-10^{13} kg and consists primarily of electrons, protons and some traces of heavier elements such as helium, oxygen and iron (Vourlidas et al., 2010). While the most energetic of flares are accompanied by CMEs it is important to note that this is not always the case. Many CMEs have been observed without a flare (Vršnak et al., 2005) but also inversely, many flares are not accompanied by CMEs (Vršnak et al., 2005). CMEs have also been associated with prominence eruptions and with the disappearance of filaments on the solar disk (Gopalswamy et al., 2003; Mawad et al., 2015). Fundamentally CMEs are the result of an abrupt change in the coronal magnetic field and represent the conversion of magnetic energy into primarily kinetic energy.

Typically CMEs exhibit a three-part structure, which consists of (1) a bright plasma pile up that envelopes (2) a dark cavity of low electron density with (3) a dense bright core. Figure 1.9 illustrates a textbook example of a CME observed in white-light by the Large Angle and Spectrometric Coronagraph (LASCO; Brueckner et al., 1995). The bright leading edge is referred to as the front, the apex of the CME is referred to as the nose and the sides of the CME are called the flanks. Although the examples in Figure 1.9 are considered to be typical CMEs, numerous observations have shown CMEs to contain no aspect of this three-part structure though (Pick and Vilmer, 2008). Their complex morphologies can sometimes be attributed to projection effects, that is the effect of a three-dimensional structure being projected onto a two-dimensional plane. If the intensity enhancements in consecutive white-light images of a CME are small, difference images are used to detect and enhance CME structures. For example, base difference images involve subtracting a pre-event image from each image taken during an event. Alternatively, running difference images involves subtracting two consecutive images from each other. Although rare, CMEs have also been observed

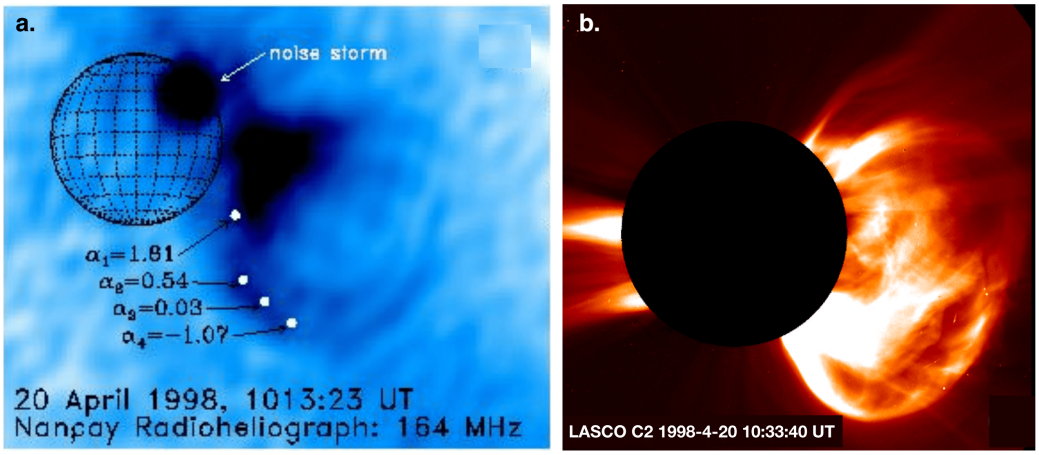

Figure 1.10: Coronal mass ejection observed by (a) Nançay Radioheliograph at radio wavelengths (Bastian et al., 2001) and (b) LASCO C2 at visible wavelengths. The CME shows a similar structure in both images.

at radio wavelengths (Bastian et al., 2001; Maia et al., 2007). Radio CMEs show a similar structure to white-light CMEs as shown in Figure 1.10. The radio emission is believed to be generated via gyrosynchrotron emission from the magnetic fields of the CME (see Chapter 3).

CMEs speeds can range from 100 to 3000 kms^{-1} with the fastest CMEs being most commonly associated with strong flares (Guo et al., 2007; Bein et al., 2012; Veronig et al., 2018). Based on their velocity profile, the CME evolution is divided into three phases, (1) the initial slow rising motion, (2) the impulsive phase during which the maximum acceleration and velocity are reached and (3) the propagation phase during which the CME decelerates as it interacts with the solar wind (Carley et al., 2012). CMEs can also propagate with more or less the constant speed once it has speed similar to the solar wind speed.

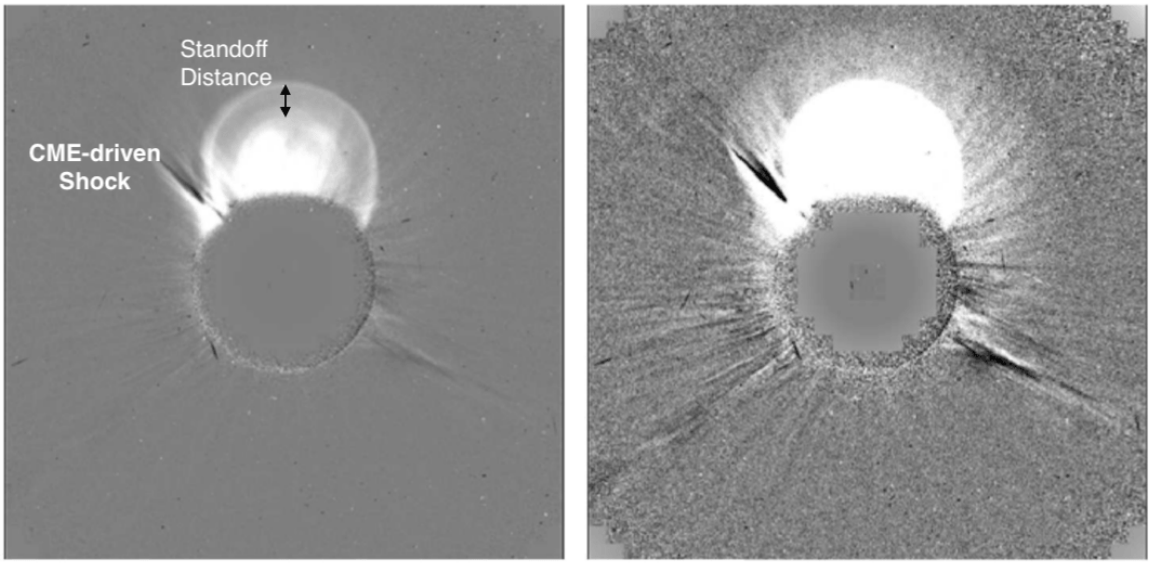

Figure 1.11: CME-driven shock observed in white-light by the coronagraph LASCO C2. Left: The three-part morphology is clear in this example. The much fainter secondary front is a candidate for a shock. Right: The same image is set to a higher contrast ratio. It is important to note that the visibility of the shock depends strongly on the direction of propagation. Adapted from Vourlidas et al. (2013).

1.1.3.6 CME-Driven Shocks

In a magnetised plasma like the corona, information travels at the Alfvén speed v_A (see Section 2.1.3.1). It has a characteristic speed of

$$v_A = \frac{B_0}{\sqrt{\mu_0 \rho_0}} \tag{1.1}$$

where B_0 is the equilibrium magnetic field, μ_0 represents the magnetic permeability, and ρ_0 is the unperturbed mass density of the medium. If the mass movement of the CME travels at a speed that exceeds the local Alfvén speed, a shock may develop (Balogh and Treumann, 2013). These shocks can accelerate electrons, which may excite radio emission in the form of a type II radio burst (Melrose, 1975), along with other heavier particles known as solar energetic particles (Reames, 2013). A full theoretical description of shocks is provided in Section 2.2 and the process by which type II radio bursts are generated is discussed in Section 3.1.

Shocks most often appear close to either the CME nose (Maia et al., 2000; Ramesh et al., 2012) or the CME flank (Cho et al., 2007; Zucca et al., 2014a). Thanks to the high sensitivity of the white-light coronagraph imagers, such as LASCO, shocks that are generated in these regions can be directly imaged (Sheeley et al., 2000; Vourlidas et al., 2010, 2013). When displayed in high contrast, the white-light images reveal a faint front followed by diffuse emission and the bright loop-like CME leading edge (Vourlidas and Bemporad, 2012; Vourlidas et al., 2013). The example provided in Figure 1.11 illustrates the common two-front morphology associated with CME-driven shocks. The bright loop is caused by a pile-up of material at the outer boundary of the eruption, while the faint front is caused by compression of the ambient plasma by the wave or shock front driven by the CME (Ontiveros and Vourlidas, 2009). The distance between the shock front and the CME driver is referred to as the *standoff distance*. White-light images can not only be used to confirm the presence of shocks (a so called white-light shock) and give insight into the shock location, the shape, size, and standoff distance of a shock can be measured from white-light images to infer quantitative shock parameters (Gopalswamy, 2009; Ontiveros and Vourlidas, 2009; Vourlidas et al., 2013; Tun and Vourlidas, 2013; Maloney and Gallagher, 2011). The standoff distance is further discussed in Chapter 5. It is used to infer an important shock parameter, the Alfvén Mach number, which is a proxy for shock strength.

1.1.3.7 Coronal Bright Fronts

Strong solar eruptive events are often associated with large-scale coronal bright fronts (CBFs), observed in EUV images. They are characterised as bright fronts emanating from the source of a solar eruption that often propagates across the solar disk in under tens of minutes. An example is provided in Figure 1.12. Originally termed *EIT waves*, this phenomenon was first observed by the Extreme-ultraviolet Imaging Telescope (EIT), onboard the Solar and Heliospheric Observatory (SOHO). Generally, they propagate at speeds in the range of 200 - 500 kms^{-1} (Thompson and Myers, 2009; Muhr

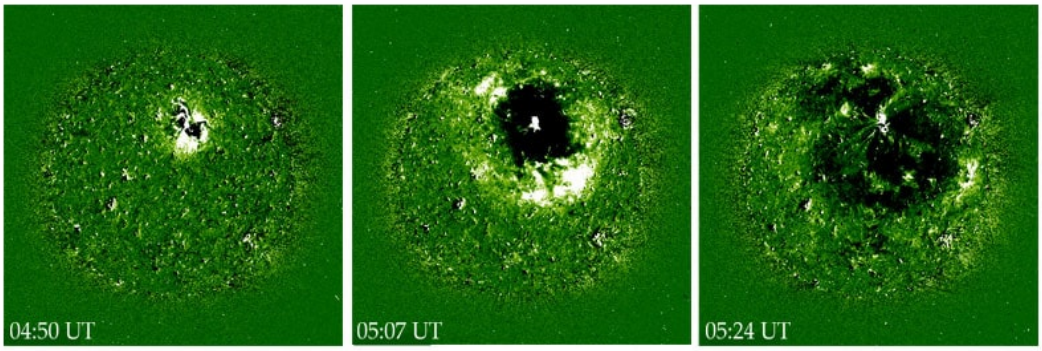

Figure 1.12: Running difference images of coronal bright fronts at several moments in time observed by EIT 195 Å passband. The bright front is hypothesized to be a magnetohydrodynamic wave, driven by an eruptive event in the solar corona. Credit: Thompson et al. (1998).

et al., 2014), however in rare cases, they have been observed to propagate at speeds up to 1400 kms $^{-1}$ (Nitta et al., 2013). Despite numerous observations, the precise physical mechanism that generates CBFs is still under debate. Currently, the proposed mechanisms are divided into two distinct branches, (1) CBFs are waves, either linear or non-linear waves or (2) CBFs are pseudo-waves. According to the wave interpretation, CBFs are fast-mode waves (see Section 2.1.3) driven by CME/flare eruptions. While CBFs have been observed to exhibit wave phenomena such as reflection (Gopalswamy, 2009), refraction (Wills-Davey et al., 1999) and transmission (Olmedo et al., 2012), CBFs have also been observed to remain stationary at coronal hole boundaries for tens of minutes to hours (Delannée et al., 1999) which is inconsistent with the wave interpretation. In the pseudo wave interpretation, a large-scale disturbance like a CME results in the restructuring or reconnecting of coronal magnetic field lines, which manifests as a CBF. The observed brightening is proposed to result from several different processes, including stretching of magnetic-field lines (Chen et al., 2002), Joule heating in a current shell (Delannée et al., 2007) or continuous small-scale reconnection (Attrill et al., 2014).

The inability of either mechanism to fully explain all CBF phenomena has led some to suggest a hybrid theory. Supported by observations (Asai et al., 2012; Shen et al., 2012; Cunha-Silva et al., 2015) and simulations (Chen et al., 2002, 2005) this theory

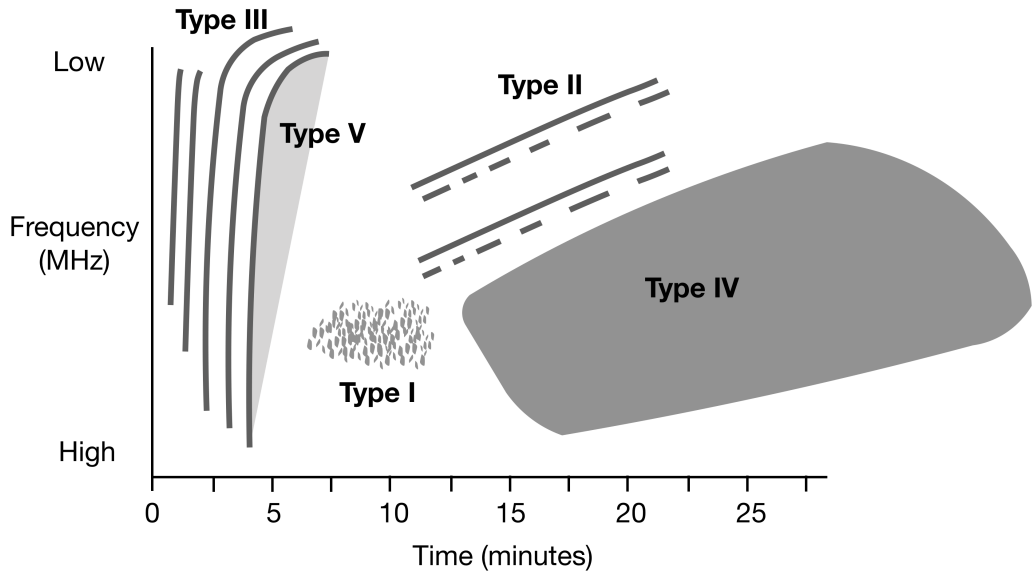

Figure 1.13: Exemplary classification of solar radio bursts by their morphology in a dynamic spectrum. Type II radio bursts are signatures of shocks propagating through the corona. The burst drifts from high to low frequencies indicating that the shock transits from a high to a lower density region.

involves two types of CBFs, a fast-mode wave and a slower pseudo-wave. Comprehensive reviews of all the different potential theories to explain the CBFs can be found in Gallagher and Long (2011), Warmuth (2015) and (Long et al., 2016). The precise relationship between CBFs and radio shock signatures (type II bursts) remains subject to investigation. Some studies suggest 90% of the metric type II bursts are associated with CBFs Klassen et al. (2000) while others suggest a much lower percentage, namely, Nitta et al. (2013) and Muhr et al. (2014) reported a 54% and 22% correlation, respectively.

1.2 Solar Radio Bursts

Solar eruptive events such as solar flares and CMEs are often associated with intense radio emissions known as *solar radio bursts* (Payne-Scott et al., 1947). Radio bursts originate in the corona and are emitted near the local plasma frequency via plasma emission (see Section 3.1). As a consequence, they can be used to infer information

on the coronal environment they were generated in, as well as their exciter. The classification of radio bursts is largely based on their appearance in a dynamic spectrum produced by a radio spectrograph (Wild and McCready, 1950). A dynamic spectrum is a color coded intensity plot of frequency versus time as shown in Figure 1.14. There are five main types of bursts as illustrated in Figure 1.13. The characteristics of each burst (intensity, morphology, duration, etc.) depend on several factors such as the movement of the radio exciter, the structure of the source region, the viewing geometry, and the medium through which the radiation propagates en route to the observer. A burst is categorised into one of five main groups based on its frequency-drift rate (df/dt), its duration (Δt) and the total bandwidth of the emission (Δf_t) as they are observed in the dynamic spectrum. It is important to note that the characteristics described below are valid for bursts observed in the metric to decametric range. The characteristics can somewhat vary at lower and higher frequencies.

Types of radio bursts

1. Type I bursts are short-duration narrow-band bursts with each burst lasting less than 1 s and 3-5 MHz in bandwidth. They are associated with the active regions and can exist for several days (Melrose, 1975). While there is no consensus on their origin, they are most likely related to continuous magnetic reconnection near active regions (Zanna et al., 2011).

2. Type II bursts are slow drifting emission bands that last from a few to tens of minutes. They are associated with shocks propagating in the solar atmosphere. The next section, Section 1.2.1, gives a detailed description of their characteristics and the mechanism by which they are generated. Section 3.2 provides an in-depth description of type II sub-structure.

3. Type III bursts are rapid drifting features that last from a fraction of a second to few seconds and are considered to be the radio signatures of electron beams

escaping along open (or quasi-open) magnetic field lines (Wild and McCready, 1950).

4. A Type IV burst is broad continuum emission that is generated over a wide frequency range and can have either a moving or stationary source (Fokker, 1963). Although the precise origin of type IV bursts is yet to be confirmed, CMEs are accompanied by type IV bursts (see statistical review by Kumari et al. (2021)).

5. Type V bursts are continuum emissions that precede type III bursts by a few seconds. There have been very few observations of type V in recent decades, leading to the belief that they are wrongly classified type III bursts' fine structure.

Solar radio observations show variations in the morphology of radio bursts and different forms of sub-structure. This has prompted the introduction of other classes and several sub-classes in addition to the five main types that are illustrated in Figure 1.13. Some examples are herringbone bursts (Cairns and Robinson, 1987), which are apart of type II bursts (see Section 3.2) and Type IIIb bursts (**?**), which are a subclass of type III bursts that exhibit fine-structures or 'striae' along the main body of the burst. Thanks to the high spectral resolution and sensitivity of modern radio instruments, such as the LOw Frequency ARray (LOFAR; Van Haarlem et al., 2013) we are now able to resolve radio bursts and their sub-structure in unprecedented detail. The fine structure of radio bursts is particularly interesting as they can provide new insight into the mechanisms responsible for the generation of radio emission as well as the nature of the ambient plasma where the radio burst was excited. In this thesis, I will focus on observations of shock-associated type II bursts and their substructure. Type II bursts will be briefly discussed in the next section while a description of their substructure is reserved for Section 3.2.

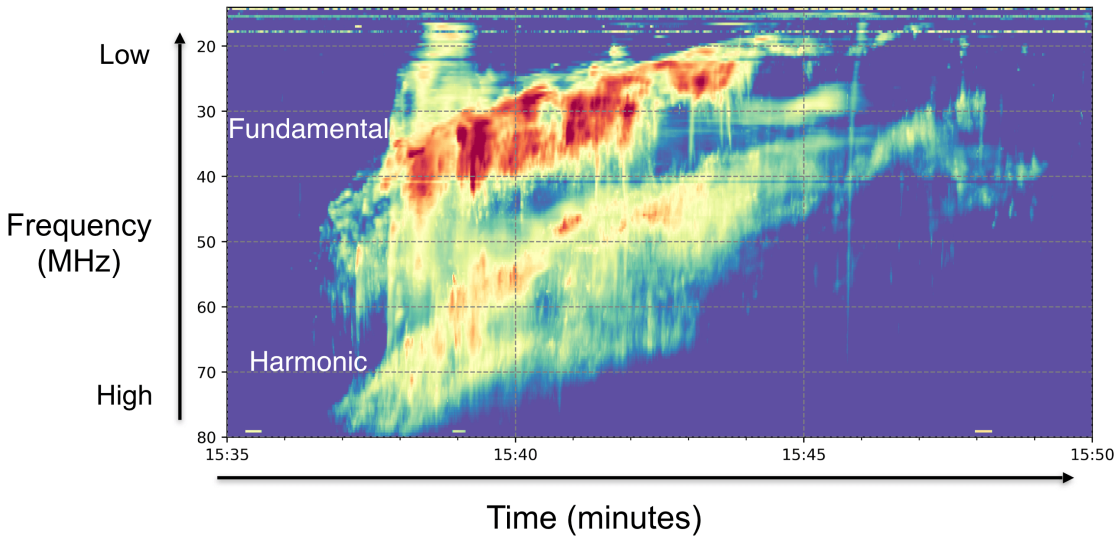

Figure 1.14: First type II radio burst observed by the Irish LOFAR station (I-LOFAR) on 2 September 2017. Both the fundamental and harmonic bands of emission are labelled.

1.2.1 Radio Shock Signature - Type II Radio Bursts

Solar shocks are an extremely complex phenomenon that can have a variety of observational manifestations such as white-light enhancements and EUV coronal bright fronts. Type II radio bursts are considered to be the most reliable and direct diagnostic tool of solar shocks and their drivers. In a dynamic spectrum, type II bursts are distinguished as bright lanes of emission that slowly drift from high to low frequencies over time, as seen in Figure 1.14. They typically have drift rates of -0.1 to -0.4 MHz s^{-1} and last on the order of tens of minutes. These bursts often exhibit two distinct emission bands with a frequency ratio of ∼2:1, which correspond to the fundamental and first harmonic of plasma emission from a single radio source (see Section 3.1 for further details). Uchida (1960) and Wild (1962) were the first to determine the mechanism that type II bursts are associated with today, namely, type II radio bursts are produced by magnetohydrodynamic shocks as non-thermal electrons are accelerated at the shock front and excite plasma oscillations (also known as Langmuir waves) via nonlinear processes. The plasma oscillations can subsequently be converted in part to electromagnetic radiation at radio wavelengths (see Section 3.1). The frequency of the

oscillation, known as the local angular electron plasma frequency ω_p, is related to the electron density n_e of the plasma that the shock transits,

$$\omega_p = \left(\frac{n_e e^2}{m_e \epsilon_o} \right)^{1/2} \tag{1.2}$$

where e is the electron charge, m_e is the mass of an electron and ϵ_o is the permittivity of free space. The value of ω_p is related to the local electron plasma frequency f_p via $\omega_p = 2\pi f_p$. The fact that the type II burst drifts from high to low densities is indicative of a shock propagating through a progressively less dense corona. From a typical coronal density distribution one can infer that bursts at deca-hecto-kilometric wavelengths are associated with interplanetary shocks ($>10\,R_\odot$) while metric and decimetric type II bursts are associated with coronal shock ($<10\,R_\odot$). While it is widely accepted that most interplanetary type II bursts are generated by CME-driven shocks (Vršnak et al., 2004a; Krupar et al., 2016, 2019; Jebaraj et al., 2021), the origin of low coronal shocks is more varied. In the low corona type II bursts have been observed in association with CMEs, erupting loops or plasmoids, ejecta-like sprays and jets (Klein et al., 1999; Dauphin et al., 2006; Zimovets et al., 2012; Carley et al., 2013; Morosan et al., 2019; Maguire et al., 2021; Chrysaphi et al., 2020). An example of a CME-driven type II burst observed by LOFAR is shown in Figure 1.15. Panel (a) illustrates a dynamic spectrum of a type II burst whereby the coloured triangles indicate the points imaged by LOFAR. Panel b shows a running-difference image of the CME observed in white-light with superimposed contours of the radio sources that are coloured to correspond to points in panel (a). The radio sources appear to be on the flank of the CME. Streamer-CME interactions (Feng et al., 2012; Eselevich et al., 2015) in the low corona are also sources of coronal shocks. Some coronal shocks are classified as flare-generated (Magdalenić et al., 2008, 2010, 2012; Pohjolainen et al., 2008; Nindos et al., 2011) because either there was no associated ejecta and/or CME or the timing and velocity of the CME did not coincide with the timing of the type II burst. The study of type II

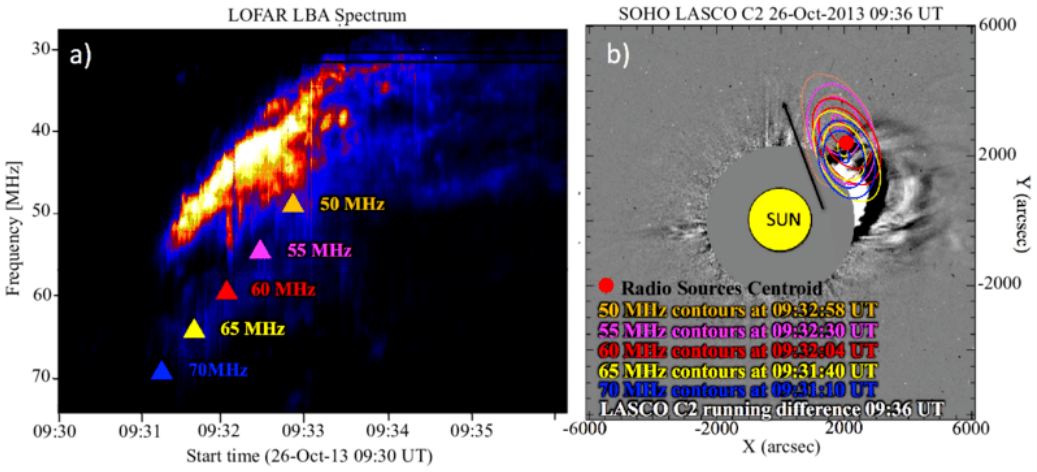

Figure 1.15: (a) Dynamic spectrum of the type II radio burst observed on 26 October 2013. The coloured triangles indicate the points imaged by LOFAR in tied array mode (see Section 4.1.2). (b) Running-difference image of the CME from SOHO/LASCO with superimposed contours of the radio sources that are coloured to correspond to points in panel (a). Credit: Zucca et al. (2014a).

bursts at low frequencies can provide insight into the precise nature of shock formation and propagation in the corona, as well as telling us how electron acceleration and radio emission are generated during these processes. In the next chapter, I outline the basic theory needed to understand shock formation and the shock acceleration processes, beginning with a background to magnetohydrodynamics.

1.3 Space Weather

It should be noted that the magnetic fields and accelerated particles propelled towards Earth during the aforementioned solar activity (Section 1.1.3) can cause a variety of potentially dangerous space weather effects. Space weather is an all-encompassing term that describes the conditions at Earth and in interplanetary space influenced by the Sun's dynamics (Schrijver et al., 2015). The hazards these conditions can create include disruption to radio and GPS communications, damage to satellites, and increased radiation risk to polar flights as illustrated in Figure 1.16. Radio observations are a particularly important tool in our efforts to make reliable and adequate space weather predictions for the Earth's environment. Solar radio burst observations are

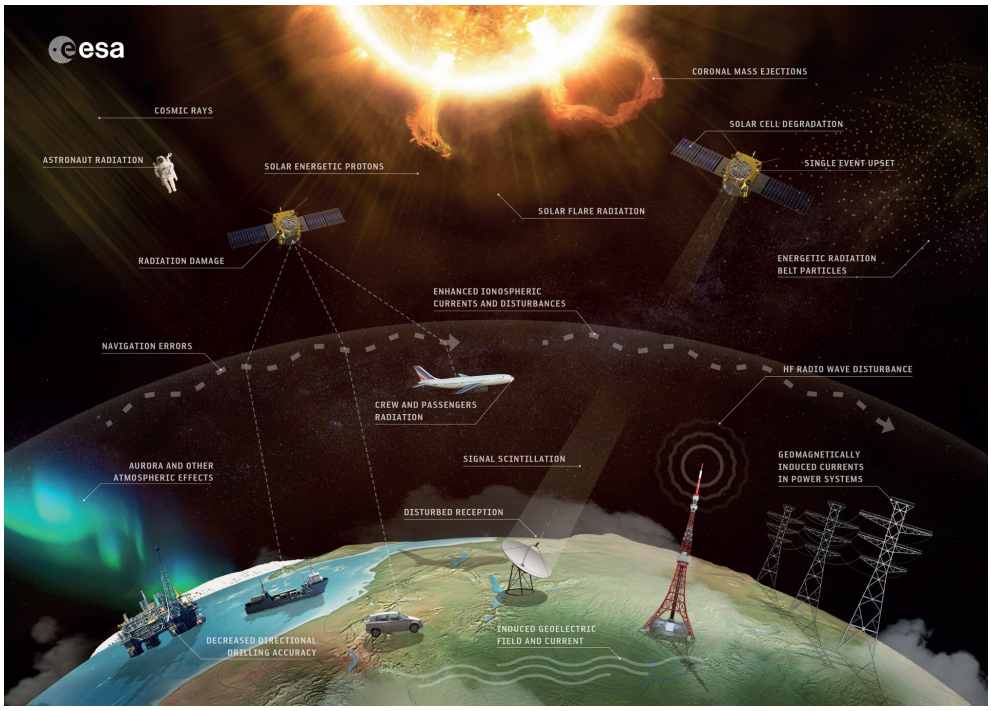

Figure 1.16: Schematic demonstrating the potential impact of solar activity on technology. Solar flares, CMEs and their associated highly energetic particles cause a variety of potentially dangerous space weather effects including interruptions or fatal damage to telecommunication satellites and the risk of dangerous doses of particle radiation for astronauts and passengers on commercial aircraft. Credit: www.esa.int

often used to predict or presage eruptions, to capture the formation stages of CMEs, to follow CME evolution and to detect and track shocks in the corona and heliosphere (Vourlidas et al., 2020). Notably, type II radio bursts that are excited by shock waves (as discussed in Section 1.2.1) are the most reliable and direct tool for detecting coronal shocks and their drivers.

1.4 Thesis Outline

The research contained in this thesis reexamines our understanding of shock formation and propagation, and how electron acceleration and radio emission are generated during these processes. In Chapter 1, an introduction to the solar corona and the main coronal phenomena relevant to this thesis was presented. It includes a description of the main solar features and eruptive activities that are associated with coronal shocks and the different types of radio bursts. This is followed by a more detailed discussion on

the radio signature of solar shocks namely, type II radio bursts. The content of the remaining chapters is outlined below:

- In Chapter 2, I introduce the theoretical frameworks that underpin the research presented in this thesis. Fundamentals of magnetohydrodynamics are described and an introduction to shock theory and shock acceleration processes are presented.

- In Chapter 3, I introduce radio emission mechanisms on the Sun, focusing on plasma emission. Following that I discuss type II radio bursts, which are generated by plasma emission and their observational traits and origin. I conclude by discussing radio-wave propagation effects and their impact on the observed properties of radio bursts.

- In Chapter 4, I describe the main instruments used in this thesis to observe coronal shocks and their associated coronal features. There is a particular focus on ground-based radio interferometers and data analysis techniques and algorithms.

- RESEARCH CHAPTER 1: In Chapter 5, I study the properties of shock in the solar atmosphere and how they evolve with time and distance. Coronal shocks can have a variety of observational manifestations that can be exploited to derive shock properties. Of particular interest is the shock Alfvén Mach number, which is a proxy for the shock strength. In this study, I investigate three commonly used methods of calculating the Alfvén Mach number. This allows us to test the consistency of the methods, but it also allows us to derive more detailed shock characteristics than would normally be available using just one method. This leads to an investigation into the conditions necessary for shocks to efficiently accelerate electrons and generate radio emission. This chapter is based on work published in Maguire et al. (2020).

- RESEARCH CHAPTER 2: In Chapter 6, the origin of a shock generated in the solar atmosphere is investigated. In this study, LOFAR interferometric ob-

servations are used to determine the location of type II burst fundamental and harmonic emission. The radio images reveal a clear separation between the type II fundamental and harmonic components, which contradicts the underlying plasma emission mechanism. Such behaviour is attributed to radio wave scattering in the corona. Using a model I account for scattering effects and determine the true propagation path of the shock. I determine where the radio burst was generated in relation to the eruptive structures and the coronal environment that led to shock formation. This allows us to infer that the type II burst was generated by a particular type of shock, called a piston shock, which was driven by the jet in the low corona. This chapter is based on work in Maguire et al. (2021).

- RESEARCH CHAPTER 3: In Chapter 7, I examine the nature of shock generation associated with a complex solar eruption. Type II bursts can often exhibit variations in morphology and fine structure, which can give us insight into the behaviour of shocks and their associated radio emission low in the solar atmosphere. In this study, radio interferometric images reveal the location of multiple short lanes of a type II emission in unprecedented detail. These observations suggest that a flare spray drove a shock and radio emission was generated in different regions of the shock as it passed through different coronal environments. I also image an intriguing type II feature called band-splitting, the origin of which is the subject of debate. I find that the upper and lower split-bands were co-spatial, which indicates that the emission comes from ahead and behind the shock front. These observations bring new insight into the nature of radio emission generated by shocks in the low corona and highlight the importance of high-resolution radio imaging. This chapter is based on work *in prep* for submission.

- Finally, in Chapter 8 the principal results of this thesis are presented along with potential directions for future work.

2

Plasma and Shock Theory

In this chapter, we introduce the theoretical frameworks that underpin the research presented in this thesis. The solar corona is a plasma, therefore all coronal phenomena can be understood in terms of plasma physics. The macroscopic behaviour of plasma is described in a framework known as magnetohydrodynamics (MHD). The MHD theory couples Maxwell's equations together with hydrodynamic equations to describe large-scale, slow dynamics of plasmas. Since coronal shocks are large scale plasma structures, they can be treated in the MHD framework. Shock particle acceleration processes (that subsequently result in radio emission) cannot be described using MHD. Instead, they must be considered in terms of distribution functions, the Boltzmann equation, and individual particle kinematics.

2.1 Plasma Physics & Magnetohydrodynamics

Before beginning a discussion on the processes that occur in a plasma, it is useful to define what constitutes a plasma. A plasma is a special kind of ionised gas comprised of positively and negatively charged particles of approximately equal charge densities. To be a plasma, long-range forces (Coulomb forces) dominate over short-range forces (van der Waals forces). In other words, the mean free time between collisions in the medium τ_c must be greater than the plasma oscillation period τ_p. Plasma oscillations are standing wave modes whose angular frequency depends only on the number density of the medium (e.g. Equation 1.2). Since many charged particles are subject to the same long-range forces, the motion of each particle is correlated such that a plasma exhibits collective behaviour. In a plasma, the densities of the negative and positive charges are almost equal. If a charge imbalance occurs, the local charges act to restore the charge neutrality. The distance over which the charge is shielded by the charged particles is referred to as the Debye length. To be defined as plasma, the length scale of the system must be much greater than the Debye length. Also, there must be a sufficient number of particles inside the Debye sphere which is a sphere with a radius equal to the Debye length.

2.1.1 Maxwell Equations

To form the basis of plasma theory, it is essential to begin with Maxwell's equations of electromagnetism. They are a set of four differential equations that relate the electric field **E** to the magnetic field **B** and their evolution in time and space,

$$\nabla \times \mathbf{B} = \mu_0 \mathbf{J} + \frac{1}{c^2}\frac{\partial \mathbf{E}}{\partial t} \qquad \text{Ampere's Law} \tag{2.1}$$

$$\nabla \times \mathbf{E} = -\frac{\partial \mathbf{B}}{\partial t} \qquad \text{Faraday's Law Constraint} \tag{2.2}$$

$$\nabla \cdot \mathbf{E} = \frac{1}{\epsilon_0}\rho_c \qquad \text{Gauss' Law} \tag{2.3}$$

$$\nabla \cdot \mathbf{B} = 0 \qquad \text{Solenoid Constraint} \tag{2.4}$$

where $\mathbf{J}$ is the current density, μ_0 is the magnetic permeability, ϵ_0 is the permittivity of free space and ρ_c is the electric charge density. Typically electron velocities are non-relativistic in plasma, therefore the displacement current can be neglected from Ampere's law. Amperes law implies that a temporally changing $\mathbf{E}$ field or electric current induces a $\mathbf{B}$ field. Faraday's and Gauss' laws imply a changing $\mathbf{B}$ field or non zero electric charge density induces an $\mathbf{E}$ field. The final equation called the solenoid constraint implies magnetic monopoles cannot exist. Maxwell's equations describe how electric and magnetic fields behave and they form an important part of the fluid description of plasmas.

2.1.2 Plasma Kinetic Theory

As previously mentioned a plasma comprises many charged particles that exhibit collective behaviour. For a large system, it is inefficient to try and determine the motion of each particle. Instead, a statistical approach is implemented to compute the average motion of a large number of particles. This approach is known as *plasma kinetic theory*. It uses particle distribution functions and differential equations to investigate the evolution of these distribution functions. The distribution function takes the form of the Maxwell-Boltzmann velocity distribution, while the differential equation used to describe its evolution is the Boltzmann equation. The particle distribution function $f(r, v, t)\, d\mathbf{v}\, d\mathbf{r}$ describes the average number of particles having velocities with a small

range from $\mathbf{v}$ to $\mathbf{v} + d\mathbf{v}$ and coordinates with a small range from $\mathbf{r}$ to $\mathbf{r} + d\mathbf{r}$ at time t. By taking appropriately weighted integrals of the distribution function one can determine several important physical properties of an ensemble of particles. This includes (1) the total number of particles, (2) the number density and (3) the bulk velocity:

$$\textbf{1.} \quad N = \int f(\mathbf{r}, \mathbf{v}, t) d^3 r d^3 v \tag{2.5a}$$

$$\textbf{2.} \quad n(\mathbf{r}, t) = \int f(\mathbf{r}, \mathbf{v}, t) d^3 v \tag{2.5b}$$

$$\textbf{3.} \quad \mathbf{u} = \frac{1}{n(\mathbf{r}, t)} \int \mathbf{v} f(\mathbf{r}, \mathbf{v}, t) d^3 v \tag{2.5c}$$

The evolution of the distribution function in time and space is described by the Boltzmann equation:

$$\frac{\partial f}{\partial t} + \mathbf{v} \cdot \frac{\partial f}{\partial \mathbf{r}} + \frac{\mathbf{F}}{m} \cdot \frac{\partial f}{\partial \mathbf{v}} = \left(\frac{\partial f(\mathbf{r}, \mathbf{v}, t)}{\partial t} \right)_{coll} \tag{2.6}$$

where $\mathbf{F} = m\mathbf{a}$ represents any external forces acting on the particles. The terms on the left treat the total time derivative of the distribution function while the term on the right describes the collisional effects experienced by the particles. This equation describes the change in the particle distribution with respect to $(\mathbf{r},\ \mathbf{v}, t)$ in phase space. The Boltzmann equation is of fundamental importance in the kinetic theory of gases and plasmas as it describes the time and space evolution of both equilibrium and non-equilibrium particle distributions. It is arguably the most general kinetic equation available from which all other macroscopic fluid dynamical equations can be derived. However, it is extremely difficult to solve so it is convenient to simplify the equation by assuming that collisional effects are negligible. In the collisionless limit, long-range forces dominate therefore the Lorentz force F_L becomes important:

$$\mathbf{F_L} = q(\mathbf{E} + v \times \mathbf{B}) \tag{2.7}$$

where q is the Coulomb charge, $\mathbf{E}$ is the electric field and $\mathbf{B}$ is the magnetic field. The Boltzmann equation becomes the *Vlasov* equation

$$\frac{\partial f}{\partial t} + \mathbf{v} \cdot \frac{\partial f}{\partial \mathbf{r}} + \frac{\mathbf{q}}{m}(\mathbf{E} + \mathbf{v} \times \mathbf{B}) \cdot \frac{\partial f}{\partial \mathbf{v}} = 0 \tag{2.8}$$

This equation describes the time evolution of the distribution function of a plasma that is interacting with electromagnetic fields and can be used to obtain information on the macroscopic properties of the plasma. A description of the plasma on a macroscopic scale can be derived by taking the appropriate integrals of the Vlasov equation, an approach referred to as taking the moments. The moments of a function are expressed as

$$\mu_n = \int x^n f(x) dx \tag{2.9}$$

where n represents the moments. For example, n=0 and n=1 are the zeroth and first moment, respectively. Taking the moments of the Vlasov equation results in a set of equations known as the *macroscopic transport equations*. They describe (1) the conservation of mass, (2) the conservation of momentum and (3) the conservation of energy and together they form the basis of plasma fluid theory:

$$\textbf{1.} \int [\text{Vlasov equation}] \times v^0 d\mathbf{v} \tag{2.10a}$$

$$\textbf{2.} \int [\text{Vlasov equation}] \times v^1 d\mathbf{v} \tag{2.10b}$$

$$\textbf{3.} \int [\text{Vlasov equation}] \times v^2 d\mathbf{v} \tag{2.10c}$$

The dynamics and conservation equations for each particle species in the plasma can be considered separately using a multi-fluid approach, that is electrons and protons are considered to have different conservation equations. Alternatively, the plasma can be considered as a single fluid and can be described under the framework of MHD. This

approach is expanded upon in the following section.

2.1.3 Magnetohydrodynamics

The first MHD equation that comes from the zeroth-order moment of the Vlasov equation describes the conservation of mass,

$$\frac{Dn}{Dt} = -n\nabla \cdot \mathbf{v} \tag{2.11}$$

where n denotes the number density, $\mathbf{v}$ is the bulk velocity and D represents a Lagrangian derivative, $D/Dt = \partial/\partial t + v \cdot \nabla$. This expression implies that the rate of change of particles into or out of a volume is controlled by the bulk flow of the fluid. The second equation which stems from the first-order moment of the Vlasov equation describes the conservation of momentum,

$$mn\frac{D\mathbf{v}}{Dt} = qn(\mathbf{E} + \mathbf{v} \times \mathbf{B}) - \nabla \cdot \mathbf{P} + \mathbf{P_{ij}} \tag{2.12}$$

where $\mathbf{P}$ is the pressure tensor and $\mathbf{P_{ij}}$ is the sum of all the forces due to collisions. This equation is also referred to as the *momentum transport equation* and it represents force balance on components of the plasma. In other words, the rate of change of momentum of a fluid is due to the Lorentz force, pressure and collisions. This equation can be further simplified to obtain the equation of motion for bulk plasma. The first step is to add in the individual transport equations for both electrons and ions. We neglect the convective term $\mathbf{v} \cdot \nabla\mathbf{v}$ since the gradient is negligible over small perturbations. The second step is to consider a simple hydrostatic case so that the pressure tensors on the system are the pressure due to gravity ($\rho\mathbf{g}$) and fluid pressure gradient (-∇p) and pressure due to Lorentz force ($\mathbf{J} \times \mathbf{B}$). The new simplified expression is

$$\rho\frac{d\mathbf{v}}{dt} = -\nabla p + \mathbf{J} \times \mathbf{B} + \rho\mathbf{g} \tag{2.13}$$

In the case of equilibrium, the acceleration term goes to zero and gravitational forces are negligible compared to the pressure and electromagnetic effects. The expression reduces further to

$$\nabla p = \mathbf{J} \times \mathbf{B} \tag{2.14}$$

Substituting in Ampere's Law (Equation 2.1) for $\mathbf{J}$ we obtain

$$\nabla p = -\frac{1}{\mu_0}(\nabla \times \mathbf{B}) \times \mathbf{B} \tag{2.15}$$

which can be further simplified using a vector identity,

$$\nabla p = \frac{1}{\mu_0}(\mathbf{B} \cdot \nabla)\mathbf{B} - \nabla\frac{B^2}{2\mu_0} \tag{2.16}$$

and rearranging

$$\nabla(p + \frac{B^2}{2\mu_0}) = \frac{1}{\mu_0}(\mathbf{B} \cdot \nabla)\mathbf{B} \tag{2.17}$$

The terms on the left denote gas and magnetic pressure while the term on the right is referred to as the magnetic tension and acts to restore a curved magnetic field line to a straight line. The above expression states that any gradient in the magnetic and gas pressure will induce a force. A plasma will achieve a state of equilibrium when there is a balance between gas and magnetic pressure. The ratio of these two terms is referred to as the plasma β,

$$\beta = \frac{P}{B^2/2\mu_0} \tag{2.18}$$

which gives a measure of the "efficiency" of plasma confinement by $\mathbf{B}$. Figure 2.1 illustrates the plasma β as a function of height in the solar atmosphere. In the photosphere the, plasma $\beta >> 1$ meaning the gas pressure term dominates so that the plasma motion carry the field lines. Ascending into the chromosphere and corona, the plasma $\beta << 1$ meaning the magnetic pressure term dominates so that plasma is constrained to flow along the magnetic field lines. Even further out into the corona, the plasma β

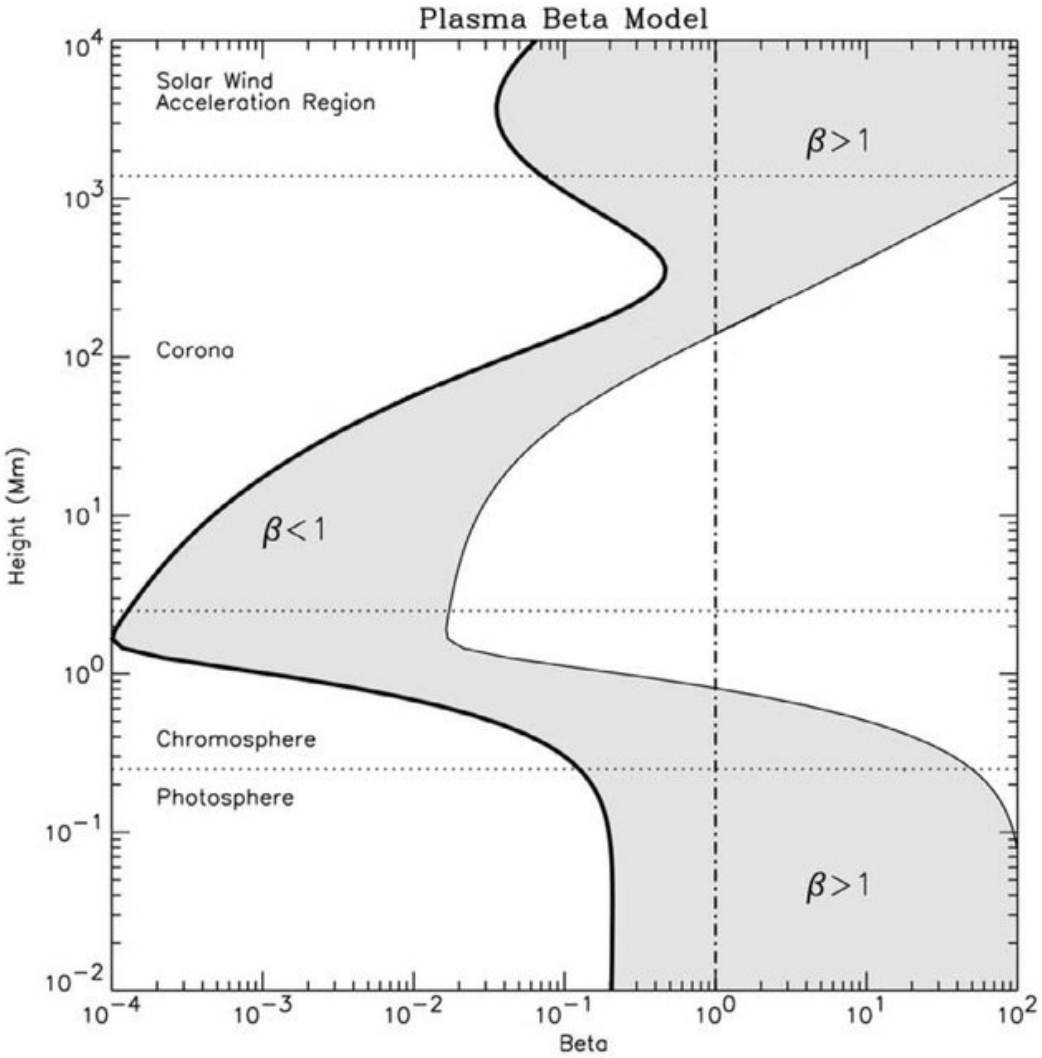

Figure 2.1: The plasma β plotted as a function of height above the photosphere, adopted from Gary (2001). The shaded region corresponds to open and closed magnetic field lines originating between a sunspot of 2500 G and a plage region of 150 G.

decreases further again.

The second moment of the Vlasov equation gives the conservation of energy equation

$$mn\frac{De}{Dt} + p\nabla \cdot \mathbf{v} = \nabla \cdot (\kappa \cdot \nabla T) + \eta_e \mathbf{j}^2 + Q_\nu - Q_r \tag{2.19}$$

where the internal energy per unit mass is

$$e = \frac{p}{(\gamma - 1)\rho} \tag{2.20}$$

γ is the ratio of specific heat capacities C_p/C_V, κ is the thermal conductivity, T is the temperature, η_e is the electrical resistivity, Q_ν is heating by viscous dissipation and Q_r is a radiative loss term. This expression describes the evolution of internal energy in terms of the divergence in the flow field, conduction, Ohmic and viscous dissipation, and radiative loss. The simplest assumption is adiabatic flow whereby there is no change in internal energy of the fluid:

$$p\rho^{-\gamma} = constant \tag{2.21}$$

The final MHD equation is an expression for the evolution of the magnetic field. Beginning with the conservation of momentum equation (Equation 2.12) we obtain a reduced version of the generalised Ohm's law for a plasma,

$$\mathbf{J} = \sigma(\mathbf{E} + \mathbf{v} \times \mathbf{B}) \tag{2.22}$$

where σ is plasma conductivity. The electric field $\mathbf{E}$ and current $\mathbf{J}$ can be eliminated by incorporating Faraday's and Ampere's laws into Ohm's Law. By the simple use of a vector identity the above equation reduces to

$$\frac{\partial \mathbf{B}}{\partial t} = \nabla \times (\mathbf{v} \times \mathbf{B}) + \eta \nabla^2 \mathbf{B} \tag{2.23}$$

where $\eta = 1/\sigma\mu$ is the magnetic diffusivity and σ is plasma conductivity. This is an important equation as it describes the evolution of a magnetic field in a plasma in terms of fluid flow velocity and magnetic diffusivity. The terms on the right describe processes of magnetic advection and diffusion, respectively. For the case of plasma $\beta >> 1$, advection dominates meaning the magnetic field is frozen into the plasma. In other words, when the plasma moves so does the magnetic field. Conversely when plasma $\beta << 1$, diffusion dominates and under this regime magnetic reconnection occurs.

In conclusion, including the equation of state

$$p = nk_BT \tag{2.24}$$

where p is the pressure, k_B is Boltzmann constant and T is temperature, we obtain a fully closed set of MHD equations:

$$\frac{D\rho}{Dt} = -\rho\nabla\cdot\mathbf{v} \tag{2.25}$$

$$\rho\frac{D\mathbf{v}}{Dt} = -\nabla p + \frac{1}{\mu_0}(\nabla\times\mathbf{B})\times\mathbf{B} + \mathbf{f} \tag{2.26}$$

$$\frac{D\rho}{Dt} = -\gamma p\nabla\cdot\mathbf{v} + (\gamma-1)\frac{\eta}{\mu_0}(\nabla\times\mathbf{B})^2 \tag{2.27}$$

$$\frac{\partial\mathbf{B}}{\partial t} = \nabla\times(\mathbf{v}\times\mathbf{B}) + \eta\nabla^2\mathbf{B} \tag{2.28}$$

$$\nabla\cdot\mathbf{B} = 0 \tag{2.29}$$

We get the MHD wave modes when we perturb and linearize the MHD equations, and assume time and space harmonic solutions.

2.1.3.1 MHD waves modes

Perturbations in gas pressure, magnetic field, density or any other macroscopic property of the plasma results in the generation of several wave modes. These wave modes can be solely acoustic, with waves propagating at the speed of sound due to gas pressure perturbations, or solely magnetic, such as Alfvén waves where the restoring force is provided by magnetic tension. A combination of the two wave modes can result in magneto-acoustic waves, characterised by perturbations in both gas and magnetic pressure. Linearisation of the MHD equations allows one to derive important properties of each of the plasma wave modes, namely their phase velocity, group velocity, or their longitudinal or transverse nature. Of particular interest in this thesis is the Alfvén wave (Equation 1.1). Alfvén waves are incompressible waves that propagate parallel

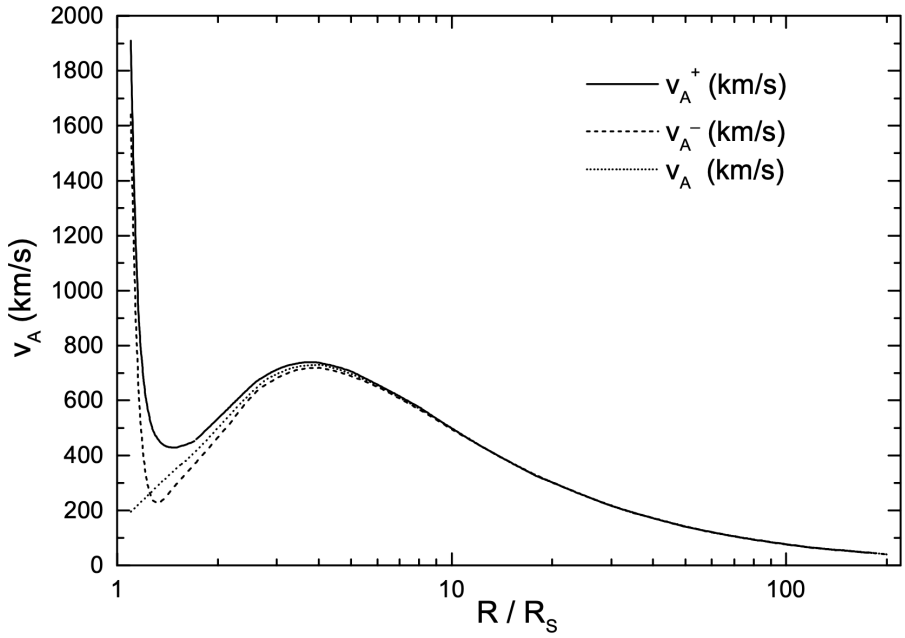

Figure 2.2: Model of Alfvén speed v_A in the corona under different conditions. The dotted line is the v_A for quiet Sun conditions, assuming the Sun's global magnetic field is a dipole. The solid line is the v_A for a combination of the global dipole field and a smaller active region dipole field oriented parallel to the global dipole. The dashed line is the v_A when the active region dipole is anti-parallel to the global field. Credit: Mann et al. (2003)

to the magnetic field and owe their existence to tension in magnetic field lines. For the case of a quiet solar corona in the range 1 to $3\,R_\odot$, the magnetic field decreases from 100 to 1 G and the electron number density decreases from 10^9 to 10^6 cm^{-3}, therefore the Alfvén speed is typically on the order of 10^2 to 10^3 kms^{-1}. In contrast to Alfvén waves, magneto-acoustic waves are compressible, with magnetic and gas pressure forces acting as the restoring forces. Their characteristic speeds are

$$v_{f/s} = \left(\frac{1}{2}\left[v_A^2 + c_s^2 \pm \sqrt{(v_A^2 + c_s^2)^2 - 4v_A^2 c_s^2 cos^2\theta_B}\right]\right)^{1/2} \tag{2.30}$$

where c_s is the speed of sound. The positive option of the $\pm$ gives the fast magneto-acoustic mode, the negative option gives the slow magneto-acoustic mode. The fast magneto-acoustic can propagate in almost any direction provided that the gas and magnetic pressure are in phase. While the slow magneto-acoustic waves propagate with

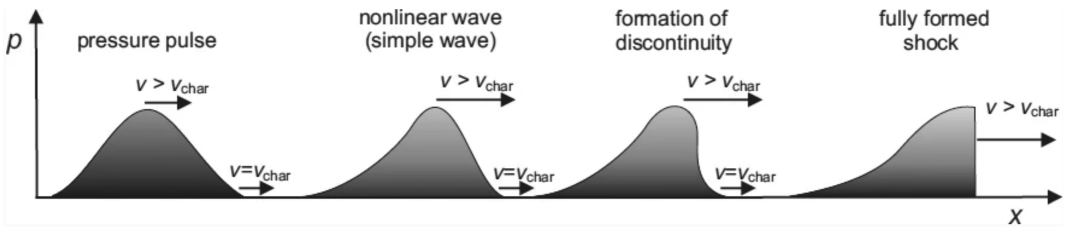

Figure 2.3: Schematic showing the evolution of a nonlinear wave and formation of shock. The pressure of the wave is expressed as a function of distance. An initial large-amplitude pressure pulse propagates with speed v in medium with the characteristic velocity v_{char}. The crest of a wave propagates faster than the leading or trailing edge to form a nonlinear or simple wave. The wavefront steepens until a discontinuity is established and a shock may form. Adapted from Warmuth (2015).

the gas and magnetic pressure out of phase and are much slower than Alfvén waves. In the corona since the magnetic pressure dominates (plasma $\beta << 1$), magnetic perturbations propagate faster than gas pressure perturbations, therefore the Alfvén wave is the most dominant mode for information to travel in the low corona. Figure 2.2 illustrates the (Mann et al., 2003) one dimensional model of Alfvén speeds in a quiet and active corona as a function of heliocentric distance. Any solar ejecta that propagates in excess of the Alfvén speed will produce a shock.

2.2 Coronal Shocks

Thus far we have discussed linear MHD waves (the linear solutions to the ideal MHD equations), which is a reasonable approach when the amplitude of the disturbance is small. In the case of large-amplitude disturbances, like those generated by eruptive events in the corona, nonlinear terms become important and nonlinear wave steepening occurs. Figure 2.3 displays a schematic of the evolution of a nonlinear wave to a shock. In this scenario, the crest of the wave propagates faster than the leading or trailing edge, due to the compression of the density and the magnetic field. This leads to a reshaping of the wave profile as the wave crest catches up with the wave troughs. The result is a nonlinear large-amplitude wave or simple wave as shown in the schematic. The wavefront may continue to steepen until a discontinuity is

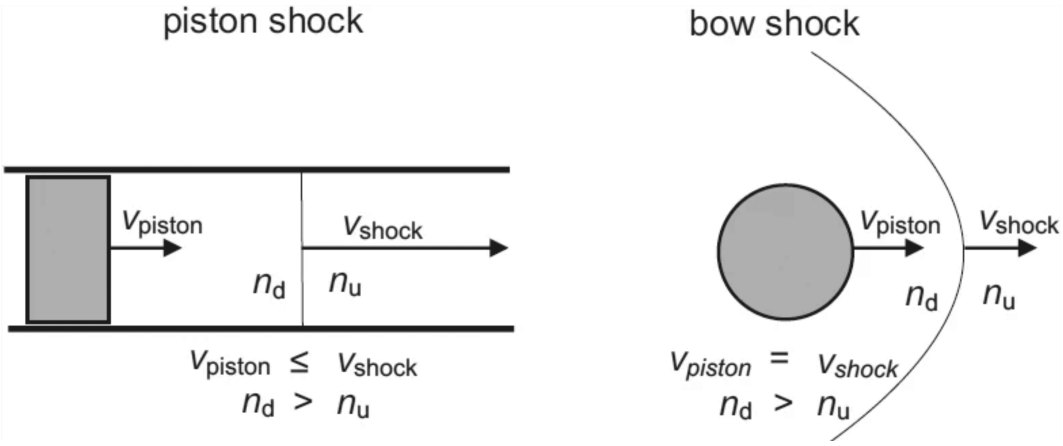

Figure 2.4: Schematic of a piston-driven shock (left) and bow shock (right). In a piston-driven case, the shock travels faster than the driver and decouples from the piston before it propagates freely. In the bow-shock scenario, both the shock and driver propagate at the same velocity. Adapted from Warmuth (2007).

established and a shock forms. Essentially, a shock is a disturbance across which physical parameters of the medium, such as velocity, density, pressure and temperature, change almost discontinuously. Both fast-mode and slow-mode nonlinear MHD waves can form shocks. For example, in the case of a fast-mode shock, the shock speed exceeds the fast-mode speed of the upstream region, the density downstream is greater than the density upstream ($n_d > n_u$) and the magnetic field component parallel to the shock front increases in magnitude by the same ratio as the density ($B_d > B_u$). With these constraints, most astrophysical shocks are fast-mode shocks (Balogh and Treumann, 2013). The theory of shocks in plasma and shock particle acceleration that result in plasma emission is discussed in the following sections.

2.2.1 Shock Classification

Shocks can be categorised according to how they are generated. There are two possible mechanisms, (1) a propagating blast wave or (2) a driven shock. In the blast wave scenario, nonlinear steepening occurs in a large-amplitude wave generated by a blast/explosion. The local wave speed increases with amplitude so that the wave crest is faster than the trough. The wave profile becomes infinitely steep, until a disconti-

nuity is established and a shock is formed. As the shock propagates, the amplitude of the wave drops due to geometric expansion, dissipation and widening of the wave profile. Eventually, the shock decays to a small amplitude wave. In a solar context, blast waves are generally associated with explosive energy conversion in flares (Hudson and Warmuth, 2004; Kumar et al., 2016; Eselevich et al., 2019).

In the driven shock scenario, the driver provides a constant supply of energy to the shock. In a solar context, driven shocks are most often attributed to CMEs, jets, erupting loops and other plasma ejecta. The two types of driven shocks are (1) piston-driven and (2) bow shock as illustrated in Figure 2.4. In a three-dimensional (3D) piston-driven shock scenario, the expanding driver pushes the plasma in all directions. The one-dimensional counterpart is a piston moving in a tube, such that the medium ahead of the piston cannot flow around the driver. In such a case even if the piston has a velocity slower than the characteristic speed of the medium (subsonic/sub-Alfvénic), a shock can form. The distance between the driver and shock increases with time and the shock speed can be several times that of the driver. In some special cases if the piston-shock is only temporarily driven then a freely propagating shock or blast wave is established. In the case of a bow shock, the ambient medium can flow around the driver so that the shock and driver are seen to propagate at the same speed (Cho et al., 2007; Schmidt et al., 2016). In this case, the driver must be supersonic/super-Alfvénic to produce the shock. The standoff distance between the bow-shock depends on the driver velocity, as well as on the size and the shape of the driver (Russell and Mulligan, 2002).

2.2.2 Shock Theory

Shocks can be generated across a wide range of spatial and temporal scales under diverse conditions, examples of astrophysical shocks include the shock at the edge of the heliosphere (Jokipii, 2013), planetary bow shocks (Balogh and Treumann, 2013) and supernova shock waves (Weaver, 1976). They can occur in both collision dominated

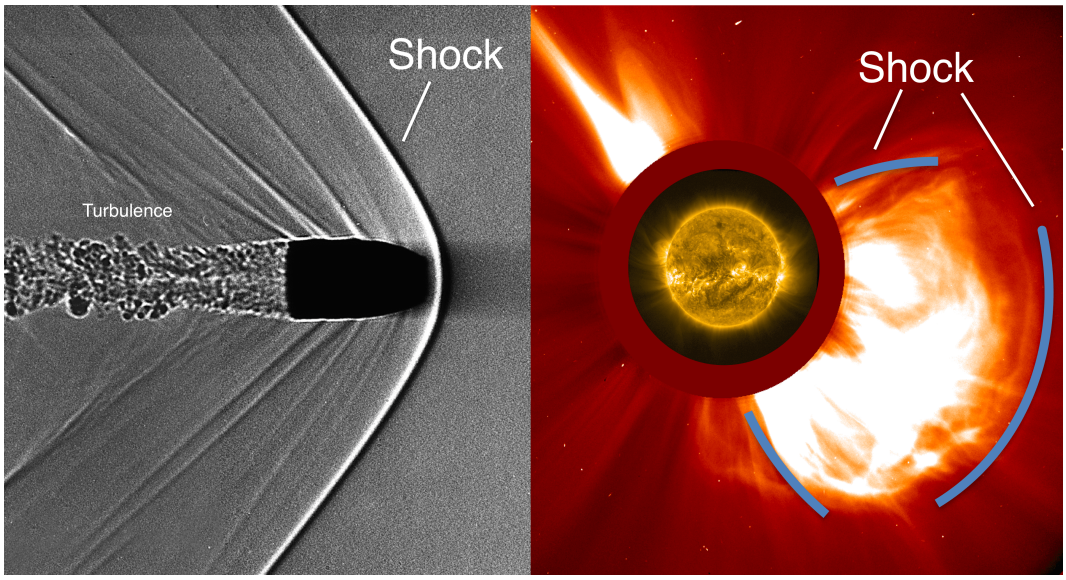

Figure 2.5: (Left) An example of a collisional shock. An image of a bullet travelling through air at speeds faster than the speed of sound. The curved line ahead of the bullet indicates the bow shock and turbulent wake trails behind it. Credit: NASA.GOV. (Right) An example of a collisionless shock. A CME-driven white-light shock observed by the coronagraph, LASCO. An image of the EUV Sun is overlaid for context. Credit: NASA.GOV.

media like Earth's atmosphere and in collisionless media like the corona. Examples of a collisional and collisionless shock are shown in Figure 2.5. The shock thickness is considered to be a thin surface compared to the mean free path for collisions for a gas or Debye length scales for a plasma. In collisional shocks, the binary collisions between particles cause temperature and density perturbations to propagate resulting in kinetic energy dissipation. The collisions allow for the temperature equalisation of different species of molecules. Collisional shocks are described in terms of the macroscopic fluid equations containing quantities such as density, temperature and bulk (rather than thermal) velocity. Conversely, shocks in astrophysics are considered to be collisionless since the Coulomb energy of the inter-particle interaction is small compared to the kinetic energy of the particle random motion. This means non-collisional processes are required to dissipate the kinetic energy. Complex interactions between particles and the electromagnetic fields that permeate the shock facilitate energy dissipation in collisionless media.

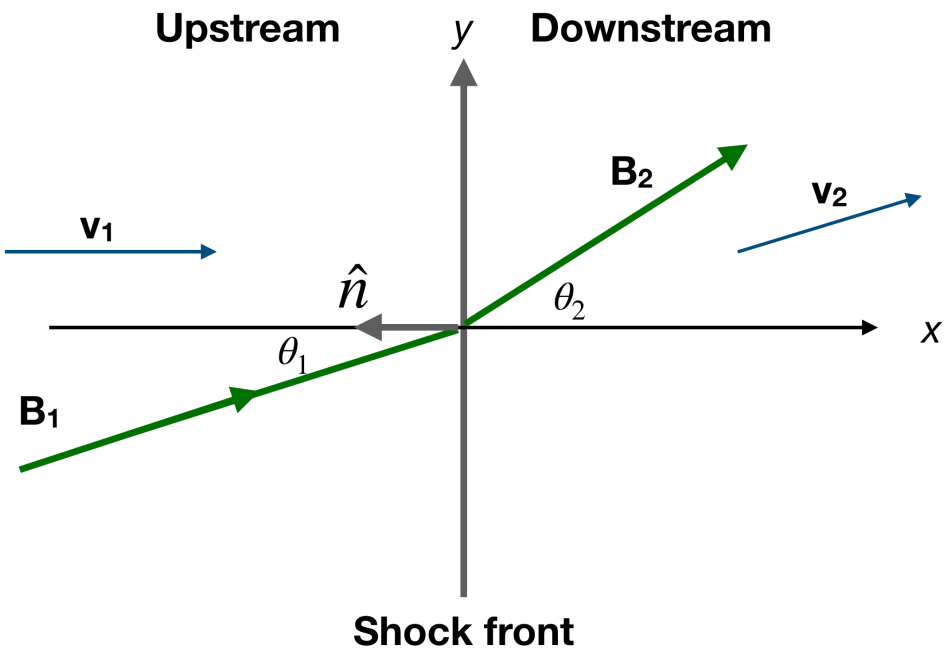

Figure 2.6: Schematic of the various fields, flow and normal vectors in the Normal Incidence Frame (NIF). In this frame, the shock is at rest and the upstream plasma is directed along the shock norm. The subscript 1 and 2 denotes the upstream and downstream region, respectively.

Conveniently, collisionless shocks can be described using the same theoretical framework used to describe collisional shocks. This involves applying MHD conservation equations across the shock front as a means to relate the upstream gas pressure, magnetic pressure, density, flow speed, and temperature to their downstream counterparts. The resulting set of equations are referred to as Rankine-Hugoniot jump conditions. It is customary to treat the jump conditions in a reference frame known as the Normal Incidence Frame (NIF), whereby the shock is at rest and the upstream flow is directed along the shock normal as shown in Figure 2.6. The velocity v and magnetic field B are interpreted as being in the xy-plane. In this frame, the upstream plasma has a velocity $\mathbf{v}$ along the normal to the shock front, the magnetic field lines make an angle θ with the shock normal and the downstream components have corresponding values v_2 and B_2. The Rankine-Hugoniot jump conditions are derived from the equations of

continuity for mass, momentum and energy, together with boundary conditions arising from Maxwell's equations:

$$[\rho v_x] = 0 \tag{2.31}$$

$$[\rho v_x^2 + p + \frac{B_y^2}{2\mu}] = 0 \tag{2.32}$$

$$[\frac{1}{2}v^2 + \frac{\gamma p}{(\gamma - 1)p} + \frac{B_y(v_x B_y - v_y B_x)}{\mu \rho v_x}] = 0 \tag{2.33}$$

$$[B_x] = 0 \tag{2.34}$$

$$[v_x B_x - v_y B_x] = 0 \tag{2.35}$$

where ρ is the mass density, p is the gas pressure, γ is the ratio of specific heat capacities or the adiabatic index. The square brackets represent the change in any quantity across the shock boundary, for example $[A] = A_1 - A_2$ where 1 and 2 represent the upstream and downstream regions of the shock, respectively. The significance of each equations is outlined below,

- Equation 2.31 is an expression for the conservation of mass across the shock front. It states that mass flux entering and leaving the shock must equate.
- Equation 2.32 describes the conservation of momentum across the shock front. This equation implies that the change in momentum across the shock is due to thermal and magnetic pressures.
- Equation 2.33 is the expression for the conservation of energy. The first term represents the kinetic energy flux, the second term is the flux of thermal energy and the third term is the electromagnetic energy flux or Poynting vector. This equation states that the growth or loss in internal energy and kinetic across the

shock front is related to the rate at which gas and magnetic pressure do work per unit area at the shock.

- Equation 2.34 states that the x component of the magnetic field is continuous, i.e it is unaffected by the shock interface.

- Equation 2.35 is derived from the fact that the tangential component of the electric field is continuous across the shock and $\mathbf{E} = |v \times \mathbf{B}|$. This equation describes the relationship between the orientation of upstream and downstream magnetic fields to the flow speed parallel and perpendicular to shock normal.

Using this set of five Rankine-Hugoniot jump conditions and knowledge of the properties of the pre-shock or upstream region (region 1), properties of the post-shock region (region 2) can be derived, or vice versa. Solving for the general case of the Rankine-Hugoniot jump conditions are difficult, ergo it is insightful to examine some special shock cases. Before doing so, we shall introduce some essential shock parameters.

Important Shock Parameters

Firstly, the angle between the shock normal and magnetic field θ_{Bn} referred to as the *shock obliquity* is an important shock parameter. The two main geometries observed in astrophysical shocks are quasi-parallel and quasi-perpendicular. In the quasi-parallel case, θ_{Bn} is $\leq 45°$, while for the quasi-perpendicular case θ_{Bn} is $\geq 45°$. It is important to note that in solar physics the quasi-parallel case is considered to be close 0 ° and the quasi perpendicular case is considered to be close 90°. Figure 2.7 illustrates both these geometries in a solar context. The compression ratio r is another important shock parameter, defined as the ratio between the density in the downstream to upstream region, $r = n_2/n_1$. In addition to θ_{Bn} and r, a key shock parameter is the sonic Mach

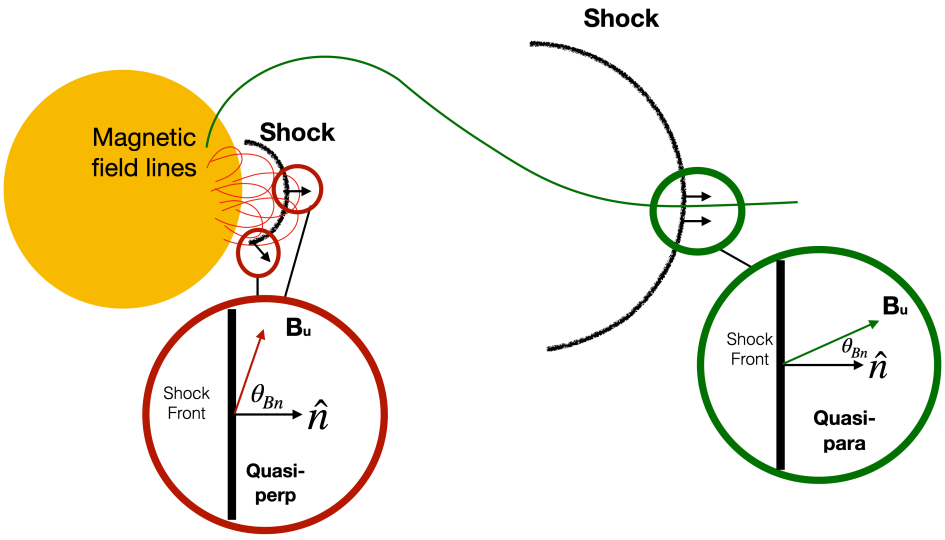

Figure 2.7: Schematic of the angle θ_{Bn} between the local shock normal $\hat{n}$ and upstream magnetic field direction B_u in quasi-perpendicular and quasi-parallel scenarios.

number M_s or in the MHD case the Alfvén Mach number M_A,

$$M_s = \frac{v_1}{c_s} \tag{2.36a}$$

$$M_A = \frac{v_1}{v_A} \tag{2.36b}$$

where v_1 is the upstream velocity, c_s is the speed of sound, and v_A is the Alfvén speed.

Perpendicular shock

Let us now investigate the special case of a perpendicular shock and express the upstream and downstream plasma properties in terms of the compression ratio and Mach number. In a perpendicular shock, both the upstream and downstream plasma flows are perpendicular to the magnetic field, which means the x and y subscripts in the jump conditions (Equations 2.31-2.35) are omitted. This reduces the jump conditions

to the following

$$\frac{B_2}{B_1} = r \tag{2.37}$$

$$\frac{\rho_2}{\rho_1} = r \tag{2.38}$$

$$\frac{v_2}{v_1} = \frac{1}{r} \tag{2.39}$$

$$\frac{p_2}{p_1} = \gamma M_s^2(1 - \frac{1}{r}) - \frac{1 - r^2}{\beta_1} \tag{2.40}$$

where $\beta_1 = 2\mu_0 p_1/B_1^2$ is the plasma β in the upstream region. Eliminating p from the conservation of momentum and energy equations, and incorporating the other jump conditions leads to a quadratic for r in terms of M_s :

$$2(2-\gamma)r^2 + \gamma[2(1+\beta_1) + (\gamma-1)\beta_1 M_s^2]r - \gamma(\gamma+1)\beta_1 M_s^2 = 0 \tag{2.41}$$

This quadratic has one real positive root

$$1 < r < \frac{\gamma+1}{\gamma-1} \tag{2.42}$$

For most astrophysical shocks $\gamma = 5/3$ (assuming a monatomic gas) therefore the limiting value of r is 4. This means that no shock can produce compression in density larger than a factor of four. According to Equation 2.37, the increase in the magnetic field at the shock front is also limited to a factor of four. This limit determines the maximum energy gained by a particle subject to the shock acceleration mechanism called shock drift acceleration (Holman and Pesses, 1983). This process will be discussed in Section 2.2.3. Furthermore, in the case of perpendicular shock, Equation 2.41 can be simplified to

$$M_A = \sqrt{\frac{r(r+5+5\beta)}{2(4-r)}} \tag{2.43}$$

so that knowledge of β and r enables us to determine the M_A.

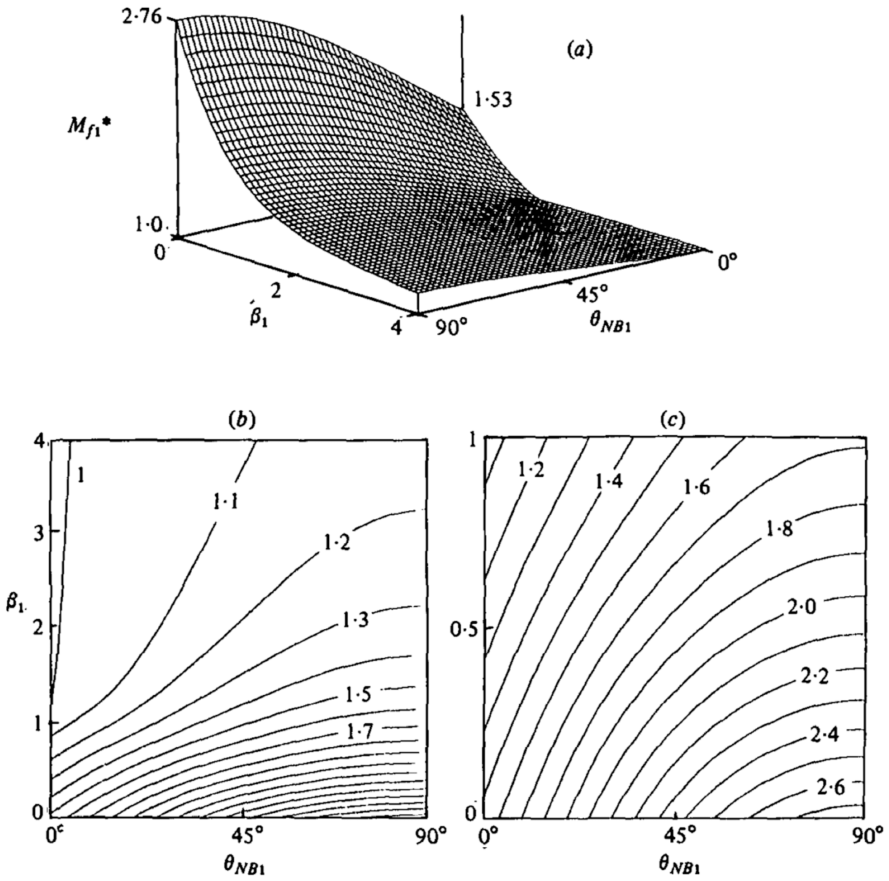

Figure 2.8: Critical Mach number as a function of upstream β and shock angle θ_{Bn}. Figure credit: Edmiston and Kennel (1984)

Shock criticality

An MHD shock forms when a fluid flow in the plasma exceeds the Alfvén speed. The shock converts kinetic energy to thermal energy, thereby dissipating the kinetic energy and generating entropy. Before discussing energy dissipation processes in MHD shocks, it is convenient to introduce the concept of criticality. Shocks are classified as either being sub or super critical depending on their Mach number being smaller or larger than a critical value (Edmiston and Kennel, 1984; Kennel and F., 1987). A subcritical shock dissipates energy via wave-particle interactions between the shocked plasma and shock-excited turbulent wave fields. Supercritical shocks must invoke extra mechanisms other than just simple wave-particle interaction to generate sufficient dissipation. The most efficient way of energy dissipation is reflection/acceleration of ions back to the

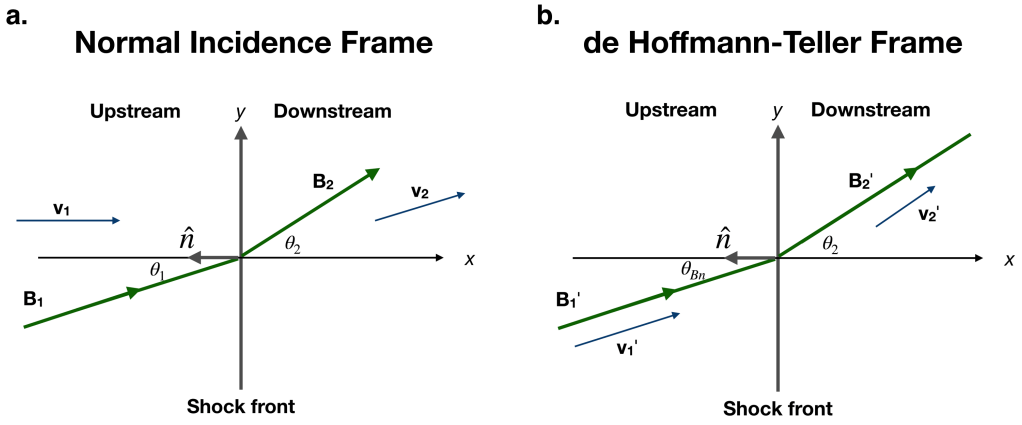

Figure 2.9: Schematic of the normal incidence frame (left) and de Hoffmann-Teller frame (right). The normal incidence frame is such that the upstream flow is directed along the shock normal. The de Hoffman-Teller frame ensures that the plasma velocity and magnetic field are in the same direction on both sides of the shock.

upstream flow. The Mach number at which supercriticality is achieved varies depending on the shock obliquity and upstream β. Figure 2.8 shows the critical Mach number as a function of upstream β and shock angle θ_{Bn} in the case of a monatomic gas ($\gamma = 5/3$) as per the Edmiston and Kennel (1984) model. In the solar context, a coronal shock will accelerate electrons provided the M_A reaches criticality. The process by which electrons are accelerated at the shock front is described in the next section.

2.2.3 Shock Drift Acceleration

MHD shocks in the solar atmosphere can accelerate electrons via a process known as shock drift acceleration (SDA; Holman and Pesses, 1983). SDA is associated with quasi-perpendicular shocks (scenario illustrated in Figure 2.7) and is believed to be the prevalent acceleration mechanism in the generation of type II radio bursts (Holman and Pesses, 1983; Street et al., 1994).

Figure 2.9 (a) shows a shock in the aforementioned NIF where the shock is at rest, v is the velocity flow, B is the magnetic field and θ_{Bn} is the angle between the shock normal and magnetic field. Let's consider the motion of an individual particle, namely an electron as it approaches the shock front. The increase in the magnetic field

across the shock means that the gyroradius of the particle is smaller in the downstream compared to the upstream region, this causes the particle to undergo a drift referred to as the ∇B drift with velocity $v_E = (\mathbf{E} \times \mathbf{B})/B^2$ as illustrated in Figure 2.10. The upstream and downstream convection electric field is identical:

$$\mathbf{E} = -\mathbf{v_1} \times \mathbf{B_1} = \mathbf{v_2} \times \mathbf{B_2} \tag{2.44}$$

This electric field accelerates the particle's motion when it is in the upstream region and decelerates the particle's motion when it is in the downstream region. Since the particle spends more time in the upstream region (due to the larger gyroradius) overall the particle gains energy. Alternatively, the SDA process can be considered in terms of particle reflection by the shock in a process known as *magnetic mirroring*. This process is best treated in a special frame of reference called the de Hoffmann-Teller (dHT) frame (De Hoffmann and Teller, 1950). In the dHT frame, the flow is parallel to the magnetic field, as illustrated in Figure 2.9(b) so that the convection electric field vanishes. Additionally, due to the constancy of the tangential electric field across the shock, the velocity flow and magnetic field are aligned in the downstream region. All the shock parameters in the dHT frame are denoted by primes. Let's now consider the path of a particle as it encounters the shock. The magnetic moment μ of the particle crossing the shock must be conserved so that,

$$\mu = \frac{p'_1 \sin^2 \alpha'_2}{B'_2} = \frac{p'_2 \sin^2 \alpha'_1}{B'_1} = \text{ constant} \tag{2.45}$$

where α is the pitch angle that is the angle between the velocity vector and magnetic field. The law of conservation of energy implies $|p'_1| = |p'_2|$, so that Equation 2.45 reduces to

$$\sin^2 \alpha'_2 = \frac{B'_2}{B'_1} \sin^2 \alpha'_1 \tag{2.46}$$

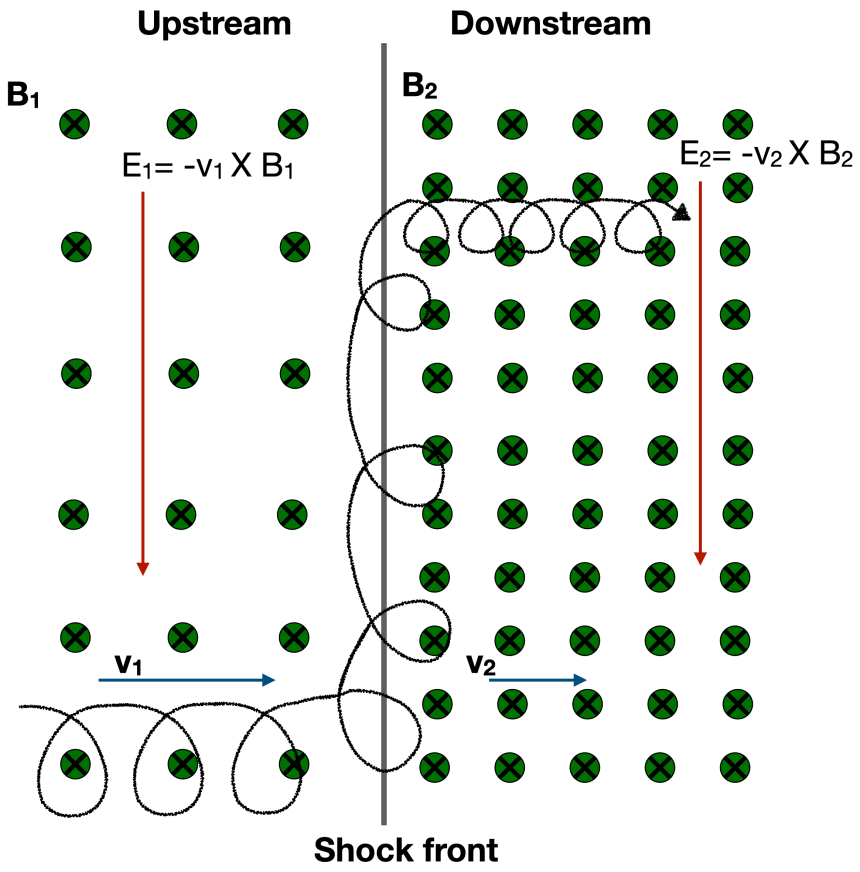

Figure 2.10: Schematic of a negatively charged particle drift experiencing shock drift acceleration. shock drift acceleration. Due to the magnetic field gradient at the shock front, the negative charge drifts anti-parallel to the electric field and, thus, gain energy. This schematic illustrates the process for a transmitted particle, but the process is the same for a reflected one.

In the dHT frame, particles that satisfy the condition

$$\alpha_1' > \alpha_c' \text{ where } \sin^2 \alpha_c = \frac{B_1'}{B_2'} \tag{2.47}$$

undergo reflection at the shock front. The reflected particles have a loss cone distribution defined by the pitch angle α_c, whereby particles that lie outside the loss cone are reflected while particles within the loss cone are transmitted downstream.

As previously mentioned particles gain energy as they cross the shock. While the particle reflection/transmission is best treated in the dHT frame, the energy gain of the particle is best investigated in the NIF. Ball and Melrose (2001) demonstrated that

the energy gain associated with particle reflection is

$$\frac{\epsilon_r}{\epsilon_i} = \frac{1 + (1 - B_1/B_2)^{1/2}}{1 - (1 - B_1/B_2)^{1/2}} \tag{2.48}$$

where ϵ_i, r is the kinetic energy incident and reflected particle, respectively. The energy gain depends on the relative strengths of the upstream and downstream magnetic fields, therefore, considering the limiting condition from Equation 2.42, the increase in energy is, at most, a factor of 13.93 for a single encounter. Typically it is much less than that. However, larger energy gains are possible if the particle crosses the shock numerous times. Scattering processes due to coronal turbulence and/or shock inhomogeneities may play an important role in increasing the number of crossings (Carley et al., 2013).

There are several other acceleration mechanisms, aside from SDA, that have been used to describe shock particle acceleration. The most notable mechanism is Diffusive Shock Acceleration (DSA) (Drury, 1983; Jokipii, 1987) or so-called first-order Fermi acceleration, which involves particles gaining energy from repeated crossings of the shock interface caused by scattering in the upstream and downstream region. It is the dominant acceleration mechanism in quasi-parallel shocks, which are found in interplanetary shocks. In summary, both quasi-parallel and quasi-perpendicular shocks are capable of producing energetic electrons at the shock front. These electrons excite plasma instabilities that induce a process called plasma emission. In the next chapter, we will discuss plasma emission and how it results in radio emission. For the sake of completeness, we will begin with a brief overview of all the solar radio emission processes. We will conclude the chapter with a discussion on radio-wave propagation effects.

3

Solar Radio Emission and Radio-Wave Propagation Effects

This chapter introduces solar radio emission mechanisms. Special consideration is given to plasma emission as it underpins the research in this thesis. Following that, we discuss type II radio bursts, which are generated by plasma emission and their observational traits and origin. We will conclude by discussing radio wave propagation effects and their impact on the observed properties of radio bursts. We give particular attention to the most dominant propagation effect, namely radio wave scattering.

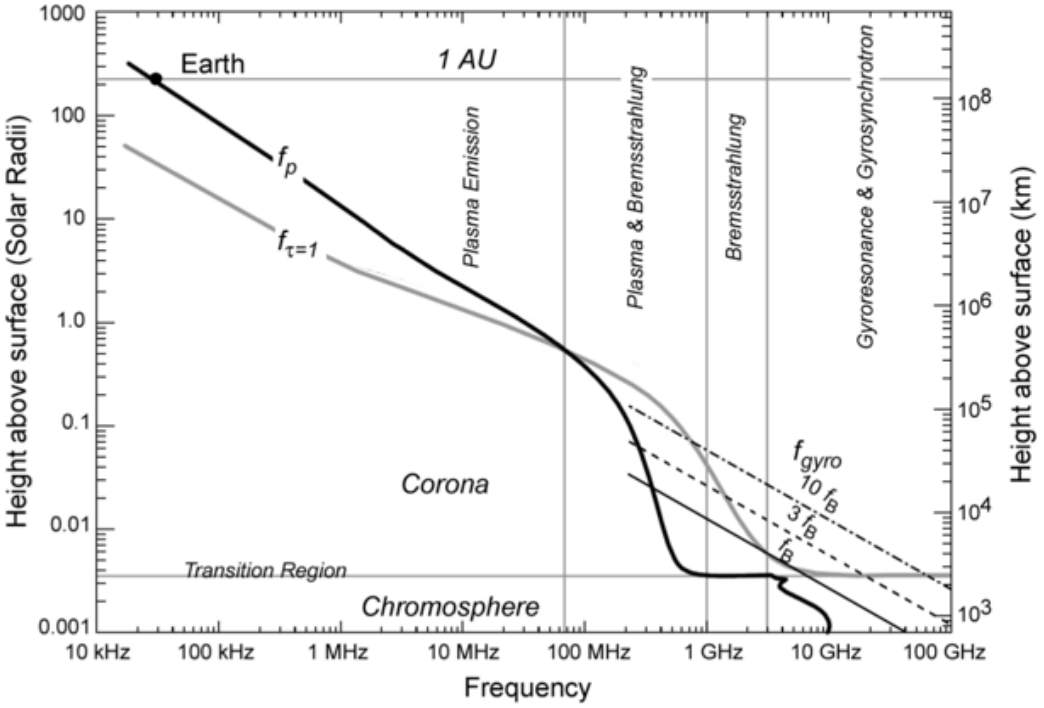

Figure 3.1: Characteristics radio frequencies in the chromosphere and corona. The top curve indicates the dominant emission mechanism at a specific height based on the relative sizes of plasma frequency f_p, the electron-cyclotron frequency f_B, and the frequency at which bremsstrahlung emission reaches an optical depth of one [$f_\tau = 1$]. Credit: Gary and Hurford (2004)

Radio Emission Mechanisms

Solar radio emission is generated via four known mechanisms, each of which operates largely by converting the energy of moving electrons into radiation. The four emission mechanisms, thermal bremsstrahlung (free-free) emission, gyromagnetic emission electron-cyclotron maser emission, and plasma emission each operate under different regimes with varying levels of complexity. Each mechanism is classified as either an *incoherent* or *coherent* emission process. In incoherent emission, electrons act separately to generate radiation that shows no phase association. Coherent emission involves some plasma instability followed by wave-particle and wave-wave interactions that cause particles to be accelerated in phase. As a consequence, the emitted photons are in phase. One fundamental parameter used to distinguish between coherent and incoherent is brightness temperature. The brightness temperature is the temperature a blackbody

in equilibrium would need to be as bright as the observed source. A blackbody refers to an opaque object in thermal equilibrium at a definite temperature, which absorbs all radiation falling on it and emits radiation as a function of temperature according to Planck's Law. In the case of incoherent emission, the brightness temperature is equal to or less than the actual source temperature (e.g. the electron temperature), mainly dependent on the density and temperature of emitting material along the line of sight. Whilst coherent emission can produce brightness temperatures that are far greater than the source temperature. This implies that coherent emission involves non-thermal processes. Any source that is intrinsically too bright to be explained by incoherent emission, is therefore deemed to be a product of coherent emission. Figure 3.1 shows the characteristic frequencies of the solar atmosphere and their associated emission mechanisms. The top curve in the plot delineates which emission mechanism dominates at various frequencies. At high radio frequencies (>1 GHz), radio emission is associated with incoherent emission processes namely bremsstrahlung emission or gyromagnetic emission. Bremsstrahlung emission, from the German "braking radiation" is produced from collisions between ions and thermal electrons. Gyromagnetic emission is generated when particles, mainly electrons, spiral along magnetic lines and produce radiation. At lower radio frequencies (<1 GHz), electrons can also be accelerated coherently by non-linear resonant processes. Generally, plasma emission is the principal mechanism in transient solar phenomena at frequencies below 1-2 GHz but other rarer mechanisms do exist (such as electron-cyclotron maser; ECM). Plasma emission dominates at metric and decimetric wavelengths and is believed to be the mechanism responsible for generating low-frequency solar radio bursts. It is thus the focus of this thesis and will be described in detail in the next section.

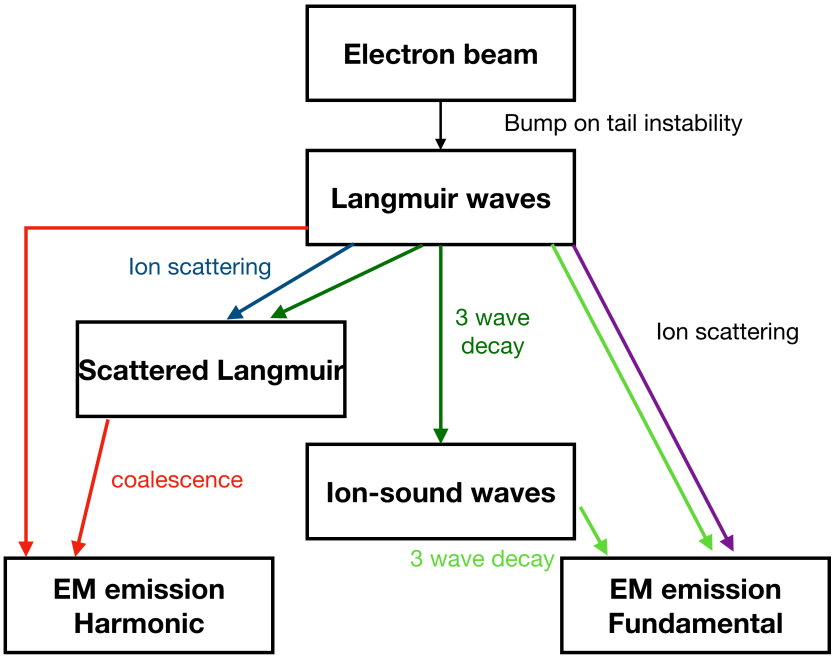

Figure 3.2: A flowchart illustrating the stages of the plasma emission mechanism. Adopted from Reid and Ratcliffe (2014)

3.1 Plasma Emission

The original theory of plasma emission was proposed by Ginzburg et al. (1958) as a possible emission mechanism to explain the observational properties of solar radio bursts, established over the preceding decade. The flow chart shown in Figure 3.2 outlines our current understanding of the stages of plasma emission (Kontar, 2001; Reid and Kontar, 2010; Ratcliffe et al., 2012). Plasma emission is a multi-stage process with the first stage being the acceleration of electrons to non-thermal velocities, facilitated by shocks or magnetic reconnection. The higher energy accelerated electrons outpace the lower-energy electrons, creating a small Gaussian or *bump* in the high tail of the thermal Maxwellian-Boltzmann velocity distribution as illustrated in Figure 3.3. The high energy electrons that produce the secondary positive slope in the distribution are referred to as an *electron beam*. Plasma oscillations grow in resonant response to this beam in a process called the two-stream instability or the bump-on-tail instabil-

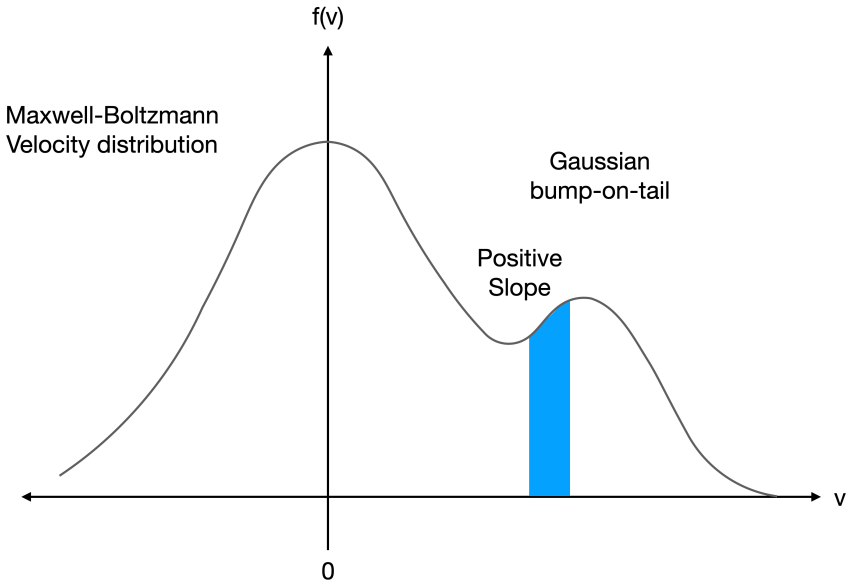

Figure 3.3: Maxwell-Boltzmann velocity distribution with a Gaussian 'bump-on-tail' representing the electron beam. The growth of Langmuir waves is a resonant response to this beam.

ity. These plasma oscillations are also referred to as Langmuir waves and are simply oscillations in the plasma's electron density (Tonks et al., 1929). Once the Langmuir waves are induced, they may undergo a number of interactions with other wave modes such as ion sound wave S, electromagnetic waves T or other Langmuir waves L. These wave interactions are formally described in a mathematical framework known as the three-wave interaction (McLean and Labrum, 1985; Melrose, 2017). This involves either the coalescence of two waves into a third or the decay of one wave into two. The coalescence of a Langmuir wave and ion sound wave gives

$$L + S \rightarrow T_1 \tag{3.1}$$

where T_1 is a transverse wave T_1 at the fundamental plasma frequency. The decay of Langmuir waves can result in

$$L \rightarrow T_1 + S \tag{3.2a}$$

$$\text{or } L \rightarrow L' + S \tag{3.2b}$$

where L' is a scattered Langmuir wave. L' propagates in the opposite direction to L. The product of a Langmuir wave and a scattered Langmuir wave gives

$$L + L' \rightarrow T_2 \tag{3.3}$$

where T_2 is another transverse wave at harmonic emission. The third harmonic is generated via the interaction,

$$L + L' + L'' \rightarrow T_3 \tag{3.4}$$

although, this interaction is highly improbable as it demands some specific conditions at the shock front (see Zlotnik et al. (1998)). For the above wave interactions to occur, two conditions must be satisfied

$$\omega_1 + \omega_2 \rightarrow \omega_3 \text{ and } k_1 + k_2 \rightarrow k_3 \tag{3.5}$$

which correspond to the conservation of energy and momentum respectively. The dispersion relations describes each wave mode in terms of its angular frequency ω and wave vector k such that

$$\text{Langmuir waves} \qquad \omega_L^2 = \omega_p^2 + \frac{3}{2} v_{th}^2 k_L^2 \tag{3.6}$$

$$\text{Sound waves} \qquad \omega_s^2 = k v_s \tag{3.7}$$

$$\text{Transverse waves} \qquad \omega_T^2 = \omega_p^2 + k^2 c^2 \tag{3.8}$$

where v_{th} is the thermal velocity, v_s is the sound velocity, c is the speed of light and

the electron plasma frequency is

$$\omega_p = \left(\frac{n_e e^2}{m_e \epsilon_0} \right)^{\frac{1}{2}} \tag{3.9}$$

where n_e is the electron density, m_e is the electron mass, e is the charge of an electron and ϵ_0 is the permittivity of free space. According to the conservation laws for fundamental emission to be generated

$$\omega_L + \omega_s \rightarrow \omega_{T_1} \text{ and } k_L + k_s \rightarrow k_{T_1} \tag{3.10}$$

and correspondingly for harmonic emission

$$\omega_L + \omega_{L'} \rightarrow \omega_{T_2} \text{ and } k_L + k_{L'} \rightarrow k_{T_2} \tag{3.11}$$

where T_1 and T_2 represent the fundamental and harmonic emission, respectively as previously mentioned. In the case of fundamental emission, Equations 3.6 and 3.10 imply that $\omega_L \approx \omega_{T_1} \approx \omega_p$, therefore, ω_S has a must be a lower value in comparison. Likewise for harmonic emission, $\omega_{T_2} \approx 2\omega_p$ is required in order to satisfy Equations 3.6 and 3.11.

3.1.1 Frequency Drift

As illustrated from Equation 3.9, when plasma emission is excited, the frequency of the plasma radiation is dependent on the local electron density. The plasma frequency is most commonly expressed as

$$f_p = \frac{\omega_p}{2\pi} = 8980\sqrt{n_e} \text{ Hz} \tag{3.12}$$

with n_e, the electron density given in cm^{-3}. Whilst the electron density generally decreases radially with distance from the solar surface, it can also vary depending on

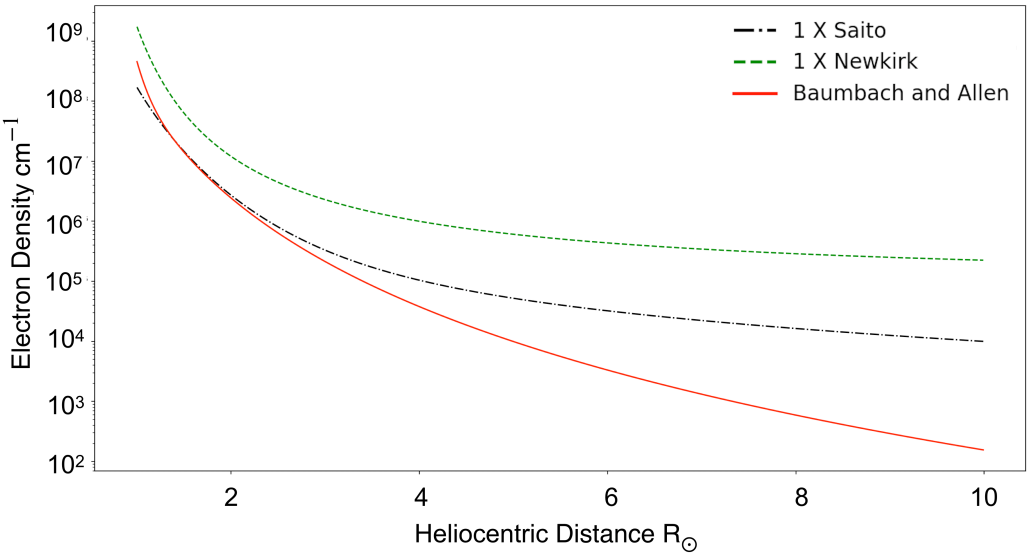

Figure 3.4: Electron number density as a function of height as defined by the Saito, Newkirk and Baumbach Allen models. Each describes an equatorial quiet corona electron density profile.

the coronal structures (like streamers) and disturbances (like CMEs), as discussed in Chapter 1. A variety of semi-empirical one-dimensional models have been derived to describe the density profile for different solar conditions such as quiet corona (Allen, 1947) and active regions (Newkirk, 1967; Saito et al., 1977) as shown in Figure 3.4. The Newkirk density model, which is used in this thesis, is expressed as,

$$n_e = N\, n_o\, 10^{4.32\, R_\odot / r} \tag{3.13}$$

where N is constant (if N=1 it is referred to as the one-fold Newkirk model), n_o is $4.2{\times}10^4 \mathrm{cm}^{-3}$ and r is a range of heights in solar radii. Incorporating such a density model into Equation 3.12 gives an expression for the plasma frequency in terms of height. Hence a set of frequency and time values obtained from a dynamic spectrum can be converted to a set of height and time values,

$$(f, t) \rightarrow (n, t) \rightarrow n(r) \rightarrow (r, t) \tag{3.14}$$

As the plasma emission exciter moves to greater altitudes, it will produce plasma emission at correspondingly decreasing frequency. This is the reason why radio bursts drift from high to low frequencies in a dynamic spectrum. The frequency drift rate df/dt of radio bursts can be used to infer the velocity of the exciter

$$v = \frac{2\sqrt{n_e}}{C}\left(\frac{dn_e}{dr}\right)^{-1}\frac{df}{dt} \tag{3.15}$$

where C= 8980 cm $^{3/2}$. Notably, one must err on the side of caution when choosing a density model as it greatly influences the derived height and velocity values. It is also important to note that the velocity derived from Equation 3.15 is the radial velocity since the density model characterises the radial density profile in the corona.

3.2 Type II Radio Bursts in Detail

Section 1.2.1 briefly introduced type II bursts as the radio signature to propagating shocks. The fact that type II bursts decrease in frequency over time is indicative of a radio source propagating through an environment of progressively decreasing density (since $f_p \propto \sqrt{n_e(r)}$). Type II bursts often exhibit two distinct emission bands with a frequency ratio of ∼2:1, which correspond to the fundamental and first harmonic of plasma emission from a single radio source, as described in Section 3.1.

Band-splitting

The fundamental and/or harmonic emission bands may be split into two thinner subbands of similar morphology and intensity variation. This phenomenon is referred to as band-splitting (Nelson and Melrose, 1985). The subbands can appear as either distinct separate bands (Vršnak et al., 2002), fragmented subbands (Chrysaphi et al., 2018; Mahrous et al., 2018) or a single emission band with a large bandwidth (Mann et al., 1995; Maguire et al., 2020). A striking example of clearly defined band-splitting

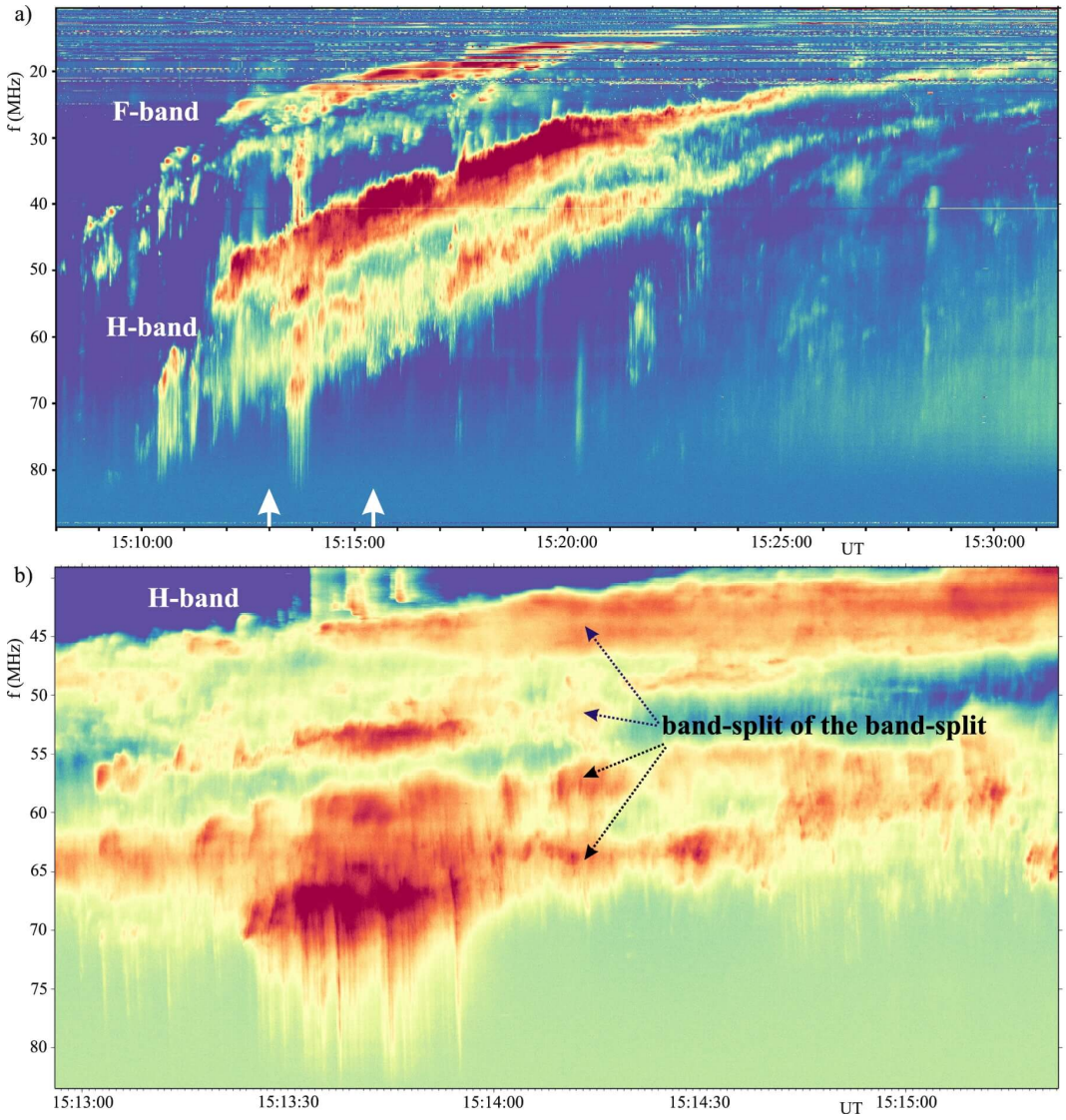

Figure 3.5: Dynamic spectrum observed by LOFAR on 25 August 2014 showing (a) type II fundamental and harmonic bands that both exhibit band-splitting and (b) a zoom-in of the harmonic component that exhibits band-splitting of the band-split. Credit: Magdalenić et al. (2020)

is shown in Figure 3.5 (a). The underlying mechanism that causes band-splitting remains subject to debate. One popular theory referred to as the *upstream-downstream theory*, proposes that the two lanes of emission are a consequence of simultaneous emission from the upstream and downstream region of the shock (Smerd et al., 1974). The separation between the split bands thus provides information about the density jump across the shock front and can be used to estimate important shock properties such as the shock compression ratio, the Alfvén Mach number and the coronal magnetic

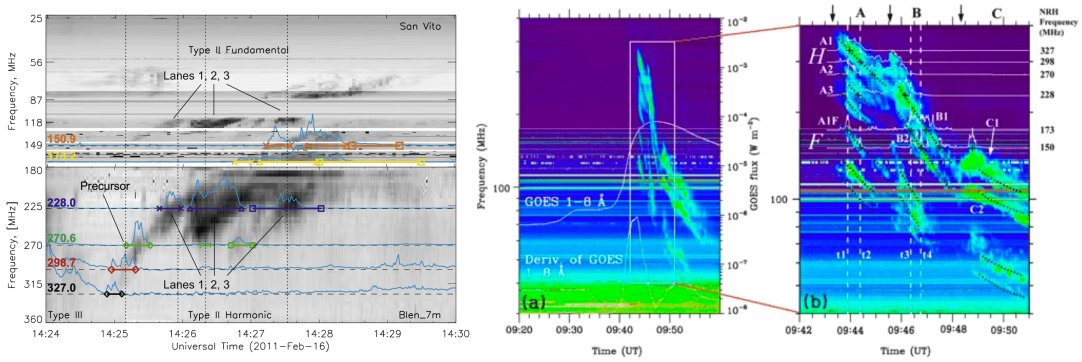

Figure 3.6: Multi-lane type II observations from (left) Zimovets and Sadykov (2015) and Lv et al. (2017) (right). The lanes typically have different start times and frequencies, drift rates, morphologies, and intensity variations.

field strength (Vršnak et al., 2001, 2002, 2004b; Mahrous et al., 2018; Chrysaphi et al., 2018; Maguire et al., 2020). Despite observational evidence in support of this theory (e.g. Vršnak et al. (2001); Zucca et al. (2014b); Zimovets et al. (2012); Chrysaphi et al. (2018)), arguments remain against as it is said that plasma emission from the downstream region is not likely due to its inability to generate sufficient Langmuir waves (Schmidt and Cairns, 2012). An alternative theory is that band-splitting is a consequence of plasma emission excited in different sections of the shock, which are transiting regions with dissimilar electron densities, magnetic field and/or Alfvén speed (Holman and Pesses, 1983). To add to the enigma, Magdalenić et al. (2020) recently reported unusual splitting of an already-split type II band, as illustrated in Figure 3.5 (b).

Multiple lanes

Type II bursts can also exhibit multiple lanes that are neither harmonically associated nor a typical band-split feature (McLean and Labrum, 1985; Feng et al., 2015; Zimovets and Sadykov, 2015; Zucca et al., 2018). Two examples of multi-lane events are provided in Figure 3.6. The lanes typically have different start times and frequencies, drift rates, morphologies, and intensity variations. Because of these differences, earlier studies speculated that the different lanes may originate from different drivers. Currently,

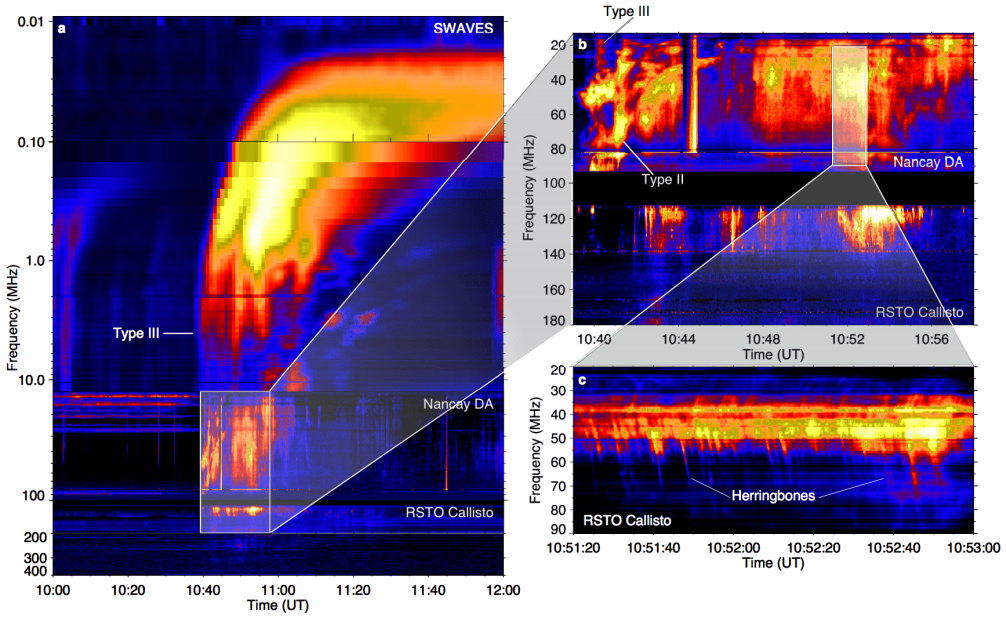

Figure 3.7: Radio dynamic spectra observed 22 September 2011 with STEREO-B/WAVES (0.01–16 MHz), Nançay Decametric Array (20–90 MHz), and the Rosse Solar Terrestrial Observatory eCallisto (10–400 MHz). Panel (c) clearly illustrated fine structure observed in the type II radio burst known as herringbone bursts. The spikes are regarded as signatures of beam of electrons accelerating into the upstream and downstream region of the shock. Credit: Carley et al. (2013)

the proposed mechanisms can be divided into two distinct theories (1) the different lanes are driven by separate shocks Cho et al. (2011) or (2) the different lanes originate from different regions of the same shock as it interacts with different coronal structures/conditions (Feng et al., 2013, 2015). The use of simultaneous imaging at radio, EUV and white-light wavelengths have helped to unravel the secret of the multi-lane type II origin (Zimovets and Sadykov, 2015; Lv et al., 2017). Chapter 7 endeavours to provide new insight into the multi-lane phenomena by combining high-resolution radio imaging with EUV and white-light observations.

Short duration fine structure

In addition to band-splitting and multi-lane features, type II bursts can exhibit a plethora of complex, fine-scale substructures. One intriguing fine structure feature is *herringbone* bursts, an example shown in Figure 3.7. Herringbone bursts are narrow-

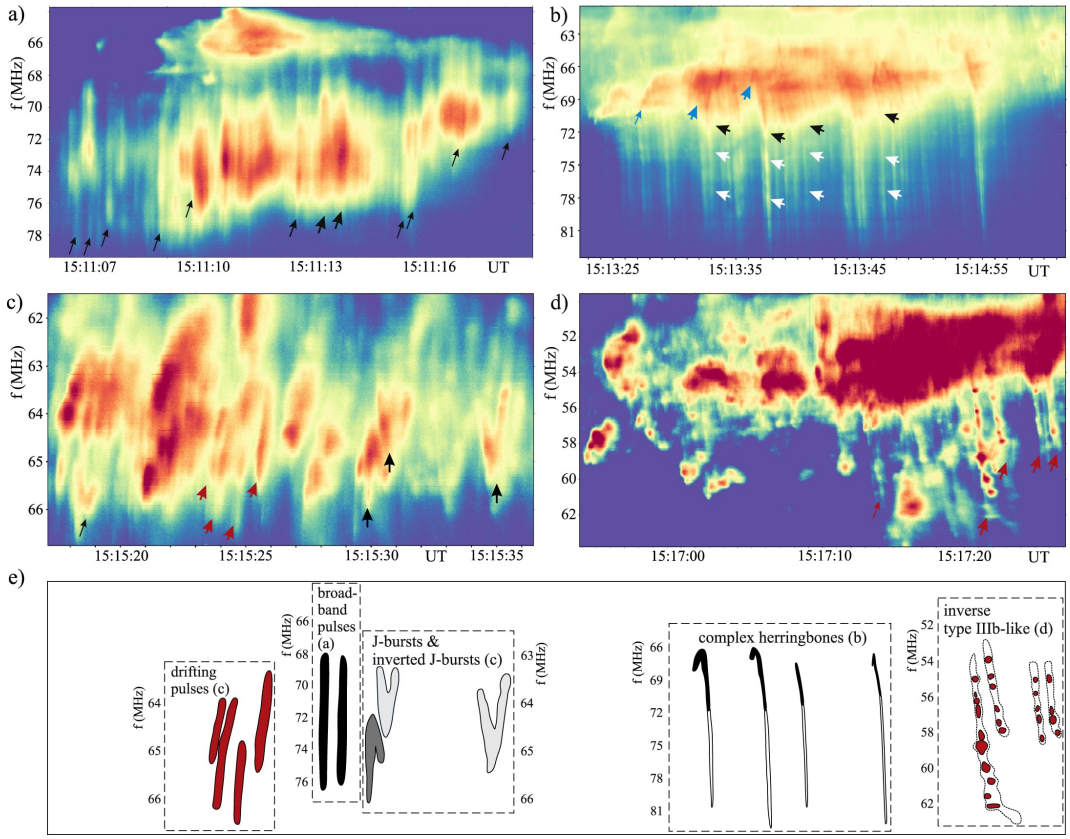

Figure 3.8: LOFAR dynamic spectra showing (a) broadband pulses, (b) complex herringbones, (c) J-bursts and drifting pulses, (d) inverse type IIIb-like bursts composed of narrowband dot-like fine-structures in a faint drifting envelope, and (e) a one-to-one schematic presentation of the broadband fine structure shown in panels (a)–(d). Credit: Magdalenić et al. (2020)

band spikes of emission that emanate from the backbone of the type II burst, which drift rapidly toward both high and low frequencies (Cairns et al., 1987; Cane and White, 1989; Mann and Klassen, 2005; Carley et al., 2013, 2015; Mann et al., 2018; Carley et al., 2021). The name stems from the morphology of the burst as it is reminiscent of a fishbone. They are considered to be the signatures of electron acceleration occurring at a coronal shock front. An individual herringbone spike represents a beam of electrons travelling away from the shock. Moreover, the fact that there are spikes of emission that simultaneously drift to high and low frequencies implies that electron beams propagate into the downstream and upstream regions of the shock, respectively. Electron acceleration at the shock front is most likely to occur via the SDA, which is discussed in Section 2.2.3. In this mechanism, the electrons experience a ∇B drift along the

shock front and gain energy due to the induced electric field, a result of $\mathbf{v} \times \mathbf{B}$ flow at the shock boundary. Herringbone burst drift rates suggest electron beam speeds of up to ∼0.1c, which correspond to energies of a few keV (Mann et al., 2002). According to SDA theory single-particle reflection from the shock has limited energy gain, therefore multiple reflections are required to produce relativistic energies (Burgess, 2006; Guo and Giacalone, 2010a). This multiple reflection process may be explained by inhomogeneity in the shock front, a so-called 'wavy' or 'rippled' shock front, brought on by turbulence in the corona (Zlobec et al., 1993; Vandas and Karlický, 2011; Carley et al., 2013, 2021).

In addition to herringbone bursts, other forms of type II fine structure have been reported. The general consensus is that the type II fine structure is due to the associated shock propagating through a strongly inhomogeneous and turbulent corona (see Section 8.2.2). A recent study by Magdalenić et al. (2020) endeavoured to classify fine structures observed in high time and frequency resolution dynamic spectra from LOFAR. They proposed three main categories, (1) simple narrowband, (2) broadband, and (3) complex fine structures. Figure 3.8 presents their high-resolution observations of (a) broadband pulses, (b) complex herringbones, (c) J-bursts and drifting pulses and (d) inverse type IIIb-like bursts. They suggested that the morphology of fine structures may not be unique to just this event or to one generation mechanism.

.

3.3 Radio-Wave Propagation Effects

The propagation of Radio waves from a source to the observer, particularly at low frequencies, is dramatically impacted by the corona. As discussed in Section 1.1.3, the dynamic nature of the Sun means that the corona is highly structured and variable. There are often significant density contrasts or inhomogeneities in the corona at both small scales (due to turbulent processes) and large scale (due to CMEs and

streamers). Radio emission that originates in the corona interacts with these density inhomogeneities and may undergo *refraction, scattering* or *absorption*. Collectively these interactions are referred to as radio wave propagation effects. Understanding which is the dominant effect (under certain conditions) is best described in terms of the refractive index μ. As discussed in Section 3.1 radio waves in an unmagnetised plasma with angular frequency ω and wave-vector k in an unmagnetised plasma follows the dispersion relation

$$\omega = \omega_p + c_s^2 k^2 \tag{3.16}$$

where ω_p is the plasma frequency. Given that the refractive index $\mu = kc_s/\omega$ and $\omega = 2\pi/f$,

$$\mu = \left[1 - \left(\frac{\omega_p}{\omega}\right)^2\right]^{1/2} = \left[1 - \left(\frac{f_p}{f}\right)^2\right]^{1/2} \tag{3.17}$$

The refractive index approaches zero when the frequency of the radio emission f is close to the plasma frequency f_p. This implies that refraction and scattering effects are most significant near the radio emission source. Given that harmonic emission is $f = 2f_p$, it is less inclined to experience such propagation effects. When plasma frequency and frequency of the radio emission is precisely equivalent ($f = f_p$) then $\mu = 0$ and total internal reflection occurs. For frequencies much smaller than the plasma frequency ($f << f_p$), the refractive index is imaginary, which means that those waves cannot propagate in the medium and are thus absorbed.

Observed effects

Propagation effects have a significant impact on the observed properties of solar radio emission (size, position, time duration, decay time, etc.). Scattering due to coronal turbulence causes angular broadening of radio sources, both compact radio sources and quiet Sun radio emission. The apparent source size increases thereby reducing the observed brightness temperature (Thejappa and MacDowall, 2008). Angular broad-

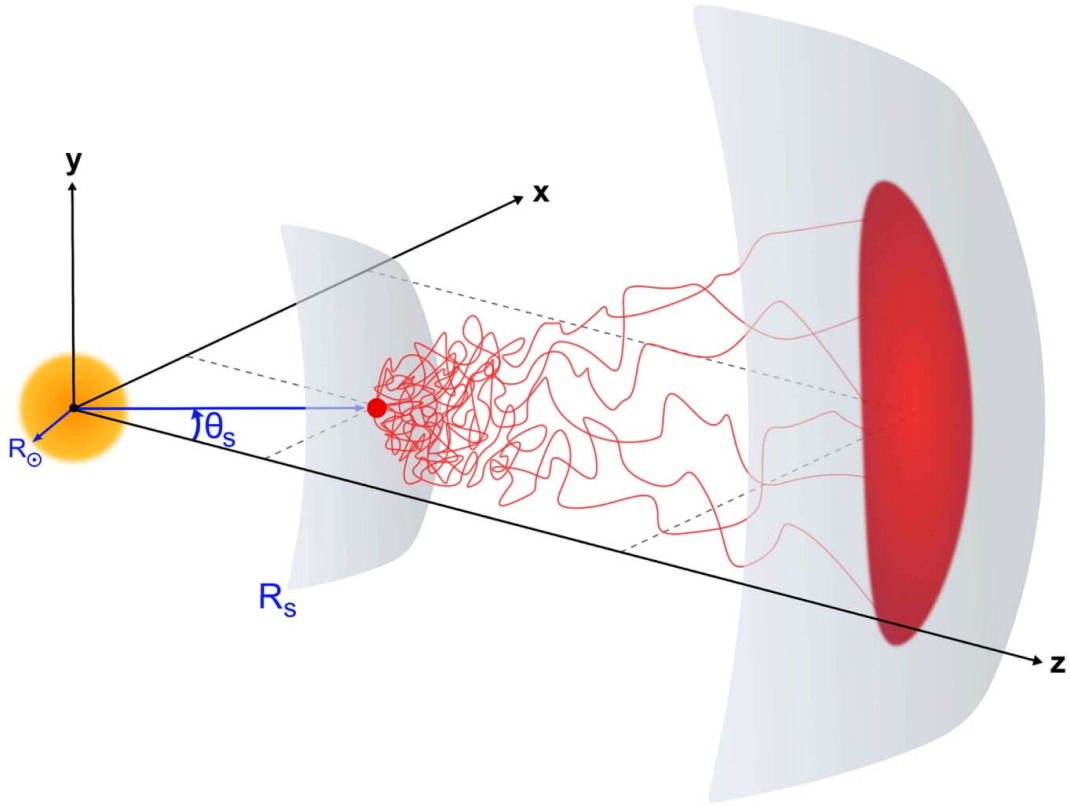

Figure 3.9: Schematic diagram of radio wave scattering, presented in a Sun-centered Cartesian coordinate system (x, y, z), where the z-axis is directed toward the observer. The radio emission is generated at a location given by the radial coordinate R_s and polar angle θ_s. The radio waves repeatedly encounter density inhomogeneities until eventually they escape and make it to the observer. As a consequence, the radio source appears enlarged and its position is radially shifted away from the Sun. Credit: Kontar et al. (2019)

ening observations have been employed to constrain turbulence models (Ingale et al., 2015). As well as broadening, scattering can affect the apparent position of radio sources. That is, sources experience a systematic radial shift away from the Sun as illustrated in Figure 3.9. This effect is best demonstrated in simultaneous imaging of the fundamental and harmonic components of a radio burst. Since only the fundamental emission experiences scattering, it appears displaced with respect to unscattered harmonic emission (see Chapter 6).

In addition to scattering, refraction may have an effect on radio emission (Steinberg et al., 1971; Suzuki et al., 1985). The electron density decreases radially with altitude in the corona, meaning that refracted radio emission should be shifted inwards. In

particular fundamental emission is refracted more than harmonic emission. In the case of the low corona, numerous observations have shown that the fundamental emission is shifted radially outward with respect to the harmonic (Kai and McLean, 1968; Sheridan et al., 1972; Nelson and Sheridan, 1974; Nelson and Robinson, 1975; Suzuki et al., 1985; Maguire et al., 2020). This provides evidence that scattering is the dominant propagation effect in the low corona.

In summary, propagation effects have a significant impact on the spatio-temporal characteristics of solar radio emission. For decades attempts have been made to simulate radio wave propagation effects in the heliosphere and quantify to what extent radio source properties are modified. In the following section, a description of radio wave propagation models past and present is provided.

3.3.1 Radio wave propagation models

Early Work

The study of radio wave scattering in the solar corona has its origins in the 60s and 70s. Seminal work by Chandrasekhar et al. (1952) on stellar scintillation formed the basis for statistically modelling the scattering of radio waves by random plasma inhomogeneities. Fokker (1965) later adapted this work for a solar corona with small scale density inhomogeneities and used geometric optic methods, namely ray-tracing, to investigate the source size of type I burst. Their results suggested that type I radio emission must have undergone scattering to account for the observed diameters of the noise storm. Hollweg (1968) used statistical ray analysis similar to that of Chandrasekhar et al. (1952) to model the effect of the corona on pulsar signals. The model assumed an anisotropic turbulent, spherically symmetric corona that exhibited large-scale refraction. Following this Steinberg et al. (1971) and Riddle (1972) examined models applicable for decametric type III and type II emission. Their models assumed a spherically symmetric corona with small scale density inhomogeneities and included

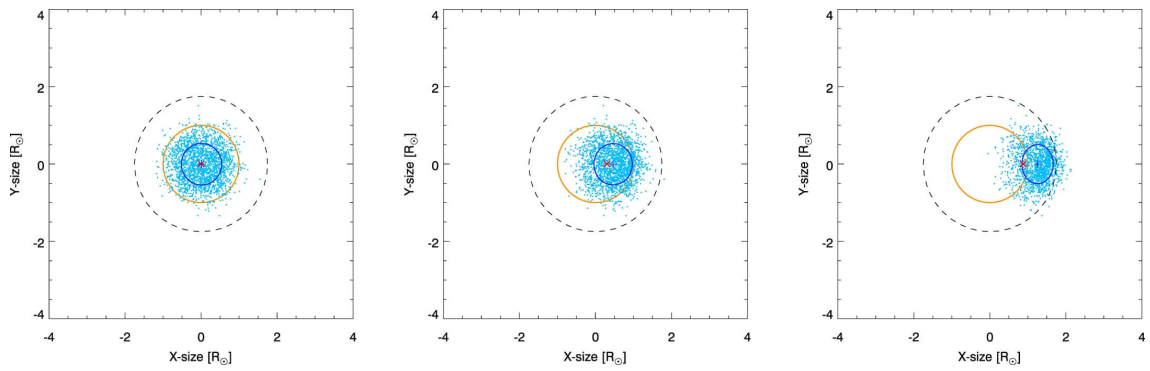

Figure 3.10: Simulations of the propagation path of a 32 MHz radio source generated at different angles to the observer's line of sight. The left, middle and right panels illustrate a radio source at an angle of $\theta = 0°, 10°, 30°$ to the line of sight of the observer, respectively. The red dot indicates where the radio source was generated and the blue dots represent the scattered photons. Credit: Kontar et al. (2019)

scattering and refraction effects. Their results showed that the size, shape, location, intensity and time profile of radio sources are controlled by the scattering efficiency. Steinberg (1972) built upon this, investigating type III emission at wavelengths in the hectometer and kilometre range at distance from 6 to 200 $R_\odot$. Riddle (1974) showed that for the case of harmonic emission, the source is subject to angular broadening but the effects of refraction are diminished. Simulations that assumed a smoothly varying corona with small-scale density inhomogeneities fell out of favour in the 1980s as they failed to account for both the large source sizes and the highly directional nature of radio bursts. Robinson (1983) proposed an alternative more realistic coronal model that comprised numerous thin, over-dense, small-scale features called fibres. The Riddle (1974) ray tracing model formed the basis for the simulation with the addition of weak density inhomogeneities, which were assumed to originate in magnetic flux tubes. The streamers and fibres were modelled as Gaussian density structures while the magnetic flux tubes were modelled as long cylindrical features. Robinson showed that random reflection off over-dense fibres shifted the observed emission site to higher altitudes. The high-density fibres were not randomly arranged but aligned with the (dominant) radial magnetic field causing scattered rays to curve towards the radial direction.

Revived Interest

In recent years, prompted by the advancements in high-resolution low-frequency radio observations (Van Haarlem et al., 2013) there has been renewed interest in quantitatively evaluating radio wave propagation effects. Kontar et al. (2017) showed using LOFAR imaging spectroscopy observations of a type III-b radio burst, that the sizes of striae emission sources and their dynamics are determined by the radio wave scattering effects. Most notably the Kontar et al. (2017) analysis suggested that radio wave scattering in the corona is highly anisotropic due to the anisotropic morphology of the density inhomogeneities. This means that radio sources are expected to elongate perpendicular to the heliospheric radial direction due to enhanced scattering perpendicular to the large-scale (radial) magnetic field of the Sun or elongated sources. In light of this, Kontar et al. (2019) developed a three-dimensional (3D) ray-tracing simulation including anisotropic density inhomogeneities. The simulations considered scattering on small-scale density inhomogeneities, large-scale refraction due to the gradual variation of the ambient coronal density, and collisional (free-free) absorption. Figure 3.10 presents results from the Kontar et al. (2019) model, namely the expected propagation path of a 32 MHz radio source generated at different angles to the observer's line of sight.

A simple analytical approximation was developed by Chrysaphi et al. (2018) to estimate the extent to which fundamental emission is shifted by scattering. This model is of particular interest in this thesis as it was employed in Chapter 6. Based on the seminal work of the 1970s, the Chrysaphi et al. (2018) model is a relatively simple model that assumes homogeneous, isotropic, and stationary density inhomogeneities. They adopted the spatial autocorrelation function proposed by Steinberg et al. (1971) to describe density inhomogeneities in the solar corona,

$$\langle \delta n(\mathbf{r}_1)\delta n(\mathbf{r}_1)\rangle = \langle \delta n^2\rangle exp\Big(\frac{-(\mathbf{r}_1-\mathbf{r}_2)^2}{h^2}\Big) \tag{3.18}$$

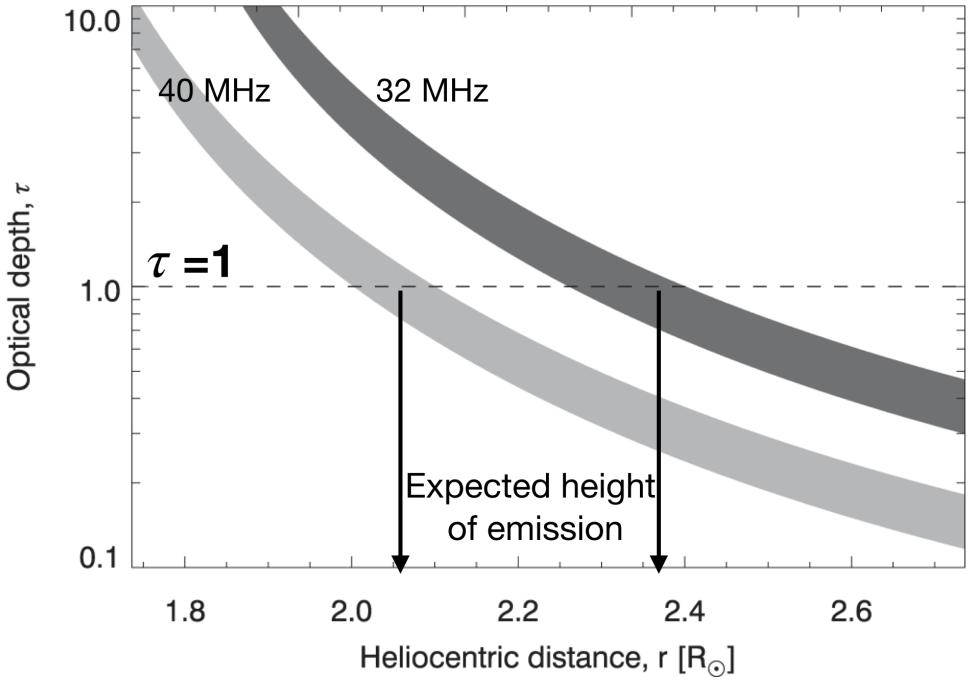

Figure 3.11: Radio wave optical depth as a function of heliocentric distance for two frequencies. The dashed line indicates the point at which $\tau = 1$. The light and dark grey lines represent the solutions for a radio source emitted at 40 and 32 MHz, respectively. The drop-down arrows indicate the height at which the emission is expected to appear. Adopted from Chrysaphi et al. (2018)

where $\mathbf{r}_1$ and $\mathbf{r}_2$ are positional vectors, $\delta n(r_i)$ is the density inhomogeneities at r_i, $\langle \delta n^2 \rangle$ is the mean square fluctuation of n and h is the characteristic scale length of density inhomogeneities. The mean scattering of a radio wave of frequency f propagating in a plasma with local plasma frequency f_p per unit length can be expressed as

$$\frac{\langle \Delta\theta^2 \rangle}{dr} = \frac{\pi}{h} \frac{f_p^4(r)}{(f^2 - f_p^2(r))} \frac{\langle \Delta n^2 \rangle}{n^2} \tag{3.19}$$

where $\langle\ \Delta n^2\ \rangle$ is the normalised mean power of plasma turbulence and h is the characteristic scale length of density inhomogeneities. The mean scattering rate is related to the optical depth such that

$$\tau(r) = \int_r^{1AU} \frac{\langle \Delta\theta^2 \rangle}{dr} = \int_r^{1AU} \frac{\sqrt{\pi}}{2} \frac{f_p^4(r)}{(f^2 - f_p^2(r))} \frac{\epsilon^2}{h} dr \tag{3.20}$$

where $\varepsilon = \sqrt{\langle \delta n^2 \rangle}/n$ is the relative level of electron density fluctuations. Evidently $\tau(r)$ depends on the extent of scattering in the corona characterised by ϵ and the characteristic scale on which scattering occurs h such that ϵ^2/h is taken to be constant (Steinberg et al., 1971; Riddle, 1974). When $\tau(r) > 1$ (optically thick regime) radio waves propagate diffusely, while for $\tau(r) < 1$ (optically thin regime) radio waves propagate uninterrupted. The dividing point between the two regimes ($\tau(r) = 1$) corresponds to the heliocentric distance at which the radio emission will escape. Figure 3.11 illustrates τ as a function of distance for 40 MHz (light grey) and 32 MHz (dark grey). The drop-down arrows indicate the heights at which each frequency is expected to be observed. Chrysaphi et al. (2018) used this model to demonstrate that the apparent positions of band-split radio sources are a consequence of radio wave scattering. This method gives a simple yet powerful method to calculate the expected height of a scattered radio source.

Correcting for the effects of radio wave scattering has become an essential step in processing and interpreting solar radio images, as will be demonstrated in Chapter 6.

4

Observing the Solar Corona

This chapter describes the main instruments used in this thesis to observe coronal shocks and their associated coronal features. There is a particular focus on radio observations from the ground-based instrument, the LOw Frequency ARay (LOFAR). Here, we outline the instrument's modus operandi and describe the relevant data analysis techniques. The chapter concludes with a brief description of EUV and white-light telescopes onboard various spacecraft, which are also used in this thesis.

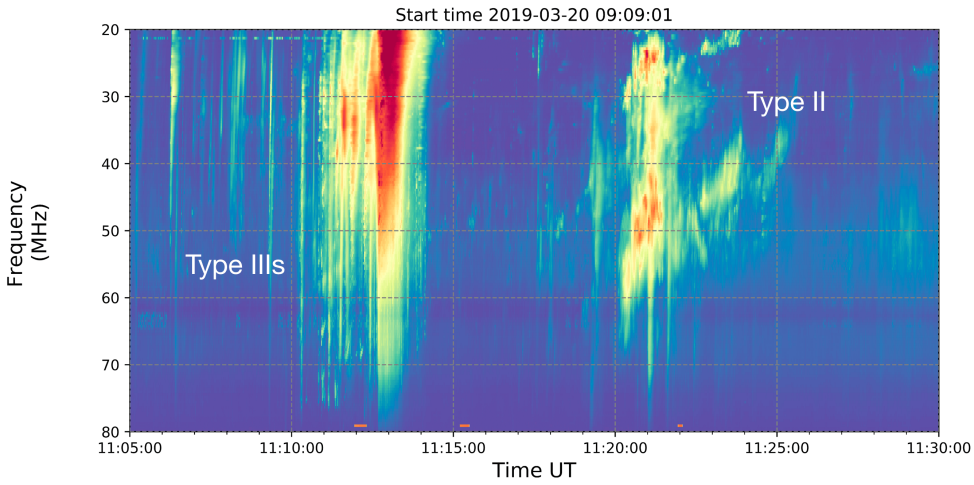

Figure 4.1: Dynamic spectrum observed on 20 March 2019 by I-LOFAR's low band antennas. A group of type III bursts and a type II burst are labelled.

4.1 Radio Observations

Radio observations can provide both spectroscopic and imaging information of a source in the sky. Dynamic spectroscopic radio instruments measure the intensity of radio emission as a function of frequency and time as illustrated in Figure 4.1. These intensity plots, referred to as dynamic spectra, allow us to identify the different types of solar radio bursts that were discussed in Section 1.2. While dynamic spectra provide insight into the type of radio burst, they do not necessarily provide any spatial information. Interferometric imaging is required to locate the radio emission with respect to other coronal features and study the radio exciter's propagation path. In the next section, interferometric imaging is described in detail, beginning with the basic concept of interferometry and then focusing on data analysis techniques.

4.1.1 Interferometric Imaging

The performance of astronomical observations is determined by two main parameters; sensitivity and angular resolution. The sensitivity is proportional to the telescope size because a larger telescope collects more photons. The angular resolution $\Delta\theta$ is

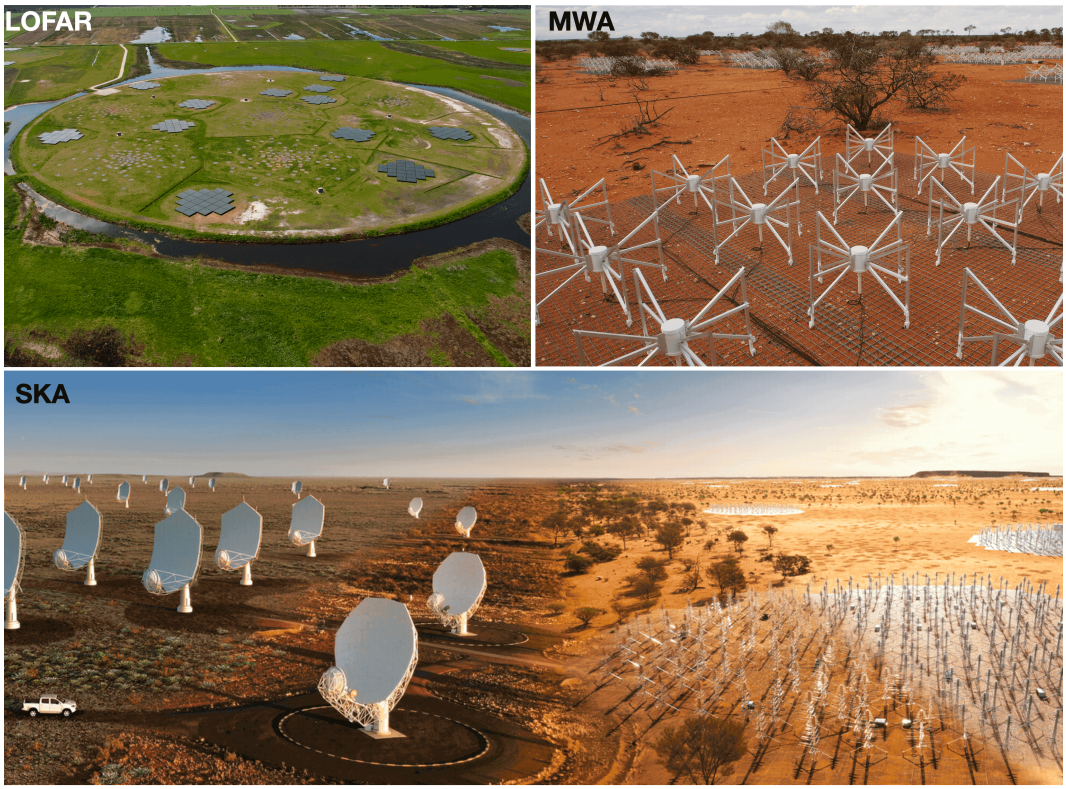

Figure 4.2: Current and next generation radio interferometers. (top left) the LOw Frequency ARay in The Netherlands, (top right) the Murchison Widefield Array in Australia and (bottom) an artist's impression of the Square Kilometer Array that will be in Australia and South Africa.

the minimum angular separation that two point sources can have to be recognized as separate objects. *Rayleigh's Criterion* specifies angular resolution as

$$\Delta\theta \sim \frac{\lambda}{D} \tag{4.1}$$

where λ is the wavelength of the radiation and D is the instrument aperture diameter. According to this criterion, two objects are considered resolved when the centre of the diffraction pattern of one object coincides with the first minimum of the diffraction pattern of the other. A consequence of Equation 4.1 is that longer wavelengths (e.g. radio wavelengths) need extremely large telescopes to achieve even modest angular resolution. For example, the Five-hundred-meter Aperture Spherical Telescope (FAST; Nan, 2006), located in Pingtang, Guizhou province, China, is currently the world's

largest single-dish radio telescope with a 500 m diameter. Obviously, the construction and maintenance of such a large structure is a huge undertaking. The limitations and challenges associated with single-dish telescopes, has led to the development of *radio interferometers*. An interferometer consists of multiple strategically-placed smaller telescopes or antennas that are linked together to synthesize a larger aperture telescope. The angular resolution of an interferometer is limited by the distance between the antennas, rather than the size of the individual telescopes. An interferometer's angular resolution is expressed as

$$\Delta\theta \sim \frac{\lambda}{B} \tag{4.2}$$

where B is the distance between antennas and is more commonly referred to as the *baseline*. It is, therefore, possible to build an interferometer that has the equivalent angular resolution of a single telescope that is hundreds of kilometers in size. Such interferometric arrays include the LOFAR (see Section 4.1.2), the Murchison Widefield Array (MWA; Tingay et al., 2013), and, in development, the Square Kilometer Array (SKA; Dewdney et al., 2009) as seen in Figure 4.2. In the following section, we introduce the basic concept of interferometry, common terminology, as well as a description of the main instrument used in this thesis and how its data is analysed.

4.1.1.1 The Two-element Interferometer

In order to understand how an interferometric image is produced, we will first consider an interferometer in its most basic form as two antennas separated by a baseline $\overrightarrow{b}$ observing over a narrow frequency range, $\nu = \omega/2\pi$. As illustrated in Figure 4.3, a plane wave incident on the antennas by angle θ, results in the signal reaching antenna 1 at a later time compared to antenna 2. Therefore the output voltage of the first antenna is the same as the voltage of the second antenna but has an associated temporal delay,

$$\tau_g = \frac{\overrightarrow{b} \cdot \hat{s}}{c} \tag{4.3}$$

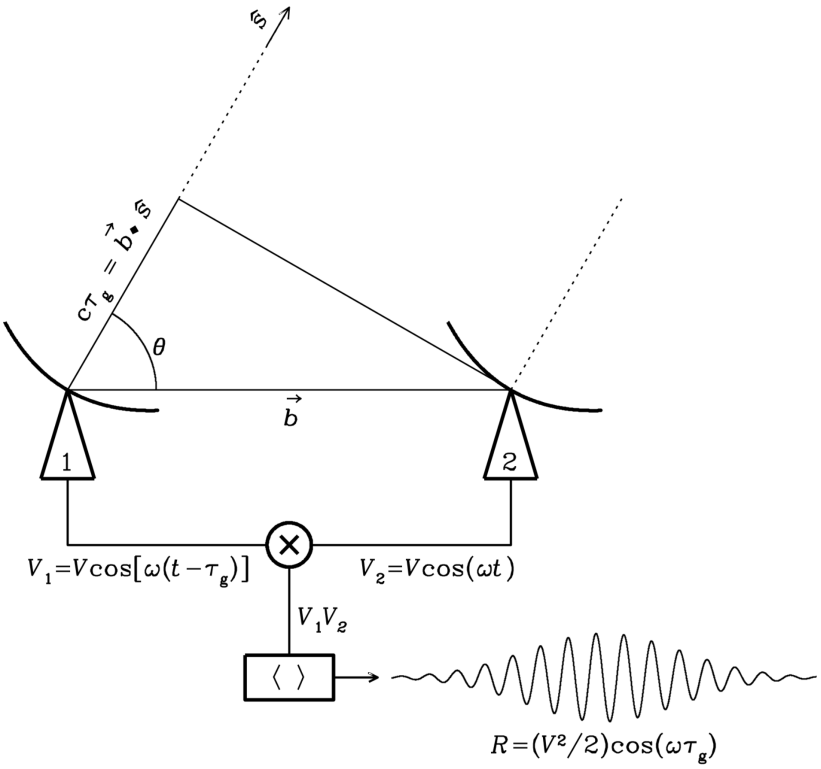

Figure 4.3: Two element interferometer observing a point source. The two antennas, labelled 1 and 2, are separated by a baseline $\vec{b}$. The signal arriving at antenna 1 experiences a time delay, τ_g, compared to antenna 2. v_1 and v_2 are the voltages produced by each antenna in response to the radiation from the point source. The correlation of the two signals produces the response function R_c. The correlator is denoted by $\otimes$.Credit: National Radio Astronomy Observatory (nrao.edu).

where $\hat{s} = \cos(\theta)$ is the unit vector in the direction of that point source and c is the speed of light. The output voltage of both antennas can be expressed as

$$v_1 = v\cos(\omega t - \omega\tau_g) \tag{4.4}$$

$$v_2 = v\cos(\omega t) \tag{4.5}$$

The signals are correlated in the correlator as illustrated in Figure 4.3. The interferometer response R_c is the correlation of the two output signals, which entails the multiplication and averaging of the output voltages. Multiplication of the two output

signals give

$$v_1 v_2 = \left(v \cos\left(\omega t - \omega\tau_g\right)\right)\left(v \cos\left(\omega t\right)\right) \tag{4.6}$$

which can also be expressed as

$$v_1 v_2 = \frac{v^2}{2}\left(\cos\left(2\omega t - \omega\tau_g\right) + \cos\left(\omega\tau_g\right)\right) \tag{4.7}$$

Now taking the average over a time interval δt that is much larger than $1/2\omega$, gives

$$R_c = \langle v_1 v_2 \rangle = \frac{v^2}{2}\left[\cos\left(\omega\tau_g\right)\right] = \frac{v^2}{2}\left[\cos\left(\omega\frac{\overrightarrow{b}\cdot\hat{s}}{c}\right)\right] \tag{4.8}$$

The correlator can be thought of as casting a cosinusodial coherence pattern of angular scale $\lambda/\overrightarrow{b}$ radians onto the sky. The correlator multiplies the source brightness on the sky by these coherence patterns and sums (integrates) across the sky. Provided that the emission is spatially incoherent, the response can be expressed as

$$R_c = \int\int I_v(\hat{s}) cos\left(\omega\frac{\overrightarrow{b}\cdot\hat{s}}{c}\right) d\Omega \tag{4.9}$$

where $I_v(\hat{s})$ is the source brightness of the sky and Ω is the solid angle on the sky. We now have a means of relating what we want to know, $I_v(\hat{s})$, to something we can measure, R_c. This expression is referred to as the *cosine* or *even* component of the interferometer response as the fringe pattern is even. The *sine* or *odd* component R_s is generated by inserting a 90° phase shift into one of the signal paths and repeating the analysis. Using Euler's Theorem, the two real correlator outputs, R_c and R_s, are combined to produce a complex exponential referred to as a complex visibility V.

$$V = R_c - iR_s = Ae^{-i\phi} \tag{4.10}$$

where A=$\sqrt{R_c^2 + R_s^2}$ is the amplitude and ϕ=$\tan^{-1}(R_s/R_c)$ is the phase. The source brightness and response of an interferometer with a complex correlator to an extended source can be succinctly related

$$V = R_c - iR_s = \int\int I_v(\hat{s}) e^{\frac{-i2\pi b\cdot\hat{s}}{\lambda}} d\Omega \tag{4.11}$$

This is referred to as the visibility function and is a 2D Fourier transform, which means it is possible to recover $I(\hat{s})$ from $V(b)$. The visibility function is most commonly expressed in terms of the (u, v, w) coordinate system. *u, v* and *w* are vector components in units of wavelength that describe the baseline vector $\overrightarrow{b}$ in three dimensions. The w axis points in the direction of the radio source and is orthogonal to both the u axis, which points towards the east, and the v axis, which points towards the north celestial pole. The unit direction vector $\hat{s}$ is defined by its projections *(l,m,n)* on the (u, v, w) axes,

$$V(u, v, w) = \int\int \frac{I_v(l, m)}{(1 - l^2 - m^2)^{1/2}} e^{[-i2\pi(ul+vm+wn])]} dl\, dm \tag{4.12}$$

By setting $w = 0$, the above integral is the 2D Fourier transform of the sky brightness distribution. Alternatively, the inverse Fourier transform of visibility function (the interferometer's data output) provides the brightness distribution,

$$I(l, m) = \int\int V(u, v) e^{i2\pi(lu+mv)} du\, dv \tag{4.13}$$

4.1.1.2 Imaging - Producing a Dirty Image

We have just shown that for every sky brightness distribution $I(l, m)$ there is a corresponding continuous complex visibility function, $V(u, v)$, which is its Fourier transform. However, an array of antennas will only measure a certain subset of values in the *u,v* plane and therefore $V(u, v)$ is not continuous. The measured set of values from the

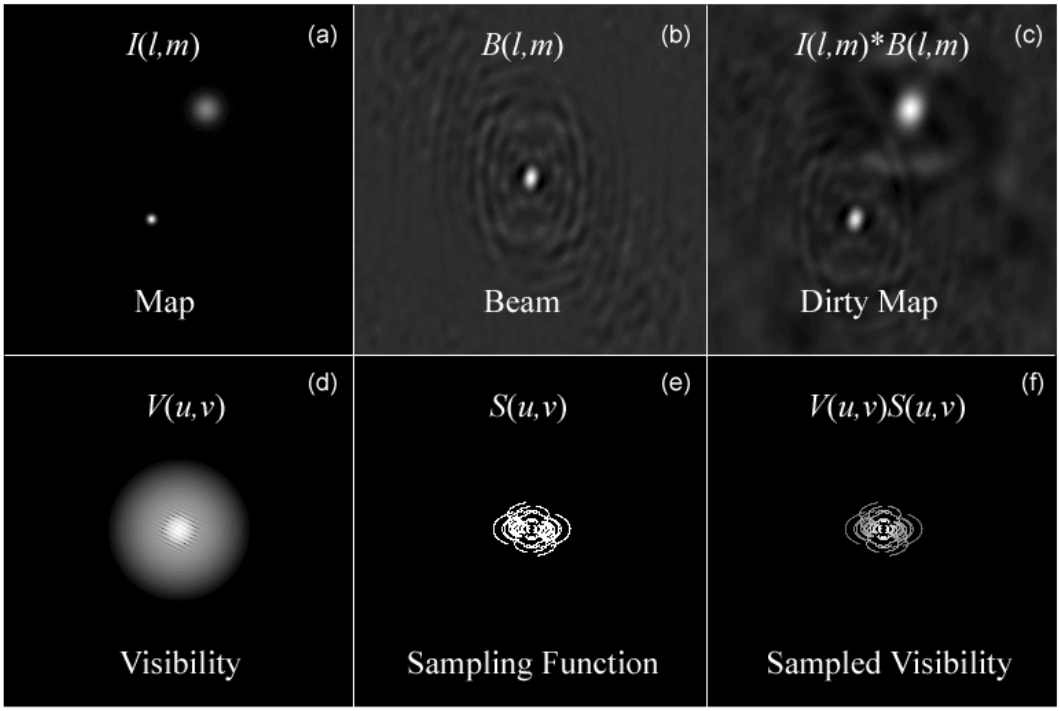

Figure 4.4: Visualisation of the interferometric process. (a) Sky brightness distribution, $I(l, m)$. (b) Point Spread Function or synthesised beam of the antenna array $B(l, m)$. (c) Convolution of the (a) and (b) to produce a dirty image/map (d) The 2D Fourier transform of (a) known as the visibilities (e) Sampling function of the array whose Fourier transform gives the beam (f) The sampled visibilities which is the product of the (d) and (e). The inverse Fourier transform of (f) is the dirty map (c). Credit: https://web.njit.edu/ gary/728/Lecture6.html.

visibility function is referred to as the sampling function or uv coverage $S(u, v)$. The actual data provided by the interferometer is just $S(u, v) \cdot V(u, v)$, which is called the sampled visibility function. By taking the inverse Fourier transform of this function we get what is known as the *dirty image* I^D where

$$I_v^D(l, m) = \int \int S(u, v)V(u, v)e^{(-i2\pi(ul+vm))}du\,dv \tag{4.14}$$

Applying the convolution theorem to the above expression, the dirty image can be related to the sky brightness distribution,

$$I_v^D(l, m) = I_v(l, m) * B(l, m) \tag{4.15}$$

where $*$ denotes convolution and

$$B(l,m) = \int_{-\infty}^{\infty}\int_{-\infty}^{\infty} S(u,v)e^{2\pi i(ul+vm)}du\,dv \tag{4.16}$$

$B(l,m)$ is known as the *synthesised beam*, *dirty beam* or *point spread function* (PSF). The PSF is the inverse Fourier transform of the sampling function and is unique to each interferometer. The shape of the PSF usually consists of a large main beam and several positive or negative sidelobes. To retrieve the source brightness, deconvolution must be performed. This process is explained in further detail in Section 4.1.1.3.

Calibration and Weighting

Preparatory to deconvolution the visibility data must be (1) calibrated and (2) weighted appropriately. The role of calibration is to correct for instrumental and atmospheric effects that may corrupt the visibilities. The relationship between the observed visibilities V^{obs} and the true visibilities V^{true} is

$$V_{ij}^{obs}(v,t) = G_{ij}(t)B_{ij}(v,t)V_{ij}^{true}(v,t) \tag{4.17}$$

where ij denotes a pair of antenna or baseline, G_{ij} is the complex gain and B_{ij} is the bandpass gain. The bandpass calibration corrects for the instrumental effects and varies as a function of frequency. It can also vary with time but very slowly, therefore it is often disregarded in solar imaging. The gain calibration corrects for temporal variations in the amplitude and phase of the source, which is most commonly due to the changing instrument response and atmospheric conditions. The calibration step for solar imaging involves observing a bright radio point source of known flux-density and spectrum (such as Cygnus A and Virgo A) in order to characterise the absolute flux calibration. The derived scaling factors for both the phase and flux calibrators are then applied to the solar observations.

The second step that is often performed before deconvolution is weighting. A weighting scheme is applied to the calibrated visibility data based on the uv sampling. Adopting a weighting scheme allows one to favour longer baselines (to emphasise small scale features) or shorter baselines (to emphasise large scale, diffuse structures). As previously discussed the dirty image is the inverse Fourier transform of the product of the sampling function $S(u,v)$ and the visibilities, $V(u,v)$

$$I^{dirty} = \mathscr{F}^{-1}[S(u,v) \cdot V(u,v)] \tag{4.18}$$

The dirty image becomes the weighted average of the data when a weighting scheme is applied

$$I^{dirty} = \frac{\mathscr{F}^{-1}[S(u,v) \cdot V(u,v) \cdot W(u,v)]}{\Sigma_{u,v} W(u,v)} \tag{4.19}$$

where $W(u,v)$ is the weighting function. The choice of weighting scheme depends on the scientific goals of the imaging. Two common weighting schemes implemented in radio astronomy are

$$\text{1. Natural} \qquad D_k = 1 \tag{4.20}$$

$$\text{2. Uniform,} \quad D_k = \frac{1}{N_s(k)} \tag{4.21}$$

where D_k denotes the weight applied to a uv cell k, $N_s(k)$ is the number of uv points inside the cell k, which has a characteristic width s. Under the natural weighting scheme, each uv point is weighted equally, causing scales that have more baselines to dominate the image. Since most arrays have a larger number of smaller baselines, large scale features will dominate in the imaging. This scheme ensures a high signal-to-noise but reduces spatial resolution. Under uniform weighting, the weight is inversely proportional to the sampling density function. If a uv cell has multiple visibility points the cell is down-weighted, to ensure that sparse and densely populated cells are weighted equally. This weighting scheme manages to maximise spatial resolution and minimize

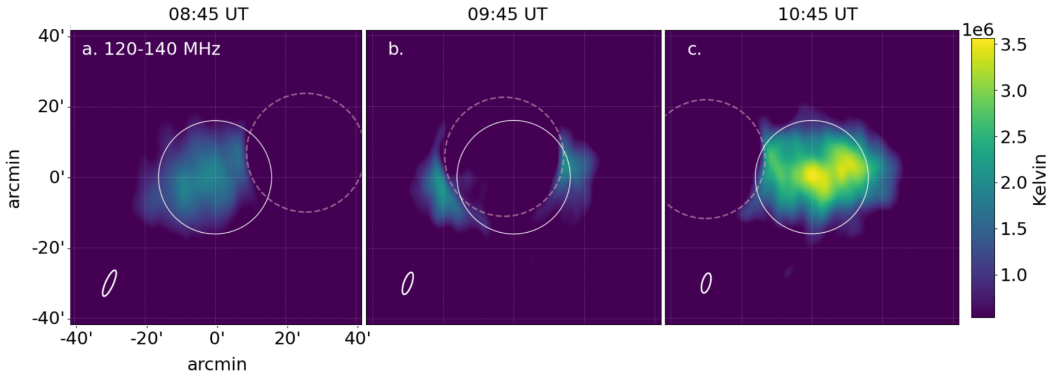

Figure 4.5: LOFAR interferometric images of 20 March 2015 solar eclipse. Credit: Ryan et al. (2021)

PSF sidelobes but has poor signal-to-noise. The most common weighting scheme in solar imaging is a hybrid scheme called Briggs weighting (Briggs et al., 1995). It is considered to be the ideal compromise between uniform and natural weighting. Under the Briggs weighting scheme, a parameter called robustness controls how uniform-like or natural-like the weighting scheme is. Robustness ranges from -2 to 2, where negative values give more uniform weighting and higher numbers give more natural weighting. Once images have been calibrated and weighted appropriately deconvolution is performed.

4.1.1.3 Deconvolution- Producing a CLEAN Image

Deconvolution of the true sky brightness distribution from the dirty beam is not a straightforward process. As previously mentioned the *uv* coverage is incomplete, this gives rise to undesirable sidelobes in the dirty beam. In order to overcome this problem, a number of deconvolution algorithms have been developed that try to determine reasonable values for the null, unmeasured *uv* data. The CLEAN algorithm (Högbom, 1974; Schwarz, 1978; Cornwell et al., 1999) is one of the most widely implemented deconvolution algorithms in radio interferometry and is employed in this thesis. The fundamental steps of the algorithm are as follows:

- Beginning with a dirty image, locate the peak emission in the image and find its

strength.

- At this position on the dirty image, subtract the dirty beam multiplied by the peak emission and a specified gain.
- Create an empty image and record onto that image what is subtracted from the dirty image. This is called the model.
- This process is repeated in an iterative way until the peak emission in the dirty image is below a certain limit or threshold. What remains in the dirty image is referred to as the *residuals*.
- The accumulated model is convolved with a *CLEAN* beam. This is most commonly an elliptical Gaussian of the same size and shape as the central lobe of the dirty beam. The product is an image of the sky brightness distribution uncontaminated by the beams sidelobes.
- The residuals are added back in to produce the final *CLEAN* image. This is done to account for variations in the intensity of the different sources.

CLEAN Algorithms

Multiple variants of CLEAN have been developed over the years, mainly driven by advancements in computing power. The first implementation of CLEAN was proposed by Högbom (1974). This simple procedure reconstructs the sky brightness by iteratively identifying the point-source components in the dirty image and removing the effects of the PSF. The algorithm assumes that the radio sky can be represented by a few well-separated point sources in an otherwise empty field of view. The Clark method (Clark, 1980) and the Cotton–Schwab method (Schwab, 1984) improved upon the CLEAN algorithm offering faster deconvolution speed and reduced errors. In contrast to the Högbom (1974) algorithms, these implementations decompose objects into a set of point sources. The Cotton-Schwab method is the most common implementation today and is

the basis for most subsequent CLEAN implementations. More recently Cornwell (2008) improved the CLEAN algorithm by developing a feature referred to as *multi-scale*. When implemented, the CLEAN algorithm assumes that sources in the sky are actually extended structures of different scales, which can include point sources. Multi-scale CLEAN removes large-scale structure before finer details while the CLEAN algorithm cannot distinguish noise peaks from faint real signals (Rich et al., 2008). Multi-scale CLEAN has become a popular choice in the radio community as it provides a more realistic representation of the sky brightness distribution for complex radio sources. Figure 4.5 is an example of LOFAR interferometric images that have undergone a multi-scale CLEAN. In addition to the development of CLEAN algorithms, imaging software has been developed to easily implement these aforementioned algorithms. WSClean (Offringa et al., 2014) [1] (w-stacking clean) is one of the most widely used imagers. It offers several deconvolution algorithms and can perform fully automated multi-scale, multi-frequency deconvolution. WSCLEAN is popular due to its reliability and speed.

To date, there is no standard imaging pipeline for processing LOFAR's solar interferometric data. As part of the work in this thesis, a novel solar imaging pipeline was developed using state-of-the-art algorithms and novel data analysis routines. This required a deep understanding of LOFAR's observing modes, storage of interferometric data (namely, in a format called a measurement sets), interferometric data reduction techniques (including flagging and calibration) as well as knowledge of the WSCLEAN algorithm. This novel pipeline was used in the analysis in Chapters 6 and 7.

4.1.2 The LOw Frequency ARray

This section provides a general overview of the radio interferometer, LOFAR[2], including a description of its components. LOFAR is currently the world's largest and most

[1] https://gitlab.com/aroffringa/wsclean/
[2] https://www.astron.nl/telescopes/lofar

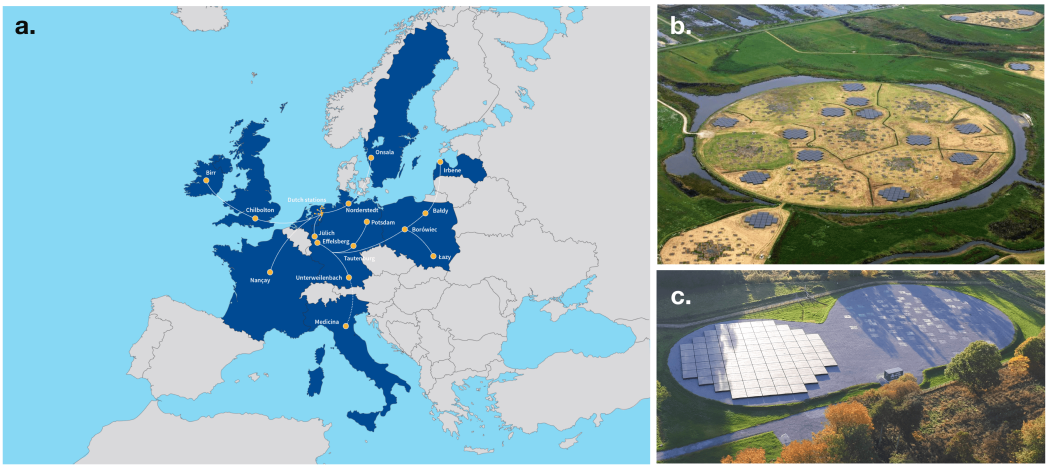

Figure 4.6: (a) Map of international LOFAR stations. The network spans nine countries namely; The Netherlands (38 stations), Germany (six stations), Poland (three stations), France, Ireland, Latvia, Sweden, and the United Kingdom (one station each); a station in Italy soon to be built. (b) Aerial image of the core stations of LOFAR located in Buinen, Netherlands. The large circular island encompasses the six core stations and is known as the Superterp. Credit: ASTRON (c) Aerial image of the Irish LOFAR station in Birr, Co.Offaly. Credit: Birr Castle.

sensitive low-frequency radio telescope. It is a phased array interferometer, spread across 7 European countries, which has been in operation since the late 2010s. The system is operated by The Netherlands Institute for Radio Astronomy (ASTRON), observes in the frequency range of ∼10–240 MHz, and is used for a variety of astrophysical science goals. LOFAR consists of many dipole antennas distributed in 13 international stations across Europe, with a central hub of 24 core and 16 remote stations in The Netherlands, as shown in the map in Figure 4.6. The 12 inner-most core stations are located in a compact area known as the *Superterp* as seen panel (b). The pan-European array is called the International LOFAR Telescope (ILT). The design of each LOFAR station varies but each is made up of two distinct antenna fields namely the low-band antenna (LBA) and the high-band antenna (HBA) which are detailed in the next section. The core and remote stations consist of 48 HBA and 96 LBA antennas, and each of the core HBA stations is split into two sub-stations (2×24 antennas each) while the international stations have 96 HBA and LBA antennas each. The received signals are digitalised at each station and sent to the Central Processing System (CPS)

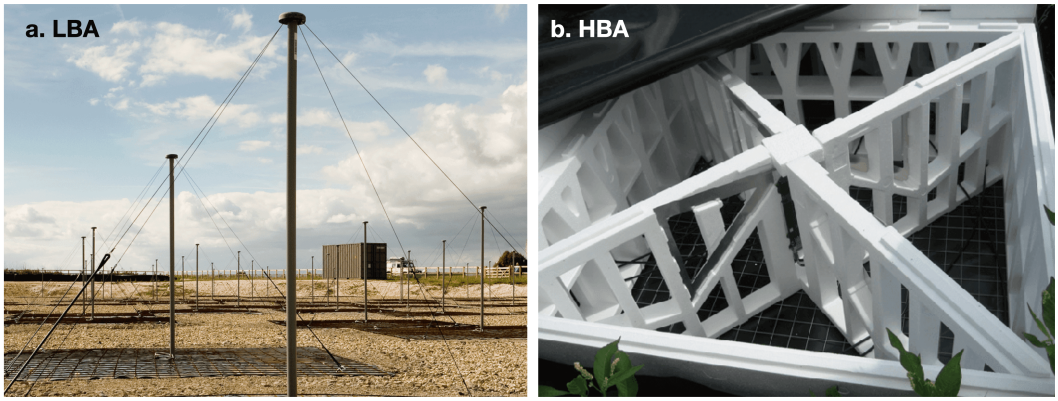

Figure 4.7: (a) Low band antenna (LBA) performing observations between 10 and 90 MHz. (b) High band antenna performing observations between 110 and240 MHz.

in Groningen, The Netherlands and where the data is combined. LOFAR is a highly flexible instrument that can quickly change observing programs to respond to transient solar events.

4.1.2.1 Low Band Antenna

The Low Band Antenna (LBA) shown in Figure 4.7(a), measures frequencies starting from ∼10 MHz to ∼90 MHz. The Earth's ionosphere blocks out any radiation below 10 MHz and the FM broadcast band begins at ∼90 MHz. An LBA consists of a simple dual-polarization dipole made of two copper wires that are in an inverted V shape orthogonal to each other. The dipole arms are 1.38 m in length resulting in a resonance frequency of ∼52 MHz although the impedance of the amplifier shifts this value to 58 MHz. The copper wires are connected to a moulded top containing a low noise amplifier which is clamped to a PVC rod 1.7 m high. The other ends of the copper wires are anchored to the ground to hold the antenna upright and minimize the antenna wire resonances due to wind loading. A reflective ground plane made from steel concrete reinforcement rods lays under the copper wires and acts as a reflector of radio waves. The LBA are capable of observing the entire visible sky producing an LBA dipole beam but the sensitivity decreases below 30°.

4.1.2.2 High Band Antenna

The High Band Antenna (HBA) shown in Figure 4.7(b), operates in the frequency range of 110-240 MHz. Each HBA tile which is a 5 m × 5 m Styrofoam structure, has 4 elements. Each element contains 4 bow-tie shaped dual polarised dipole antennas that are connected to a pre-amplifier in the centre. A metal ground plane or reflector lies beneath the tile. An HBA has an analogue radio frequency beamformer that combines the signals from all 16 dipole antennas to form a single tile beam in a given direction before the data is sent to the station container. Unlike the LBAs which are sensitive to the entire sky, HBAs are more sensitive to a small portion of the sky.

4.1.2.3 LOFAR Operations

ASTRON's headquarters in Dwingeloo, The Netherlands, coordinates and controls daily LOFAR operations. Operators are in charge of the instrument's comprehensive scheduling and configuration, which includes setting up the appropriate online processing chain and data destination. Observing time is divided between LOFAR's six key science projects (KSP), namely, (1) epoch of reionization studies, (2) deep extragalactic surveys, (3) transient sources and pulsars studies, (4) ultra-high-energy cosmic rays studies, (5) solar science and space weather and (6) cosmic magnetism studies. Each KSP team can apply for observing time by submitting a proposal, which outlines the overall science goals and describes the proposed technical setup. Observing and processing time (and hence the use of the appropriate data processing resources) is allocated by the LOFAR Programme Committee and the ILT director during the regular proposal evaluation stages. In the case of transient events, such as sudden solar activity, proposals for director's discretionary time may be submitted at any time [1].

[1] http://old.astron.nl/radio-observatory/observing/asking-time/asking-time

4.1.2.4 LOFAR Observing Modes

As discussed in Section 4.1, LOFAR can record spectroscopic and interferometric data. It is important to note that LOFAR has another observing mode, referred to as beam-formed mode (Stappers et al., 2011; Van Haarlem et al., 2013). Instead of recording visibilities, this mode involves forming multiple beams referred to as *tied-array beams* by combining data from LOFAR's core stations. The beams are combined digitally by correcting for the geometric and instrumental time and phase delays. The beams can be arranged to point at the Sun covering a large field of view from the solar centre to several solar radii (Morosan et al., 2014). This observing mode has been used to study a variety of solar radio bursts (e.g. Morosan et al. (2015); Kontar et al. (2017); Gordovskyy et al. (2019); Morosan et al. (2019)). While tied-array mode offers higher temporal resolution compared to the standard interferometric mode (0.0105 s versus 0.17 s), the spatial resolution offered by interferometric observations is far superior. For example at 75 MHz tied array mode, which only utilises the core stations will achieve a spatial resolution of 2.21′ while interferometric mode uses the remote stations to give a spatial resolution of 0.07′.

LOFAR interferometric imaging capabilities

The spatial resolution of the LOFAR array is calculated as the full width half maximum (FWHM) of the synthesized beam in radians

$$\theta = \alpha \left(\frac{\lambda}{B} \right) \tag{4.22}$$

where λ is the wavelength, B is the maximum baseline and α is a factor that depends on the array configuration, declination of the source and the weighting scheme used. Depending on the array configuration, LOFAR can attain spatial resolutions ranging from half a degree to sub-arcsecond scales. The spectral and temporal resolution of LOFAR interferometric data is limited by the capabilities of the central correlator,

COBALT (Broekema et al., 2018). Currently, the highest spectral and temporal resolution possible is 195.3 kHz and 0.0105 s, respectively. Depending on the science goal, the data can be integrated over time and/or frequency. This is predominantly done to increase signal-to-noise and speed up processing time.

4.2 Ultraviolet Observations

Ultraviolet (UV) wavelengths allow observations of the high-temperature features in the low corona. As discussed in Section 1.1.1, the temperature in the corona is typically ∼1 MK but can vary across different regions, exceeding tens of MK in flaring active regions. The extreme temperatures of the coronal plasma ionise heavy elements such as iron, oxygen and magnesium. These ionized species emit strongly at UV and EUV wavelengths. Space-based imagers have been developed with passbands centred on UV and EUV wavelengths allowing us to probe coronal features (both quiet Sun and flaring). In this section, we provide a brief overview of the EUV instruments that feature in this thesis, which includes the Atmospheric Imaging Assembly (AIA; Lemen, 2012) onboard the Solar Dynamics Observatory (SDO; Pesnell et al., 2012) and Solar Ultraviolet Imager (SUVI; Seaton and Darnel, 2018) onboard the Geostationary Operational Environmental Satellite (GOES; Baker et al., 1975).

4.2.1 SDO/AIA

The SDO is a satellite situated at Lagrangian point 1[1]. The goal of the mission is to observe the dynamics of the solar interior, provide data on the sun's magnetic field structure, characterize the release of mass and energy from the Sun into the heliosphere, and monitor variations in solar irradiance. There are three instruments onboard the Atmospheric Imaging Assembly (AIA; Lemen, 2012) the Heliospheric and

[1] One of the five locations of gravitational stability in the Earth-Sun system. L1 is located on the Sun-Earth line, at a distance of 1.5×10^6 km from Earth centre.

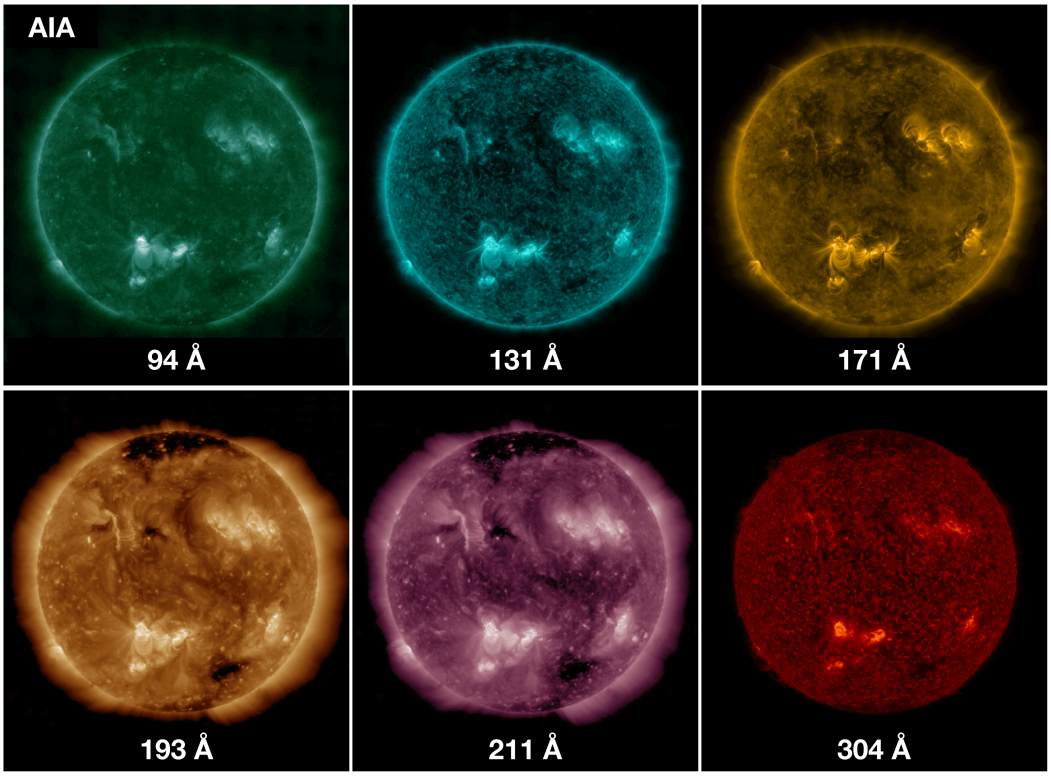

Figure 4.8: Panels showing some of the different passbands available from SDO/AIA on 8 September 2021. Each passband has been plotted with the appropriate colour table for clarity, with the passbands identified in the bottom of each panel.

Magnetic Imager (HMI; Scherrer et al., 2012) and the Extreme Ultraviolet Variability Experiment (EVE; Woods et al., 2010). AIA is the main instrument used in this thesis.

The AIA instruments, which consists of four Cassegrain telescopes, provide continuous full-disk images of the solar atmosphere up to 1.3 $R_\odot$. AIA measures seven EUV passbands centred on specific lines: Fe XVII (94 Å), Fe VII, XXIV (131 Å), Fe IX (171 Å), Fe XII, XXIV (193 Å), Fe XIV(211 Å), He II (304 Å), and Fe XVI (335 Å). Figure 4.8 illustrates the Sun observed in six different passbands, which corresponds to observing different plasma temperatures. There are also two UV filters that observe continuum emission (1700 Å) and also contributions from the C IV line (1600 Å). One filter, the 4500 Å passband, provides observations in the visible range. The full temperature coverage of AIA spans 5×10^3 K to 2×10^7 K which provides observations of the cooler photosphere up to the hot flaring corona (Boerner et al., 2012). AIA records images on a 4096×4096 pixel charged coupled device (CCD) detector with a $6''\text{px}^{-1}$

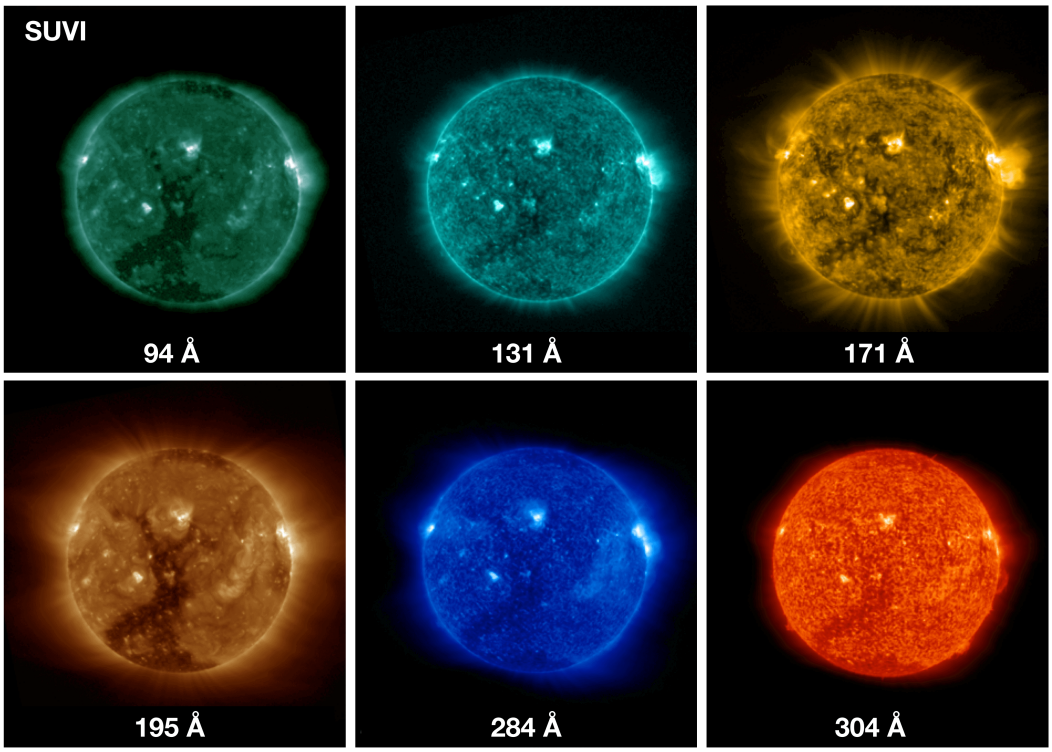

Figure 4.9: The first image taken by the SUVI on 29 January 2017. SUVI observes in six EUV channels namely; 94, 131, 171, 195, 284 and 304 Å. Credit: GOES, NASA/NOAA.

spatial resolution every 12 s. Images from AIA were used to study a coronal jet and spray in Chapters 6 and 7, respectively.

4.2.2 GOES/SUVI

GOES are a series of satellites launched and maintained by the National Oceanographic and Atmospheric Association (NOAA). GOES-1 was initially deployed in 1975, and since then at least one GOES satellite has always been in operation, with GOES-17 being the latest launch as of March 2018. The SUVI instrument is in operation onboard GOES-16. The design of SUVI was based largely on that of AIA. SUVI is a generalized Cassegrain telescope that employs multi-layer coatings optimized to operate in six EUV narrow passbands centred 94, 131, 171, 195, 284 and 304 Å. The instrument has a resolution of 2.5″, a cadence of 10 s and images up to 1.6 $R_\odot$. In Chapter 5 we exploited SUVI's wider field-of-view to observe the early evolution of a

CME in the low corona.

4.3 White-Light Observations

Up until the early 20th century, solar eclipses were the only way to observe the corona. As discussed in Section 1.1.1, during a solar eclipse the Moon blocks the intense emission from the solar disk revealing the very faint emission from the corona. The emission arises from the scattering of the photospheric light incident on the rapidly moving free electrons in the coronal plasma via the Thomson scattering process. In the 1930s, the French astronomer Bernard Lyot developed an instrument that enabled observation of the solar corona when the Sun was not in eclipse (Lyot, 1939). The instrument, known as a coronagraph, was designed to capture the diffracted light generated at the edges of the aperture and an internal occulter, enabling the routine observation of the corona from the ground. Evans (1948) proposed the use of an external occulter to block the light before the entrance aperture of the system in order to observe the extended corona. All modern-day coronagraphs use the classical design by Lyot modified for an external occulting of the entrance aperture. One of the most prolific modern coronagraphs is the Large Angle and Spectrometric Coronagraph (LASCO; Brueckner et al., 1995) onboard the space-based Solar and Heliospheric Observatory (SOHO; Domingo et al., 1995). In the next section, we provide a brief overview of the instrument.

4.3.1 SOHO/LASCO

The SOHO mission was launched 2 December 1995 into orbit around the Earth–Sun Lagrangian 1 point. It carries a suite of in-situ and remote sensing instruments for solar observations and space weather purposes including investigating the chromosphere, transition region, and the corona, in-situ solar wind observations and helioseismology to probe the solar interior. Of particular interest in this thesis are the coronagraphs collectively known as the LASCO. LASCO consists of three different coronagraphs C1,

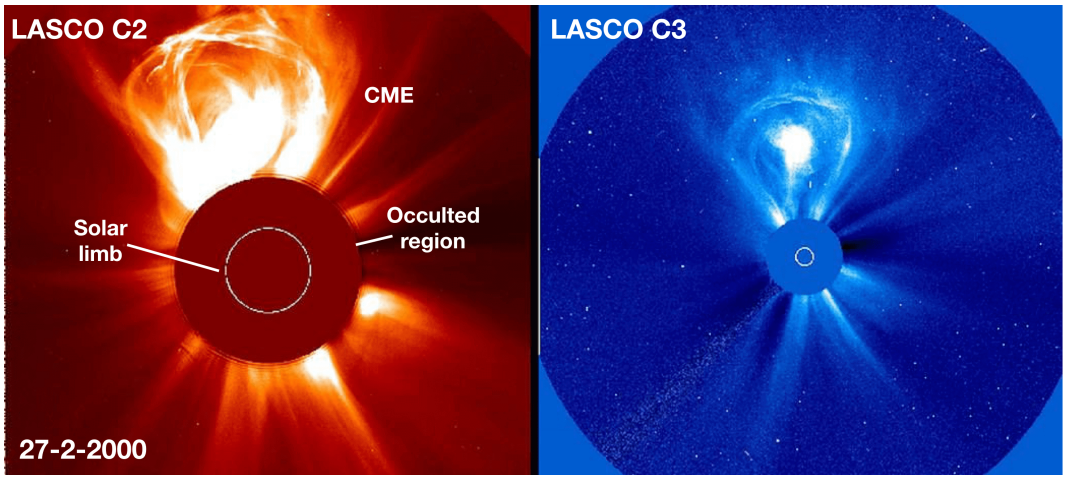

Figure 4.10: A CME eruption observed by LASCO C2 (left) and C3 (right) on 27 February 2000. Credit: SOHO ESA & NASA.

C2 and C3, which image the corona from 1.1 to 32 $R_\odot$. While the C1 coronograph has not been in operation since 1998, C2 and C3 continue to image the corona from 2.2–6.0 $R_\odot$ and 3.7–30 $R_\odot$, respectively. C2 and C3 are externally occulted Lyot type coronagraphs that image the corona with a spatial resolution of 11.2″ and 56″, respectively, at a temporal resolution of ∼20 min. An example of a CME observed by LASCO C2 and C3 is shown in Figure 4.10. LASCO images are the most suitable to use in conjunction with LOFAR low-frequency data as they often provide a context between solar radio bursts and large scale eruptions in the corona.

5

Evolution of the Alfvén Mach number associated with a CME shock

The Sun produces large-scale eruptive events such as CMEs that can drive shocks through the solar corona. Such shocks can accelerate electrons and generate radio emission in the form of a type II radio burst. So far, the early-phase evolution of shock properties and its relationship to type II burst evolution is an area of interest is not fully understood (Magdalenić et al. (2010); Nindos et al. (2011) and references therein. In this chapter, I study the evolution of a CME-driven shock by comparing three commonly used methods of calculating the Alfvén Mach number M_A in solar physics; (1) stand-off distance in EUV images, (2) a comparison of CME speed to a

model of the coronal Alfvén speed, and (3) the type II band-splitting method. I applied the three methods to the 2 September 2017 event, focusing on the shock observed in EUV by the GOES-16/SUVI, in white-light by SOHO/LASCO and the type II radio burst observed by the Irish LOFAR station (I-LOFAR). I show that the three different methods of estimating shock M_A yield consistent results and provide a means of relating shock property evolution to the type II emission duration. The type II radio emission came from the nose of the CME when it reached a heliocentric distance of $\sim$1.6 $R_\odot$ and the shock M_A became supercritical at $\sim$1.7. The emission ceased when the CME nose reached $\sim$2.4 $R_\odot$ despite an increasing Alfvén Mach number (up to 4). I suggest the radio emission cessation is due to the lack of quasi-perpendicular geometry at this altitude, which inhibits efficient electron acceleration and subsequent radio emission. This work has been published in Maguire et al. (2020) in *Astronomy & Astrophysics*.

5.1 Introduction

CMEs are large eruptions of plasma and magnetic fields that propagate from the low solar corona into the heliosphere (Klimchuk, 2001). If a CME reaches a speed that exceeds the local background Alfvén speed a plasma shock forms, most commonly at the CME nose and/or flanks (Cho et al., 2007; Carley et al., 2013; Zucca et al., 2014a). CME-driven shock properties, such as Alfvén Mach number M_A, have been calculated from a variety of observational methods in the past. However, these methods have not been directly compared and hence their reliability is not well established. In this chapter, I compare three commonly used methods to derive M_A, providing a measure of their consistency and also giving insight into the evolution of shock and radio emission characteristics in the early phases of CME eruption. CME-driven shock signatures can be observed at a variety of wavelengths, most predominantly in EUV, white-light, and radio (Grechnev et al., 2011; Vourlidas and Bemporad, 2012; Mancuso et al., 2019) as discussed in Sections 1.1.3.6, 1.1.3.7 and 1.2.1. Each wavelength range offers

an independent and unique method of determining M_A. The three methods used to derive M_A in this work are outlined below.

Method 1: Stand-off Distance

The geometry of the driver and shock can be derived from EUV and white-light images, which provides a measure of various shock properties (e.g. compression ratio and M_A). This method has its origin in laboratory experiments in the 1960s, which were designed to study shock formation around various types of blunt obstacles. Seiff (1962) performed experiments involving a spherical obstacle to mimic the terrestrial magnetosphere and used measurements of the densities upstream and downstream (n_u and n_d) to produce the semi-empirical relation:

$$\frac{\Delta}{D_o} = 0.78\frac{n_u}{n_d} \tag{5.1}$$

where Δ is the stand-off distance and D_o is the distance from the centre to the nose of the obstacle. Spreiter et al. (1966) and later Priest (1984) used gas-dynamic to illustrate that n_u/n_d can be written in terms of the sonic Mach number M_s and the adiabatic index γ. As a result, Equation 5.1 was modified to

$$\frac{\Delta}{D_o} = 1.1\frac{(\gamma-1)(M_s^2)+2}{(\gamma+1)(M_s^2)} \tag{5.2}$$

Farris et al. (1994) later adapted the theory to describe the Earth's magnetospheric bow shock. Since M_s is low in this regime, the denominator was modified:

$$\frac{\Delta}{D_o} = 1.1\frac{(\gamma-1)(M_s^2)+2}{(\gamma+1)(M_s^2-1)} \tag{5.3}$$

where the additional term in the denominator ensures that the shock moves a large distance as the M_s approaches unity. They also noted that the radius of curvature of the nose of the Earth's magnetopause can be estimated to be the vertical extent of the

magnetosphere such that:

$$\frac{R_c}{D_o} = 1.35 \tag{5.4}$$

Russell and Mulligan (2002) subsequently adapted this expression to understand the relationship between Interplanetary CMEs and the preceding thickness of the Earth's magnetosheath. They related the stand-off distance Δ and radius of curvature of the CME driver R_c to the Mach M by the semi-empirical formula:

$$\Delta/R_c = 0.81[(\gamma-1)M^2+2]/[(\gamma+1)(M^2+1)] \tag{5.5}$$

Here I take the M to be the Alfvén Mach number M_A. Rearranging and writing Equation 5.5 in terms of the normalised stand-off distance δ=Δ/R_c gives

$$M_A = \sqrt{1+[1.24\delta-(\gamma-1)/(\gamma+1)]^{-1}} \tag{5.6}$$

The application of this method to coronal shocks was first used by Gopalswamy and Yashiro (2011) to derive the solar coronal magnetic field using measurements of the stand-off distance at the shock nose from white-light coronagraph images. Numerous authors have used this technique on white-light observations (Gopalswamy and Yashiro, 2011; Kim et al., 2012; Poomvises et al., 2012) and on EUV observations (Gopalswamy et al., 2011) to derive coronal magnetic fields and to estimate the M_A in the low corona ($<2\,R_\odot$) and in the outer corona up to ~0.5 A.U. (Maloney and Gallagher, 2011).

Method 2: CME Speed to Alfvén Speed Ratio

A different approach that makes use of EUV and white-light observations is to compare CME speed (derived from images) to a data-driven model of the coronal Alfvén speed (see Section 5.3.2). This method has been modified to produce measures of M_A in three-dimensional coronal environments, showing values of 1 to 3 at heliocentric distances of $<2\ R_\odot$ (Rouillard et al., 2016; Zucca et al., 2018; Morosan et al., 2019). Some studies

have used EUV observations to derive coronal plasma properties by taking the ratio of filter bands in EUV telescopes (Berger et al., 2012). Differential emission measure analysis has also been used to estimate changes in temperature and density in the shock sheath to infer compression ratios and M_A values (Kozarev et al., 2011, 2015; Frassati et al., 2019).

Method 3: Type II band-splitting

While EUV and white-light images provide an indirect measure of shock properties from their geometry and kinematics, radio observations can be used to probe plasma shock properties more directly. At radio wavelengths, we observe type II radio bursts as evidence for shocks, often with two emission bands corresponding to the fundamental and first harmonic of the local plasma frequency (see Section 1.2.1). The emission bands are sometimes split into two thinner sub-bands with similar morphology and intensity variations, a phenomenon known as band-splitting as discussed in Section 3.2. These sub-bands can often appear as distinct separate bands (Zucca et al., 2018), fragmented sub-bands (Chrysaphi et al., 2018; Mahrous et al., 2018) or a single emission band with a large bandwidth (Mann et al., 1995). One popular interpretation is that the split lanes are emitted from the shock upstream and downstream, respectively. This theory is thus referred to as the upstream-downstream theory (Smerd et al., 1974) (see Section 3.2 for alternative theories). Applying the Rankine Hugoniot jump conditions and using the relative bandwidth of the band-split one can derive the shock compression ratio and estimate M_A. Several authors calculated values in the range of 1.3 to 1.6 at heliocentric distances of $\sim$1.2 to 2 $R_\odot$ (Vršnak et al., 2002; Zimovets et al., 2012; Zucca et al., 2018). This method is in question, however, as the precise nature of the band-splitting is still under debate (Du et al., 2015).

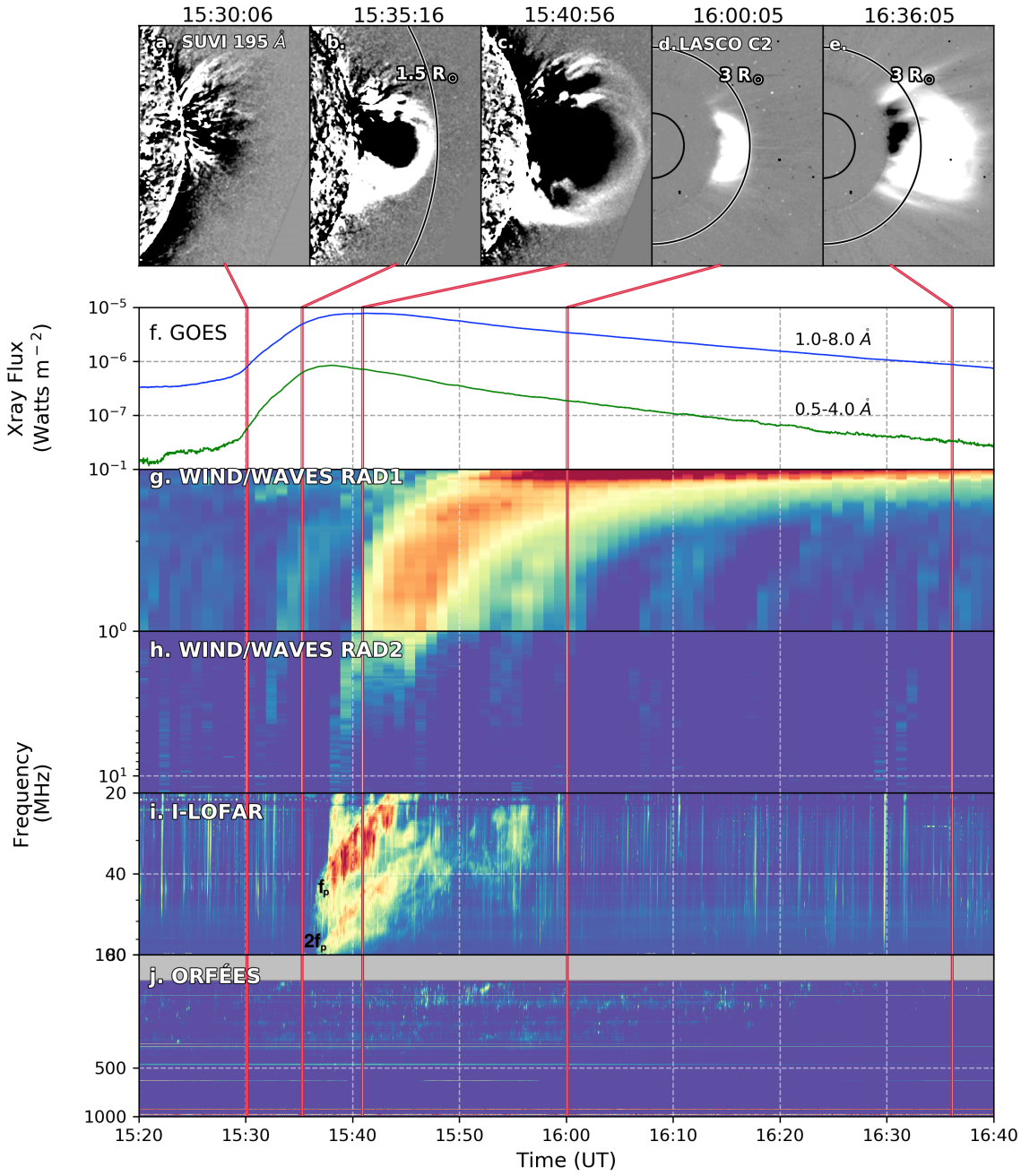

Figure 5.1: Base difference images of the CME observed with SUVI 195 Å (a-c) and LASCO C2 (d & e). (f) GOES 0.5-4 Å and 1-8 Å soft X-ray flux of the C7.7 class solar flare. The central panels plot the radio dynamic spectra from the event covering a frequency range from 0.5-1000 MHz; (g) WIND/WAVES RAD 1 (20–1040 kHz), (h) WIND/WAVES RAD 2 (0.5-16 MHz), (i) I-LOFAR (20-88 MHz), (j) ORFÉES (140-1000 MHz). The I-LOFAR dynamic spectrum shows a type II radio burst with fundamental (F) and harmonic (H) components.

Research Goal

To date, a variety of methods have been developed to estimate shock characteristics from different wavelength observations, but they have not been comprehensively com-

pared. In this chapter, I compare three commonly used methods to derive M_A namely: (1) stand-off distance in EUV images in EUV images, (2) a comparison of CME speed to a data-driven model of Alfvén speed, and (3) the type II band-splitting method. This allows us to test the consistency of the methods but also allows us to derive more detailed shock characteristics than would normally be available using just one method. I determine the location of the type II radio emission along the CME front, and I relate the change in the angle between the local shock normal and coronal magnetic field direction to the onset and ceasing of the type II radio emission. In Section 5.2 the observations of a specific CME and type II radio burst are presented. The three methods to determine shock characteristics and evaluate M_A are explained in Section 5.3. In Section 5.4 I compare the results from the three methods and conclusions are discussed in Section 5.6.

5.2 Observations

A GOES C7.7 class flare (Figure 5.1f) began on 2 September 2017 at ∼15:23 UT from the active region (AR) NOAA 12672 (N05W90). The flare was associated with a CME that was observed at EUV wavelengths by GOES/SUVI and in white-light by LASCO C2. The CME propagated with an average velocity of ∼710 km s^{-1}, derived from a linear fit to the height-time measurements from SUVI and LASCO C2. Both flare and CME occurred on the western solar limb providing a plane-of-sky (POS) view of the eruption, as shown in Figure 5.1 (a) to (e).

In Figure 5.1 (g) to (j) the spectral radio observations from various ground-and-space instruments are shown, namely, WIND WAVES spectrographs RAD1 and RAD2 (Bougeret et al., 1995) observing between 20-1040 kHz and 1.075-13.825 MHz, respectively (g & h), I-LOFAR observing between 10-240 MHz (i) and the radio spectrograph, Observation Radio Frequence pour l'Étude des Eruptions Solaires (ORFÉES) observing between 140-1000 MHz (j). Panel (i) shows the type II burst observed by I-LOFAR

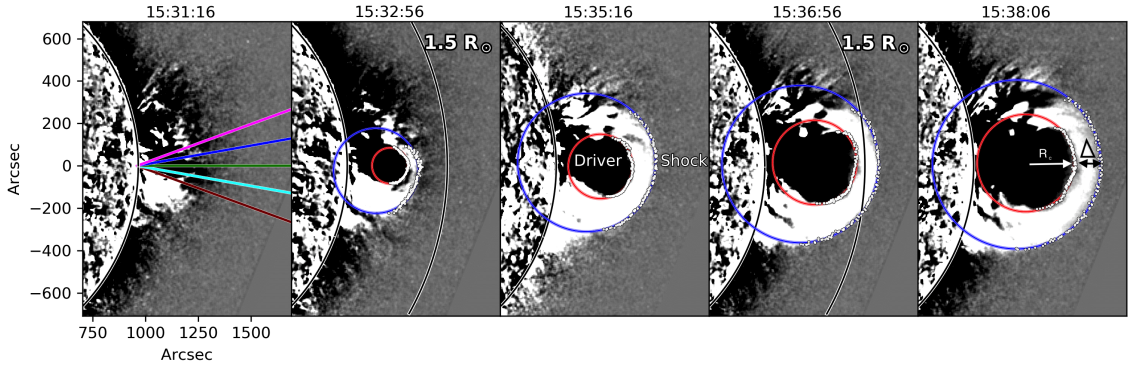

Figure 5.2: Base-difference images of the flaring region on the western limb of the Sun made by SUVI in the 195 Å channel from 15:31:16 to 15:38:06 UT, showing a dark region (interpreted as the driver) surrounded by an intensity enhancement (interpreted to be the shock sheath). The image contrast range was reduced to enhance these features. The SUVI base image is the average of 5 images before the start of the flare. The fives traces examined to determine the CME apex are shown in the first image. The large red and blue circles indicate the fitting to the edges of the eruptive plasma and shock front respectively, with the circle width representing a $\pm 1\,\sigma$ ($\pm 6''$) uncertainty. The dots are the points along the driver and shock front chosen using a simple edge detection method.

at ∼15:36 UT with well defined fundamental (f_p) and first harmonic ($2f_p$) components. The centre of the fundamental and harmonic components was first observed at ∼35 and ∼75 MHz respectively. The fundamental drifted gradually with a mean rate of -0.05 MHz s^{-1}. Superimposed over the type II is a type III radio burst that extends from ∼40 to ∼1 MHz observed at ∼15:37 UT.

5.3 Data Analysis

In this section, I discuss the implementation of the three aforementioned methods. The comparison of these methods allow us to determine if the results given by each are consistent and which method/s should be used by future studies. The shock characteristics provided by each method also allow us to determine the relationship between the eruptive structure seen in EUV, and the type II burst as observed in radio. Specifically, I determine where the radio burst was generated in relation to the CME (nose or flank) and the type of coronal environment that lead to shock-accelerated electrons and subsequent radio emission.

5.3.1 Method 1: Stand-off Distance

As discussed in Section 5.1, it is possible to derive shock properties from its geometry in images. Equation 5.6 relates the M_A to the normalised stand-off distance δ, which is the ratio of the stand-off distance Δ to the radius of curvature of the CME R_c. I applied this method to base difference images from GOES/SUVI in which we clearly see the eruption on the western limb of the Sun. In Figure 5.2 the brighter region is interpreted as the coronal plasma compressed by the transit of the shock driven by the CME, a region often referred to as the shock sheath. The darker circular feature that propagates away from the flaring region is identified as the CME that drives the shock.

Edge detection by eye is a common method used in solar physics and was deemed the most appropriate method for this study as the edge is quite pronounced. In ten trials, ten points were manually chosen along the leading edge of the driver and shock fronts respectively. The selected points are marked as small white dots in Figure 5.2. The driver and shock fronts were subsequently fitted with circles, indicated by the red and blue overlying circles. The line-width of the circles represents a ± 1 sigma uncertainty (2 pixels, 6.02″, 4 Mm), which was taken to be the uncertainty in position. I then examined the motion of the eruption along five traces as seen in the first panel of Figure 5.2. The traces originate at the active region from the solar limb, starting at 70° to the solar north and are separated by 10°. I determined where each trace intersected the blue circle to obtain a height-time profile of the shock along each trace. The height-time profile associated with the green trace was found to be at the largest height and was therefore taken to be the apex of the CME. Under this assumption, the stand-off distance was taken to be the distance between the nose of the CME driver and the shock front along the green trace.

The stand-off distance and radius of curvature of the CME were evaluated for nine instances from 15:32:56 to 15:40:56 UT. Over this time frame, the leading edge of the shock travelled from a heliocentric distance of $\sim$1.4 to $\sim$1.9 $R_\odot$ as shown in Figure

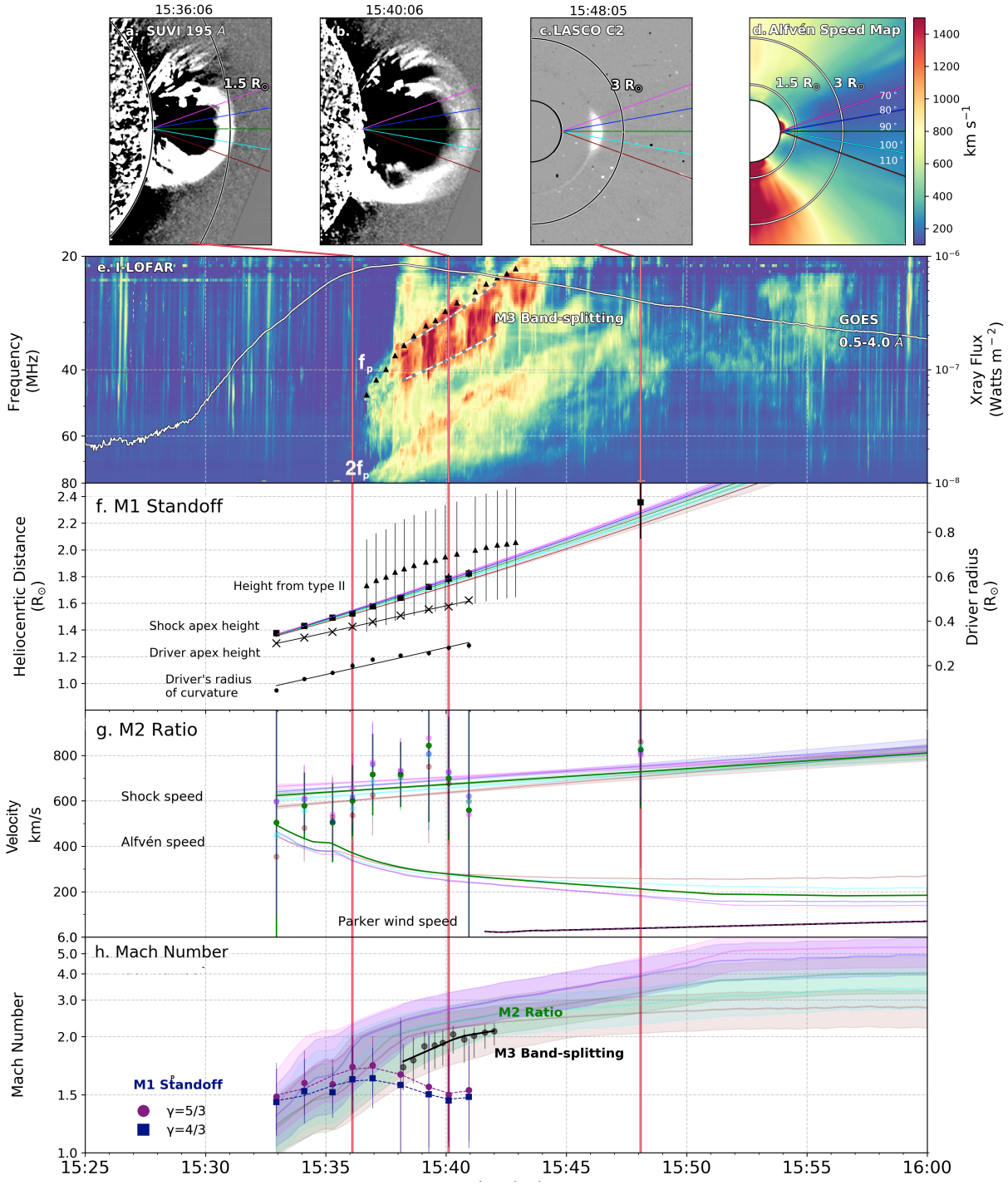

Figure 5.3: (a-c) Base difference images from SUVI 195 Å and LASCO C2. (d) 2D Alfvén speed map from Zucca et al. (2014a) model. Overlaid are the colour coded traces used in M2. (e) I-LOFAR type II burst observed showing fundamental (f_p) and harmonic ($2f_p$) bands. The grey points indicate the upper and lower edges of the f_p component. The black triangles on the f_p mark the points used in height of radio source calculations. Overlaid is GOES X-ray flux. (f) The triangles indicate the source height of type II f_p derived from a 2D electron density map. The squares are the shock front height along the green trace from SUVI and LASCO images. The height-time profiles of the shock front from each trace, with the colours corresponding to the traces indicated in panels a-c. The CME driver height along the green trace is marked by crosses and the radius of curvature of the CME is denoted by dots. (g) The estimated shock speed with uncertainties and Alfvén speed along the aforementioned five traces. The black line is the solar wind solution from Mann et al. (2002). (h) M_A evaluated using the 3 methods.

5.3(f). For each observation, M_A was calculated using Equation 5.6, the results of which are shown in Figure 5.3(h) and discussed in Section 5.4.1.

5.3.2 Method 2: CME Speed to Alfvén Speed Ratio

M_A was calculated by taking the ratio of the CME speed v_{CME} to the local background Alfvén speed v_A. The CME propagation speed was derived from EUV and white light imaging while the Alfvén speed was derived using a model called the Zucca et al. (2014a) model. This model will be discussed in detail in the coming section.

CME Speed

A height-time profile of the CME was derived from SUVI and LASCO C2 base difference images using a edge detection technique to track the CME's leading-edge above the solar limb. It is possible that the shock formed over an extended region around the nose, hence I examined five traces around the shock nose (same five traces from Method 1). Five traces were sufficient to capture all of the required detail in the relevant direction of motion. They are marked and colour-coded in Figure 5.3(a-d). The traces originate at the active region from the solar limb, starting at 70° to the solar north and are separated by 10°. The height-time profiles along each trace were fitted using a second-order polynomial, shown in Figure 5.3(f). The faint bands represent the uncertainty in position at all points in time ($\pm 1\sigma$), which was determined from the fit. The derivative of the height-time fits gave continuous velocity profiles, shown in Figure 5.3(g) and the velocity uncertainties were propagated from the position uncertainties. The motivation for using a parametric fit was to obtain smooth velocity profiles, as the velocities obtained by taking the first numerical derivative of the height measurements have a large scatter (see coloured points in Figure 5.3g).

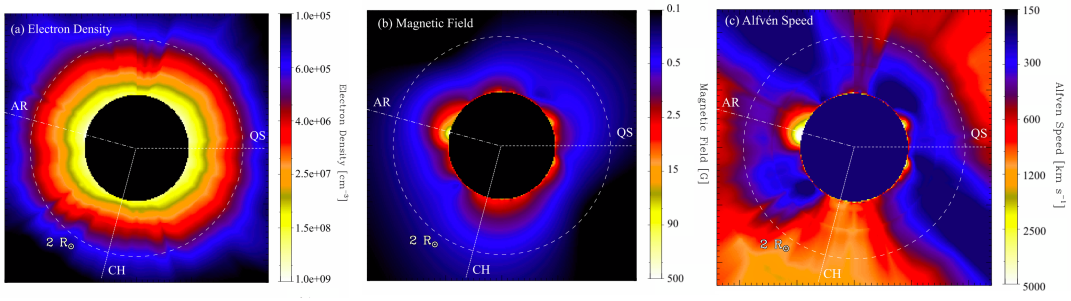

Figure 5.4: The Zucca Model. (a) 2D electron density map from 22 September 2011. (b) Magnetic field strength from PFSS (c) Alfvén speed map obtained from the electron density and magnetic field strength values. The active region (AR), quiet Sun (QS), and coronal hole (CH) radial profiles are labelled. Credit: Zucca et al. (2014a).

Alfvén Speed - The Zucca Model

Equation 1.1 illustrates that v_A is dependent on the magnetic field strength and ion density. The Zucca et al. (2014a) model produces a 2D plane-of-sky v_A map of the solar corona by combining measurements of (1) magnetic field strength and (2) electron density. In this model, an electron density map of the corona is generated using three different methods depending on the height range. For the heights ranging from 1.3 to 2.5 $R_\odot$, the electron densities are estimated from the differential emission measure (DEM) using the six EUV passbands on SDO/AIA. The DEM is a physical quantity proportional to the electron density and temperature gradient of a plasma which is linked to the distribution of the plasma temperature. For the height range of 2.5 to 5 $R_\odot$, electron densities are derived from the inversion of polarised brightness measurements from LASCO. For the intermediate height range of 1.3 to 2.5 $R_\odot$, a combined plane-parallel and spherically symmetric electron density model is employed.

An approximation of the coronal magnetic field up to 2.5 $R_\odot$ is estimated using the potential field source surface (PFSS) model (Schatten et al., 1969; Schrijver and DeRosa, 2003). PFSS modelling assumes that $\nabla \times B = 0$ and that the source surface is a surface of zero potential. At the source surface radius ($\sim 2.5\,R_\odot$), the magnetic field lines are forced to be radial. The PFSS code uses spherical harmonic coefficients calculated by Wilcox Solar Observatory using photospheric fields observed by the He-

lioseismic and Magnetic Imager on SDO. Figure 5.4 shows an example of a 2D electron density map, magnetic field strength map and the resulting Alfvén speed map. Figure 5.3(d) shows a section of the 2D plane-of-sky Alfvén speed map on the day of the event, produced from the Zucca et al. (2014a) model. Alfvén speeds reached $\sim 10^3$ km s^{-1} around the active region and decreased to $\sim$200 km s^{-1} at higher altitudes. The Alfvén speed profiles along the five traces marked in Figure 5.3(d) were extracted from the map.

When calculating M_A for each trace the speed of the CME relative to the solar wind speed is used such that M_A is $(v_{CME}\text{-}v_{wind})/v_A$ where v_{wind} is taken as the Parker solution to the solar wind, as in Mann et al. (2002). The results for M_A using this ratio method are shown in Figure 5.3(h) and discussed in Section 5.4.1.

5.3.3 Method 3: Band-splitting

The type II observed by I-LOFAR shown in Figure 5.3(e), does not present "classical" band-splitting in the form of distinctive split bands. Instead, I observe emission bands with large bandwidths. Similar observations presented by Mann et al. (1995) suggest that the relative instantaneous bandwidth of the type II can be used to infer the density jump across the shock, and therefore the M_A value. Points were selected along the lower and upper boundaries of the fundamental, marked by grey dots in Figure 5.3(e). The obtained points were then used to derive the relative instantaneous bandwidth $\Delta f_s/f$ which is related to the density jump across the shock front by

$$\frac{\Delta f_s}{f} = \frac{f_u - f_l}{f_l} = \frac{f_u}{f_l} - 1 = \sqrt{\frac{n_u}{n_l}} - 1 \tag{5.7}$$

where n is the electron density and the subscripts u and l denote the upper-frequency and lower-frequency bands, respectively. To determine M_A values, I used the expression

Method	Distance Range ($R_\odot$)	Alfvén Mach Values
M1. Shock Geometry	1.4 - 1.6	1.5 ±0.3 - 1.8±0.3
M2. $V_{cme}/V_{Alfvén}$	1.4 - 3.0	1.5 up to 4.0
M3. Type II band-splitting	1.6 - 1.8	1.8 - 2.0

Table 5.1: Comparison of three methods to derive Alfvén Mach.

from Vršnak et al. (2002) for a quasi-perpendicular shock:

$$M_A = \sqrt{\frac{X(X+5+5\beta)}{2(4-X)}} \tag{5.8}$$

where X is the compression ratio (n_d/n_u) and β is the plasma-to-magnetic pressure ratio. The plasma β was assumed to be 0.8, which is a typical value for a height of 1.5 $R_\odot$ above an active region (see Figure 2.1 adopted from Gary (2001)). The values of M_A derived from the bandwidth of the fundamental are shown in Figure 5.3(h) and discussed in Section 5.4.1.

5.4 Results

5.4.1 Comparison of three methods

I employed three commonly used methods to derive M_A of a CME-driven shock associated with a C7.7 class flare on 2 September 2017. The results from each method will now be discussed.

(M1) Stand-off distance: The first method involved measuring the stand-off distance at the shock nose and radius of curvature of the CME from EUV images taken by SUVI. I tracked the CME from a heliocentric distance of 1.2 to 1.9 $R_\odot$, until both the shock and CME expanded outside the instrument's field of view. The shock normalised stand-off distance ($\delta = \Delta/R_c$) was found to be approximately constant with a mean of 0.7±0.2. For an adiabatic index of 5/3, M_A steadily increased from 1.5±0.3 to 1.8±0.3 before decreasing steadily again to 1.5±0.1. An adiabatic index of 4/3 showed similar

behaviour as seen in Figure 5.3(h). These results are comparable to Gopalswamy et al. (2011) who studied a CME in a similar range of heights.

(M2) CME Speed to Alfvén Speed Ratio: The second method involved deriving the CME speed and Alfvén speed and taking the ratio to evaluate M_A (whilst accounting for the solar wind). As it is possible that the shock formed over an extended region around the nose, I examined five traces over this region. I found the Alfvén speed decreased from ∼500 km s^{-1} at a heliocentric distance of ∼1.4 $R_\odot$ to ∼200 km s^{-1} at ≥2 $R_\odot$. The uncertainty associated with the Alfvén speed model output is ∼20% (private communications with P. Zucca). Using (v_{CME}-v_{wind})/v_A, I found that on average M_A increased steadily from ∼1.5 up to ∼4 over a time frame of ∼17 minutes, which is in agreement with results from Zucca et al. (2018) and (Morosan et al., 2019). The faint bands represent the uncertainty in M_A values, which was propagated from the uncertainties associated with the Alfvén speed model and CME speed calculations.

(M3) Type II band-splitting: The third method, which used measurements of the relative instantaneous bandwidth in the type II fundamental component found M_A values to lie in the range of 1.8 to 2, which agree with previous studies (Vršnak et al., 2001; Zucca et al., 2014b; Chrysaphi et al., 2018).

Overview

The results from all three methods are summarised in Table 5.1. Notably, for all three methods the M_A values were initially similar (∼1.5) but diverge after ∼10 min. The inherent uncertainties associated with each method may explain the discrepancy between the results. M_A values from the stand-off method deviate after ∼15:37 UT, which may be due to the CME front leaving the field of view at this time, making the M_A more difficult to determine and less reliable. After ∼15:39 UT, M_A values from the ratio method were slightly larger (>2) than those derived from the band-splitting method (1.8 to 2), which may be a consequence of the uncertainties that exist in deriving v_{CME} from imaging, v_A from the Zucca et al. (2014a) model (given that the model is based on a combination of electron density models and a Potential Field Source Surface (PFSS)

model and v_{wind} from the Mann et al. (2002) model. Furthermore, the band-splitting method is also model-dependent and assumes a quasi-perpendicular shock and $\beta = 0.8$, which may not always be the case.

Future studies of coronal shock properties must err on the side of caution and use more than one method to determine values of M_A. In this study, I consider results from all three methods and look at the general trend, which suggests when the shock was at a heliocentric distance of 1.4 $R_\odot$ M_A was ∼1.5 and increased up to ∼4 as the shock propagated to ∼3 $R_\odot$.

5.4.2 Comparison of shock EUV kinematics with type II kinematics to determine radio source location

To determine where the radio burst was generated with respect to the driver, I use the type II and an electron density model to calculate the source height of the emission.

$$f_p = 8980\sqrt{n_e} \tag{5.9}$$

where n_e is expressed in cm^3 and f_p is in MHz. Using the electron density map produced by the Zucca et al. (2014a) model, I found that the type II propagated from a heliocentric distance of ∼1.8 to ∼2 $R_\odot$, as shown in Figure 5.3(f). The uncertainties in height are estimated to be ∼20%, which was propagated from the uncertainties associated with the density model (private communications with P. Zucca). In addition, the type II height estimations (black triangles) were cross checked with height estimations calculated using a standard Newkirk density model and they were found to be consistent. A comparison with shock EUV kinematics suggests the type II was at a larger altitude than the CME apex and therefore likely located around the nose of the CME (as opposed to the flanks).

5.5 Discussion

5.5.1 Why does the type II emission start?

As seen in Figure 5.3(h), at 15:33 UT, M_A is greater than unity according to Methods 1 and 3, which would imply shock formation yet type II emission does not start until 15:37 UT when M_A ∼1.7. To investigate why this is the case I study the relationship between the shock geometry with respect to the magnetic field and the associated type II. This requires the calculation of the magnetic field before the eruption using a PFSS model (Stansby et al., 2020). No flares occurred in the days prior to the event meaning the magnetic field did not change significantly and I can assume the PFSS model is reasonably reliable. The PFSS model overplotted on a SUVI 195 Å image is shown in Figure 5.5, with closed magnetic field lines in red and the open magnetic field lines in green. The two cyan arcs represent the position of the shock at (1) the onset and (2) cessation of the type II burst. At ∼15:36 UT the CME was at a heliocentric distance of ∼1.6 $R_\odot$ and passed through a region with numerous closed magnetic field lines.

As discussed in Section 2.2.2, the angle θ_{Bn} between the local shock normal $\hat{n}$ and upstream magnetic field direction $\hat{B}$ is an important quantity in deciding what electron acceleration mechanism occurs as discussed in Section 2.2.3. In the quasi-perpendicular case ($\theta_{Bn} \geq 90°$), electron reflection and acceleration at the shock is more likely to occur via the shock drift acceleration (SDA) mechanism. In this mechanism, the charged particles experience a grad-B drift along the shock front and gain energy due to the induced electric field, a result of $\mathbf{v} \times \mathbf{B}$ flow at the shock boundary (De Hoffmann and Teller, 1950). The accelerated electrons result in type II radio emission through the plasma emission mechanism (Melrose, 1975; Ginzburg and Zhelezniakov, 1993). As seen in Figure 5.5, during the initial stages (the first cyan arc) of the eruption the shock-to-field geometry was mostly quasi-perpendicular. This suggests conditions were favourable for SDA. Despite favourable shock geometry and a M_A greater than

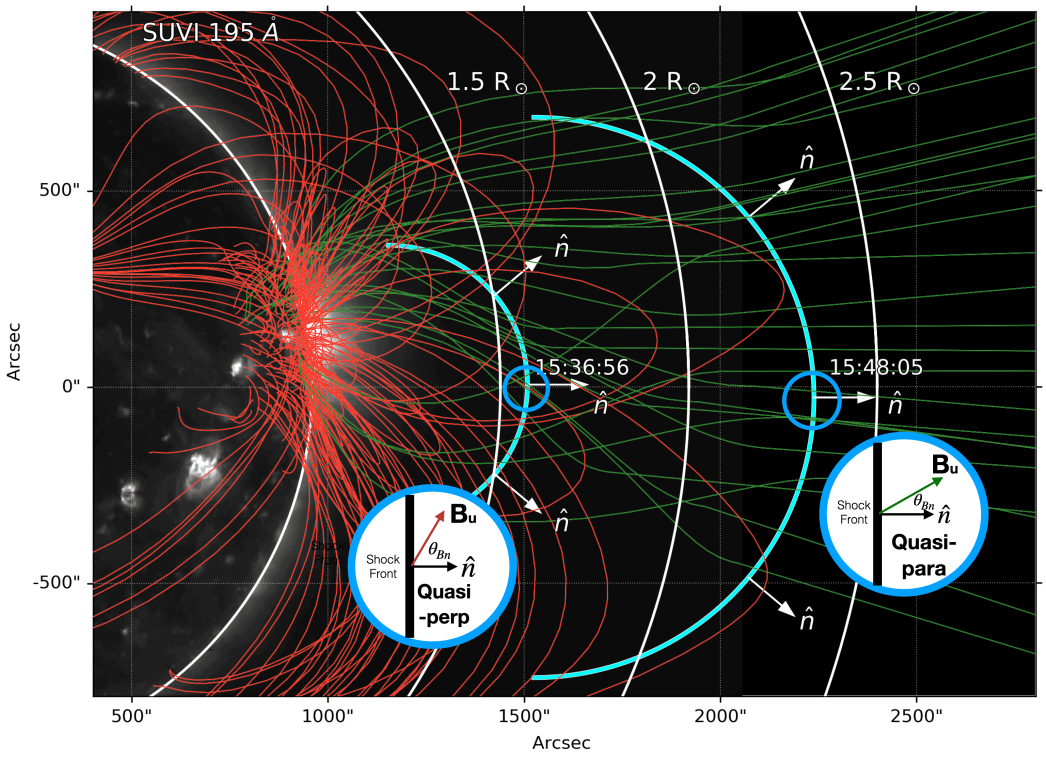

Figure 5.5: Magnetic field lines around the region of interest on 2 September 2017 overlaid on a GOES/SUVI image. A selection of closed (red) and open (green) field lines are shown. The cyan arcs represent the position of shock's leading edge when the type II emission began at 15:36:56 UT and ceased at 15:48:05 UT. The white arrows indicate the direction of the shock normal. The shock geometry is more likely to be quasi-perpendicular at the type II onset while a quasi-parallel configuration is more probable when radio emission ceases.

unity the type II only forms when the shock reached a heliocentric distance of ∼1.6 $R_\odot$ and M_A was ∼1.7. The onset of the type II may be explained when the shock M_A becomes supercritical, when the shock starts accelerating particles (see Section 2.2). The supercritical M_A number is greater than unity and depends on various shock parameters, including upstream β and shock angle θ_{Bn}. Edmiston and Kennel (1984) showed that for β ∼1 and a quasi-perpendicular shock, the Mach number reaches supercriticality at ∼1.7. This matches the M_A number I calculate at the time of radio emission start, as seen in Figure 5.3(h). This may explain why the type II emission was not observed despite a M_A greater than unity e.g., a supercritical M_A was required before particle acceleration began and radio emission was generated.

5.5.2 Why does the type II emission stop?

At ∼15:48 UT, the CME nose reached a heliocentric distance of ∼2.4 $R_\odot$ and the type II emission ceased despite the shock being super-Alfvénic and a M_A greater than 4, as seen in Figure 5.3(h). The cessation of radio emission could imply the conditions were no longer favourable for electron acceleration. This may be a result of a change in shock geometry with respect to the magnetic field. As seen in Figure 5.5, at the time of the type II onset the shock nose propagated through a region where the geometry is mostly quasi-perpendicular. Several minutes later at ∼15:48 UT, the shock reached a heliocentric distance of ∼2.3 $R_\odot$ where the magnetic field lines extend mainly in a radial direction and the type II radio emission ceased. Beyond ∼2 $R_\odot$ the shock-to-field geometry becomes predominantly quasi-parallel ($\theta_{Bn} \approx 90°$) in which case diffusive shock acceleration is the dominant particle acceleration mechanism. In this mechanism, particles are accelerated by successive reflections between the shock down and upstream regions due to the presence of magnetic turbulence. According to DSA theory, the rate of electron acceleration and hence the maximum energy attained is dependent on the shock-to-field geometry, as well as the shock strength (Jokipii, 1987). The electron acceleration efficiency would be considerably lower in the quasi-parallel configuration due to the long time required to energize particles. That is, particles spend most of their time random walking in the upstream or downstream regions (Guo and Giacalone, 2010b; Verkhoglyadova et al., 2015). Given that the shock nose becomes quasi-parallel, the electron acceleration efficiency may have reduced at this point and may be an explanation of the cessation of the radio emission despite an increasing M_A. This suggests that shock geometry is an important factor in the acceleration of electrons and the presence of radio emission similar to the results of Kozarev et al. (2015), Salas-Matamoros et al. (2016) and Zucca et al. (2018).

5.6 Conclusion

In this chapter, I presented a study of the formation and evolution of a CME-driven shock using three commonly used methods, namely: (1) stand-off distance in EUV images in EUV images, (2) a comparison of CME speed to a model of the coronal Alfvén speed, and (3) the type II band-splitting method. I was able to determine M_A in the corona at a heliocentric distance ranging from ∼1.4 to ∼3 $R_\odot$. It is important to note that the three different methods do not cover the same ranges of heights. Namely, the results from method 1 and 2 are in agreement when the shock propagates from a heliocentric distance of ∼1.4 to ∼1.6 $R_\odot$. At ∼1.6 $R_\odot$, the results from method 1 and 2 diverge, while the results from method 3 agree with method 2. Several factors play onto the divergence of method 2 but the most impactful is the inherent uncertainties associated with the method. In particular SUVI's limited spatial resolution and FOV. As a general trend, the results suggest M_A was initially ∼1.5 and increased up to 4 over a time frame of ∼17 min. Type II radio emission, coming from the nose region of the CME, began when the shock achieved supercriticality at a heliocentric distance of ∼1.6 $R_\odot$ when M_A was ∼1.7. Despite an increasing M_A (up to 4), the emission ceased when the shock front reached ∼2.4 $R_\odot$. I suggest this is a result of a change in shock geometry i.e., the shock was no longer quasi-perpendicular and efficient electron acceleration and therefore radio emission was inhibited. These results provide insight into the conditions necessary for the generation of type II radio bursts in the lower corona and explain why some fast CMEs propagating in the lower corona, which presumably drive shocks, are not associated with type II radio bursts, while other slower events do have type II bursts associated with them Gopalswamy et al. (2008, 2010); Suresh and Shanmugaraju (2015). It is important to note however, that type II radio bursts are also observed in interplanetary space (see Jebaraj et al. (2021) and references therein), where the majority of CME-driven shocks would not be in a quasi-perpendicular regime. In this case, dominant shock acceleration mechanism is diffusive shock acceleration (Drury,

1983; Jokipii, 1987), therefore the conditions necessary for type II radio emission are different. In interplanetary space plasma turbulence is believed to facilitate the efficient acceleration of low-energy particles and provide a means for overcoming the well known injection problem at interplanetary shocks (Guo et al., 2021). In conclusion, the speed of the exciters and M_A play an important role, however, they are not sufficient criteria for the occurrence of type II emission. For shocks in the lower corona, a supercritical M_A and favourable shock geometry is also required for the acceleration of energetic electrons.

6

LOFAR observations of a jet-driven piston shock in the low corona

The Sun produces highly dynamic and eruptive events that can drive shocks through the corona. As discussed in previous chapters, these shocks can accelerate electrons, which result in plasma emission in the form of a type II radio burst. Despite a large number of type II radio bursts observations, the precise origin of coronal shocks is still subject to investigation. In this chapter, I present a well-observed solar eruptive event that occurred on 16 October 2015, focusing on a jet observed in the EUV by SDO/AIA, a streamer observed in white-light by SOHO/LASCO, and a metric type II radio burst observed by LOFAR. For the first time, LOFAR observations were used

to interferometrically image the fundamental and harmonic emission of a type II radio burst. The imaging reveals that the sources did not appear to be co-spatial, as would be expected from the plasma emission mechanism. I correct for the separation between the fundamental and harmonic using a model which accounts for the scattering of radio waves by electron density fluctuations in a turbulent plasma. This allows us to show the type II radio sources were located $\sim$0.5 $R_\odot$ above the jet and propagated at a speed of $\sim$1000 km s^{-1}, which was significantly faster than the jet speed of $\sim$200 km s^{-1}. This suggests that the type II burst was generated by a piston shock driven by the jet in the low corona. This work was published in Maguire et al. (2021) in *The Astrophysical Journal*.

6.1 Introduction

As discussed in Chapter 1, the Sun regularly produces a variety of highly dynamic and energetic explosive events such as CMEs, flares, erupting loops or plasmoids, ejecta-like sprays and jets (Klein et al., 1999; Dauphin et al., 2006; Zimovets et al., 2012; Carley et al., 2013; Morosan et al., 2019; Maguire et al., 2020; Chrysaphi et al., 2020). The mass motions during these eruptive events can often travel with speeds that exceed the local Alfvén speed, which might result in the formation of shocks. The acceleration of electrons at the shock front can prompt coherent plasma emission at both the fundamental (f_p) and second harmonic ($2f_p$) of the plasma frequency (see Section 3.1). The type II radio emission generated in this process, provide a useful diagnostic of local coronal conditions and shock parameters. Furthermore, observations of type II bursts can provide insight into the origin of coronal shocks and help us determine whether they are (1) flare related due to blast waves (Hudson and Warmuth, 2004) or (2) CME or small scale ejecta related (Vršnak and Cliver, 2008). The shock can be further classified as a bow shock or a piston-driven shock as discussed in Section 2.2.1. For the bow shock scenario, the ambient plasma is able to flow around the driver so

that the shock and driver are seen to propagate at the same velocity (Cho et al., 2007; Schmidt et al., 2016). While in the case of a piston-driven shock, the plasma is unable to flow around the driver so that the distance between the driver and shock increases with time and the shock speed can be several times that of the driver (Pomoell et al., 2008; Nindos et al., 2011; Bain et al., 2012; Grechnev et al., 2018).

To date, the origin of plasma shocks have predominantly been studied in terms of highly energetic events namely; strong flares (Zucca et al., 2018), X-ray jets (Klein et al., 1999), erupting coronal loops (Dauphin et al., 2006), eruptive magnetic flux rope (Wang et al., 2017), plasmoids (Bain et al., 2012; Zimovets et al., 2012) and CMEs (Grechnev et al., 2018). However few studies have investigated type II bursts associated with EUV jets and weak CMEs (see Magdalenić et al. (2010) and Chrysaphi et al. (2020) as examples). In this chapter, I present observations of a C-class flare and a narrow jet that resulted in a metric type II radio burst. I determine the location of the type II burst and carry out a multi-wavelength kinematic analysis to infer the origin of the shock.

Our kinematic analysis includes an investigation of low-frequency radio wave scattering in the corona, which is necessary to account for radio source displacements from their true position. Early observations by the Culgoora Radioheliograph revealed that type II fundamental emission is radially shifted outwards with respect to harmonic emission (Kai and McLean, 1968; Sheridan et al., 1972; Nelson and Sheridan, 1974; Nelson and Robinson, 1975; Suzuki et al., 1985). Such behaviour is attributed to radio wave scattering as discussed in Section 3.3.1. More recently, LOFAR tied-array beam observations (see Section 4.1.2.4) demonstrated that band-split type II fundamental sources experience displacement due to radio wave scattering in a turbulent medium (Chrysaphi et al., 2018). In this chapter, I use LOFAR interferometric observations, which have superior spatial resolution with respect to tied-array observations, to image the separation between type II fundamental and harmonic components with unprecedented spatial and temporal resolution (see Section 4.1.2.4). I account for the spatial

displacement between fundamental and harmonic sources using a model of radio wave scattering in the corona which allows for a necessary correction of radio source positions and their comparison with the shock driver imaged in EUV, showing they follow the kinematics of a piston-driven shock.

In Section 6.2, observations of the flare, jet and type II radio burst are presented. The observational method and models used to determine the radio source location are described in Section 6.3. I discuss the shock origin and the nature of radio wave scattering in Section 6.4, and finally, conclusions are presented in Section 6.5.

6.2 Observations

A GOES C4.3 class flare (Figure 6.1b) began 16 October 2015 at ∼13:20 UT from active region NOAA 12435. The flare was located on the solar eastern limb and inspection of data from the Extreme Ultraviolet Imager (EUVI; Wuelser et al., 2004) onboard the STEREO-A spacecraft near the time of the flare revealed that the active region extended around the far side of the Sun. Base difference images shown in Figure 6.1(a) from the 304 Å passband of the AIA onboard SDO illustrate the evolution of a jet that emerged from the active region during the impulsive phase of the flare. The jet originates from a foot point of the AR on the limb, meaning it most likely propagated close to the plane-of-sky (POS). The ejected material initially moved radially before moving slightly southward. Below the jet, a spray-like feature was observed to propagate in a southward direction. The spray emerged an hour prior to the flare and persisted for the duration of the eruption.

In Figure 6.1 (c) to (f) the spectral radio observations from various ground instruments are shown, namely LOFAR's remote station RS509 observing between 10-240 MHz, the radio spectrograph Observation Radio Frequence pour l'Étude des Eruptions Solaires (ORFÉES) [1], observing between 140-1000 MHz and the Learmonth site

[1] http://secchirh.obspm.fr/spip.php?article19

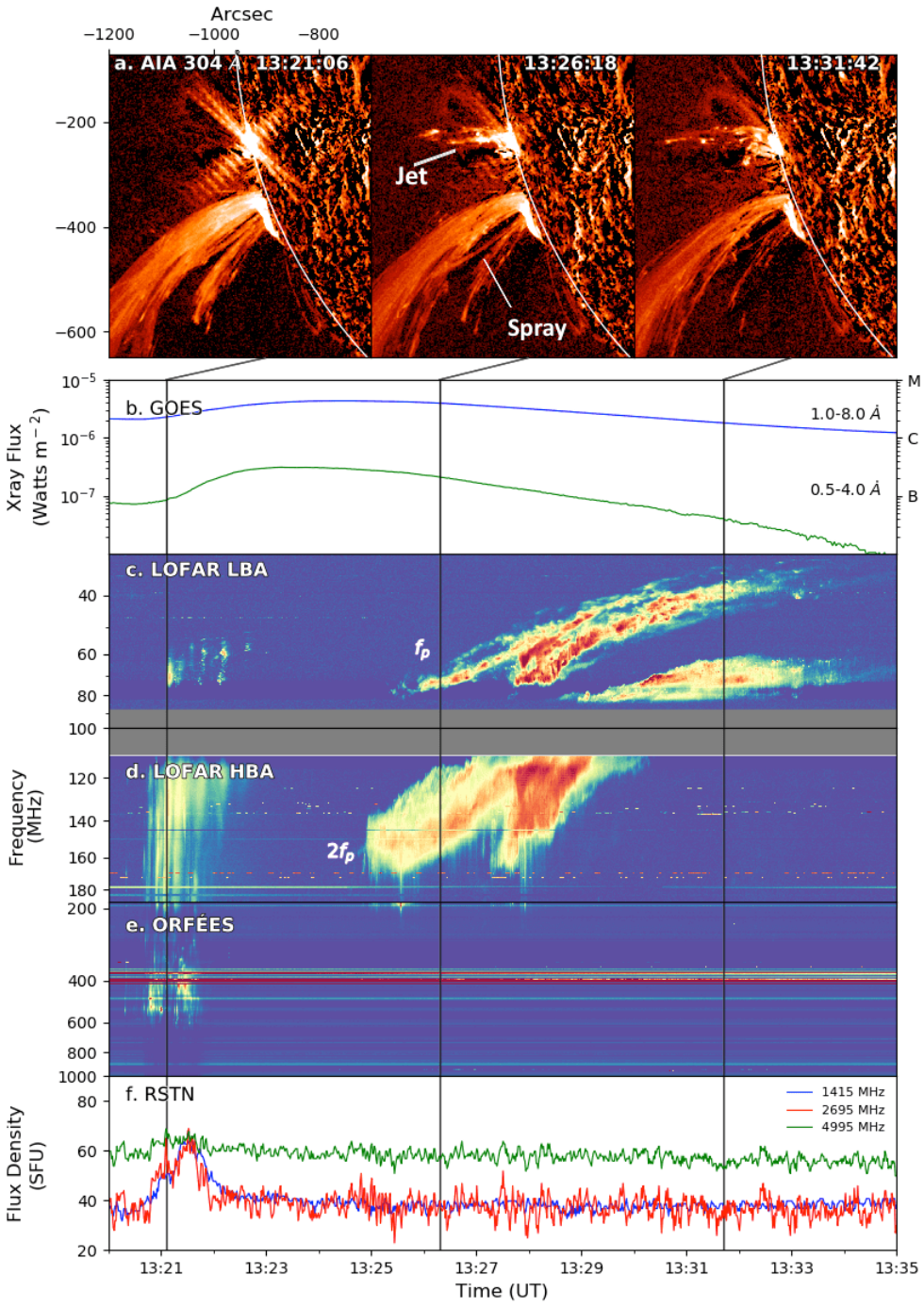

Figure 6.1: (a) Base difference images of the jet and spray observed with AIA 304 Å, (b) GOES 0.5-4 Å and 1-8 Å soft X-ray flux of the C4.3 class solar flare. The remaining panels show the radio emission as observed by (c) LOFAR's low band antennae (LBA) (30-90 MHz), (d) LOFAR's high band antennae (HBA) (110-240 MHz), (e) ORFÉES (140-1000 MHz) and (f) RSTN channels (1415, 2695, 4995 MHz). The LOFAR dynamic spectra show a type II radio burst with fundamental (f_p) and harmonic ($2f_p$) components initiating at 13:25 UT and ceasing at 13:34 UT.

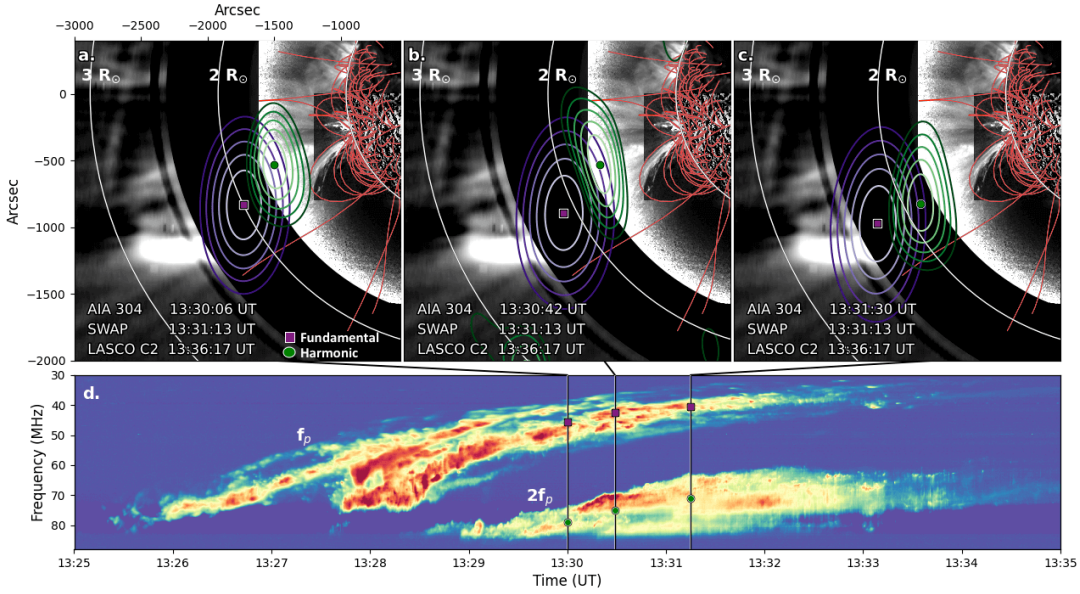

Figure 6.2: (a-c) Type II radio burst observed by LOFAR at three separate times. The purple and green contours represent 50-90% of the peak flux density of the fundamental (f_p) and harmonic ($2f_p$) radio sources, respectively. The purple square and green dot represent the bursts' centroid position. The burst contours are overlaid on a composite of images from AIA 304 Å (innermost image), SWAP 174 Å (central image) and LASCO C2 (outermost image). The coronal magnetic field determined from the PFSS is shown by red lines. The solid white circles indicate distances of 2 and 3 $R_\odot$. (d) The corresponding dynamic spectrum showing the f_p and $2f_p$ components. Purple squares and green dots denote the points along the burst that have been imaged.

of the Radio Solar Telescope Network (RSTN)[1] measuring solar radio flux density. Coinciding with the onset of the GOES X-ray at 13:20 UT, a group of type IIIs were detected by LOFAR and ORFÉES, as shown in panels (c) to (e) in Figure 6.1. Subsequently at ∼13:25 UT, LOFAR observed a strong type II radio burst with well-defined fundamental and first harmonic emission bands, indicated in Figure 6.1(c & d) by f_p and $2f_p$, respectively. At the time of the type II burst there was no significant radio emission above 200 MHz (see panel e & f), which suggests that no radio emission was generated or escaped from low in the corona and that the flare may have been partially occulted. LOFAR also provided interferometric observations of the event until 14:00 UT using the low band antennas (10-90 MHz) from 36 stations (24 core and 16 remotes). The maximum baseline of the LOFAR observation was 84 km, which gave

[1] http://www.ngdc.noaa.gov

sub-arcminute resolution across almost all of the observed frequency range. Observations of the calibrator source, Virgo A, were taken simultaneously over all subbands. The visibility data was recorded with a correlator integration time of 0.167 s. The data was processed using the Default Processing Pipeline (DPPP; van Diepen et al., 2018) followed by an implementation of WSCLEAN (Offringa et al., 2014) (see Section 4.1.1.3) to produce images with a spectral resolution of 195.3 kHz and cadence of 1 s.

6.3 Data Analysis and Results

The type II emission was temporally coincident with the motion of the EUV jet, therefore it is assumed to be the shock driver. In the following section, I determine the location of the fundamental and harmonic components of the type II burst in relation to the jet observed in EUV. This can only be done after accounting for radio wave propagation effects, allowing us to determine where the radio burst was generated in relation to the eruptive structure and the kind of coronal environment that leads to shock formation.

6.3.1 Imaging of radio burst

To track the motion of the shock, I image the fundamental and harmonic components of the type II burst at multiple moments in time. Figure 6.2(a-c) illustrates the position of the fundamental (purple contours) and harmonic (green contours) component of the type II burst overlaid on a composite of images from AIA 304 Å (innermost), Sun Watcher using Active Pixel (SWAP; Berghmans et al., 2006) 174 Å (central) and LASCO C2 (outermost). The red lines represent the Sun's coronal magnetic field, which was extrapolated from the photospheric magnetic field using the Potential-Field Source-Surface model (PFSS; Stansby et al., 2020) with data from the Global Oscillation Network Group (GONG; Harvey et al., 1996). It is important to note a PFSS on the eastern solar limb should be interpreted with caution. Coronal fields are inferred using

photospheric measurements that are obtained in a region close to the central meridian on the solar disk and are then compared with coronagraphic images at the limbs, taken at least seven days before or after to account for solar rotation. This implicitly assumes that no significant changes in the corona occurred over that time. Indeed this most certainly is not the case in the active Sun. Figure 6.2(d) demonstrates the type II radio burst dynamic spectrum with the fundamental and harmonic emission bands labelled as f_p and $2f_p$, respectively. The purple squares and green dots indicate the points imaged along the burst as seen in panels a-c. The imaging reveals that the fundamental source (purple contours) is shifted outwards with respect to the harmonic source (green contours) by 0.3-0.5 $R_\odot$. I find that regardless of where I image on the emission bands at one particular time, there is a clear separation between the fundamental and harmonic sources. Such behaviour contradicts the underlying plasma emission mechanism according to which fundamental and harmonic radio waves are generated in the same location and should therefore appear co-spatial (see Section 3.1). The observed displacement is potentially due to the scattering of radio waves by electron density fluctuations that exist due to turbulent plasma processes in the corona (Steinberg et al., 1971; Stewart, 1972; Riddle, 1974; Nelson and Sheridan, 1974). Scattering effects are particularly significant on fundamental (as opposed to harmonic) radio waves because the fundamental emission is close to the plasma frequency and therefore strongly affected by propagation effects, e.g., due to small-scale variations in the background density of the plasma. This variation in the background density determines the level of scattering of radio waves and is described by the relative level of root mean squared (r.m.s) density fluctuations $\varepsilon = \sqrt{\langle \delta n^2 \rangle}/n$, where n is the electron density.

In the next section, I account for the effects of scattering on fundamental emission to correctly interpret the type II observations for this event and in the process gain insight into the parameters that describe radio wave scattering.

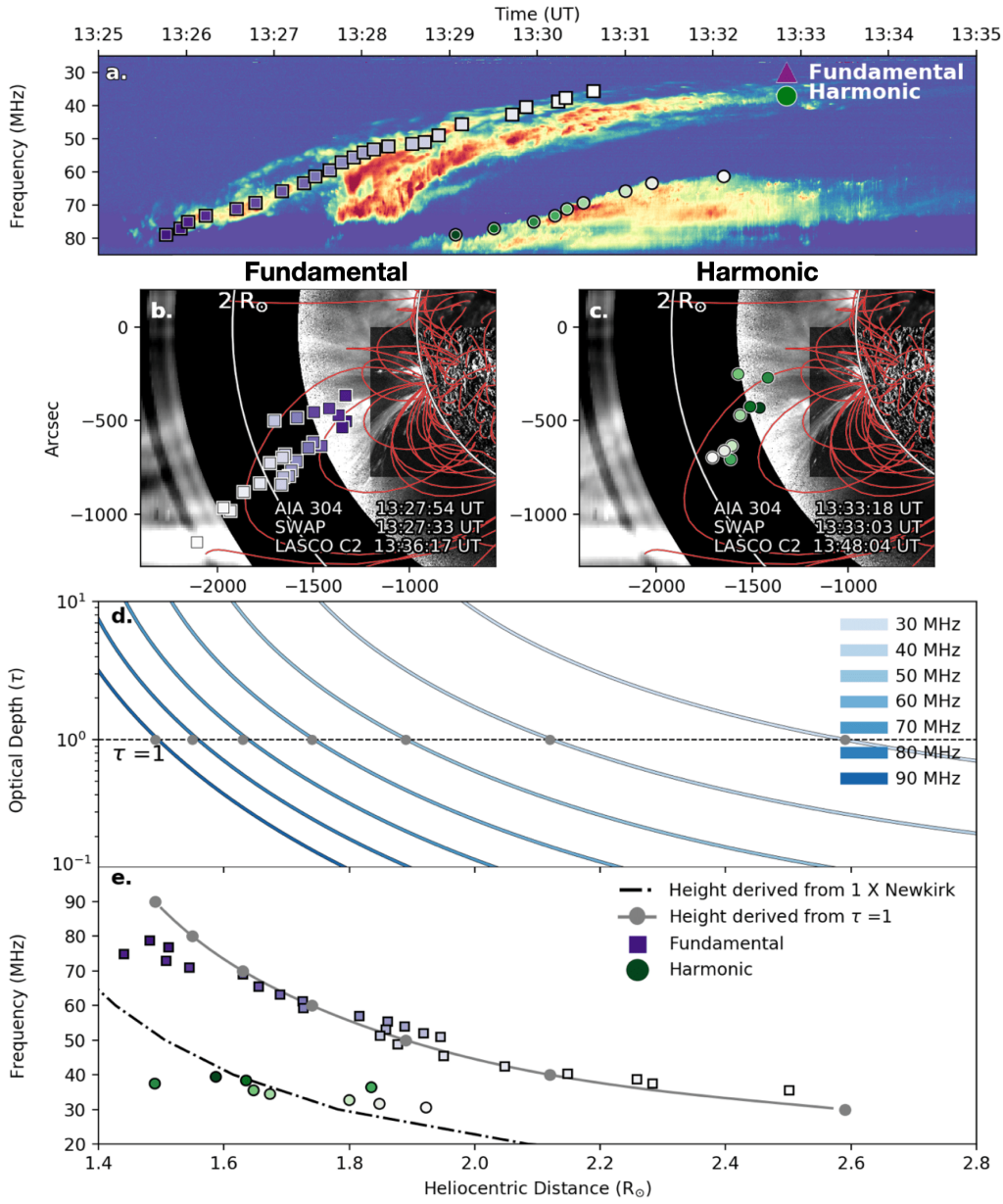

Figure 6.3: (a) LOFAR dynamic spectrum of a type II burst with fundamental and harmonic emission. The purple squares and green circles overlaid indicate the frequency and times that were imaged, with dark-to-light shading representing progression in time. (b & c) show the centroids of the type II burst f_p (purple) and $2f_p$ component (green) on a composite image from AIA 304 Å, SWAP 174 Å and LASCO C2. The coronal magnetic field determined from the PFSS is shown by red lines. (d) The optical depth with respect to scattering for radio waves as a function of heliocentric distance. The dashed line indicates τ=1. The grey dots indicate the height at which the radio source is predicted to appear for each frequency. (e) The heights of f_p (purple squares) and $2f_p$ (green dots) sources as observed by LOFAR. The grey line represents where the scattering model predicts the fundamental radiation escapes and the dashed black line represents where the emission is generated.

6.3.2 Scattering of fundamental plasma emission

The dynamic spectrum presented in Figure 6.3(a) shows the type II fundamental and harmonic emission bands marked with purple squares and green circles, respectively,

with dark-to-light shading representing progression in time. The time-frequency points were selected using a fundamental to harmonic frequency ratio of 1.8-1.9, to be consistent with observations (Melnik et al., 2018). Panels (b) and (c) depict the positions of the fundamental and harmonic sources on a composite image from AIA 304 Å, SWAP 174 Å and LASCO C2. The coronal magnetic field determined from the PFSS is shown by red lines. Here I assume the displacement between the fundamental and harmonic emission is caused by radio wave scattering. To estimate the extent to which the fundamental is shifted by scattering, I adopt the Chrysaphi et al. (2018) model. As discussed in Section 3.3.1, this model assumes that as radio waves propagate through the corona, they undergo repeated small-angle deflections due to isotropic fluctuations in the plasma density caused by turbulence. The optical depth with respect to scattering for radio waves in the corona is described as

$$\tau(r) = \int_{r}^{1AU} \pi \frac{f_p^4(r)}{(f^2 - f_p^2(r))} \frac{\varepsilon^2}{h} dr \tag{6.1}$$

where f_p is the plasma frequency, h is the effective scale length of density fluctuations and ε is the relative level of electron density fluctuations[1]. A given model of f_p predicts where the emission is generated, and where I expect to see harmonic emission, since it undergoes very little scattering. The Newkirk model (Equation 3.13) best describes the positions of the harmonic sources, assuming the shock propagated close to POS (see Figure 6.3e). Considering Equation 6.1, $\tau(r) = 1$ corresponds to the heliocentric distance at which fundamental radio emission is expected to escape. The value of ε^2/h was obtained from optimising the fit between the heights predicted at τ=1 with the radial positions of the fundamental emission. Using this approach ε^2/h was found to be $2\times10^5\,\mathrm{km}^{-1}$.

Figure 6.3(d) illustrates the solution to Equation 6.1, showing how τ varies with r

[1]Eq.6.1 is adopted from Eq.9 of Chrysaphi et al. (2018), where I have assumed a power-law spectrum of electron density fluctuations, which is more consistent with in-situ observations (Bastian, 1994). This means that the coefficient $\sqrt{(\pi)}/2$ is now π (following Eq.31 of Thejappa et al. (2007) and Eq.34 of Thejappa and MacDowall (2008)

for different values of f (where f ranges from 30 to 90 MHz in steps of 10 MHz). The dashed line indicates the point at which $\tau(r) = 1$. The expected height of scattered fundamental emission at each frequency is marked by a grey dot. In Figure 6.3(e), the grey line represents where the model predicts the fundamental radiation eventual escapes. The dashed black line is where the emission is generated (according to the Newkirk density model), and where the harmonic emission should be observed. The heights of fundamental sources (purple squares) agree quite well with the scattering model (grey line) while the harmonic sources (green dots) are in agreement with the Newkirk model (dashed black line). This shows the spatial displacement of these radio sources is accounted for by the scattering model.

It should be noted that there is a deviation between the models and data at higher frequencies and this may be an effect of the Newkirk model's inability to accurately describe the complex structure of the low corona. There are a plethora of density models such as Mann, Baumbach–Allen and Saito, however, these models predict even lower densities at these heights (Baumbach, 1937; Allen, 1947; Saito et al., 1970; Mann et al., 1999). The Newkirk model was therefore established as the most appropriate to describe the observed source positions.

To summarize, LOFAR provided images of the fundamental and harmonic emission so that I was able to identify where the radio waves were generated (location of harmonic) as well as where the scattered radio waves escaped (location of fundamental). Overall the Chrysaphi et al. (2018) model successfully accounts for the spatial separation between the fundamental and harmonic emission. The model proved to be a reliable means to correct for the positional shift due to scattering so that I can accurately determine the type II burst kinematics.

6.3.3 Kinematics of ejecta and type II radio burst

Figure 6.4(a) presents a composite of base difference images from SDO/AIA 304 Å and LASCO C2 showing the jet on the solar limb and an overarching helmet streamer

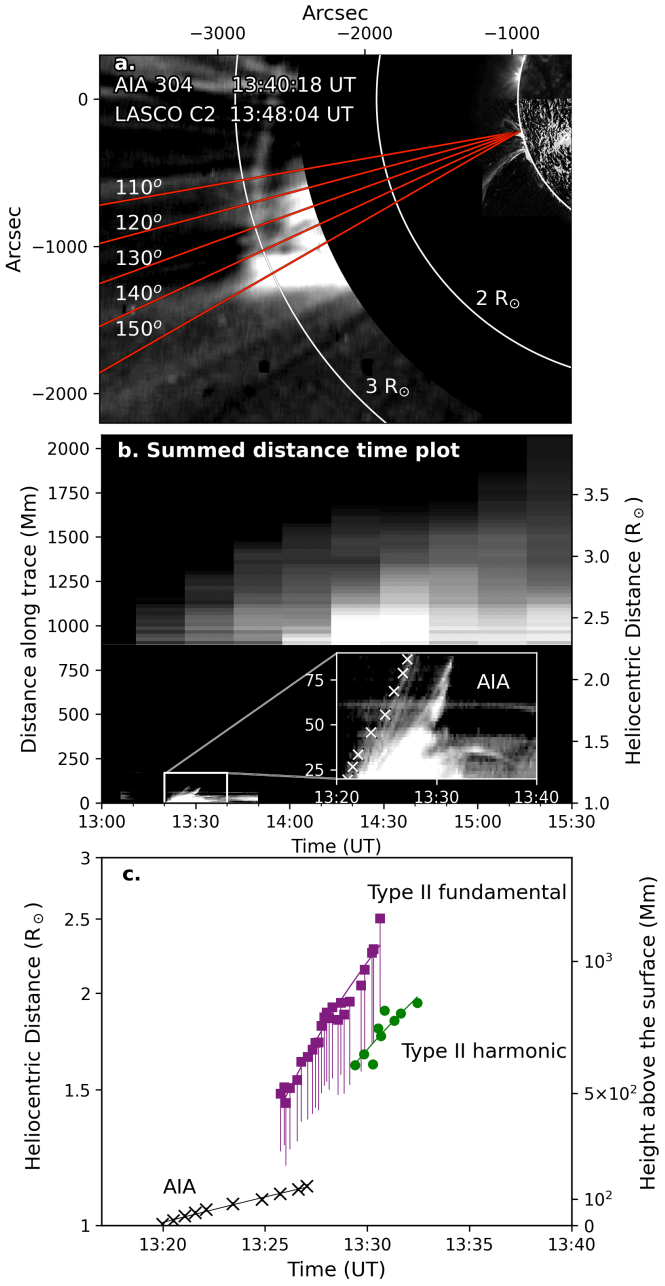

Figure 6.4: (a) Composite of base difference images from AIA 304 Å and LASCO C2, with five red traces over the region of interest. The traces start at 110° to the solar north and are separated by 10°. (b) The sum of the time distance plots generated along the five traces and a zoom-in of the AIA field of view. (c) The height time profiles of the EUV and radio features. The jet as seen by AIA is marked by black crosses and the position of the fundamental and harmonic type II radio emission are marked by purple squares and green dots, respectively. The error bars associated with the fundamental emission represent the scattering induced radial displacement.

positioned ∼100° to solar north. To determine the ejecta kinematics, five traces were examined around the region of interest, indicated by five red lines in Figure 6.4(a).

The traces originate at the active region from the solar limb, starting 110° to the solar north and are separated by 10°. A space-time plot was obtained for each of the five traces. The sum of five space-time plots is illustrated in Figure 6.4(b). The inset is a zoom-in on the AIA FOV showing the jet, which appears to have a few components, as indicated by the two-prong structure. I take the foremost component as a measure of the jet front. The crosses overlaid in Figure 6.4(b) indicate the points selected using a point-and-click technique. The fundamental and harmonic emission heights were taken as the distance between the source centroid to the solar centre. Combing the EUV and radio data, a height time profile was constructed as shown in Figure 6.4(c). The jet is marked by black crosses and the height of the type II fundamental and harmonic emission are marked by purple squares and green dots, respectively. The error bars associated with the fundamental emission represents the scattering induced radial shift, which was calculated in Section 6.3.2. The error associated with the EUV heights was deduced from 10 trial measurements of height in Figure 6.4(b) and was found to be ∼0.1 $R_{\odot}$ (∼10 pixels). The jet was observed to have an average velocity of ∼200 $\mathrm{km\,s^{-1}}$ and the type II fundamental and harmonic travelled at ∼1000 $\mathrm{km\,s^{-1}}$ and ∼1090 $\mathrm{km\,s^{-1}}$, respectively. The significance of these results are discussed in Section 6.4.1. I note that although there is slight movement in the streamer observed by LASCO C2, it is unclear whether this is associated with the motion that lead to the type II burst therefore I concentrate on the kinematics of the jet and type II burst in this study.

6.4 Discussion

6.4.1 What is the origin of the shock?

As seen in Figure 6.1, the EUV jet emerged at 13:20 UT from the solar limb and propagated outwards at a speed of ∼200 $\mathrm{km\,s^{-1}}$. Although the jet initially moved radially, the PFSS in Figure 6.3(b&c) suggests that the ejected material later moved

southward due to the closed magnetic field lines. About five minutes later, the type II burst was observed $\sim 0.5 R_{\odot}$ above the jet and had a significantly larger velocity ($\sim$1000 km s^{-1}), which is indicative of a piston-driven shock as discussed in Section 2.2.1 (Maxwell et al., 1985; Liepmann and Roshko, 1957; Pomoell et al., 2008; Vršnak and Cliver, 2008). It is important to note that I have based this analysis on the assumption that the driver and shock propagate close to the plane-of-sky, even if this was not precisely the case our interpretation is still valid. For example, if the shock propagated at an angle of 20° from the plane-of-sky, the shock speed would still exceed the speed of the driver, which is characteristic of a piston-driven shock.

I found the local Alfvén speed (Equation 1.1) in the region of interest by combining the Newkirk electron density model and a 2D plane-of-sky magnetic field map (derived from a PFSS model). Considering the five traces in Figure 6.4(a), the average Alfvén speed at 2 $R_{\odot}$ was found to be 740$\pm$70 km s^{-1}. The fact the jet (shock-driver) propagated at sub-Alfvénic velocities ($\sim$200 km s^{-1}), provides further evidence that the shock was piston-driven (Vršnak and Cliver, 2008). The Alfvén Mach number M_A of the shock was estimated to be $\sim$1.35 by taking the ratio of the shock speed ($\sim$1000 km s^{-1}) to Alfvén speed (740$\pm$70 km s^{-1}). This M_A value is consistent with previous studies (Vršnak et al., 2001; Zucca et al., 2014a; Maguire et al., 2020). The M_A was also estimated from the band-splitting seen in the type II fundamental emission band at 13:27:30 - 13:30:00 UT. Using the relative instantaneous bandwidth between the upper and lower split bands, the compression ratio X was found to be in the range 1.3-1.5. To determine M_A values, I used the expression from Vršnak et al. (2002) for a perpendicular shock:

$$M_A = \sqrt{\frac{X(X+5+5\beta)}{2(4-X)}} \tag{6.2}$$

where β is the plasma-to-magnetic pressure ratio ($\beta << 1$). The values for M_A were found to be 1.3-1.4, which is consistent with M_A derived from the shock speed to Alfvén speed ratio.

In summary, I suggest that as the jet erupted, a piston-driven shock was established ahead of it and the streamer may have acted as a tube for the shock to propagate down (Eselevich et al., 2015). Piston-driven shocks with type II emission have often been associated with wide and fast CME drivers (Kahler et al., 2019) but few have reported piston shocks resulting from narrow ejecta low in the corona as is the case in this event Maxwell et al. (1985).

6.4.2 Radio wave scattering in the low corona

In Section 6.3.2 I showed that the scattering model successfully accounts for the spatial separation between the type II fundamental and harmonic emission. Let us consider the validity of the model's assumptions, namely, that scattering is the dominant radio wave propagation effect in the low corona and that scattering is due to isotropic density fluctuations.

I provide evidence that scattering is the dominant propagation effect on radio waves by comparing the size of the fundamental and harmonic sources, normalised to the point spread function of LOFAR (see Figure 6.2 a-c). The fundamental sources were found to be 1.6-1.9 times larger than the harmonic sources. This is as expected since scattering from density fluctuations is known to have a more significant effect on the fundamental emission rather than the harmonic (Nelson and Robinson, 1975; Lengyel-Frey et al., 1985).

The model used in this work also assumes radio wave scattering by isotropic density fluctuations. However, previous work suggests that density fluctuations are in fact anisotropic, which would imply ε^2/h has both a parallel and perpendicular component (Armstrong et al., 1990; Anantharamaiah et al., 1994). In order to determine whether this assumption changes our results, I consider the effects of anisotropic scattering on radio sources. Numerical models by Kontar et al. (2019) suggest the radial shift experienced by a radio source due to anisotropic scattering is slightly less than in the isotropic scenario ($\sim$0.52 $R_\odot$ compared to $\sim$0.68 $R_\odot$ for a source propagating in POS).

To account for the displacement under anisotropic scattering conditions, the values of ε^2/h would have to be slightly larger. It is important to note that although anisotropy does not have a dramatic effect on the radial shift, it does affect source morphology, e.g. sources are expected to elongate perpendicular to the heliospheric radial direction due to enhanced scattering perpendicular to the large-scale (radial) magnetic field of the Sun or elongated sources (Ingale et al., 2015; Kontar et al., 2017).

While the simple analytical model used in this analysis can successfully account for shifted positions of the radio sources, it can not account for all observed properties of scattered sources (for example size and morphology). As such, future studies that combine fully developed numerical scattering models with interferometric observations from LOFAR are needed to comprehensively understand radio wave propagation in the turbulent plasma near coronal shocks.

6.5 Conclusion

I present a study of a flare, jet and type II radio burst that occurred on 16 October 2015 on the eastern limb of the Sun. The purpose of this study was to determine the location of the type II burst and the origin of the associated plasma shock. I carried out a multi-wavelength kinematic analysis, which included an investigation of low-frequency radio wave scattering in the corona. For the first time, LOFAR interferometrically imaged both the fundamental and harmonic emission of a metric type II and revealed that the sources are not co-spatial, as would be expected from the plasma emission mechanism. I account for their spatial displacement using a model of radio scattering in the corona. This model allowed for the necessary correction of the source positions and their comparison with the shock driver. Furthermore, optimisation of the model to the data provided information about scattering parameters in particular the level of density fluctuations in the turbulent corona e.g. I found that $\varepsilon^2/h \sim 2\times10^5\,\mathrm{km}^{-1}$, which is slightly lower compared to previous studies (Chrysaphi et al., 2018).

After accounting for radio wave scattering effects, I determined where the radio burst was generated in relation to the eruptive structure and the coronal environment that lead to shock formation. I found that the type II burst was located at a much higher altitude than the EUV jet and had a significantly larger velocity, namely the jet speed was $\sim$200 km s^{-1} while the type II burst propagated at $\sim$1000 km s^{-1}. The association of the sub-Alfvénic jet with the type II burst and the relative velocities of the jet and the type II emission provides strong evidence of a shock that was initially piston-driven.

The benefits of this study were twofold. Firstly, I accounted for radio wave scattering effects using a simple model and determined the true propagation path of the shock. This in turn highlighted the importance of accounting for scattering effects in radio imaging. Secondly, the combination of EUV, white-light and radio imaging allowed us to diagnose the shock driver and infer the precise origin of the shock.

7

LOFAR observations of multi-lane type II radio burst driven by complex flare spray

It is widely accepted that type II radio bursts are one of the most reliable radio signatures of shock formation in the solar corona. These bursts can often exhibit variations in morphology and substructure, which can give us insight into the behaviour of the shock driver and ambient coronal conditions. Current generation radio interferometers such as LOFAR, are providing an unprecedented opportunity to study shock formation and its relationship to type II morphology and substructure. In this chapter, I present unique observations of a solar eruptive event that occurred on 16 October 2015, focusing on a spray observed in the EUV by SDO/AIA and a multi-lane type

II radio burst observed by LOFAR spectroscopically and interferometrically. LOFAR observations were used to interferometrically image the type II emission and reveal multiple distinct regions of radio emission along the shock, including three pairs of band-split sources. The type II emission was temporally coincident with the motion of a EUV spray that propagated in multiple directions, at speeds ranging from 50 to 200 $\mathrm{km s^{-1}}$. These observations suggest that the spray drove a shock and radio emission was generated in different regions of the shock where the local plasma conditions were favourable for plasma emission, namely where shock obliquity is quasi-perpendicular. Furthermore, the three pairs of band-split sources were found to be co-spatial within the observational uncertainty. This is in agreement with the theory that band splitting is caused by radio emission emitted simultaneously from upstream and downstream of the shock front. This study highlights the importance of high-resolution radio imaging and how imaging is needed to correctly interpret type II spectroscopic data. This work is *in prep* for submission to the *Astrophysical Journal*.

7.1 Introduction

Type II radio bursts can often exhibit variations in morphology and substructure, which provide insight into the nature of the shock driver and ambient medium conditions (e.g. Vršnak et al. (2001, 2002); Dorovskyy et al. (2015); Maguire et al. (2020); Chrysaphi et al. (2020); Magdalenić et al. (2020)). In some cases, either or both the fundamental and harmonic emission of the type II split into two thinner sub-bands with similar morphology, intensity variations and drift in a phenomenon known as band-splitting (see Section 3.2). Currently, there are two main theories to explain band-splitting. Each of which makes opposing predictions regarding the location of the split-band sources. The first popular interpretation is that band-split sources result from simultaneous emission from the plasma in front of and behind the shock (Smerd et al., 1974). In this case, the sources are expected to appear co-spatial. An alternative theory to explain

band-splitting proposed by (Holman and Pesses, 1983) suggests that the upper and lower split bands are generated at different locations along the shock front. In this scenario, the sources are expected not to be co-spatial. Although a few studies have been able to spatially resolve the sources of the split bands with details of the eruptive structure, they have either imaged the phenomena interferometrically at low-frequency or time resolution (Zimovets et al., 2012) or used tied array LOFAR observations (see Section 4.1.2.4), which has an inferior spatial resolution to interferometric observations (Zucca et al., 2018; Chrysaphi et al., 2018).

Type II bursts can also exhibit multiple lanes that are neither harmonically associated nor a typical band-split feature. This special group of type II events are called multi-lane type II bursts (see Section 3.2). These lanes typically have different start times and frequencies, drift rates, morphologies, and intensity variations. Similarly to band-splitting, there is no consensus on the origin of the type II multi-lane feature. The proposed mechanisms for this phenomenon have been divided into two distinct theories (1) the different lanes are driven by separate disturbances or shocks (Cho et al., 2011) and (2) the different lanes originate from different regions of the same shock as it interacts with different coronal structures (Feng et al., 2013, 2015). To date, multi-lane events have been studied predominately in terms of large scale eruptive events namely; strong flares with EUV coronal bright fronts and fast CMEs (Feng et al., 2013, 2015; Zimovets and Sadykov, 2015; Lv et al., 2017). Furthermore, these events have predominately been observed by the Nancay Radioheliograph (NRH; Kerdraon and Delouis, 1997), which has limited spatial and spectral resolution and only observes ten frequency bands between 150.9 MHz and 445.0 MHz. Few studies have imaged type II bursts substructure (i.e.multi-lane and band-splitting features) at low frequencies <100 MHz (Zucca et al., 2018; Chrysaphi et al., 2020). The lack of high-resolution imaging of these multi-lane features at low frequencies, especially when they are related to less energetic events, was the motivation for this chapter. For the first time, low-frequency LOFAR interferometric observations are used to image a type

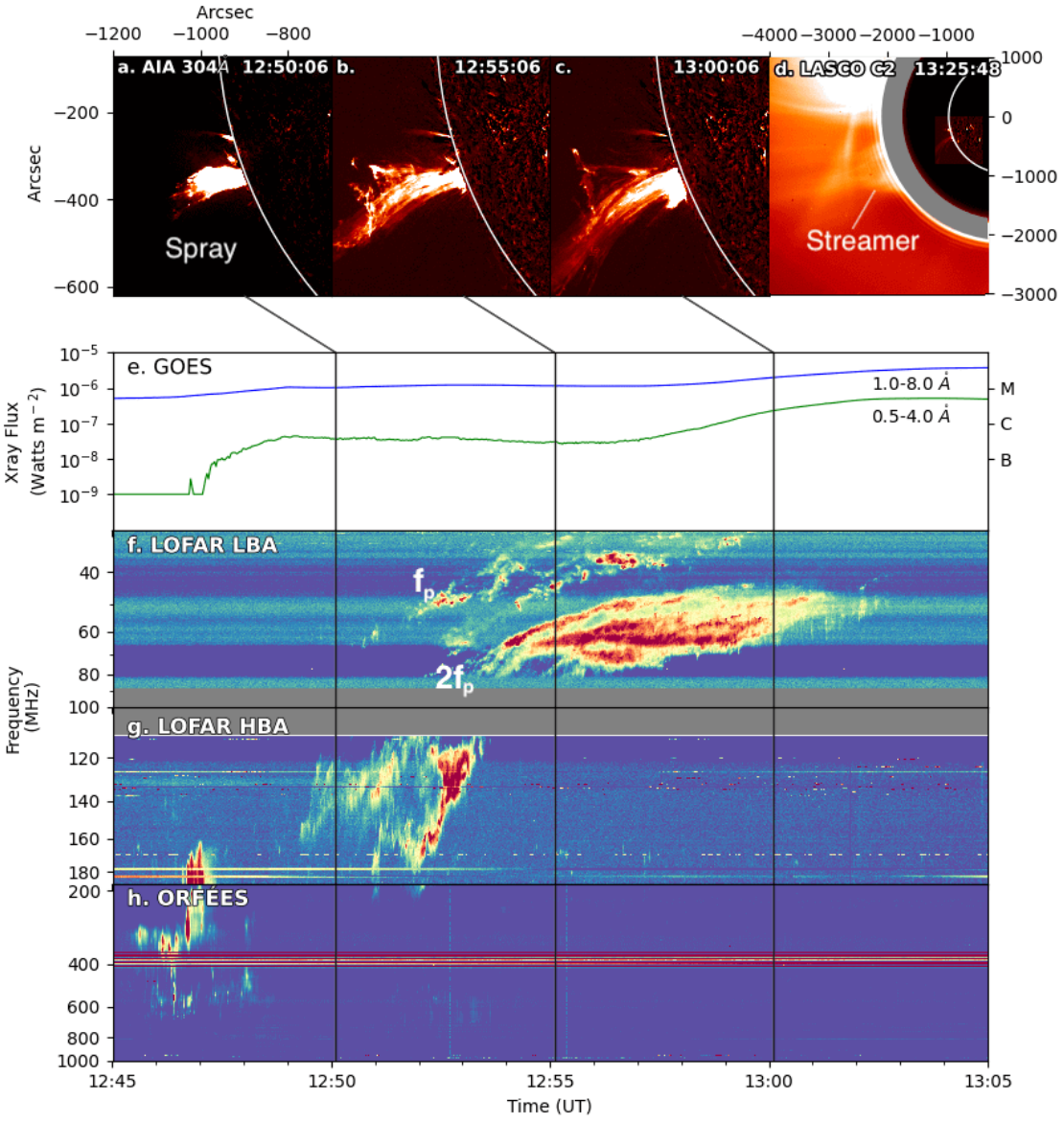

Figure 7.1: (a-c) Base-difference images of the spray observed with AIA 304 Å and (d) streamer observed by LASCO C2 . (e)GOES 0.5-4 Å and 1-8 Å soft X-ray flux of the C4.3 class solar flare. The remaining panels show the radio emission as observed by (f) LOFAR's low-band antennae (LBA; 30-90 MHz), (g) LOFAR's high band antennae (HBA; 110-240 MHz), (h) ORFÉES (140-1000 MHz). A type II precursor is observed in ORFÉES followed by type II radio burst with fundamental (f_p) and harmonic ($2f_p$) components are seen in the LOFAR dynamic spectra.

II burst with multi-lanes and band-splitting associated with a EUV spray.

7.2 Observations

A GOES C3.8 class flare began on 16 October 2015 from active region NOAA 12435 and reached peak intensity at 12:50 UT. The flare was located on the eastern solar limb, and inspection of data from the Extreme Ultraviolet Imager (EUVI; Wuelser et al., 2004) onboard the STEREO-A spacecraft (positioned on the far side of the Sun) near the time of the flare revealed that the active region extended longitudinally around the far side of the Sun. The flare was associated with a spray observed by SDO/AIA as shown in Figure 7.1(a). The spray initially propagates more radially before being strongly deflected southward. There was also a weak CME that was first observed at 13:25 UT in white light by LASCO C2 propagating with an average plane-of-sky speed of 200 kms^{-1}. The ejecta appears to be constrained by the magnetic field lines of an overarching helmet streamer situated $\sim$100° to solar north.

In Figure 7.1 the spectral radio observations from several ground instruments are shown, namely LOFAR's remote station RS509 observing between 10 MHz and 240 MHz, the radio spectrograph Observation Radio Frequence pour l'Ètude des Eruptions Solaires (ORFÈES), observing between 140 MHz and 1000 MHz. Coinciding with the onset of the GOES X-ray emission at 12:50 UT, a type II precursor (Klassen et al., 1999; Vršnak and Lulić, 2000; Klassen et al., 2003) is evident in the ORFÈES observations. Panel (f) show the subsequent type II burst observed by LOFAR at $\sim$12:52 UT with a highly fragmented faint fundamental and intense first harmonic component, indicated by f_p and $2f_p$ in the figure. The emission seen in panel (g) may be an extension of the type II harmonic emission or possibly it is the type II third harmonic. The second harmonic emission consists of multiple lanes that appear to last for several minutes. At the time of the type II burst there was no significant radio emission above 200 MHz (see panels h), which suggests that no radio emission was generated or escaped from low in the corona. This can be explained by the fact that the flare was partially occulted. Unfortunately, there were no STEREO A images at the time of the

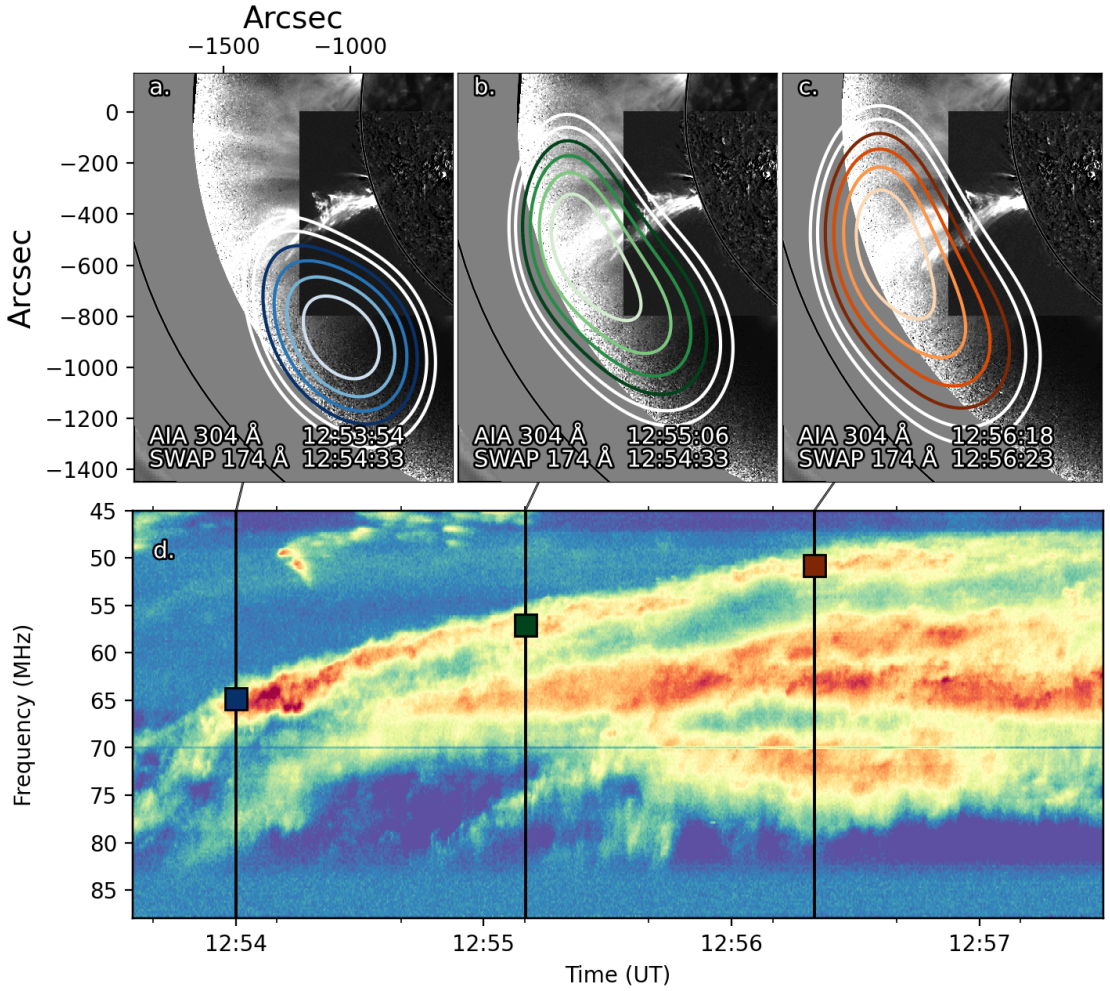

Figure 7.2: (a-c) Type II radio burst observed by LOFAR at three separate times. The coloured contours represent 50-90% of the peak flux density of the radio sources. The burst contours are overlaid on a composite of images from AIA 304 Å and SWAP 174 Å. The solid black circles indicate distances of $2\,R_{\odot}$. (d) The corresponding dynamic spectrum showing the type II harmonic emission. The coloured squares denote the points along the burst that have been imaged.

eruption to observe the evolving flaring region. STEREO A would have provided an alternative viewing angle and thus, information on the 3D structure of the spray.

LOFAR also provided interferometric observations for this event using the low-band antennas (10-90 MHz) from 36 stations (24 core and 16 remotes). The maximum baseline of the LOFAR observation was 84 km, which gave subarcminute resolution across almost all of the observed frequency range. Observations of the calibrator source, Virgo A, were taken simultaneously over all sub-bands. The visibility data was recorded

with a correlator integration time of 0.167 s. The data was processed using the Default Processing Pipeline (DPPP; van Diepen et al., 2018) followed by an implementation of WSCLEAN (Offringa et al., 2014) to produce images with a spectral resolution of 195.3 kHz and cadence of 1 s. As an example Figure 7.2(a-c) illustrates the position of the type II harmonic emission at three points in time. The radio sources are overlaid on a composite image from AIA 304 Å and SWAP 174 Å. Panel (d) provides the type II burst dynamic spectrum with coloured squares that indicate the points imaged along the burst, as seen in panels a-c. A full discussion on the radio imaging is reserved for Section 7.3.2.

7.3 Data Analysis and Results

In the following, I determine the kinematics of the spray observed in EUV, which is understood to be the shock driver. I then determine where the radio emission was generated in relation to the eruptive structure and the kind of coronal environment that lead to the type II emission. I also examine the spatial relationship between band-split pairs to determine the origin of the band-splitting phenomenon.

7.3.1 EUV Spray Kinematics

To determine the spray kinematics, I employ a Fourier Local Correlation Tracking (FLCT; Welsch et al., 2004; Fisher and Welsch, 2007) on base-difference AIA 304 Å images. The FLCT technique is a reliable way to infer appropriate structural motions in a time series of images. It is a valuable tool in solar physics for studying complex plasma dynamics and the evolution of magnetic fields in the solar atmosphere at various spatial and temporal scales (e.g., Welsch et al. (2009); McKenzie (2013); Su et al. (2013)). The following are the basic steps of the FLCT technique:

1. The technique requires two input images as a function of pixel coordinates x and y. Sub-images are formed for each reference pixel in both images by multiplying

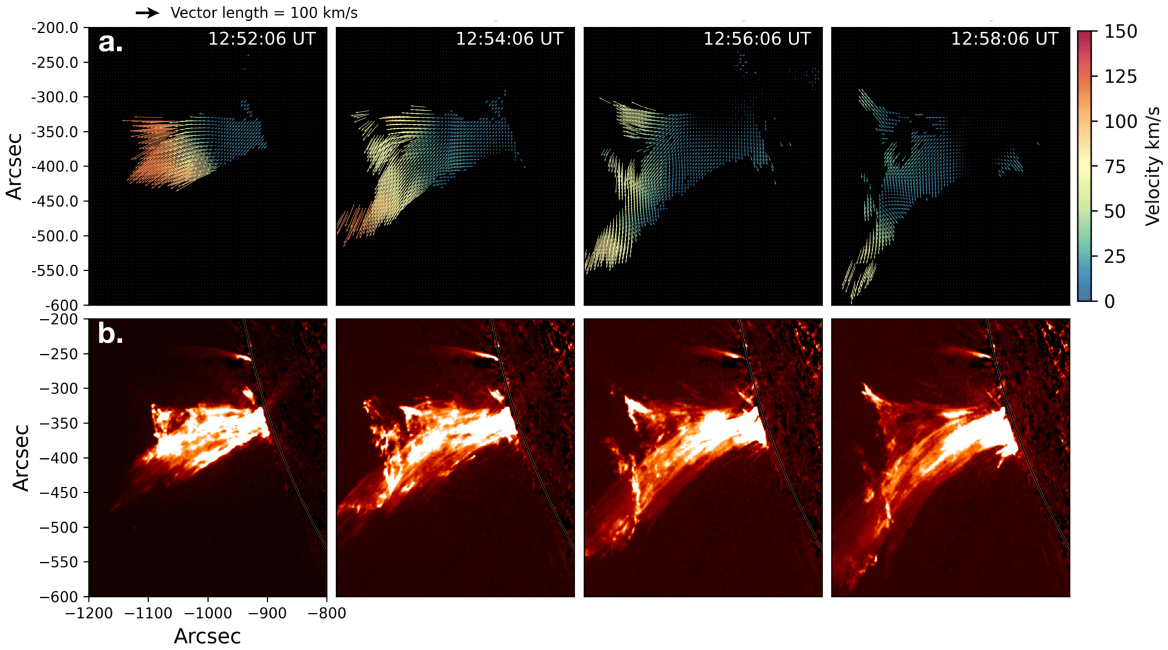

Figure 7.3: (a) Velocity flow map of EUV spray. Each map is obtained by using the FLCT method on a pair of AIA 304 Å images taken 12 s apart. The coloured arrows indicate the velocity vectors which range from 0 to 150 kms^{-1}. (b) The corresponding AIA base-difference images show the evolution of the spray.

the corresponding image with a 2D Gaussian function (separable in x and y) that decreases with distance from the reference pixels. This reduces the weight of pixels that are far away from the reference. The standard deviation of the 2D Gaussian function is a critical parameter for this windowing procedure as it specifies the typical length scale of the structures for which the algorithm will determine the pixel shifts. Too large a window will smear out the resulting velocities, resulting in a loss of spatial resolution, while too narrow a window results in excessive noise.

2. The FLCT code then computes the cross-covariance of all combinations of sub-images as a function of pixel shifts δx and δy. Fourier transforms are used to calculate the cross-covariance.

3. Find the maximum of a quadratic Taylor expansion to the absolute of the cross-covariance function yields the pixel shifts for which the sub-images match best.

4. The resultant 2D pixel shift for each pixel is divided by the time lag δt between the two input images to produce a 2D velocity vector. See Fisher and Welsch (2007) for more information.

The FLCT method is particularly useful in investigating complex plasma motion as was seen in this event. I assume that fluctuations observed in the intensity images are associated with the bulk motion of the plasma and not due to heating. Figure 7.3(a) shows the 2D flow velocity maps of the spray at several moments in time between 12:52:06 UT[1] and 12:58:06 UT. Panel (b) shows the corresponding EUV image observed by AIA 304 Å. The spray initially propagates radially before being deflected southward. Over the time frame shown in Figure 7.3, the spray propagates in multiple directions and reaches a maximum velocity vector (projected onto the radial direction) of $\sim$140 kms^{-1}. This method has one obvious limitation in that this method assumes plane-of-sky motion, which may not be the case considering the complex nature of the spray. The velocities found using the FLCT method therefore may underestimate the true velocities. For example, if the maximum radial speed achieved by the spray is $\sim$140 kms^{-1} and it propagated at an angle of 45° from the plane-of-sky, the spray speed would in fact be $\sim$198 kms^{-1}. Taking into consideration motion out of the plane-of-sky, the leading edge of the spray propagated at speeds ranging from 50 to 200 kms^{-1}.

7.3.2 Imaging of radio burst

Figure 7.2 presents the position of the type II harmonic emission at three moments in time. Since LOFAR observations offer a very high temporal and spectral resolution, it is possible to image at almost every point along the emission lanes. The imaging reveals that the type II emission is actually composed of short-duration emission lanes that are generated in multiple locations around the spray. Figure 7.4 (a-c) show the position of multiple type II lanes overlaid on composite images from AIA 304 Å and

[1]Type II emission is initially observed by LOFAR LBA's at $\sim$12:52 UT

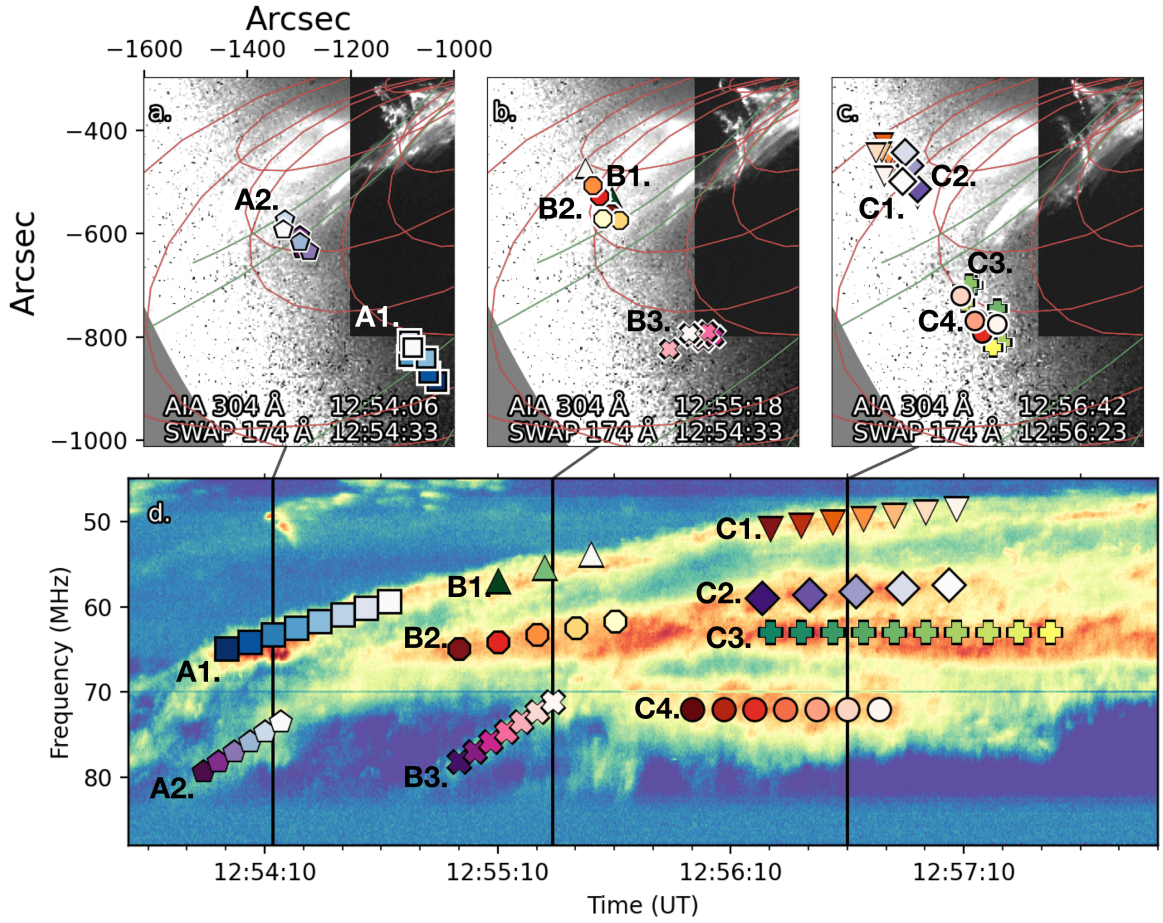

Figure 7.4: (a)-(c) Source locations of different lanes observed by LOFAR at three separate times. The colour-coded symbols and lines denote the bursts' centroid position and minor and major axes respectively. The bursts are overlaid on composite images from AIA 304 Å images (inner image) and SWAP 174 Å (outer image). A selection of closed (red) and open (green) field lines determined from the PFSS are shown. (d) The corresponding dynamic spectrum showing the multi-lane type II harmonic emission. colour-coded symbols denote the points along the burst that have been imaged.

SWAP 174 Å. The Sun's coronal magnetic field, which was derived from a PFSS model (PFSS; Stansby et al., 2020) is also shown. The closed magnetic field lines are in red while the open magnetic field lines are in green. The colour-coded symbols mark the location of the maximum intensity in the burst. Figure 7.4(d) shows the type II burst dynamic spectrum focusing on the multiple lanes in the type II harmonic emission. The coloured-coded symbols indicate the points imaged along the burst as shown in panels a-c. The short lanes of emission are labelled as A1, A2, B1, B2, B3, C1, C2, C3 and C4 in the figure and appear either ahead or south of the spray in regions of closed

magnetic field lines. In panel (a) the A1 sources show a clear separation of $\sim 250''$ from the A2 sources. Both sources appear in regions of closed magnetic field lines $\sim 0.5 R_\odot$ above the solar surface but the A1 sources are observed south of the spray while the A2 sources appear ahead of the spray. As seen in the dynamic spectrum in panel (d), the two lanes B1 and B2 show similar intensity, spectral variation, and a frequency ratio much lower than 2, which is indicative of band-splitting (see Section 3.2). Similarly, the pair of lanes C1-2 and C3-4 represent two more examples of band-splitting. Within the resolution of this observation, the band-split sources (B1-2, C1-2 and C3-4) appear to be co-spatial as shown in panels (b) and (c). The significance of these results is discussed in detail in Section 7.4.2.

Taking into consideration that some of the short lanes are band-split pairs, there are six distinct locations of radio emission. That is the A1, A2, B1-2, B3, C1-2 and C3-4 sources appear in six distinct locations around the spray. There does not appear to be any correlation between the motion of each short lane. The fact that some of the short lane sources appear in clusters suggests that the emitting source propagated only a short distance ($<100''$ or 72.5 Mm) and/or that the emitting source moved predominantly along the observer's line of sight. As seen in the dynamic spectrum in panel (d), most of the short lanes have similar intensities aside from the A2 and B3 lanes. These short lanes are fainter and have a steeper drift rate compared to the other short lanes. An explanation for this is proposed in Section 7.4.1.

Considering the radio sources are observed in multiple locations, it is most likely that the type II lanes are associated with emission from different parts of the propagating shock. I propose the full scenario to explain these intriguing observations in Section 7.4.1

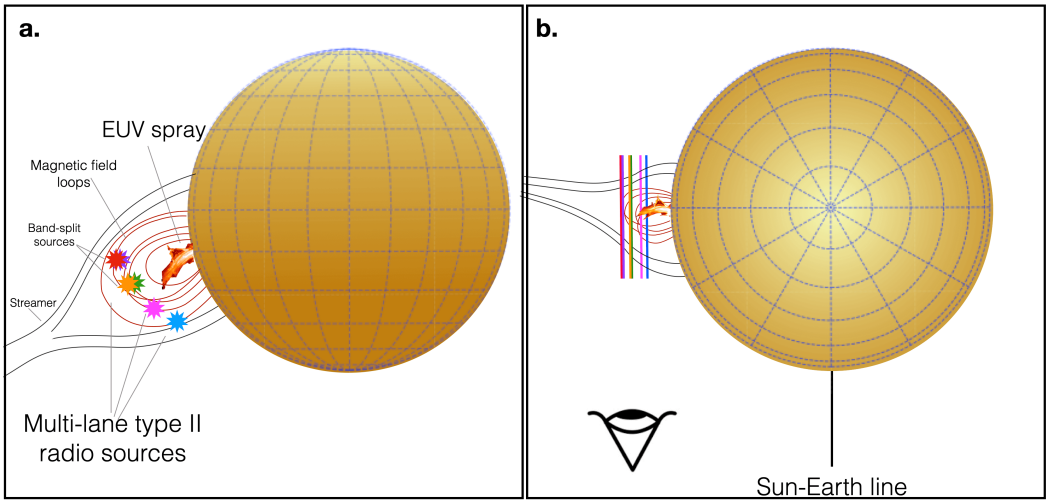

Figure 7.5: Schematic illustration showing the spray, coronal streamer and type II sources from a line-of-sight perspective. The magnetic field configuration is represented by red loops. The radio sources are denoted by colored stars. The band-split sources are indicated by co-spatial colored stars. (b) The event from the solar north-pole perspective. The color-coded lines represent the possible locations of the type II sources.

7.4 Discussion

7.4.1 Proposed Generation Mechanism

In this section, I propose a scenario that accounts for the position of the radio sources in relation to the spray and other coronal features. As illustrated in Figure 7.1, the type II emission is associated with a EUV spray observed in the low corona. However, it is only with high-resolution radio imaging that the complex nature of the type II emission is revealed, namely the type II emission lanes are made up of shorter short lanes some of which are band-split. Figure 7.5 presents a schematic of the proposed scenario from two perspectives. The schematic includes the magnetic field configuration, the spray, the streamer and the type II radio sources from (a) a line-of-sight perspective and (b) a solar north-pole perspective. Considering the complex motion of the spray, it is important to consider the scenario from both perspectives. In panel (a), the type II short lane sources, including band-split sources, are represented by coloured stars. Panel (b) illustrates the event from the solar north-pole perspective with the coloured

lines corresponding to the radio sources in panel (a). It is difficult to determine where along these lines the radio bursts are precisely located. The sequence of events that resulted in the type II substructure is outlined below:

1. The EUV spray emerged from the eastern solar limb at 12:45 UT. When the leading-edge of the spray reached a height of $\sim$0.1 $R_\odot$ above the solar surface, the spray became more fan-like. I suggest that the spray impacted overlying magnetic field lines, which caused the ejecta to be deflected in different directions. The spray's components propagate at speeds ranging from 50 kms^{-1} to 200 kms^{-1}, taking into account motion out the plane-of-sky.

2. The motion of the spray likely drove a shock in the low corona. Different regions of the shock subsequently excited type II emission that lasted less than a minute. The different frequency drifts and intensity of each type II short lane (seen in the LOFAR dynamic spectrum) is likely due to the distinct propagation paths of different regions of the shock as it moved through different coronal conditions.

3. Certain regions of the shock driven by the spray encountered regions where the conditions were favourable for electron acceleration and consequently plasma emission. The position of the radio sources in relation to the magnetic field configuration (see Figure 7.4) suggest that the shock obliquity was mostly quasi-perpendicular (see Section 2.2.3). Under this regime, electrons are efficiently accelerated to high energies by the shock drift acceleration mechanism (see Section 2.2.3) and radio emission is generated via plasma emission processes.

4. Notably, three band-split pairs (B1-2, C1-2 and C3-4) were identified. In all three cases, the upper and lower lanes were found to be co-spatial. Since the shock front is an infinitesimally thin surface, the upstream and downstream regions of the shock are virtually co-spatial. This suggests that the upper and lower band-split lanes were associated with emissions from the upstream and down-

Band-split lane	Compression Ratio	Alfvén Mach number
B1-2	1.33	1.58
C1-2	1.35	1.62
C3-4	1.31	1.52

Table 7.1: The compression ratio and Alfvén Mach number inferred from band-split lanes.

stream regions, respectively. These observations provide strong support for the upstream-downstream theory (Smerd et al., 1974).

7.4.2 Band-splitting

As seen in Figure 7.4, three distinct examples of band-splitting (B1-2, C1-2 and C3-4) are observed. In all three cases, the band-split pairs appear to be co-spatial. These observations are in agreement with the upstream-downstream theory proposed by Smerd et al. (1974). According to this theory, the upper and lower split lanes are emission from upstream and downstream of the shock, respectively. The relative frequency split $\Delta f_s/f$ between the lanes is thus related to the density jump between the upstream and downstream regions of the shock via,

$$\frac{\Delta f_s}{f} = \frac{f_u - f_l}{f_l} = \frac{f_u}{f_l} - 1 = \sqrt{\frac{n_u}{n_l}} - 1 \tag{7.1}$$

where n is the electron density and the subscripts u and l denote the upper-frequency and lower-frequency bands, respectively. The compression ratio $r = n_l/n_u$ was estimated from the relative frequency split since

$$r = \frac{n_u}{n_l} = \left(\frac{f_u - f_l}{f_l}\right)^2 = \left(\frac{\Delta f}{f} + 1\right)^2 \tag{7.2}$$

To determine the Alfvén Mach values M_A, I used the expression from Vršnak et al. (2002) for a perpendicular shock:

$$M_A = \sqrt{\frac{r(r+5+5\beta)}{2(4-r)}} \tag{7.3}$$

whereby plasma β is the plasma-to-magnetic pressure ratio ($\beta << 1$). The average value of r and M_A for each of the band-split sources are presented in Table 7.1. The values for M_A were found to be in the range 1.52 to 1.62, which is consistent with previous studies (Vršnak et al., 2001; Zucca et al., 2014a; Maguire et al., 2020). The fact that all three band-split pairs appear co-spatial provides strong evidence for the upstream-downstream scenario.

7.5 Conclusion

I report on an intriguing, multi-lane type II event associated with a complex EUV spray that occurred on 16 October 2015. The complex motion of the spray was attributed to the spray interacting with overlying magnetic field lines, which caused the spray to propagate in multiple directions. An FLCT method was employed to derive the spray kinematics, namely, the radial velocity of the spray's components ranged from 50 kms^{-1} to 200 kms^{-1}. LOFAR was used to interferometrically image the type II emission and revealed multiple distinct regions of radio emission associated with short type II lanes. It was most likely that lanes were associated with radio emission from different parts of the shock as it propagated through different coronal conditions. These observations suggest that the radio emission was generated in different regions along the spray-driven shock where the local plasma conditions were favourable for plasma emission, namely where shock obliquity is quasi-perpendicular. Multi-lane type II events have been reported before but mostly in terms of strong flares with obvious EUV waves and/or fast CMEs (Feng et al., 2013, 2015; Zimovets and Sadykov, 2015; Lv et al., 2017).

This is the first report of a type II event with multiple short lanes associated with a complex EUV spray. The high-resolution LOFAR observations enabled us to identify and locate the short lanes, which would not be evident in lower-resolution observations. In conjunction with this, I present the first LOFAR interferometric images of type II band-splitting. Three of the short lanes experience band-splitting. In each of the three cases, the band-split pairs appear to be co-spatial, which provides strong evidence for the upstream-downstream theory (Zimovets et al., 2012; Chrysaphi et al., 2018; Zucca et al., 2018). The observations presented in this study bring new insight into the complex nature of radio emission generated by shocks in the low corona. This study also highlights the importance of high-resolution radio imaging and how imaging is needed to correctly interpret type II spectroscopic data.

8

Conclusions and Future Work

The research outlined in this thesis has aimed to further our current understanding of shock formation and propagation and how electron acceleration and radio emission are generated during these processes. The first goal of this research was to investigate the early-phase evolution of shock properties and their relationship to type II burst emission. The second research goal was to determine the precise origin of a coronal shock and examine the effects of scattering on fundamental radio emission. The third and final research goal was to study a multi-lane type II burst and its relationship to a complex solar eruption and to investigate the origin of band-split pairs. In this chapter, I review and summarize the principal results from the three research chapters of this thesis and explore future work directions.

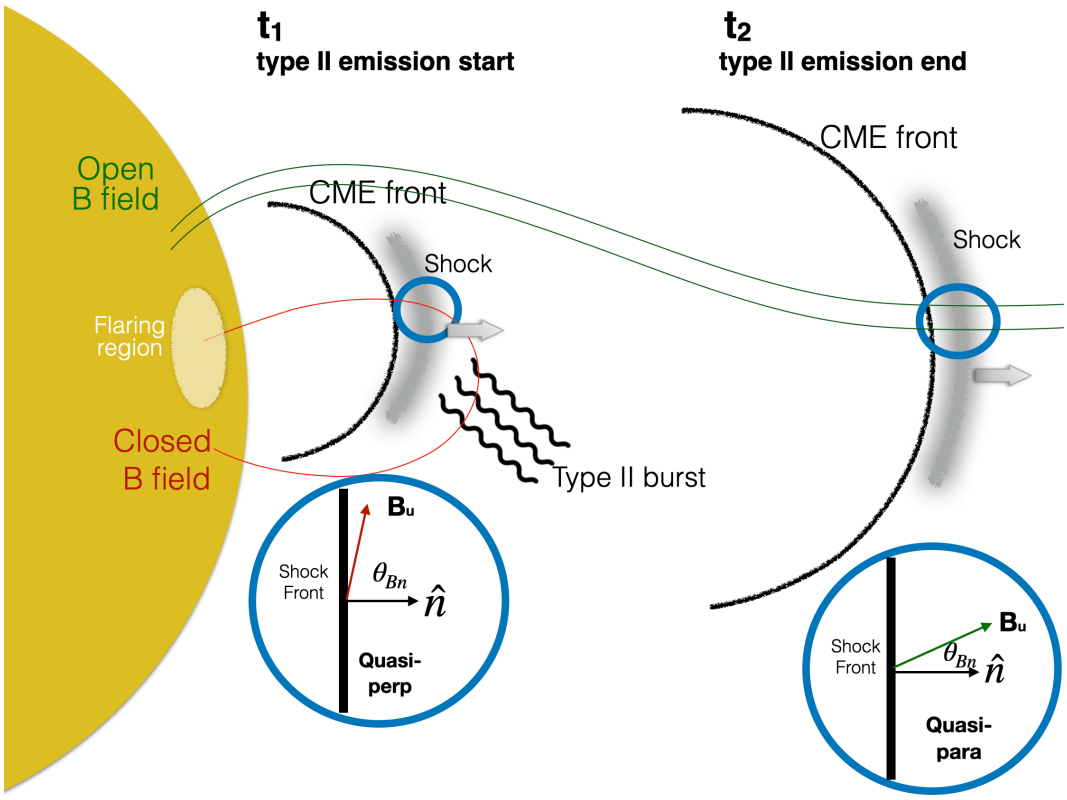

Figure 8.1: Schematic of research chapter 1: To investigate the early-phase evolution of shock properties and its relationship to type II burst evolution

8.1 Principal Thesis Results

8.1.1 RESEARCH CHAPTER 1:

Evolution of the Alfvén Mach number associated with a CME shock

Maguire et al. (2020)

In Chapter 5, a multi-wavelength investigation of a metric type II event from 2 September 2017 was presented. In this study, I focused on the evolution of a CME-driven shock by comparing three commonly used methods in solar physics of calculating the M_A; (1) stand-off distance between the shock wave and the CME as observed in EUV images, (2) a comparison of CME speed to a model of the coronal Alfvén speed, and (3) the type II band-splitting method. This allowed us to test the consistency of the methods, but it also allowed us to derive more detailed shock characteristics than would

normally be available using just one method. I determined the location of the type II radio emission along the CME front and I related the change in the angle between the local shock norm and coronal magnetic field direction to the onset and ceasing of the type II radio emission. This research was published in Maguire et al. (2020) and the main results of this study are as follows:

- I was able to determine M_A in the corona at heliocentric distances ranging from $\sim$1.4 to $\sim$3 $R_\odot$. The results from all three methods were initially similar ($\sim$1.5) but diverge after $\sim$10 min. The divergence may be a result of the inherent uncertainties associated with each method. As a general trend, the M_A was initially $\sim$1.5 and increased up to 4 over a time frame of $\sim$17 min. This means the shock became progressively stronger over this time frame.

- Type II radio emission, coming from the nose region of the CME, began when the shock reached a heliocentric distance of $\sim$1.6 $R_\odot$ and M_A was in the range 1.4 - 2.4. The type II emission ceased 10 min later when the shock front reached $\sim$2.4 $R_\odot$, despite an increasing M_A (up to 4).

- I attribute this behaviour to the change in shock obliquity as the shock propagates into the outer corona. That is, the shock was no longer quasi-perpendicular and efficient electron acceleration and radio emission was inhibited.

- These results provide insight into the shock conditions necessary for producing type II emission. A supercritical M_A and favourable shock geometry is required for the efficient acceleration of energetic electrons and generation of radio emission.

For the first time in the literature, I showed that three commonly-used methods of estimating shock Alfvén Mach number yield consistent results. This work also provided new observational evidence that to accelerate energetic electrons to excite radio emission, a critical Alfvén Mach number must be reached and a quasi-perpendicular shock

to magnetic field geometry is required. These results provide insight into the conditions necessary for the generation of metric and decametric type II radio bursts and may explain why some fast CMEs, which presumably drive shocks, are not associated with type II radio bursts, while other slower events do have type II bursts associated with them. Future work to this chapter could include estimating the shock-to-field angle in a 3D context. This would involve fitting a spherical geometric surface to the shock front and calculating the shock obliquity across the entire 3D surface (Rouillard et al., 2016; Zucca et al., 2018; Morosan et al., 2019). This will allow us to determine the region of electron acceleration along the shock front in a 3D context and give quantitative properties of shock geometry necessary for type II emission. Recently, Kouloumvakos et al. (2021) presented detailed 3D modelling of the shock and estimation of its properties during the expansion in the low corona. They found that type II radio emission throughout the event originated from regions where the shock is strong and supercritical, with a relatively high density compression ratio and quasi-perpendicular geometry. A similar study was carried out by Jebaraj et al. (2021) focusing on the conditions needed for the generation of type II radio emission in the interplanetary space.

8.1.2 RESEARCH CHAPTER 2:

LOFAR observations of a jet-driven piston shock in the low solar corona

Maguire et al. (2021)

In Chapter 6, I presented a multi-wavelength investigation of a solar eruptive event that occurred on 16 October 2015. In this study, I determined the origin of the shock by investigating the propagation path of the type II burst and shock driver. LOFAR interferometric observations were used to image the separation between type II fundamental and harmonic components with unprecedented spatial and temporal resolution. I then accounted for the spatial displacement between fundamental and harmonic components using a model of radio wave scattering in the corona. This allowed for the necessary correction of radio source positions. The comparison of the radio source position with

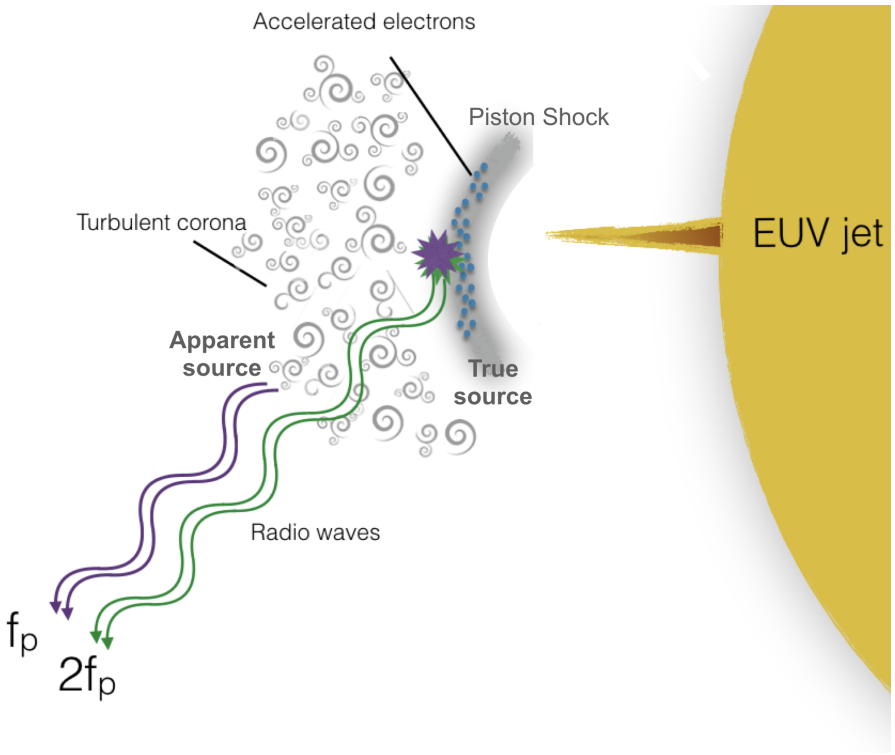

Figure 8.2: Schematic of research chapter 2: To determine the precise origin of a coronal shock and examine the effects of scattering on fundamental radio emission.

the shock driver imaged in EUV showed they followed the kinematics of a piston-driven shock. This research is published in Maguire et al. (2021) and the principal results of this study are as follows:

- LOFAR interferometrically imaged both the fundamental and harmonic emission of a type II burst and revealed that the sources were not co-spatial. They were 0.3-0.5 $R_\odot$ apart. According to the underlying plasma emission mechanism, the fundamental and harmonic emissions are generated in the same location.

- I accounted for their spatial displacement using a model of radio scattering in the corona proposed by Chrysaphi et al. (2018). This model allowed for the necessary correction of source positions and their comparison with the shock driver. Furthermore, optimization of the model to the data provided information about scattering parameters, e.g. I found that $\varepsilon^2/h \sim 2\times10^5\,\mathrm{km}^{-1}$, which is slightly lower compared to that found in previous studies (Chrysaphi et al., 2018).

- After accounting for radio wave scattering effects, I determined where the radio burst was generated in relation to the eruptive structure and the coronal environment that lead to shock formation. Ultimately, I found that the type II burst was located at a much higher altitude than the EUV jet and had a significantly larger velocity, namely the jet speed was $\sim$200 km s^{-1} while the type II burst propagated at $\sim$1000 km s^{-1}.

- The association of the sub-Alfvénic jet with the type II burst and the relative velocities of the jet and the type II emission provides strong evidence of a shock that was initially piston driven.

For the first time, LOFAR was used to image the separation between type II fundamental and harmonic emission. In doing so, I imaged this phenomenon in the highest spatial, spectral and temporal resolution to date (Kai and McLean, 1968; Sheridan et al., 1972; Nelson and Sheridan, 1974; Nelson and Robinson, 1975; Suzuki et al., 1985). Furthermore, I showed that the Chrysaphi et al. (2018) model proved to be a reliable means to correct for the positional shift of fundamental emission due to scattering. This work highlighted the importance of accounting for radio wave scattering in radio imaging so that I can accurately determine the type II burst kinematics. Future work to test the validity of this analysis may include using full numerical models of turbulent radio wave scattering in the solar corona such as the Kontar et al. (2019) model. This would allow us to validate the assumptions made in this study and provide useful constraints on the quantities characterizing density turbulence.

8.1.3 RESEARCH CHAPTER 3:

LOFAR observations of multi-lane type II radio burst driven by complex flare spray. ***Maguire et al. (in prep)***

In Chapter 7, I presented a multi-wavelength analysis of a unique solar eruptive event that occurred on 16 October 2015. In this study, I examined the relationship between

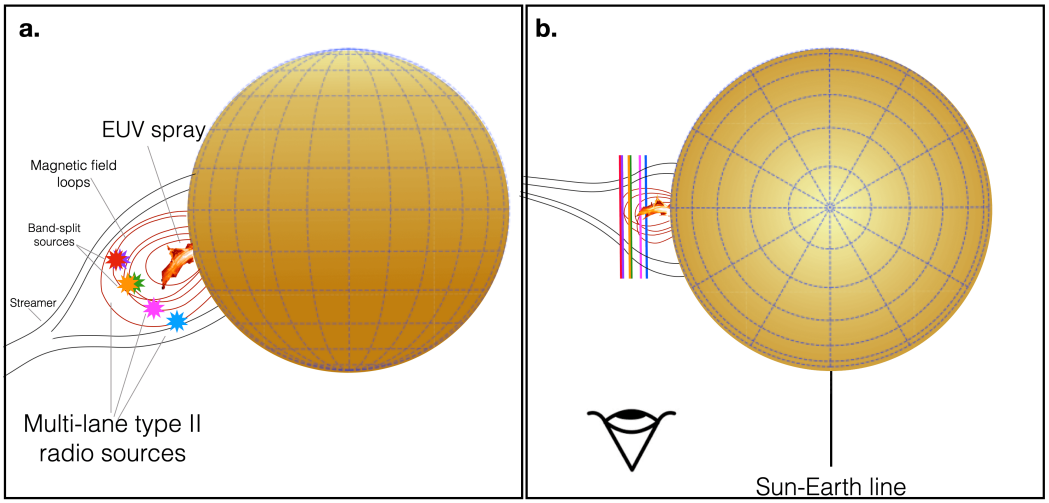

Figure 8.3: Schematic of research chapter 3: To investigate type II burst sub structure to give us insight into the behaviour of shock radio emission in the low corona.

the multi-lane type II burst and the complex EUV spray. I also investigated the origin of band-split pairs. LOFAR imaging revealed multiple distinct regions of radio emission along the shock, that corresponded to short-duration lanes of emission in the type II dynamic spectrum. The three pairs of band-split sources were found to be co-spatial within the observational uncertainty. This study highlighted the importance of high-resolution radio imaging and how imaging is needed to correctly interpret type II spectroscopic data. The research in this chapter is currently in preparation to submit to *The Astrophysical Journal*. The main results are as follows:

- The complex motion of the spray was attributed to the spray interacting with overlying magnetic field lines, which caused the spray to propagate in multiple directions. The radial velocity of the spray was found using an FLCT method to range from $50\,\mathrm{kms}^{-1}$ to $200\,\mathrm{kms}^{-1}$.

- LOFAR interferometrically imaged the type II radio burst associated with the spray to reveal multiple regions of radio emission including three pairs of band-split sources. It is likely that the motion of the spray drove a shock in the low corona and different regions of the shock subsequently excited type II emission that lasted less than a minute. The different frequency drifts and intensity of

each type II short lane seen in the LOFAR dynamic spectrum is likely due to the distinct propagation paths of parts of the shock as it moved through different coronal conditions.

- The radio source positions relative to the magnetic field configuration suggest that the type II emission was generated in regions where the shock obliquity was quasi-perpendicular.

- In each of the three cases of band-splitting, the band-split pairs appear to be co-spatial, which provides strong evidence for the upstream/downstream theory and is consistent with previous observations (Zimovets et al., 2012; Chrysaphi et al., 2018; Zucca et al., 2018). This was the first LOFAR interferometric observations of type II band-splitting.

This unique set of observations revealed that the type II burst was composed of multiple short lanes, which were associated with radio emission from different parts of the propagating shock. The high-resolution LOFAR observations enabled us to identify and locate the mini-lanes, which would not be evident in lower-resolution observations (like those in Feng et al. (2013, 2015); Zimovets and Sadykov (2015); Lv et al. (2017)). In conjunction with this, I presented the first LOFAR interferometric images of type II band-splitting. These observations provide strong evidence for the upstream-downstream theory. Namely, in all three cases, the upper and lower split lanes are co-spatial (Zucca et al., 2018; Chrysaphi et al., 2018). The observations presented in this study brought new insight into the complex nature of radio emission from a shock in the low corona. This study also emphasized how it is difficult, if not impossible, to determine the precise location of the radio sources in the absence of imaging, particularly for complex eruptive events. Future studies should focus on imaging type II multi-lane and split-band events, making use of the high spectral and temporal resolution of the LOFAR interferometric imaging mode.

8.2 Future Work

The work in this thesis has provided insight into shock formation and propagation and how electron acceleration and radio emission are generated during these processes. However, there is still much more to be understood about the relationship between solar shocks and the production of type II emission, and the physical processes that drive shocks and accelerate electrons. In this section, the potential direction for carrying out future studies that build upon the work in this thesis is presented in three science goals (SG):

Science Goal 1. To image coronal shocks and their drivers at radio wavelengths in unprecedented temporal, spectral and spatial resolution.

Science Goal 2. To investigate type II fine-scale structure.

Science Goal 3. To image interplanetary shocks at radio wavelengths.

8.2.1 SG 1: Radio imaging of shocks and CMEs in unprecedented temporal, spectral and spatial resolution

LOFAR2.0

In the coming years, developments in existing radio instrumentation and the construction of new facilities promise to provide new insight into coronal shocks and acceleration processes. Presently, interferometric data from the LOFAR high-band and low-band antennas cannot be recorded simultaneously. Over the coming years, LOFAR will receive several major upgrades, collectively referred to as LOFAR2.0, which will allow simultaneous observations with high-band and low-band antennas [1]. Such a system upgrade will include redesigning and replacing station electronics, improving clock and reference signal accuracy for core and remote stations and tripling the number of receiver units and beamlets for the final system (full LBA and HBA in the core and

[1] https://www.astron.nl/what-we-look-forward-to-in-lofar-2-0-live-warning-system-to-study-solar-eruptions/

Instrument	Frequency Range (MHz)	Spectral Resolution (MHz)	Time Resolution (s)	Angular Resolution (")
LOFAR	10-240	0.1	0.001	60-540
SKA1-LOW	50-350	0.005	0.001-9	4-24

Table 8.1: Comparison of SKA1-LOW and LOFAR imaging capabilities.

remote stations). LOFAR2.0 will extend the technical capabilities of LOFAR allowing for imaging of radio sources across the entire frequency range (10-240 MHz). In a solar context, type II emission will be tracked from the point of formation in the low corona to several solar radii (1-3 $R_{\odot}$). This will be the first time in the field that the propagation path of a solar shock has been tracked in its entirety and will provide insight into the fundamental physics governing shock propagation.

LOFAR4SW

Currently, LOFAR is not a heliophysics dedicated facility. A Horizon 2020 design study referred to as LOFAR for Space Weather (LOFAR4SW)[1] aims to design an upgrade to LOFAR so that it can observe solar, heliospheric, and ionospheric phenomena in parallel with its core radio astronomy remit (Carley et al., 2020). This project involves redesigning both front-end and back-end systems, developing an imaging pipeline for solar observations, as well as a redesigning the operational and administrative aspects of the entire system. Once in operation, LOFAR4SW will provide constant monitoring of solar activity including radio-loud coronal shocks. Since type II bursts are the most reliable and direct diagnostic of coronal shocks, their spectral characteristics and imaging of their radio sources will provide insight into the evolution of shock properties and properties of the associated accelerated electrons. Type II radio emission studies with LOFAR4SW will be integral to the advancement of space weather research.

SKA

LOFAR is a pathfinder for the next-generation Square Kilometre Array (SKA; Dewdney et al., 2009) telescope. The SKA will be the world's largest radio telescope, aiming to

[1] http://www.lofar4sw.eu

provide over 1 km^2 of collecting area. It will consist of two independent instruments, SKA-LOW in Australia and SKA-MID in South Africa. Due to be completed in July 2029, the first phase of SKA-LOW (referred to as SKA1-LOW) will include an array of 132,000 dipole antennas with baselines of up to 65 km. SKA1-LOW will operate between 50 and 350 MHz with a time resolution of 0.001-9 s, the frequency resolution of 5 kHz and angular resolution 4-24". For reference, a comparison between SKA1-LOW and LOFAR specifications is presented in Table 8.1.

Once in operation SKA1-LOW will provide a unique tool to diagnose various solar phenomena (see Nindos et al. (2019) for key solar studies). With its superior angular-spectral resolution and dynamic range, SKA1-LOW will be capable of simultaneously imaging the type II radio emission and the CME. The combination of radio observations with EUV, white-light and X-ray imaging as well as magnetic field models will enable us to determine explicitly the role of each eruption component in the development of the shock. The wide field of view offered by SKA1-LOW will allow us to probe heights that are typically obscured by the occulting disk of coronagraphs. This will help us to monitor the early development of CME and study the relationship between CMEs and shock properties. SKA1-LOW observations will open a new window in which to study the fundamental physics of CMEs and CME shocks. Furthermore, SKA1-LOW will be capable of observing type II burst fine structure in unprecedented detail, the significance of this is outlined in SG 2.

8.2.2 SG 2: Investigate type II fine-scale structure

As discussed in Section 3.2, type II bursts can have a variety of different forms of fine-scale structure. These features can appear as short-duration narrow-band or broad-band bursts of emission. These fine-scale structures are most identifiable in dynamic spectra with adequate temporal and spectral resolutions (Magdalenić et al., 2020). The precise origin of type II fine-scale structure is largely unexplored.

The general consensus is that type II fine-scale structures are generated as a con-

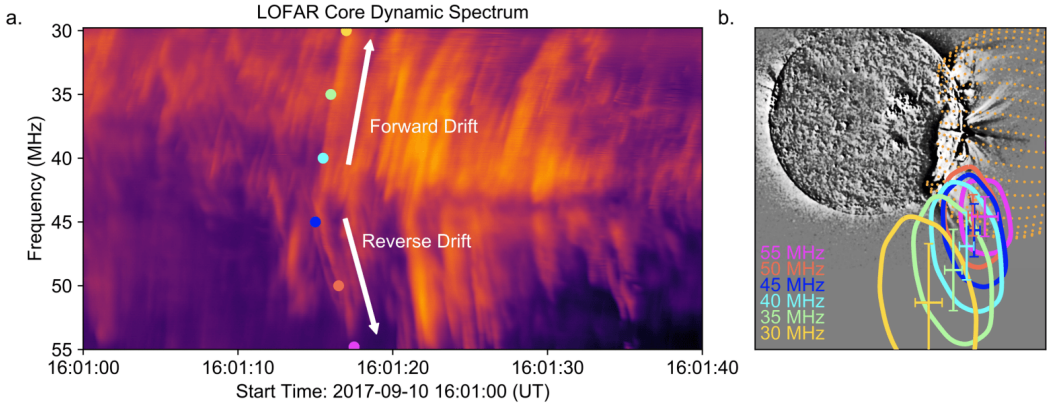

Figure 8.4: LOFAR tied-array imaging of a herringbone burst associated with CME-driven shock. (a) LOFAR dynamic spectrum with several herringbone bursts. The points imaged along the burst are denoted by coloured dots. (b) The position of the corresponding radio sources in relation to the CME-driven shock. The orange mesh represents a 3D model of the CME. The forward and reverse drifting emission of the herringbone burst correspond to electron beams moving away and towards the solar surface, respectively. Credit: Morosan et al. (2019).

sequence of the shock propagating through a strongly inhomogeneous and turbulent corona. It is expected that the properties of type II fine-scale structures are related to the density inhomogeneities caused by turbulence in the corona. For example, the extent in frequency space of any emission feature is defined by the extent of the emission source in real space and thus provides insight into the size scales of density inhomogeneities. The intensity of the fine-scale structure emission also depends upon the characteristics of coronal turbulence. Numerical modelling has shown that density inhomogeneities cause modulations in the growth rate of Langmuir waves, which leads to a modulation in the intensity of radio waves (Reid and Kontar, 2017; Reid et al., 2021). Consequently, high-resolution spectroscopic observations of fine-scale structures are needed to help us constrain properties of coronal turbulence close to the shock surface and better understand the role of shocks in particle acceleration (Carley et al., 2021).

In addition to the spectroscopic data, high-resolution radio imaging is needed to determine the precise location of the different fine-scale structures. Can we associate a certain set of fine-scale structures to a particular coronal phenomenon? For example, do

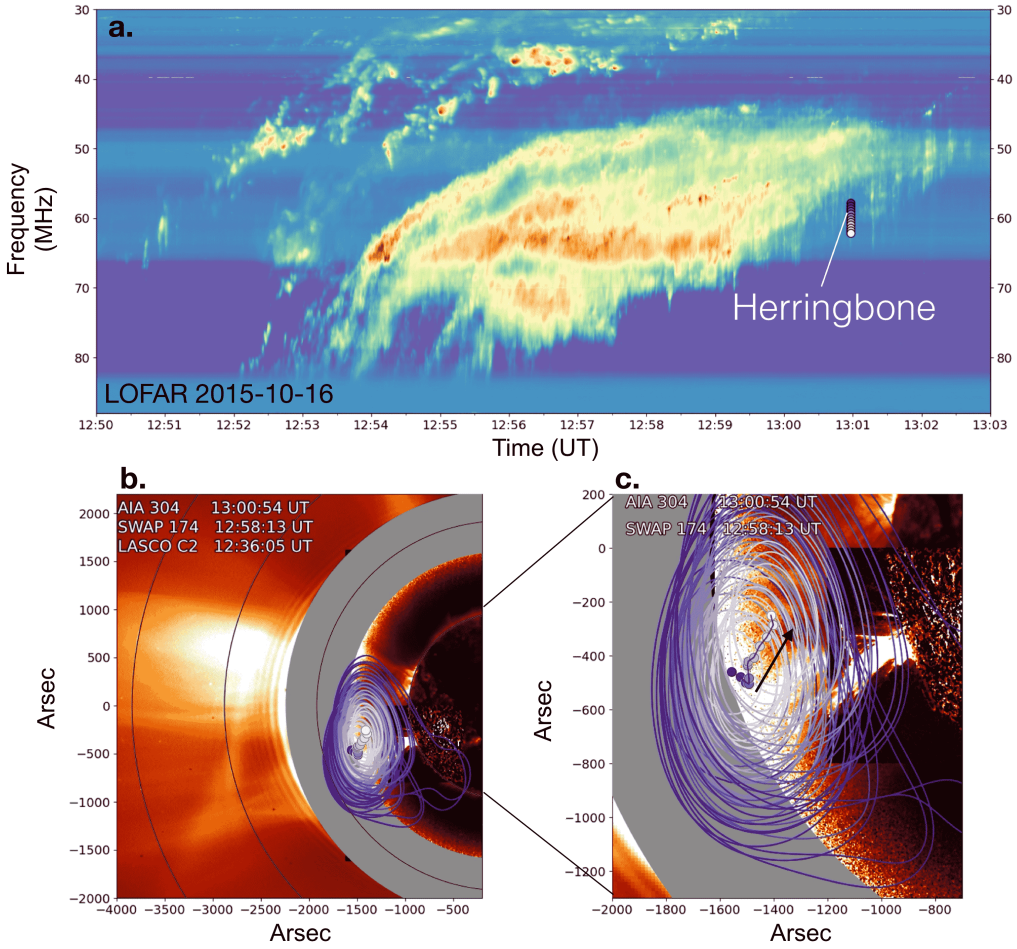

Figure 8.5: (a)Dynamic spectrum of type II radio burst observed by LOFAR on 16 October 2015. Several herringbone bursts are visible towards the end of the burst. The purple dots indicate the points along a negatively drifting herringbone that were interferometrically imaged by LOFAR. (b) EUV and white-light composite image of the event overlaid with the position of radio sources. (c) A zoom-in of the propagation path of the herringbone burst. The radio source appears to propagate towards the solar surface.

certain features come from the nose of a CME while others come from the flank? While type II fine-scale structures have been observed in the past, these studies have tended to use LOFAR tied-array imaging (Morosan et al., 2019) as seen in Figure 8.4. Preliminary analysis of a herringbone burst interferometrically imaged by LOFAR is provided in Figure 8.5. LOFAR interferometric observations have superior spatial resolution with respect to tied-array observations and will allow us to track the propagation path of the herringbone source more precisely (Maguire et al, in prep). Furthermore, once SKA1-LOW is in operation, it will provide even higher resolution observations of type

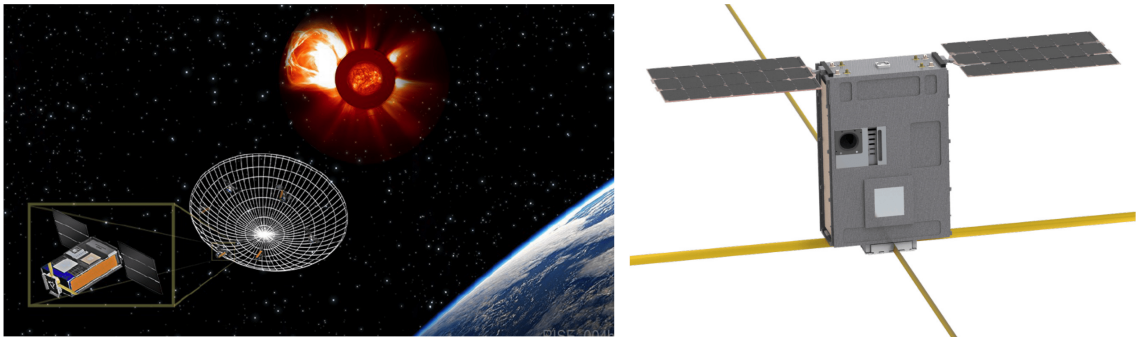

Figure 8.6: (Left) Artist's impression of the SunRISE constellation of CubeSats forming a synthetic aperture and observing a solar radio burst. (Right) Artist's impression of one of the CubeSats. Credit: Joseph Lazio et al. (2017).

II fine-scale structure. The combination of radio, EUV, UV and white-light imaging will provide insight into where fine-scale structure emission is generated in relation to eruptive structures and the kind of coronal environment (large-scale density structures and magnetic field configuration) that lead to its formation.

8.2.3 SG 3: Radio imaging of interplanetary shocks

As discussed in the previous SGs, current and future low-frequency radio instrumentation will provide new insight into the shocks physics and the turbulent nature of the plasma in the low corona. It is important to note however that, ground-based radio observations at frequencies below 30 MHz are severely impacted by a number of factors including man-made radio frequency interference (RFI), ionospheric distortion as well as the complete attenuation of radio waves below 10 MHz by the ionosphere. Therefore, this low-frequency window remains largely unexplored. One important future mission is the Sun Radio Interferometer Space Experiment (SunRISE; Joseph Lazio et al., 2017), which is scheduled to launch in mid-2023. The mission will deploy an array of six CubeSats, a type of miniaturized satellite, that will orbit within 10 km of each other and work together as a space-based interferometer. The constellation of CubeSats will observe between 0.1-25 MHz which corresponds to observing radio emission between $\sim$2–20 $R_{\odot}$. SunRISE will provide 3D radio maps, which will enable

us to (1) track the propagation of coronal shocks into interplanetary space and (2) for the first time image the formation and propagation of interplanetary shocks. This in turn will tell us more about the propagation path of interplanetary shocks and where they are generated relative to the CME driver (Jebaraj et al., 2021). Chapter 5 showed that the Alfvén Mach number of a CME-driven shock in the low corona continued to increase over time and distance. It would be interesting to investigate whether this is also true for interplanetary shocks. Is there a Alfvén Mach number limit and what is the relationship between Alfvén Mach number and type II emission for interplanetary shocks? Furthermore, SunRISE observations will provide new insight into shock acceleration mechanisms associated with interplanetary shocks. As mentioned in Section 2.2.3, interplanetary shocks accelerate electrons via Diffusive Shock Acceleration (DSA), since this mechanism is understood to dominate when the magnetic field to shock geometry is quasi-parallel. SunRISE observations may provide new insight into the conditions necessary for DSA processes to initiate.

The research outlined in this thesis revealed new insight into shock formation and propagation in the low corona and how electron acceleration and radio emission are generated during these processes. I investigated the early-phase evolution of shock properties and their relationship to type II burst emission. I determined the precise origin of a coronal shock and examined the effects of scattering on fundamental radio emission. I investigated a multi-lane type II burst and its relationship to a complex solar eruption and determined the origin of band-split pairs. Future research that furthers our understanding of the link between type II emission characteristics and coronal shock properties will be essential in constructing a complete picture of shock formation and propagation. Developments in present-day radio instrumentation and those planned for the near future will provide insight into the fundamental physics governing activity in the solar atmosphere.

References

Allen, C. W. (1947). Interpretation of electron densities from Corona brightness. *Monthly Notices of the Royal Astronomical Society*, 107(5-6):426–432. (Cited on pages 64 and 133.)

Anantharamaiah, K. R., Gothoskar, P., and Cornwell, T. J. (1994). Radio synthesis imaging of anisotropic angular broadening in the solar wind. *Journal of Astrophysics and Astronomy*, 15(4):387–414. (Cited on page 137.)

Antiochos, S. K., Sturrock, P. A., Antiochos, S. K., and Sturrock, P. A. (1978). Evaporative cooling of flare plasma. *The Astronomical Journal*, 220:1137–1143. (Cited on page 14.)

Antonucci, E., Harra, L., Susino, R., and Telloni, D. (2020). Observations of the Solar Corona from Space. *Space Science Reviews*, 216(8):1–40. (Cited on page 15.)

Armstrong, J. W., Coles, W. A., Rickett, B. J., and Kojima, M. (1990). Observations of field-aligned density fluctuations in the inner solar wind. *The Astrophysical Journal*, 358:685. (Cited on page 137.)

Asai, A., Ishii, T. T., Isobe, H., Kitai, R., Ichimoto, K., UeNo, S., Nagata, S., Morita, S., Nishida, K., Shiota, D., Oi, A., Akioka, M., Shibata, K., Asai, A., Ishii, T. T., Isobe, H., Kitai, R., Ichimoto, K., UeNo, S., Nagata, S., Morita, S., Nishida, K., Shiota, D., Oi, A., Akioka, M., and Shibata, K. (2012). First Simultaneous Observation of an Hα Moreton Wave, EUV Wave, and Filament/Prominence Oscillations. *The Astrophysical Journal*, 745(2):L18. (Cited on page 21.)

Aschwanden, M. J. (2004). Physics of the Solar Corona. An Introduction. *Springer*, page 842. (Cited on page 15.)

Attrill, G. D. R., Long, D. M., Green, L. M., Harra, L. K., van Driel-Gesztelyi, L., Attrill, G. D. R., Long, D. M., Green, L. M., Harra, L. K., and van Driel-Gesztelyi, L. (2014). Extreme-ultraviolet Observations of Global Coronal Wave Rotation. *Astrophysical Journal*, 796(1):55. (Cited on page 21.)

Babcock, H. W., Wilson, M., and Observatories, P. (1961). The Topology of the Sun's Magnetic Field and the 22-YEAR Cycle. *Astrophysical Journal*, 133:572. (Cited on page 8.)

Bain, H. M., Krucker, S., Glesener, L., and Lin, R. P. (2012). Radio imaging of shock-accelerated electrons associated with an erupting plasmoid on 2010 November 3. *Astrophysical Journal*, 750(1):44. (Cited on page 125.)

Baker, W. L., Savides, J., Baker, W. L., and Savides, J. (1975). The geostationary operational environmental satellite /GOES/ imaging communication system. In *International Telemetering Conference*, pages 464–471. (Cited on page 96.)

Ball, L. and Melrose, D. B. (2001). Shock Drift Acceleration of Electrons. *Publications of the Astronomical Society of Australia*, 18:361–373. (Cited on page 54.)

Balogh, A. and Treumann, R. A. (2013). *Physics of Collisionless Shocks*. Springer New York, New York, NY. (Cited on pages 19, 43 and 44.)

Bastian, T. S. (1994). Angular scattering of solar radio emission by coronal turbulence. *The Astrophysical Journal*, 426:774. (Cited on page 132.)

Bastian, T. S., Pick, M., Kerdraon, A., Maia, D., and Vourlidas, A. (2001). The Coronal Mass Ejection of 1998 April 20: Direct Imaging at Radio Wavelengths. *The Astrophysical Journal Letters*, 558(1):L65–L69. (Cited on page 18.)

Baumbach, S. (1937). Strahlung, Ergiebigkeit und Elektronendichte der Sonnenkorona. *Astronomische Nachrichten*, 263(6):121–134. (Cited on page 133.)

Bein, B. M., Berkebile-Stoiser, S., Veronig, A. M., Temmer, M., Vršnak, B., Bein, B. M., Berkebile-Stoiser, S., Veronig, A. M., Temmer, M., and Vršnak, B. (2012). Impulsive Acceleration of Coronal Mass Ejections. II. Relation to Soft X-Ray Flares and Filament Eruptions. *The Astrophysical Journal*, 755(1):44. (Cited on page 18.)

Bemporad, A., Sterling, A. C., Moore, R. L., and Poletto, G. (2005). A New Variety of Coronal Mass Ejection: Streamer Puffs from Compact Ejective Flares. *The Astrophysical Journal*, 635(2):L189. (Cited on page 16.)

Benz, A. O. (2016). Flare Observations. *Living Reviews in Solar Physics*, 14(1):1–59. (Cited on page 13.)

Berger, T. E., Liu, W., and Low, B. C. (2012). SDO/AIA Detection of Solar Prominence Formation within a Coronal Cavity. *The Astrophysical Journal*, 758(2):L37. (Cited on page 105.)

Berghmans, D., Hochedez, J. F., Defise, J. M., Lecat, J. H., Nicula, B., Slemzin, V., Lawrence, G., Katsyiannis, A. C., van der Linden, R., Zhukov, A., Clette, F., Rochus, P., Mazy, E., Thibert, T., Nicolosi, P., Pelizzo, M. G., Schühle, U., Berghmans, D., Hochedez, J. F., Defise, J. M., Lecat, J. H., Nicula, B., Slemzin, V., Lawrence, G., Katsyiannis, A. C., van der Linden, R., Zhukov, A., Clette, F., Rochus, P., Mazy, E., Thibert, T., Nicolosi, P., Pelizzo, M. G., and Schühle, U. (2006). SWAP onboard PROBA 2, a new EUV imager for solar monitoring. *Advances in Space Research*, 38(8):1807–1811. (Cited on page 129.)

Birn, J., Fletcher, L., Hesse, M., and Neukirch, T. (2009). Energy release and transfer in solar flares: Simulations of three-dimensional reconnection. *The Astrophysical Journal*, 695(2):1151–1162. (Cited on page 14.)

Boerner, P., Edwards, C., Lemen, J., Rausch, A., Schrijver, C., Shine, R., Shing, L., Stern, R., Tarbell, T., Title, A., Wolfson, C. J., Soufli, R., Spiller, E., Gullikson, E., McKenzie, D., Windt, D., Golub, L., Podgorski, W., Testa, P., and Weber, M. (2012). Initial Calibration of the Atmospheric Imaging Assembly (AIA) on the Solar Dynamics Observatory (SDO). *Solar Physics*, 275(1-2):41–66. (Cited on page 97.)

Bougeret, J., Kaiser, M., Kellogg, P., Manning, R., Goetz, K., Monson, S., Monge, N., Friel, L., Meetre, C., Perche, C., Sitruk, L., and Hoang, S. (1995). WAVES: The radio plasma wave instrument on the WIND instrument. *Space Science Reviews*, 71(1-4):231–263. (Cited on page 107.)

Briggs, D. S., Briggs, and S., D. (1995). High Fidelity Interferometric Imaging: Robust Weighting and NNLS Deconvolution. *Bulletin of the American Astronomical Society*, 27:1444. (Cited on page 89.)

Broekema, P. C., Mol, J. J. D., Nijboer, R., van Amesfoort, A. S., Brentjens, M. A., Loose, G. M., Klijn, W. F., and Romein, J. W. (2018). Cobalt: A GPU-based correlator and beamformer for LOFAR. *Astronomy and Computing*, 23:180–192. (Cited on page 96.)

Brueckner, G. E., Howard, R. A., Koomen, M. J., Korendyke, C. M., Michels, D. J., Moses, J. D., Socker, D. G., Dere, K. P., Lamy, P. L., Llebaria, A., Bout, M. V., Schwenn, R., Simnett, G. M., Bedford, D. K., and Eyles, C. J. (1995). The Large Angle Spectroscopic Coronagraph (LASCO). *Solar Physics*, 162(1-2):357–402. (Cited on pages 17 and 99.)

Burgess, D. (2006). Simulations of Electron Acceleration at Collisionless Shocks: The Effects of Surface Fluctuations. *The Astrophysical Journal*, 653(1):316–324. (Cited on page 70.)

Cairns, I. H. and Robinson, R. D. (1987). Herringbone bursts associated with type II solar radio emission. *Solar Physics 1987 111:2*, 111(2):365–383. (Cited on page 24.)

Cairns, I. H., Robinson, R. D., Cairns, I. H., and Robinson, R. D. (1987). Herringbone bursts associated with type II solar radio emission. *Solar Physics*, 111(2):365–383. (Cited on page 69.)

Cane, H. V. and White, S. M. (1989). On the Source Conditions for Herringbone Structure in Type-II Solar Radio Bursts. *Solar Physics*, 120(1):137–144. (Cited on page 69.)

Carley, E. P., Baldovin, C., Benthem, P., Bisi, M. M., Fallows, R. A., Gallagher, P. T., Olberg, M., Rothkaehl, H., Vermeulen, R., Vilmer, N., and Barnes, D. (2020). Radio observatories and instrumentation used in space weather science and operations. *Journal of Space Weather and Space Climate*, 10:7. (Cited on page 166.)

Carley, E. P., Cecconi, B., Reid, H. A., Briand, C., Raja, S., Masson, S., Dorovskyy, V. V., Tiburzi, C., Vilmer, N., Zucca, P., Zarka, P., Tagger, M., Griessmeier, J.-M., Corbel, S., Theureau, G., Loh, A., and Girard, J. (2021). Observations of shock propagation through turbulent plasma in the solar corona. *Astrophysical Journal*. (Cited on pages 69, 70 and 168.)

Carley, E. P., Long, D. M., Byrne, J. P., Zucca, P., Shaun Bloomfield, D., McCauley, J., and Gallagher, P. T. (2013). Quasiperiodic acceleration of electrons by a plasmoid-driven shock in the solar atmosphere. *Nature Physics*, 9(12):811–816. (Cited on pages 26, 55, 68, 69, 70, 102 and 124.)

Carley, E. P., McAteer, R. T. J., Gallagher, P. T., Carley, E. P., McAteer, R. T. J., and Gallagher, P. T. (2012). Coronal Mass Ejection Mass, Energy, and Force Estimates Using STEREO. *The Astrophysical Journal*, 752(1):36. (Cited on page 18.)

Carley, E. P., Reid, H., Vilmer, N., and Gallagher, P. T. (2015). Low frequency radio observations of bi-directional electron beams in the solar corona. *Astronomy & Astrophysics*, 581:A100. (Cited on page 69.)

Carrington, R. C. (1859). Description of a Singular Appearance seen in the Sun on September 1, 1859. *Monthly Notices of the Royal Astronomical Society*, 20(1):13–15. (Cited on page 11.)

Chandrasekhar, S., Chandrasekhar, and S. (1952). A statistical basis for the theory of stellar scintillation. *Monthly Notices of the Royal Astronomical Society*, 112(5):475. (Cited on page 73.)

Charbonneau and Paul (2010). Dynamo Models of the Solar Cycle. *Living Reviews in Solar Physics*, 7(1):3. (Cited on page 8.)

Chen, P. F., Fang, C., and Shibata, K. (2005). A Full View of EIT Waves. *The Astrophysical Journal*, 622(2):1202. (Cited on page 21.)

Chen, P. F., Wu, S. T., Shibata, K., and Fang, C. (2002). Evidence of EIT and Moreton Waves in Numerical Simulations. *The Astrophysical Journal*, 572(1):L99. (Cited on page 21.)

Cho, K.-S., Bong, S.-C., Moon, Y.-J., Shanmugaraju, A., Kwon, R.-Y., and Park, Y. D. (2011). Relationship between multiple type II solar radio bursts and CME observed by STEREO/SECCHI. *Astronomy & Astrophysics*, 530:A16. (Cited on pages 68 and 143.)

Cho, K.-S., Gary, D. E., Lee, J., Moon, Y.-J., and Park, Y. D. (2007). Magnetic Field Strength in the Solar Corona from Type II Band Splitting. *The Astrophysical Journal*, 665(1):799–804. (Cited on pages 20, 44, 102 and 125.)

Chrysaphi, N., Kontar, E. P., Holman, G. D., and Temmer, M. (2018). CME-driven shock and Type II solar radio burst band-splitting. *The Astrophysical Journal*, 868(79):10. (Cited on pages xvi, 65, 67, 75, 76, 77, 105, 115, 125, 132, 133, 138, 143, 156, 161, 162 and 164.)

Chrysaphi, N., Reid, H. A. S., and Kontar, E. P. (2020). First Observation of a Type II Solar Radio Burst Transitioning between a Stationary and Drifting State. *The Astrophysical Journal*, 893(2):115. (Cited on pages 26, 124, 125, 142 and 143.)

Clark, B. G. (1980). An efficient implementation of the algorithm 'CLEAN'. *Astronomy and Astrophysics*, 89(3):377. (Cited on page 90.)

Cornwell, T., Braun, R., and Briggs, D. S. (1999). Deconvolution. In *Synthesis Imaging in Radio Astronomy II, A Collection of Lectures from the Sixth NRAO/NMIMT Synthesis Imaging Summer School.*, volume 180, page 151. (Cited on page 89.)

Cornwell, T. J. (2008). Multiscale CLEAN Deconvolution of Radio Synthesis Images. *IEEE Journal of Selected Topics in Signal Processing*, 2(5):793–801. (Cited on page 91.)

Cunha-Silva, R., Fernandes, F., and Selhorst, C. (2015). Shock wave driven by CME evidenced by metric type II burst and EUV wave. *Advances in Space Research*, 56(12):2804–2810. (Cited on page 21.)

Dauphin, C., Vilmer, N., and Krucker, S. (2006). Observations of a soft X-ray rising loop associated with a type II burst and a coronal mass ejection in the 03 November 2003 X-ray flare. *Astronomy & Astrophysics*, 455(1):339–348. (Cited on pages 26, 124 and 125.)

De Hoffmann, F. and Teller, E. (1950). Magneto-Hydrodynamic Shocks. *Physical Review*, 80(4):692–703. (Cited on pages 53 and 117.)

de Jong, T. and van Soldt, W. H. (1989). The earliest known solar eclipse record redated. *Nature*, 338(6212):238–240. (Cited on page 3.)

Delannée, C., Aulanier, G., Delannée, C., and Aulanier, G. (1999). CME Associated with Transequatorial Loops and a Bald Patch Flare. *Solar Physics*, 190(1-2):107–129. (Cited on page 21.)

Delannée, C., Hochedez, J. F., Aulanier, G., Delannée, C., Hochedez, J. F., and Aulanier, G. (2007). Stationary parts of an EIT and Moreton wave: a topological model. *Astronomy & Astrophysics*, 465(2):603–612. (Cited on page 21.)

Dewdney, P. E., Hall, P. J., Schilizzi, R. T., Joseph, T., and Lazio, L. W. (2009). The Square Kilometre Array. In *Proceedings of the IEEE*, pages 1482 –1496. (Cited on pages 82 and 166.)

Dikpati, M. and Gilman, P. A. (2009). Flux-transport solar dynamos. *Space Science Reviews*, 144(1-4):67–75. (Cited on page 7.)

Domingo, V., Fleck, B., and Poland, A. I. (1995). The SOHO mission: An overview. *Solar Physics*, 162(1-2):1–37. (Cited on page 99.)

Dorovskyy, V. V., Melnik, V. N., Konovalenko, A. A., Brazhenko, A. I., Panchenko, M., Poedts, S., and Mykhaylov, V. A. (2015). Fine and Superfine Structure of the Decameter–Hectometer Type II Burst on 7 June 2011. *Solar Physics*, 290(7):2031–2042. (Cited on page 142.)

Drury, L. O. (1983). REVIEW ARTICLE: An introduction to the theory of diffusive shock acceleration of energetic particles in tenuous plasmas. *Reports on Progress in Physics*, 46(8):973–1027. (Cited on pages 55 and 120.)

Du, G., Kong, X., Chen, Y., Feng, S., Wang, B., Li, G., Du, G., Kong, X., Chen, Y., Feng, S., Wang, B., and Li, G. (2015). An Observational Revisit of Band-split Solar Type-II Radio Bursts. *The Astrophysical Journal*, 812(1):52. (Cited on page 105.)

Edlén, B. (1943). Die Deutung der Emissionslinien im Spektrum der Sonnenkorona. Mit 6 Abbildungen. *Zeitschrift für Astrophysik*, 22:30. (Cited on page 4.)

Edmiston, J. P. and Kennel, C. F. (1984). A parametric survey of the first critical Mach number for a fast MHD shock. *Journal of Plasma Physics*, 32(3):429–441. (Cited on pages 51, 52 and 118.)

Emslie, A. G., Kucharek, H., Dennis, B. R., Gopalswamy, N., Holman, G. D., Share, G. H., Vourlidas, A., Forbes, T. G., Gallagher, P. T., Mason, G. M., Metcalf, T. R., Mewaldt, R. A., Murphy, R. J., Schwartz, R. A., and Zurbuchen, T. H. (2004). Energy partition in two solar flare/CME events. *Journal of Geophysical Research*, 109(A10):A10104. (Cited on page 11.)

Eselevich, V. G., Eselevich, M. V., Sadykov, V. M., and Zimovets, I. V. (2015). Evidence of a blast shock wave formation in a "CME-streamer" interaction. *Advances in Space Research*, 56(12):2793–2803. (Cited on pages 26 and 137.)

Eselevich, V. G., Eselevich, M. V., and Zimovets, I. V. (2019). Observations of a Flare-Generated Blast Wave in a Pseudo Coronal Mass Ejection Event. *Solar Physics*, 294(6):1–20. (Cited on page 44.)

Evans, J. W. (1948). Photometer for measurement of sky brightness near the sun. *Journal of the Optical Society of America*, 38(12):1083. (Cited on page 99.)

Fan, Y., Fisher, G. H., and Deluca, E. E. (1993). The Origin of Morphological Asymmetries in Bipolar Active Regions. *Astrophysical Journal*, 405:390. (Cited on page 8.)

Farris, M. H., Russell, C. T., Fitzenreiter, R. J., and Ogilvie, K. W. (1994). The subcritical, quasi-parallel, switch-on shock. *Geophysical Research Letters*, 21(9):837–840. (Cited on page 103.)

Feng, S. W., Chen, Y., Kong, X. L., Li, G., Song, H. Q., Feng, X. S., Guo, F., Feng, S. W., Chen, Y., Kong, X. L., Li, G., Song, H. Q., Feng, X. S., and Guo, F. (2013). Diagnostics on the Source Properties of a Type II Radio Burst with Spectral Bumps. *The Astronomical Journal*, 767(1):29. (Cited on pages 68, 143, 155 and 164.)

Feng, S. W., Chen, Y., Kong, X. L., Li, G., Song, H. Q., Feng, X. S., and Liu, Y. (2012). Radio signatures of CME-streamer interaction and source diagnostics of type II radio burst. *The Astrophysical Journal*, 753(1). (Cited on page 26.)

Feng, S. W., Du, G. H., Chen, Y., Kong, X. L., Li, G., Guo, F., Feng, S. W., Du, G. H., Chen, Y., Kong, X. L., Li, G., and Guo, F. (2015). Simultaneous Radio and EUV Imaging of a Multi-lane Coronal Type II Radio Burst. *Solar Physics*, 290(4):1195–1205. (Cited on pages 67, 68, 143, 155 and 164.)

Fisher, G. H. and Welsch, B. T. (2007). FLCT: A Fast, Efficient Method for Performing Local Correlation Tracking. *Subsurface and Atmospheric Influences on Solar Activity - ASP Conference Series*, 383. (Cited on pages 147 and 149.)

Fletcher, L., Dennis, B. R., Hudson, H. S., Krucker, S., Phillips, K., Veronig, A., Battaglia, M., Bone, L., Caspi, A., Chen, Q., Gallagher, P., Grigis, P. T., Ji, H., Liu, W., Milligan, R. O., Temmer, M., Fletcher, L., Dennis, B. R., Hudson, H. S., Krucker, S., Phillips, K., Veronig, A., Battaglia, M., Bone, L., Caspi, A., Chen, Q., Gallagher, P., Grigis, P. T., Ji, H., Liu, W., Milligan, R. O., and Temmer, M. (2011). An Observational Overview of Solar Flares. *Space Science Reviews*, 159(1-4):19–106. (Cited on pages 12 and 13.)

Fokker, A. (1963). Type IV solar radio emission. *Space Science Reviews*, 2(1):70–90. (Cited on page 24.)

Fokker, A. D. (1965). Coronal scattering of radiation from solar radio sources. *Bulletin of the Astronomical Institutes of the Netherlands,*, 18:111. (Cited on page 73.)

Frassati, F., Susino, R., Mancuso, S., and Bemporad, A. (2019). Comprehensive Analysis of the Formation of a Shock Wave Associated with a Coronal Mass Ejection. *The Astrophysical Journal*, 871(2):212. (Cited on page 105.)

Gallagher, P. T. and Long, D. M. (2011). Large-scale Bright Fronts in the Solar Corona: A Review of "EIT waves". *Space Science Reviews*, 158(2-4):365–396. (Cited on page 22.)

Gallagher, P. T., Williams, D. R., Phillips, K. J., Mathioudakis, M., Smartt, R. N., and Keenan, F. P. (2000). Multi-wavelength observations of the 1998 September 27 Flare spray. *Solar Physics*, 195(2):367–380. (Cited on page 14.)

Gary, D. E. and Hurford, G. J. (2004). Radio Spectral Diagnostics. *Solar and Space Weather Radiophysics*, pages 71–87. (Cited on page 58.)

Gary, G. A. (2001). Plasma Beta above a Solar Active Region: Rethinking the Paradigm. *Solar Physics*, 203(1):71–86. (Cited on pages 38 and 114.)

Ginzburg, V. L. and Zhelezniakov, V. V. (1993). On the Possible Mechanisms of Sporadic Solar Radio Emission (Radiation in an Isotropic Plasma. *Soviet Astronomy, Vol. 2, p.653*, 2:653. (Cited on page 117.)

Ginzburg, V. L., Zhelezniakov, V. V., Ginzburg, V. L., and Zhelezniakov, V. V. (1958). On the Possible Mechanisms of Sporadic Solar Radio Emission (Radiation in an Isotropic Plasma). *Soviet Astronomy,*, 2:653. (Cited on page 60.)

Gopalswamy, N. (2009). Halo coronal mass ejections and geomagnetic storms. *Earth Planets Space*, 61:595–597. (Cited on pages 20 and 21.)

Gopalswamy, N., Nitta, N., Akiyama, S., Mäkelä, P., and Yashiro, S. (2011). Coronal Magnetic Field Measurement From Euv Images Made By the Solar Dynamics Observatory. 72(September):0–6. (Cited on pages 104 and 115.)

Gopalswamy, N., Shimojo, M., Lu, W., Yashiro, S., Shibasaki, K., and Howard, R. A. (2003). Prominence Eruptions and Coronal Mass Ejection: A Statistical Study Using Microwave Observations. *The Astrophysical Journal*, 586(1):562. (Cited on page 17.)

Gopalswamy, N., Xie, H., Mäkelä, P., Akiyama, S., Yashiro, S., Kaiser, M. L., Howard, R. A., Bougeret, J. L., Gopalswamy, N., Xie, H., Mäkelä, P., Akiyama, S., Yashiro, S., Kaiser, M. L., Howard, R. A., and Bougeret, J. L. (2010). Interplanetary Shocks Lacking Type II Radio Bursts. *The Astrophysical Journal*, 710(2):1111–1126. (Cited on page 120.)

Gopalswamy, N. and Yashiro, S. (2011). The Strength and Radial Profile of Coronal Magnetic Field from the Standoff Distance of a CME-driven Shock. (Cited on page 104.)

Gopalswamy, N., Yashiro, S., Xie, H., Akiyama, S., Aguilar-Rodriguez, E., Kaiser, M. L., Howard, R. A., and Bougeret, J. L. (2008). Radio-Quiet Fast and Wide Coronal Mass Ejections. *The Astrophysical Journal*, 674(1):560–569. (Cited on page 120.)

Gordovskyy, M., Kontar, E., Browning, P., and Kuznetsov, A. (2019). Frequency-Distance Structure of Solar Radio Sources Observed by LOFAR. *The Astrophysical Journal*, 873:48. (Cited on page 95.)

Grechnev, V. V., Afanasyev, A. N., Uralov, A. M., Chertok, I. M., Eselevich, M. V., Eselevich, V. G., Rudenko, G. V., and Kubo, Y. (2011). Coronal Shock Waves, EUV Waves, and Their Relation to

CMEs. III. Shock-Associated CME/EUV Wave in an Event with a Two-Component EUV Transient. *Solar Physics*, 273(2):461–477. (Cited on page 102.)

Grechnev, V. V., Lesovoi, S. V., Kochanov, A. A., Uralov, A. M., Altyntsev, A. T., Gubin, A. V., Zhdanov, D. A., Ivanov, E. F., Smolkov, G. Y., and Kashapova, L. K. (2018). Multi-instrument view on solar eruptive events observed with the Siberian Radioheliograph: From detection of small jets up to development of a shock wave and CME. *Journal of Atmospheric and Solar-Terrestrial Physics*, 174:46–65. (Cited on page 125.)

Grotrian, W. (1939). Zur Frage der Deutung der Linien im Spektrum der Sonnenkorona. *Die Naturwissenschaften,*, 27(13):214. (Cited on page 4.)

Guerra, J. A., Park, S.-H., Gallagher, P. T., Kontogiannis, I., Georgoulis, M. K., and Bloomfield, D. S. (2018). Active Region Photospheric Magnetic Properties Derived from Line-of-Sight and Radial Fields. *Solar Physics*, 293(1):1–25. (Cited on page 10.)

Guo, F. and Giacalone, J. (2010a). The Effect of Large-scale Magnetic Turbulence on the Acceleration of Electrons by Perpendicular Collisionless Shocks. *ApJ*, 715(1):406–411. (Cited on page 70.)

Guo, F. and Giacalone, J. (2010b). The Effect of Large Scale Magnetic Turbulence on the Acceleration of Electrons by Perpendicular Collisionless Shocks. *The Astrophysical Journal*, 715(1):406–411. (Cited on page 119.)

Guo, F., Giacalone, J., and Zhao, L. (2021). Shock Propagation and Associated Particle Acceleration in the Presence of Ambient Solar-Wind Turbulence. *Frontiers in Astronomy and Space Sciences*, 8:27. (Cited on page 121.)

Guo, J., Zhang, H. Q., and Chumak, O. V. (2007). Magnetic properties of flare-CME productive active regions and CME speed. *Astronomy & Astrophysics*, 462(3):1121–1126. (Cited on page 18.)

Harkness, W. and Young, C. A. (1986). Reports on Observations of the Total Eclipse of the Sun, August 7, 1869 ... - United States Naval Observatory - Google Books. Technical report, United States Naval Observatory. (Cited on page 4.)

Harvey, J. W., Hill, F., Hubbard, R. P., Kennedy, J. R., Leibacher, J. W., Pintar, J. A., Gilman, P. A., Noyes, R. W., Title, A. M., Toomre, J., Ulrich, R. K., Bhatnagar, A., Kennewell, J. A., Marquette, W., Patrón, J., Saá, O., and Yasukawa, E. (1996). The Global Oscillation Network Group (GONG) Project. *Science*, 272(5266):1284–1286. (Cited on page 129.)

Hodgson, R. (1859). On a curious Appearance seen in the Sun. *Monthly Notices of the Royal Astronomical Society*, 20(1):15–16. (Cited on page 11.)

Högbom, J. A. (1974). Aperture Synthesis with a Non-Regular Distribution of Interferometer Baselines. *Astronomy and Astrophysics Supplement*, 15:417. (Cited on pages 89 and 90.)

Hollweg, J. V. (1968). A Statistical Ray Analysis of The Scattering of Radio Waves by the Solar Corona. *AJ*, 73(10):972. (Cited on page 73.)

Holman, G. D. and Pesses, M. E. (1983). Solar type II radio emission and the shock drift acceleration of electrons. *The Astrophysical Journal*, 267:837. (Cited on pages 50, 52, 67 and 143.)

Howard, T. (2014). Space Weather and Coronal Mass Ejections. In *SpringerBriefs in Astronomy*, SpringerBriefs in Astronomy. Springer New York, New York, NY. (Cited on page 16.)

Hudson, H. S., Acton, L. W., Hirayama, T., Uchida, Y., Hudson, H. S., Acton, L. W., Hirayama, T., and Uchida, Y. (1992). White-Light Flares Observed by YOHKOH. *Publications of the Astronomical Society of Japan*, 44:L77–L81. (Cited on page 12.)

Hudson, H. S. and Warmuth, A. (2004). Coronal Loop Oscillations and Flare Shock Waves. *The Astrophysical Journal*, 614(1):L85–L88. (Cited on pages 44 and 124.)

Ingale, M., Subramanian, P., and Cairns, I. (2015). Coronal turbulence and the angular broadening of radio sources - The role of the structure function. *Monthly Notices of the Royal Astronomical Society*, 447(4):3486–3497. (Cited on pages 72 and 138.)

Jaeggli, S. A., Norton, A. A., Jaeggli, S. A., and Norton, A. A. (2016). The Magnetic Classification of Solar Active Regions 1992-2015. *The Astrophysical Journal Letters*, 820(1):L11. (Cited on page 10.)

Jebaraj, I. C., Kouloumvakos, A., Magdalenic, J., Rouillard, A. P., Mann, G., Krupar, V., and Poedts, S. (2021). Generation of interplanetary type II radio emission. *Astronomy & Astrophysics*. (Cited on pages 26, 120, 160 and 171.)

Jiang, Y., Yang, J., Zheng, R., Bi, Y., and Yang, X. (2009). A Narrow Streamer-Puff Coronal Mass Ejection from the Nonradial Eruption of an Active-Region Filament. *The Astrophysical Journal*, 693(2):1851. (Cited on page 16.)

Jokipii, J. R. (1987). Rate of energy gain and maximum energy in diffusive shock acceleration. *The Astronomical Journal*, 313:842–846. (Cited on pages 55, 119 and 121.)

Jokipii, J. R. (2013). The Heliospheric Termination Shock. *Space Science Reviews*, 176(1-4):115–124. (Cited on page 44.)

Joseph Lazio, T. W., Kasper, J., Alibay, F., Amiri, N., Bastian, T., Cohen, C., Landi, E., Manchester, W., Reinard, A., Schwadron, N., Cecconi, B., Hallinan, G., Hegedus, A., Krupar, V., Maksimovic, M., and Zaslavsky, A. (2017). The Sun Radio Space Imaging Experiment (SunRISE). In *32nd URSI GASS*, Montreal. (Cited on page 170.)

Kahler, S. W., Ling, A. G., and Gopalswamy, N. (2019). Are Solar Energetic Particle Events and Type II Bursts Associated with Fast and Narrow Coronal Mass Ejections? *Solar Physics*, 294(9):1–13. (Cited on page 137.)

Kai, K. and McLean, D. J. (1968). Type II Solar Radio Bursts Observed with the Culgoora Radioheliograph during a Flare on 17 June 1968. *Publications of the Astronomical Society of Australia*, 1(4):141–142. (Cited on pages 73, 125 and 162.)

Kennel, C. F. and F., C. (1987). Critical Mach numbers in classical magnetohydrodynamics. *Journal of Geophysical Research*, 92(A12):13427. (Cited on page 51.)

Kerdraon, A. and Delouis, J.-M. (1997). The Nançay Radioheliograph. In *Coronal Physics from Radio and Space Observations; Proceedings of the CESRA Workshop held in Nouan le Fuzelier*, volume 483, page 192. Springer Berlin Heidelberg. (Cited on page 143.)

Kim, K.-H., Lee, D.-H., Shiokawa, K., Lee, E., Park, J.-S., Kwon, H.-J., Angelopoulos, V., Park, Y.-D., Hwang, J., Nishitani, N., Hori, T., Koga, K., Obara, T., Yumoto, K., and Baishev, D. G. (2012). Magnetospheric responses to the passage of the interplanetary shock on 24 November 2008. *Journal of Geophysical Research: Space Physics*, 117(A10):n/a–n/a. (Cited on page 104.)

Kimura, H. and Mann, I. (1998). Brightness of the solar F-corona. *Earth, Planets and Space*, 50(6):493–499. (Cited on page 6.)

Klassen, A., Aurass, H., Klein, K.-L., Hofmann, A., and Mann, G. (1999). Radio evidence on shock wave formation in the solar corona. Technical report. (Cited on page 145.)

Klassen, A., Aurass, H., Mann, G., and Thompson, B. J. (2000). Catalogue of the 1997 SOHO–EIT coronal transient waves and associated type II radio burst spectra. *Astronomy and Astrophysics Supplement Series*, 141(3):357–369. (Cited on page 22.)

Klassen, A., Pohjolainen, S., and Klein, K. L. (2003). Type II radio precursor and X-ray flare emission. *Solar Physics*, 218(1-2):197–210. (Cited on page 145.)

Klein, K. L., Khan, J. I., Vilmer, N., Delouis, J. M., and Aurass, H. (1999). X-ray and radio evidence on the origin of a coronal shock wave. *Astronomy and Astrophysics*, 346(3). (Cited on pages 26, 124 and 125.)

Klimchuk, J. A. (2001). Theory of Coronal Mass Ejections. *Geophysical Monograph Series*, 125:143–157. (Cited on page 102.)

Klimchuk, J. A., Klimchuk, and A., J. (2006). On Solving the Coronal Heating Problem. *Solar Physics*, 234(1):41–77. (Cited on page 4.)

Kontar, E. P. (2001). Dynamics of electron beams in the solar corona plasma with density fluctuations. *Astronomy & Astrophysics*, 375(2):629–637. (Cited on page 60.)

Kontar, E. P., Chen, X., Chrysaphi, N., Jeffrey, N. L. S., Emslie, A. G., Krupar, V., Maksimovic, M., Gordovskyy, M., and Browning, P. K. (2019). Anisotropic Radio-wave Scattering and the Interpretation of Solar Radio Emission Observations. *The Astrophysical Journal*, 884(2):122. (Cited on pages 72, 74, 75, 137 and 162.)

Kontar, E. P., Yu, S., Kuznetsov, A. A., Emslie, A. G., Alcock, B., Jeffrey, N. L., Melnik, V. N., Bian, N. H., and Subramanian, P. (2017). Imaging spectroscopy of solar radio burst fine structures. *Nature Communications*, 8(1):1–9. (Cited on pages 75, 95 and 138.)

Kouloumvakos, A., Rouillard, A., Warmuth, A., Magdalenic, J., Jebaraj, I. C., Mann, G., Vainio, R., and Monstein, C. (2021). Coronal Conditions for the Occurrence of Type II Radio Bursts. *The Astrophysical Journal*, 913(2):99. (Cited on page 160.)

Koutchmy, S., Baudin, F., Bocchialini, K., Daniel, J. Y., Delaboudinière, J. P., Golub, L., Lamy, P., Adjabshirizadeh, A., Koutchmy, S., Baudin, F., Bocchialini, K., Daniel, J. Y., Delaboudinière, J. P., Golub, L., Lamy, P., and Adjabshirizadeh, A. (2004). The August 11th, 1999 CME. *Astronomy & Astrophysics*, 420(2):709–718. (Cited on page 15.)

Kozarev, K. A., Korreck, K. E., Lobzin, V. V., Weber, M. A., and Schwadron, N. A. (2011). Off-limb Solar Coronal Wavefronts from SDO/AIA Extreme-ultraviolet Observations—Implications for Particle Production. *The Astrophysical Journal*, 733(2):L25. (Cited on page 105.)

Kozarev, K. A., Raymond, J. C., Lobzin, V. V., and Hammer, M. (2015). Properties of a Coronal Shock Wave as A Driver of Early SEP Acceleration. *The Astrophysical Journal*, 799(10pp):167. (Cited on pages 105 and 119.)

Krupar, V., Eastwood, J. P., Kruparova, O., Santolik, O., Soucek, J., Magdalenić, J., Vourlidas, A., Maksimovic, M., Bonnin, X., Bothmer, V., Mrotzek, N., Pluta, A., Barnes, D., Davies, J. A., Martínez Oliveros, J. C., Bale, S. D., Krupar, V., Eastwood, J. P., Kruparova, O., Santolik, O., Soucek, J., Magdalenić, J., Vourlidas, A., Maksimovic, M., Bonnin, X., Bothmer, V., Mrotzek, N., Pluta, A., Barnes, D., Davies, J. A., Martínez Oliveros, J. C., and Bale, S. D. (2016). An Analysis of Interplanetary Solar Radio Emissions Associated with a Coronal Mass Ejection. *The Astronomical Journal*, 823(1):L5. (Cited on page 26.)

Krupar, V., Magdalenić, J., Eastwood, J. P., Gopalswamy, N., Kruparova, O., Szabo, A., Němec, F., Krupar, V., Magdalenić, J., Eastwood, J. P., Gopalswamy, N., Kruparova, O., Szabo, A., and Němec, F. (2019). Statistical Survey of Coronal Mass Ejections and Interplanetary Type II Bursts. *The Astronomical Journal*, 882(2):92. (Cited on page 26.)

Kumar, P., Innes, D. E., and Cho, K.-S. (2016). Flare-generated Shock Wave Propagation through Solar Coronal Arcade Loops and an Associated Type II Radio Burst. *The Astrophysical Journal*, 828(1):28. (Cited on page 44.)

Kumari, A., Morosan, D. E., and Kilpua, E. K. J. (2021). On the Occurrence of Type IV Solar Radio Bursts in Solar Cycle 24 and Their Association with Coronal Mass Ejections. *The Astrophysical Journal*, 906(2):79. (Cited on page 24.)

Lang, K. R. (2001). *The Cambridge Encyclopedia of the Sun*. Cambridge University Press. (Cited on page 5.)

Lemen, J. R. (2012). The Atmospheric Imaging Assembly (AIA) on the Solar Dynamics Observatory (SDO). *Solar Physics*, 275:17–40. (Cited on pages 12 and 96.)

Lengyel-Frey, D., Stone, R. G., and Bougeret, J. L. (1985). Fundamental and harmonic emission in interplanetary type II radio bursts. *A&A*, 151(2):215–221. (Cited on page 137.)

Li, H., You, J., Yu, X., and Wu, Q. (2002). Multi-wavelength observations of a flare spray and CME of 1 October 2001. *Astronomy & Astrophysics*, 391(2):741–748. (Cited on page 14.)

Liepmann, H. and Roshko, A. (1957). *Elements of gasdynamics*. New York. (Cited on page 136.)

Litvinenko, Y. E. (2003). Particle Acceleration by Magnetic Reconnection. In *Energy Conversion and Particle Acceleration in the Solar Corona*, volume 612, pages 213–229. Springer, Berlin, Heidelberg. (Cited on page 13.)

Lockyer, J. N. and N., J. (1869). Spectroscopic observation of the sun. *Philosophical Transactions of the Royal Society of London*, 159:425–444. (Cited on page 4.)

Long, D. M., Bloomfield, D. S., Chen, P. F., Downs, C., Gallagher, P. T., Kwon, R.-Y., Vanninathan, K., Veronig, A. M., Vourlidas, A., Vršnak, B., Warmuth, A., and Žic, T. (2016). Understanding the Physical Nature of Coronal "EIT Waves". *Solar Physics*, 292(1):1–24. (Cited on page 22.)

Lv, M. S., Chen, Y., Li, C. Y., Zimovets, I., Du, G. H., Wang, B., Feng, S. W., and Ma, S. L. (2017). Sources of the Multi-Lane Type II Solar Radio Burst on 5 November 2014. *Solar Physics*, 292(12). (Cited on pages 67, 68, 143, 155 and 164.)

Lyot, B. (1939). The study of the solar corona and prominences without eclipses (George Darwin Lecture, 1939). *Monthly Notices of the Royal Astronomical Society*, 99:538. (Cited on page 99.)

Magdalenić, J., Marqué, C., Fallows, R. A., Mann, G., Vocks, C., Zucca, P., Dabrowski, B. P., Krankowski, A., and Melnik, V. (2020). Fine Structure of a Solar Type II Radio Burst Observed by LOFAR. *The Astrophysical Journal Letters*, 897(1):L15. (Cited on pages 66, 67, 69, 70, 142 and 167.)

Magdalenić, J., Marqué, C., Zhukov, A. N., Vrnak, B., and Veronig, A. (2012). Flare-generated type II burst without associated coronal mass ejection. *The Astrophysical Journal*, 746(2). (Cited on page 26.)

Magdalenić, J., Marque, C., Zhukov, A. N., Vršnak, B., and Žic, T. (2010). Origin of coronal shock waves associated with slow coronal mass ejections. *The Astrophysical Journal*, 718(1):266–278. (Cited on pages 26, 101 and 125.)

Magdalenić, J., Vršnak, B., Pohjolainen, S., Temmer, M., Aurass, H., and Lehtinen, N. J. (2008). A flare-generated shock during a coronal mass ejection on 24 December 1996. *Solar Physics*, 253(1-2):305–317. (Cited on page 26.)

Maguire, C. A., Carley, E. P., McCauley, J., and Gallagher, P. T. (2020). Evolution of the Alfvén Mach number associated with a coronal mass ejection shock. *Astronomy & Astrophysics*, 633:A56. (Cited on pages 29, 65, 67, 73, 102, 124, 136, 142, 155 and 159.)

Maguire, C. A., Carley, E. P., Zucca, P., Vilmer, N., Gallagher, P. T., Maguire, C. A., Carley, E. P., Zucca, P., Vilmer, N., and Gallagher, P. T. (2021). LOFAR Observations of a Jet-driven Piston Shock in the Low Solar Corona. *The Astrophysical Journal*, 909(1):2. (Cited on pages 26, 30, 124 and 161.)

Mahrous, A., Alielden, K., Vršnak, B., and Youssef, M. (2018). Type II solar radio burst band-splitting: Measure of coronal magnetic field strength. *Journal of Atmospheric and Solar-Terrestrial Physics*, 172:75–82. (Cited on pages 65, 67 and 105.)

Maia, D., Pick, M., Vourlidas, A., and Howard, R. (2000). Development of Coronal Mass Ejections: Radio Shock Signatures. *The Astrophysical Journal*, 528(1):L49–L51. (Cited on page 20.)

Maia, D. J. F., Gama, R., Mercier, C., Pick, M., Kerdraon, A., Karlický, M., Maia, D. J. F., Gama, R., Mercier, C., Pick, M., Kerdraon, A., and Karlický, M. (2007). The Radio-Coronal Mass Ejection Event on 2001 April 15. *The Astrophysical Journal*, 660(1):874–881. (Cited on page 18.)

Maloney, S. A. and Gallagher, P. T. (2011). STEREO DIRECT IMAGING OF A CORONAL MASS EJECTION-DRIVEN SHOCK TO 0.5 AU. *The Astrophysical Journal Letters*, 736(5pp):5. (Cited on pages 20 and 104.)

Mancuso, S., Frassati, F., Bemporad, A., and Barghini, D. (2019). Three-dimensional reconstruction of CME-driven shock-streamer interaction from radio and EUV observations: a different take on the diagnostics of coronal magnetic fields. *A&A*, 624:2. (Cited on page 102.)

Mann, G., Classen, H. T., Keppler, E., and Roelof, E. C. (2002). On electron acceleration at CIR related shock waves. *Astronomy & Astrophysics*, 391(2):749–756. (Cited on pages 70, 110, 113 and 116.)

Mann, G., Classen, T., and Aurass, H. (1995). Characteristics of coronal shock waves and solar type II radio bursts. *Astronomy and Astrophysics*, 295:775. (Cited on pages 65, 105 and 113.)

Mann, G., Jansen, F., Macdowall, R. J., Kaiser, M. L., and Stone, R. G. (1999). A heliospheric density model and type III radio bursts. *Astronomy & Astrophysics*, 348:614–620. (Cited on page 133.)

Mann, G. and Klassen, A. (2005). Electron beams generated by shock waves in the solar corona. *Astronomy & Astrophysics*, 441(1):319–326. (Cited on page 69.)

Mann, G., Klassen, A., Aurass, H., and Classen, H.-T. (2003). Formation and development of shock waves in the solar corona and the near-Sun interplanetary space. *Astronomy & Astrophysics*, 400:329–336. (Cited on pages 41 and 42.)

Mann, G., Melnik, V. N., Rucker, H. O., Konovalenko, A. A., and Brazhenko, A. I. (2018). Radio signatures of shock-accelerated electron beams in the solar corona. *Astronomy & Astrophysics*, 609:A41. (Cited on page 69.)

Mawad, R., Shaltout, M., Yousef, M., Yousef, S., and Ewaida, M. (2015). Filaments disappearance in relation to coronal mass ejections during the solar cycle 23. *Advances in Space Research*, 55(2):688–695. (Cited on page 17.)

Maxwell, A., Dryer, M., and McIntosh, P. (1985). A piston-driven shock in the solar corona. *Solar Physics*, 97(2):401–413. (Cited on pages 136 and 137.)

McIntosh, P. S. (1990). The Classification of Sunspot Groups. *Solar Physics*, 125(2):251–267. (Cited on page 10.)

McKenzie, D. E. (2013). Turbulent dynamics in solar flare sheet structures measured with local correlation tracking. *Astrophysical Journal*, 766(1). (Cited on page 147.)

McLean, D. J. D. J. and Labrum, N. R. N. R. (1985). *Solar radiophysics : studies of emission from the sun at metre wavelengths*. Cambridge University Press. (Cited on pages 61 and 67.)

Melnik, V. N., Brazhenko, A. I., Frantsuzenko, A. V., Dorovskyy, V. V., and Rucker, H. O. (2018). Properties of Decameter IIIb-III Pairs. *Solar Physics*, 293(2). (Cited on page 132.)

Melrose, D. B. (1975). Small-scale inhomogeneities in the solar corona: Evidence from meter-λ radio bursts. *Solar Physics*, 43(1):79–86. (Cited on pages 19, 23 and 117.)

Melrose, D. B. (2017). Coherent emission mechanisms in astrophysical plasmas. *Reviews of Modern Plasma Physics*, 1(1):1–81. (Cited on page 61.)

Milligan, R. O. and Dennis, B. R. (2009). Velocity Characteristics of Evaporated Plasma Using Hinode/EUV Imaging Spectrometer. *The Astrophysical Journal*, 699(2):968. (Cited on page 14.)

Milligan, R. O., Gallagher, P. T., Mathioudakis, M., and Keenan, F. P. (2006). Observational Evidence of Gentle Chromospheric Evaporation during the Impulsive Phase of a Solar Flare. *The Astrophysical Journal*, 642(2):L169. (Cited on page 14.)

Morosan, D. E., Carley, E. P., Hayes, L. A., Murray, S. A., Zucca, P., Fallows, R. A., McCauley, J., Kilpua, E. K. J., Mann, G., Vocks, C., and Gallagher, P. T. (2019). Multiple regions of shock-accelerated particles during a solar coronal mass ejection. *Nature Astronomy*, 3(5):452–461. (Cited on pages 26, 95, 104, 115, 124, 160, 168 and 169.)

Morosan, D. E., Gallagher, P. T., Zucca, P., Fallows, R., Carley, E. P., Mann, G., Bisi, M. M., Kerdraon, A., Konovalenko, A. A., MacKinnon, A. L., Rucker, H. O., Thidé, B., Magdalenić, J., Vocks, C., Reid, H., Anderson, J., Asgekar, A., Avruch, I. M., Bentum, M. J., Bernardi, G., Best, P., Bonafede, A., Bregman, J., Breitling, F., Broderick, J., Brüggen, M., Butcher, H. R., Ciardi, B., Conway, J. E., de Gasperin, F., de Geus, E., Deller, A., Duscha, S., Eislöffel, J., Engels, D., Falcke, H., Ferrari, C., Frieswijk, W., Garrett, M. A., Grießmeier, J., Gunst, A. W., Hassall, T. E., Hessels, J. W. T., Hoeft, M., Hörandel, J., Horneffer, A., Iacobelli, M., Juette, E., Karastergiou, A., Kondratiev, V. I., Kramer, M., Kuniyoshi, M., Kuper, G., Maat, P., Markoff, S., McKean, J. P., Mulcahy, D. D., Munk, H., Nelles, A., Norden, M. J., Orru, E., Paas, H., Pandey-Pommier, M., Pandey, V. N., Pietka, G., Pizzo, R., Polatidis, A. G., Reich, W., Röttgering, H., Scaife, A. M. M., Schwarz, D., Serylak, M., Smirnov, O., Stappers, B. W., Stewart, A., Tagger, M., Tang, Y., Tasse, C., Thoudam, S., Toribio, C., Vermeulen, R., van Weeren, R. J., Wucknitz, O., Yatawatta, S., Zarka, P., Morosan, D. E., Gallagher, P. T., Zucca, P., Fallows, R., Carley, E. P., Mann, G., Bisi, M. M., Kerdraon, A., Konovalenko, A. A., MacKinnon, A. L., Rucker, H. O., Thidé, B., Magdalenić, J., Vocks, C., Reid, H., Anderson, J., Asgekar, A., Avruch, I. M., Bentum, M. J., Bernardi, G., Best, P., Bonafede, A., Bregman, J., Breitling, F., Broderick, J., Brüggen, M., Butcher, H. R., Ciardi, B., Conway, J. E., de Gasperin, F., de Geus, E., Deller, A., Duscha, S., Eislöffel, J., Engels, D., Falcke, H., Ferrari, C., Frieswijk, W., Garrett, M. A., Grießmeier, J., Gunst, A. W., Hassall, T. E., Hessels, J. W. T., Hoeft, M., Hörandel, J., Horneffer, A., Iacobelli, M., Juette, E., Karastergiou, A., Kondratiev, V. I., Kramer, M., Kuniyoshi, M., Kuper, G., Maat, P., Markoff, S., McKean, J. P., Mulcahy, D. D., Munk, H., Nelles, A., Norden, M. J., Orru, E., Paas, H., Pandey-Pommier, M., Pandey, V. N., Pietka, G., Pizzo, R., Polatidis, A. G., Reich, W., Röttgering, H., Scaife, A. M. M., Schwarz, D., Serylak, M., Smirnov, O., Stappers, B. W., Stewart, A., Tagger, M., Tang, Y., Tasse, C., Thoudam, S., Toribio, C., Vermeulen, R., van Weeren, R. J., Wucknitz, O., Yatawatta, S., and Zarka, P. (2014). LOFAR tied-array imaging of Type III solar radio bursts. *Astronomy & Astrophysics*, 568:A67. (Cited on page 95.)

Morosan, D. E., Gallagher, P. T., Zucca, P., O'flannagain, A., Fallows, R., Reid, H., Magdalenic, J. M., Mann, G., Bisi, M. M., Kerdraon, A., Konovalenko, A. A., Mackinnon, A. L., Rucker, H. O., Vocks, C., Alexov, A., Anderson, J., Asgekar, A., Avruch, I. M., Bentum, M. J., Bernardi, G.,

Bonafede, A., Breitling, F., Broderick, J. W., Brouw, W. N., Butcher, H. R., Ciardi, B., De Geus, E., Eislöffel, J., Falcke, H., Frieswijk, W., Garrett, M. A., Grießmeier, J., Gunst, A. W., Hessels, J. W. T., Hoeft, M., Karastergiou, A., Kondratiev, V. I., Kuper, G., Van Leeuwen, J., Mckay-Bukowski, D., Mckean, J. P., Munk, H., Orru, E., Paas, H., Pizzo, R., Polatidis, A. G., Scaife, A. M. M., Sluman, J., Tasse, C., Toribio, M. C., Vermeulen, R., and Zarka, P. (2015). LOFAR tied-array imaging and spectroscopy of solar S bursts. *A&A*, 580:65. (Cited on page 95.)

Muhr, N., Veronig, A. M., Kienreich, I. W., Vršnak, B., Temmer, M., Bein, B. M., Muhr, N., Veronig, A. M., Kienreich, I. W., Vršnak, B., Temmer, M., and Bein, B. M. (2014). Statistical Analysis of Large-Scale EUV Waves Observed by STEREO/EUVI. *Solar Physics*, 289(12):4563–4588. (Cited on pages 20 and 22.)

Mulay, S. M., Tripathi, D., Zanna, G. D., and Mason, H. (2016). Multiwavelength study of 20 jets that emanate from the periphery of active regions. *Astronomy & Astrophysics*, 589:A79. (Cited on page 14.)

Nan, R. (2006). Five hundred meter aperture spherical radio telescope (FAST). *Science in China Series G*, 49(2):129–148. (Cited on page 81.)

Nelson, G. and Robinson, R. D. (1975). Multi-Frequency Heliograph Observations of Type II Bursts. *Publications of the Astronomical Society of Australia*, 2(6):370–373. (Cited on pages 73, 125, 137 and 162.)

Nelson, G. J. and Melrose, D. B. (1985). Solar Radiophysics: Studies of Emission from the Sun at Metre Wavelengths- Type II bursts. (Cited on page 65.)

Nelson, G. J. and Sheridan, K. V. (1974). Observations of Split-Band Harmonic Type II Bursts with the Culgoora Radioheliograph at 80 and 160 MHz. In *International Astronomical Union / Union Astronomique Internationale*, pages 345–348. Springer Netherlands. (Cited on pages 73, 125, 130 and 162.)

Newkirk, G. (1967). Structure of the Solar Corona. In *Annual Review of Astronomy and Astrophysics*, volume 5, pages 213–266. Annual Reviews. (Cited on page 64.)

Nindos, A., Alissandrakis, C. E., Hillaris, A., and Preka-Papadema, P. (2011). On the relationship of shock waves to flares and coronal mass ejections. *Astronomy and Astrophysics*, 531. (Cited on pages 26, 101 and 125.)

Nindos, A., Kontar, E. P., and Oberoi, D. (2019). Solar physics with the Square Kilometre Array. *Advances in Space Research*, 63(4):1404–1424. (Cited on page 167.)

Nitta, N. V., Schrijver, C. J., Title, A. M., and Liu, W. (2013). Large-scale Coronal Propagating Fronts in Solar Eruptions as Observed by the Atmospheric Imaging Assembly on Board the Solar Dynamics Observatory -An Ensemble Stud. *The Astrophysical Journal*, 776(1):58. (Cited on pages 21 and 22.)

Offringa, A. R., McKinley, B., Hurley-Walker, N., Briggs, F. H., Wayth, R. B., Kaplan, D. L., Bell, M. E., Feng, L., Neben, A. R., Hughes, J. D., Rhee, J., Murphy, T., Bhat, N. D. R., Bernardi, G., Bowman, J. D., Cappallo, R. J., Corey, B. E., Deshpande, A. A., Emrich, D., Ewall-Wice, A., Gaensler, B. M., Goeke, R., Greenhill, L. J., Hazelton, B. J., Hindson, L., Johnston-Hollitt, M., Jacobs, D. C., Kasper, J. C., Kratzenberg, E., Lenc, E., Lonsdale, C. J., Lynch, M. J., McWhirter, S. R., Mitchell, D. A., Morales, M. F., Morgan, E., Kudryavtseva, N., Oberoi, D., Ord, S. M., Pindor, B., Procopio, P., Prabu, T., Riding, J., Roshi, D. A., Shankar, N. U., Srivani, K. S., Subrahmanyan, R., Tingay, S. J., Waterson, M., Webster, R. L., Whitney, A. R., Williams, A., Williams, C. L., Offringa, A. R., McKinley, B., Hurley-Walker, N., Briggs, F. H., Wayth, R. B., Kaplan, D. L., Bell, M. E., Feng, L., Neben, A. R., Hughes, J. D., Rhee, J., Murphy, T., Bhat, N. D. R., Bernardi, G., Bowman, J. D., Cappallo, R. J., Corey, B. E., Deshpande, A. A., Emrich, D., Ewall-Wice, A., Gaensler, B. M., Goeke, R., Greenhill, L. J., Hazelton, B. J., Hindson, L., Johnston-Hollitt, M., Jacobs, D. C., Kasper, J. C., Kratzenberg, E., Lenc, E., Lonsdale, C. J., Lynch, M. J., McWhirter, S. R., Mitchell, D. A., Morales, M. F., Morgan, E., Kudryavtseva, N., Oberoi, D., Ord, S. M., Pindor, B., Procopio, P., Prabu, T., Riding, J., Roshi, D. A., Shankar, N. U., Srivani, K. S., Subrahmanyan, R., Tingay, S. J., Waterson, M., Webster, R. L., Whitney, A. R., Williams, A., and Williams, C. L. (2014). WSCLEAN: an implementation of a fast, generic wide-field imager for radio astronomy. *Monthly Notices of the Royal Astronomical Society*, 444(1):606–619. (Cited on pages 91, 129 and 147.)

Olmedo, O., Vourlidas, A., Zhang, J., Cheng, X., Olmedo, O., Vourlidas, A., Zhang, J., and Cheng, X. (2012). Secondary Waves and/or the "Reflection" from and "Transmission" through a Coronal Hole of an Extreme Ultraviolet Wave Associated with the 2011 February 15 X2.2 Flare Observed with SDO/AIA and STEREO/EUVI. *The Astrophysical Journal*, 756(2):143. (Cited on page 21.)

Ontiveros, V. and Vourlidas, A. (2009). Quantitative Measurements of Coronal Mass Ejection-Driven Shocks from LASCO Observations. *The Astrophysical Journal*, 693:267–275. (Cited on page 20.)

Parker, E. N. (1958). Dynamics of the Interplanetary Gas and Magnetic Fields. *The Astrophysical Journal*, 128:664. (Cited on page 6.)

Parker, E. N. (1975). The generation of magnetic fields in astrophysical bodies. X. Magnetic buoyancy and the solar dynamo. *Astrophysical Journal*, 198:205–209. (Cited on page 8.)

Pasachoff, J. M. and Olson, R. J. M. (2014). Astronomy: Art of the eclipse. *Nature*, 508(7496):314–315. (Cited on page 3.)

Payne-Scott, R., Yabsley, D. E., and Bolton, J. G. (1947). Relative Times of Arrival of Bursts of Solar Noise on Different Radio Frequencies. *Nature*, 160(4060):256–257. (Cited on page 22.)

Pesnell, W. D. (2015). Solar dynamics observatory (SDO). *Handbook of Cosmic Hazards and Planetary Defense*, pages 179–196. (Cited on page 12.)

Pesnell, W. D., Thompson, B. J., Chamberlin, P. C., Pesnell, W. D., Thompson, B. J., and Chamberlin, P. C. (2012). The Solar Dynamics Observatory (SDO). *Solar Physics*, 275(1-2):3–15. (Cited on page 96.)

Pick, M. and Vilmer, N. (2008). Sixty-five years of solar radioastronomy: Flares, coronal mass ejections and Sun-Earth connection. *Astronomy and Astrophysics Review*, 16(1-2):1–153. (Cited on page 17.)

Pohjolainen, S., Hori, K., and Sakurai, T. (2008). Radio bursts associated with flare and ejecta in the 13 July 2004 event. *Solar Physics*, 253(1-2):291–303. (Cited on page 26.)

Pomoell, J., Vainio, R., and Kissmann, R. (2008). MHD modeling of coronal large-amplitude waves related to CME lift-off. *Solar Physics*, 253(1-2):249–261. (Cited on pages 125 and 136.)

Poomvises, W., Gopalswamy, N., Yashiro, S., Kwon, R. Y., and Olmedo, O. (2012). Determination of the heliospheric radial magnetic field from the standoff distance of a CME-driven shock observed by the stereo spacecraft. *The Astrophysical Journal*, 758(2):1–6. (Cited on page 104.)

Priest, E. R. E. R. (1984). *Solar magneto-hydrodynamics*. D. Reidel Pub. Co. (Cited on page 103.)

Ramesh, R., Lakshmi, M. A., Kathiravan, C., Gopalswamy, N., Umapathy, S., Ramesh, R., Lakshmi, M. A., Kathiravan, C., Gopalswamy, N., and Umapathy, S. (2012). The Location of Solar Metric Type II Radio Bursts with Respect to the Associated Coronal Mass Ejections. *The Astrophysical Journal*, 752(2):107. (Cited on page 20.)

Raouafi, N. E., Patsourakos, S., Pariat, E., Young, P. R., Sterling, A. C., Savcheva, A., Shimojo, M., Moreno-Insertis, F., DeVore, C. R., Archontis, V., Török, T., Mason, H., Curdt, W., Meyer, K., Dalmasse, K., and Matsui, Y. (2016). Solar Coronal Jets: Observations, Theory, and Modeling. *Space Science Reviews*, 201(1):1–53. (Cited on page 14.)

Ratcliffe, H., Bian, N. H., and Kontar, E. P. (2012). Density Fluctuations and the Acceleration of Electrons by Beam-generated Langmuir Waves in the Solar Corona. *The Astrophysical Journal*, 761(2):176. (Cited on page 60.)

Reames, D. V. (2013). The Two Sources of Solar Energetic Particles. *Space Science Reviews*, 175(1):53–92. (Cited on page 19.)

Reid, H. A. and Kontar, E. P. (2010). Solar wind density turbulence and solar flare electron transport from the Sun to the Earth. *The Astrophysical Journal*, 721(1):864–874. (Cited on page 60.)

Reid, H. A. S. and Kontar, E. P. (2017). Imaging spectroscopy of type U and J solar radio bursts with LOFAR. *Astronomy & Astrophysics*, 606:A141. (Cited on page 168.)

Reid, H. A. S., Kontar, E. P., Reid, H. A. S., and Kontar, E. P. (2021). Fine structure of type III solar radio bursts from Langmuir wave motion in turbulent plasma. *Nature Astronomy*, 5(8):796–804. (Cited on page 168.)

Reid, H. A. S. and Ratcliffe, H. (2014). A review of solar type III radio bursts. *Research in Astronomy and Astrophysics*, 14(7):773. (Cited on page 60.)

Rich, J. W., de Blok, W. J. G., Cornwell, T. J., Brinks, E., Walter, F., Bagetakos, I., and Kennicutt Jr, R. C. (2008). Multi-Scale CLEAN: A comparison of its performance against classical CLEAN in galaxies using THINGS. *The Astronomical Journal*, 136(6):2897–2920. (Cited on page 91.)

Riddle, A. C. (1972). On the Interpretation of Solar Radio-Burst Positions in a Scattering Corona. *Proceedings of the Astronomical Society of Australia*, 2(3):148–150. (Cited on page 73.)

Riddle, A. C. (1974). On the observation of scattered radio emission from sources in the solar corona. *Solar Physics*, 35(1):153–169. (Cited on pages 74, 77 and 130.)

Robinson, R. D. (1983). Scattering of radio waves in the solar corona. *Proceedings of the Astronomical Society of Australia*, 5(2):208–211. (Cited on page 74.)

Rouillard, A. P., Plotnikov, I., Pinto, R. F., Tirole, M., Lavarra, M., Zucca, P., Vainio, R., Tylka, A. J., Vourlidas, A., Rosa, M. L. D., Linker, J., Warmuth, A., Mann, G., Cohen, C. M. S., and Mewaldt, R. A. (2016). Deriving the properties of coronal pressure fronts in 3-D: application to the 17 May 2012 ground level enhancement. *The Astrophysical Journal*, 833(1):45. (Cited on pages 104 and 160.)

Russell, C. T. and Mulligan, T. (2002). On the magnetosheath thicknesses of interplanetary coronal mass ejections. *Planetary and Space Science*, 50:527–534. (Cited on pages 44 and 104.)

Ryan, A. M., Gallagher, P. T., Carley, E. P., Brentjens, M. A., Murphy, P. C., Vocks, C., Morosan, D. E., Reid, H., Magdalenic, J., Breitling, F., Zucca, P., Fallows, R., Mann, G., Kerdraon, A., and Halfwerk, R. (2021). LOFAR imaging of the solar corona during the 2015 March 20 solar eclipse. *Astronomy & Astrophysics*, 648:A43. (Cited on page 89.)

Saito, K., Makita, M., Nishi, K., and Hata, S. (1970). A non-spherical axisymmetric model of the solar K corona of the minimum type. *AnTok*, 12(2):51–173. (Cited on page 133.)

Saito, K., Poland, A. I., and Munro, R. H. (1977). A study of the background corona near solar minimum. *Solar Physics*, 55(1):121–134. (Cited on page 64.)

Salas-Matamoros, C., Klein, K.-L., and Rouillard, A. P. (2016). Coronal mass ejection-related particle acceleration regions during a simple eruptive event. *Astronomy & Astrophysics*, 590:A135. (Cited on page 119.)

Schatten, K. H., Wilcox, J. M., and Ness, N. F. (1969). A model of interplanetary and coronal magnetic fields. *Solar Physics*, 6(3):442–455. (Cited on page 112.)

Scherrer, P. H., Schou, J., Bush, R. I., Kosovichev, A. G., Bogart, R. S., Hoeksema, J. T., Liu, Y., Duvall, T. L., Zhao, J., Title, A. M., Schrijver, C. J., Tarbell, T. D., Tomczyk, S., Scherrer, P. H., Schou, J., Bush, R. I., Kosovichev, A. G., Bogart, R. S., Hoeksema, J. T., Liu, Y., Duvall, T. L., Zhao, J., Title, A. M., Schrijver, C. J., Tarbell, T. D., and Tomczyk, S. (2012). The Helioseismic and Magnetic Imager (HMI) Investigation for the Solar Dynamics Observatory (SDO). *Solar Physics*, 275(1-2):207–227. (Cited on page 97.)

Schmidt, J. M. and Cairns, I. H. (2012). Type II radio bursts: 1. New entirely analytic formalism for the electron beams, Langmuir waves, and radio emission. *Journal of Geophysical Research: Space Physics*, 117(A4):n/a–n/a. (Cited on page 67.)

Schmidt, J. M., Cairns, I. H., Gopalswamy, N., and Yashiro, S. (2016). Coronal magnetic field profiles from shock-CME standoff distances. *Journal of Geophysical Research: Space Physics*, 121:9299–9315. (Cited on pages 44 and 125.)

Schrijver, C. J. and DeRosa, M. L. (2003). Photospheric and heliospheric magnetic fields. *Solar Physics*, 212(1):165–200. (Cited on page 112.)

Schrijver, C. J., Kauristie, K., Aylward, A. D., Denardini, C. M., Gibson, S. E., Glover, A., Gopalswamy, N., Grande, M., Hapgood, M., Heynderickx, D., Jakowski, N., Kalegaev, V. V., Lapenta, G., Linker, J. A., Liu, S., Mandrini, C. H., Mann, I. R., Nagatsuma, T., Nandy, D., Obara, T., O'Brien, T. P., Onsager, T., Opgenoorth, H. J., Terkildsen, M., Valladares, C. E., and Vilmer, N. (2015). Understanding space weather to shield society: A global road map for 2015–2025 commissioned by COSPAR and ILWS. *Advances in Space Research*, 55(12):2745–2807. (Cited on pages 1 and 27.)

Schwab, F. R. (1984). Relaxing the isoplanatism assumption in self-calibration; applications to low-frequency radio interferometry. *The Astronomical Journal*, 89:1076. (Cited on page 90.)

Schwarz, U. J. (1978). Mathematical-statistical Description of the Iterative Beam Removing Technique (Method CLEAN). *Astronomy and Astrophysics*, 65:345. (Cited on page 89.)

Seaton, D. B. and Darnel, J. M. (2018). Observations of an Eruptive Solar Flare in the Extended EUV Solar Corona. *The Astrophysical Journal*, 852(1):L9. (Cited on page 96.)

Seiff, A. (1962). Recent Information on Hypersonic Flow Fields. In *Gas Dynamics in Space Explorations: Recent Information on Hypersonic Flow Fields*, volume 24, page 19. (Cited on page 103.)

Sheeley, N. R., Hakala, W. N., Wang, Y. M., Sheeley, N. R., Hakala, W. N., and Wang, Y. M. (2000). Detection of coronal mass ejection associated shock waves in the outer corona. *Journal of Geophysical Research Atmospheres*, 105(A3):5081–5092. (Cited on page 20.)

Shen, Y., Liu, Y., Shen, Y., and Liu, Y. (2012). Simultaneous Observations of a Large-scale Wave Event in the Solar Atmosphere: From Photosphere to Corona. *The Astrophysical Journal Letters*, 752(2):L23. (Cited on page 21.)

Sheridan, K. V., Labrum, N. R., and Payten, W. J. (1972). Multiple-frequency Operation of the Culgoora Radioheliograph. *Nature Physical Science*, 238(86):115–116. (Cited on pages 73, 125 and 162.)

Shibata, K. and Magara, T. (2011). Solar Flares: Magnetohydrodynamic Processes. *Living Reviews in Solar Physics 2011 8:1*, 8(1):1–99. (Cited on page 12.)

Smerd, S. F., Sheridan, K. V., and Stewart, R. T. (1974). On Split-Band Structure in Type II Radio Bursts from the Sun. *Symposium - International Astronomical Union*, 57(July):389–393. (Cited on pages 66, 105, 142 and 154.)

Spreiter, J. R., Summers, A. L., and Alksne, A. Y. (1966). Hydromagnetic flow around the magnetosphere. *Planetary and Space Science*, 14(3):223–253. (Cited on page 103.)

Stansby, D., Yeates, A., and Badman, S. (2020). pfsspy: A Python package for potential field source surface modelling. *Journal of Open Source Software*, 5(54):2732. (Cited on pages 117, 129 and 150.)

Stappers, B. W., Hessels, J. W. T., Alexov, A., Anderson, K., Coenen, T., Hassall, T., Karastergiou, A., Kondratiev, V. I., Kramer, M., van Leeuwen, J., Mol, J. D., Noutsos, A., Romein, J. W., Weltevrede, P., Fender, R., Wijers, R. A. M. J., Bähren, L., Bell, M. E., Broderick, J., Daw, E. J., Dhillon, V. S., Eislöffel, J., Falcke, H., Griessmeier, J., Law, C., Markoff, S., Miller-Jones, J. C. A., Scheers, B., Spreeuw, H., Swinbank, J., Ter Veen, S., Wise, M. W., Wucknitz, O., Zarka, P., Anderson, J., Asgekar, A., Avruch, I. M., Beck, R., Bennema, P., Bentum, M. J., Best, P., Bregman, J., Brentjens, M., van de Brink, R. H., Broekema, P. C., Brouw, W. N., Brüggen, M., de Bruyn, A. G., Butcher, H. R., Ciardi, B., Conway, J., Dettmar, R. J., van Duin, A., van Enst, J., Garrett, M., Gerbers, M., Grit, T., Gunst, A., van Haarlem, M. P., Hamaker, J. P., Heald, G., Hoeft, M., Holties, H., Horneffer, A., Koopmans, L. V. E., Kuper, G., Loose, M., Maat, P., McKay-Bukowski, D., McKean, J. P., Miley, G., Morganti, R., Nijboer, R., Noordam, J. E., Norden, M., Olofsson, H., Pandey-Pommier, M., Polatidis, A., Reich, W., Röttgering, H., Schoenmakers, A., Sluman, J., Smirnov, O., Steinmetz, M., Sterks, C. G. M., Tagger, M., Tang, Y., Vermeulen, R., Vermaas, N., Vogt, C., de Vos, M., Wijnholds, S. J., Yatawatta, S., Zensus, A., Stappers, B. W., Hessels, J. W. T., Alexov, A., Anderson, K., Coenen, T., Hassall, T., Karastergiou, A., Kondratiev, V. I., Kramer, M., van Leeuwen, J., Mol, J. D., Noutsos, A., Romein, J. W., Weltevrede, P., Fender, R., Wijers, R. A. M. J., Bähren, L., Bell, M. E., Broderick, J., Daw, E. J., Dhillon, V. S., Eislöffel, J., Falcke, H., Griessmeier, J., Law, C., Markoff, S., Miller-Jones, J. C. A., Scheers, B., Spreeuw, H., Swinbank, J., Ter Veen, S., Wise, M. W., Wucknitz, O., Zarka, P., Anderson, J., Asgekar, A., Avruch, I. M., Beck, R., Bennema, P., Bentum, M. J., Best, P., Bregman, J., Brentjens, M., van de Brink, R. H., Broekema, P. C., Brouw, W. N., Brüggen, M., de Bruyn, A. G., Butcher, H. R., Ciardi, B., Conway, J., Dettmar, R. J., van Duin, A., van Enst, J., Garrett, M., Gerbers, M., Grit, T., Gunst, A., van Haarlem, M. P., Hamaker, J. P., Heald, G., Hoeft, M., Holties, H., Horneffer, A.,

Koopmans, L. V. E., Kuper, G., Loose, M., Maat, P., McKay-Bukowski, D., McKean, J. P., Miley, G., Morganti, R., Nijboer, R., Noordam, J. E., Norden, M., Olofsson, H., Pandey-Pommier, M., Polatidis, A., Reich, W., Röttgering, H., Schoenmakers, A., Sluman, J., Smirnov, O., Steinmetz, M., Sterks, C. G. M., Tagger, M., Tang, Y., Vermeulen, R., Vermaas, N., Vogt, C., de Vos, M., Wijnholds, S. J., Yatawatta, S., and Zensus, A. (2011). Observing pulsars and fast transients with LOFAR. *Astronomy & Astrophysics*, 530:A80. (Cited on page 95.)

Steinberg, J. L. (1972). Coronal Scattering of Radiobursts at Hectometer and Kilometer Wavelengths. *Astronomy & Astrophysics*, 18:382. (Cited on page 74.)

Steinberg, J. L., Aubier-Giraud, M., Leblanc, Y., and Boischot, A. (1971). Coronal Scattering, Absorption and Refraction of Solar Radiobursts. *Astronomy & Astrophysics*, 10:362. (Cited on pages 72, 73, 75, 77 and 130.)

Stephenson, F. R. (1997). *Historical Eclipses and Earth's Rotation*. Cambridge University Press. (Cited on page 3.)

Stewart, R. T. (1972). Relative Positions of Fundamental and Second Harmonic Type III Bursts. *Publications of the Astronomical Society of Australia*, 2(2):100–101. (Cited on page 130.)

Street, A. G., Ball, L., and Melrose, D. B. (1994). Shock Drift Acceleration and Type II Solar Radio Bursts. *Publications of the Astronomical Society of Australia*, 11(1):21–24. (Cited on page 52.)

Su, Y., Veronig, A. M., Holman, G. D., Dennis, B. R., Wang, T., Temmer, M., and Gan, W. (2013). Imaging coronal magnetic-field reconnection in a solar flare. *Nature Physics*, 9(8):489–493. (Cited on page 147.)

Suresh, K. and Shanmugaraju, A. (2015). Investigation on Radio-Quiet and Radio-Loud Fast CMEs and Their Associated Flares During Solar Cycles 23 and 24. *Solar Physics*, 290(3):875–889. (Cited on page 120.)

Suzuki, S., Dulk, G. A., Suzuki, S., and Dulk, G. A. (1985). Bursts of type III and type V. In *Cambridge University press*, pages 289–332. (Cited on pages 72, 73, 125 and 162.)

Thejappa, G. and MacDowall, R. J. (2008). Effects of Scattering on Radio Emission from the Quiet Sun at Low Frequencies. *The Astrophysical Journal*, 676(2):1338–1345. (Cited on pages 71 and 132.)

Thejappa, G., MacDowall, R. J., and Kaiser, M. L. (2007). Monte Carlo Simulation of Directivity of Interplanetary Radio Bursts. *The Astrophysical Journal*, 671(1):894–906. (Cited on page 132.)

Thompson, B. J. and Myers, D. C. (2009). A Catalog of Coronal "EIT Wave" Transients. *The Astrophysical Journal Supplement*, 183(2):225–243. (Cited on page 20.)

Thompson, B. J., Plunkett, S. P., Gurman, J. B., Newmark, J. S., St. Cyr, O. C., and Michels, D. J. (1998). SOHO /EIT observations of an Earth-directed coronal mass ejection on May 12, 1997. *Geophysical Research Letters*, 25(14):2465–2468. (Cited on page 21.)

Tingay, S. J., Goeke, R., Bowman, J. D., Emrich, D., Ord, S. M., Mitchell, D. A., Morales, M. F., Booler, T., Crosse, B., Wayth, R. B., Lonsdale, C. J., Tremblay, S., Pallot, D., Colegate, T., Wicenec, A., Kudryavtseva, N., Arcus, W., Barnes, D., Bernardi, G., Briggs, F., Burns, S., Bunton, J. D., Cappallo, R. J., Corey, B. E., Deshpande, A., Desouza, L., Gaensler, B. M., Greenhill, L. J., Hall, P. J., Hazelton, B. J., Herne, D., Hewitt, J. N., Johnston-Hollitt, M., Kaplan, D. L., Kasper, J. C., Kincaid, B. B., Koenig, R., Kratzenberg, E., Lynch, M. J., Mckinley, B., Mcwhirter, S. R., Morgan, E., Oberoi, D., Pathikulangara, J., Prabu, T., Remillard, R. A., Rogers, A. E. E., Roshi, A., Salah, J. E., Sault, R. J., Udaya-Shankar, N., Schlagenhaufer, F., Srivani, K. S., Stevens, J., Subrahmanyan, R., Waterson, M., Webster, R. L., Whitney, A. R., Williams, A., Williams, C. L., Wyithe, J. S. B., Tingay, S. J., Goeke, R., Bowman, J. D., Emrich, D., Ord, S. M., Mitchell, D. A., Morales, M. F., Booler, T., Crosse, B., Wayth, R. B., Lonsdale, C. J., Tremblay, S., Pallot, D., Colegate, T., Wicenec, A., Kudryavtseva, N., Arcus, W., Barnes, D., Bernardi, G., Briggs, F., Burns, S., Bunton, J. D., Cappallo, R. J., Corey, B. E., Deshpande, A., Desouza, L., Gaensler, B. M., Greenhill, L. J., Hall, P. J., Hazelton, B. J., Herne, D., Hewitt, J. N., Johnston-Hollitt, M., Kaplan, D. L., Kasper, J. C., Kincaid, B. B., Koenig, R., Kratzenberg, E., Lynch, M. J., Mckinley, B., Mcwhirter, S. R., Morgan, E., Oberoi, D., Pathikulangara, J., Prabu, T., Remillard, R. A., Rogers, A. E. E., Roshi, A., Salah, J. E., Sault, R. J., Udaya-Shankar, N., Schlagenhaufer, F., Srivani, K. S., Stevens, J., Subrahmanyan, R., Waterson, M., Webster, R. L., Whitney, A. R., Williams, A., Williams, C. L., and Wyithe, J. S. B. (2013). The Murchison Widefield Array: The Square Kilometre Array Precursor at Low Radio Frequencies. *Publications of the Astronomical Society of Australia*, 30(1):e007. (Cited on page 82.)

Tonks, L., Langmuir, I., Tonks, L., and Langmuir, I. (1929). Oscillations in Ionized Gases. *Physical Review*, 33(2):195–210. (Cited on page 61.)

Tun, S. D. and Vourlidas, A. (2013). Derivation of the magnetic field in a coronal mass ejection core via multi-frequency radio imaging. *The Astronomical Journal*, 766(2). (Cited on page 20.)

Uchida, Y. (1960). On the Exciters of Type II and Type III Solar Radio Bursts. *Publications of the Astronomical Society of Japan, vol. 12, p.376 (1960).*, 12:376. (Cited on page 25.)

van Diepen, G., Dijkema, T. J., and Offringa, A. (2018). DPPP: Default Pre-Processing Pipeline. *Astrophysics Source Code Library*, 1804.003. (Cited on pages 129 and 147.)

Van Haarlem, M. P., Wise, M. W., Gunst, A. W., Heald, G., McKean, J. P., Hessels, J. W., De Bruyn, A. G., Nijboer, R., Swinbank, J., Fallows, R., Brentjens, M., Nelles, A., Beck, R., Falcke, H., Fender, R., Hörandel, J., Koopmans, L. V., Mann, G., Miley, G., Röttgering, H., Stappers, B. W., Wijers, R. A., Zaroubi, S., Van Den Akker, M., Alexov, A., Anderson, J., Anderson, K., Van Ardenne, A., Arts, M., Asgekar, A., Avruch, I. M., Batejat, F., Bähren, L., Bell, M. E., Bell, M. R., Van Bemmel, I., Bennema, P., Bentum, M. J., Bernardi, G., Best, P., Bîrzan, L., Bonafede, A., Boonstra, A. J., Braun, R., Bregman, J., Breitling, F., Van De Brink, R. H., Broderick, J., Broekema, P. C., Brouw, W. N., Brüggen, M., Butcher, H. R., Van Cappellen, W., Ciardi, B., Coenen, T., Conway, J., Coolen, A., Corstanje, A., Damstra, S., Davies, O., Deller, A. T., Dettmar, R. J., Van Diepen, G., Dijkstra, K., Donker, P., Doorduin, A., Dromer, J., Drost, M., Van Duin, A., Eislöffel, J., Van Enst, J., Ferrari, C., Frieswijk, W., Gankema, H., Garrett, M. A., De Gasperin, F., Gerbers, M., De Geus, E., Grießmeier, J. M., Grit, T., Gruppen, P., Hamaker, J. P., Hassall, T., Hoeft, M., Holties, H. A., Horneffer, A., Van Der Horst, A., Van Houwelingen, A., Huijgen, A., Iacobelli, M., Intema, H., Jackson, N., Jelic, V., De Jong, A., Juette, E., Kant, D., Karastergiou, A., Koers, A., Kollen, H., Kondratiev, V. I., Kooistra, E., Koopman, Y., Koster, A., Kuniyoshi, M., Kramer, M., Kuper, G., Lambropoulos, P., Law, C., Van Leeuwen, J., Lemaitre, J., Loose, M., Maat, P., Macario, G., Markoff, S., Masters, J., McFadden, R. A., McKay-Bukowski, D., Meijering, H., Meulman, H., Mevius, M., Middelberg, E., Millenaar, R., Miller-Jones, J. C., Mohan, R. N., Mol, J. D., Morawietz, J., Morganti, R., Mulcahy, D. D., Mulder, E., Munk, H., Nieuwenhuis, L., Van Nieuwpoort, R., Noordam, J. E., Norden, M., Noutsos, A., Offringa, A. R., Olofsson, H., Omar, A., Orrú, E., Overeem, R., Paas, H., Pandey-Pommier, M., Pandey, V. N., Pizzo, R., Polatidis, A., Rafferty, D., Rawlings, S., Reich, W., De Reijer, J. P., Reitsma, J., Renting, G. A., Riemers, P., Rol, E., Romein, J. W., Roosjen, J., Ruiter, M., Scaife, A., Van Der Schaaf, K., Scheers, B., Schellart, P., Schoenmakers, A., Schoonderbeek, G., Serylak, M., Shulevski, A., Sluman, J., Smirnov, O., Sobey, C., Spreeuw, H., Steinmetz, M., Sterks, C. G., Stiepel, H. J., Stuurwold, K., Tagger, M., Tang, Y., Tasse, C., Thomas, I., Thoudam, S., Toribio, M. C., Van Der Tol, B., Usov, O., Van Veelen, M., Van Der Veen, A. J., Ter Veen, S., Verbiest, J. P., Vermeulen, R., Vermaas, N., Vocks, C., Vogt, C., De Vos, M., Van Der Wal, E., Van Weeren, R., Weggemans, H., Weltevrede, P., White, S., Wijnholds, S. J., Wilhelmsson, T., Wucknitz, O., Yatawatta, S., Zarka, P., Zensus,

A., and Van Zwieten, J. (2013). LOFAR: The low-frequency array. *Astronomy and Astrophysics*, 556(A2):52. (Cited on pages 24, 75 and 95.)

Vandas, M. and Karlický, M. (2011). Electron acceleration in a wavy shock front. *Astronomy and Astrophysics*, 531. (Cited on page 70.)

Verkhoglyadova, O. P., Zank, G. P., and Li, G. (2015). A theoretical perspective on particle acceleration by interplanetary shocks and the Solar Energetic Particle problem. *Physics Reports*, 557:1–23. (Cited on page 119.)

Vernazza, J. E., Avrett, E. H., Loeser, R., Vernazza, J. E., Avrett, E. H., and Loeser, R. (1981). Structure of the solar chromosphere. III. Models of the EUV brightness components of the quiet sun. *The Astrophysical Journal*, 45:635–725. (Cited on page 4.)

Veronig, A. M., Podladchikova, T., Dissauer, K., Temmer, M., B. Seaton, D., Long, D., Guo, J., Vršnak, B., Harra, L., and Kliem, B. (2018). Genesis and Impulsive Evolution of the 2017 September 10 Coronal Mass Ejection. *The Astrophysical Journal*, 868(2):107. (Cited on page 18.)

Vourlidas, A. and Bemporad, A. (2012). A Decade of Coronagraphic and Spectroscopic Studies of CME-Driven Shocks. *AIP Conference Proceedings*, 1436:279–284. (Cited on pages 20 and 102.)

Vourlidas, A., Carley, E. P., and Vilmer, N. (2020). Radio Observations of Coronal Mass Ejections: Space Weather Aspects. *Frontiers in Astronomy and Space Sciences*, 7:43. (Cited on page 28.)

Vourlidas, A., Howard, R. A., Esfandiari, E., Patsourakos, S., Yashiro, S., Michalek, G., Vourlidas, A., Howard, R. A., Esfandiari, E., Patsourakos, S., Yashiro, S., and Michalek, G. (2010). Comprehensive Analysis of Coronal Mass Ejection Mass and Energy Properties Over a Full Solar Cycle. *The Astrophysical Journal*, 722(2):1522–1538. (Cited on pages 16, 17 and 20.)

Vourlidas, A., Lynch, B. J., Howard, R. A., and Li, Y. (2013). How Many CMEs Have Flux Ropes? Deciphering the Signatures of Shocks, Flux Ropes, and Prominences in Coronagraph Observations of CMEs. *Solar Physics*, 284(1):179–201. (Cited on pages 19 and 20.)

Vršnak, B., Aurass, H., Magdalenić, J., and Gopalswamy, N. (2001). Band-splitting of coronal and interplanetary type II bursts. *Astronomy & Astrophysics*, 377(1):321–329. (Cited on pages 67, 115, 136, 142 and 155.)

Vršnak, B. and Cliver, E. W. (2008). Origin of coronal shock waves : II Invited review. *Solar Physics*, 253(1-2):215–235. (Cited on pages 1, 124 and 136.)

Vršnak, B. and Lulić, S. (2000). Formation Of Coronal Mhd Shock Waves – I. The Basic Mechanism. *Solar Physics*, 196(1):157–180. (Cited on page 145.)

Vršnak, B., Magdalenic, J., Aurass, H., and Mann, G. (2002). Band-splitting of coronal and interplanetary type II bursts II. Coronal magnetic field and Alfvén velocity. *Astronomy & Astrophysics*, 396:673–682. (Cited on pages 65, 67, 105, 114, 136, 142 and 155.)

Vršnak, B., Magdalenic, J., and Zlobec, P. (2004a). Band-splitting of coronal and interplanetary type II bursts. III. Physical conditions in the upper corona and interplanetary space. *Astronomy and Astrophysics*, 413:753–763. (Cited on page 26.)

Vršnak, B., Magdalenic, J., and Zlobec, P. (2004b). Band-splitting of coronal and interplanetary type II bursts. III. Physical conditions in the upper corona and interplanetary space. *Astronomy and Astrophysics*, 413:753–763. (Cited on page 67.)

Vršnak, B., Sudar, D., and Ruždjak, D. (2005). The CME-flare relationship: Are there really two types of CMEs? *Astronomy & Astrophysics*, 435(3):1149–1157. (Cited on page 17.)

Wang, W., Liu, R., Wang, Y., Hu, Q., Shen, C., Jiang, C., and Zhu, C. (2017). Buildup of a highly twisted magnetic flux rope during a solar eruption. *Nature Communications*, 8(1):1–11. (Cited on page 125.)

Warmuth, A. (2007). Large-scale Waves and Shocks in the Solar Corona. *Lecture Notes in Physics*, 725:107–138. (Cited on page 43.)

Warmuth, A. (2015). Large-scale Globally Propagating Coronal Waves. *Living Reviews in Solar Physics*, 12(1):1–101. (Cited on pages 22 and 42.)

Weaver, T. A. (1976). The structure of supernova shock waves. *Astrophysical Journal Supplement Series*, 32:233–282. (Cited on page 44.)

Welsch, B. T., Fisher, G. H., Abbett, W. P., Regnier, S., Welsch, B. T., Fisher, G. H., Abbett, W. P., and Regnier, S. (2004). ILCT: Recovering Photospheric Velocities from Magnetograms by Combining the Induction Equation with Local Correlation Tracking. *The Astrophysical Journal*, 610(2):1148–1156. (Cited on page 147.)

Welsch, B. T., Li, Y., Schuck, P. W., Fisher, G. H., Welsch, B. T., Li, Y., Schuck, P. W., and Fisher, G. H. (2009). What is the Relationship Between Photospheric Flow Fields and Solar Flares? *The Astrophysical Journal*, 705(1):821–843. (Cited on page 147.)

Westfall, J. and Sheehan, W. (2015). *To Darken the Earth.* Springer, New York, NY. (Cited on page 4.)

Wild, J. P. (1962). The Radio Emission from Solar Flares. *Journal of the Physical Society of Japan Supplement*, 17:249. (Cited on page 25.)

Wild, J. P. and McCready, L. L. (1950). Observations of the Spectrum of High-Intensity Solar Radiation at Metre Wavelengths. I. The Apparatus and Spectral Types of Solar Burst Observed. *Australian Journal of Scientific Research*, 3:387. (Cited on pages 23 and 24.)

Wills-Davey, M. J., Thompson, B. J., Wills-Davey, M. J., and Thompson, B. J. (1999). Observations of a Propagating Disturbance in TRACE. *Solar Physics*, 190(1-2):467–483. (Cited on page 21.)

Woods, T. N., Eparvier, F. G., Hock, R., Jones, A. R., Woodraska, D., Judge, D., Didkovsky, L., Lean, J., Mariska, J., Warren, H., McMullin, D., Chamberlin, P., Berthiaume, G., Bailey, S., Fuller-Rowell, T., Sojka, J., Tobiska, W. K., and Viereck, R. (2010). Extreme Ultraviolet Variability Experiment (EVE) on the Solar Dynamics Observatory (SDO): Overview of Science Objectives, Instrument Design, Data Products, and Model Developments. *Solar Physics*, 275(1):115–143. (Cited on page 97.)

Wuelser, J.-P., Lemen, J. R., Tarbell, T. D., Wolfson, C. J., Cannon, J. C., Carpenter, B. A., Duncan, D. W., Gradwohl, G. S., Meyer, S. B., Moore, A. S., Navarro, R. L., Pearson, J. D., Rossi, G. R., Springer, L. A., Howard, R. A., Moses, J. D., Newmark, J. S., Delaboudiniere, J.-P., Artzner, G. E., Auchere, F., Bougnet, M., Bouyries, P., Bridou, F., Clotaire, J.-Y., Colas, G., Delmotte, F., Jerome, A., Lamare, M., Mercier, R., Mullot, M., Ravet, M.-F., Song, X., Bothmer, V., and Deutsch, W. (2004). EUVI: the STEREO-SECCHI extreme ultraviolet imager. *Telescopes and Instrumentation for Solar Astrophysics*, 5171:111. (Cited on pages 126 and 145.)

Zanna, G. D., Aulanier, G., Klein, K.-L., and Török, T. (2011). A single picture for solar coronal outflows and radio noise storms. *Astronomy & Astrophysics*, 526(17):A137. (Cited on page 23.)

Zimovets, I., Vilmer, N., Chian, A. C. L., Sharykin, I., and Struminsky, A. (2012). Spatially resolved observations of a split-band coronal type-II radio burst. *Astronomy & Astrophysics,*, 547(A6):13. (Cited on pages 26, 67, 105, 124, 125, 143, 156 and 164.)

Zimovets, I. V. and Sadykov, V. M. (2015). Spatially resolved observations of a coronal type II radio burst with multiple lanes. *Advances in Space Research*, 56(12):2811–2832. (Cited on pages 67, 68, 143, 155 and 164.)

Zlobec, P., Messerotti, M., Karlický, M., and Urbarz, H. (1993). Fine structures in time profiles of type II bursts at frequencies above 200 MHz. *Solar Physics*, 144(2):373–384. (Cited on page 70.)

Zlotnik, E. Y., Klassen, A., Klein, K. L., Aurass, H., Mann, G., Zlotnik, E. Y., Klassen, A., Klein, K. L., Aurass, H., and Mann, G. (1998). Third harmonic plasma emission in solar type II radio bursts. *Astronomy & Astrophysics*, 331:1087–1098. (Cited on page 62.)

Zucca, P., Carley, E. P., Shaun Bloomfield, D., and Gallagher, P. T. (2014a). The formation heights of coronal shocks from 2D density and Alfvén speed maps. *Astronomy and Astrophysics*, 564:47. (Cited on pages 20, 27, 102, 110, 111, 112, 113, 115, 116, 136 and 155.)

Zucca, P., Morosan, D. E., Rouillard, A. P., Fallows, R., Gallagher, P. T., Magdalenic, J., Klein, K.-L., Mann, G., Vocks, C., Carley, E. P., Bisi, M. M., Kontar, E. P., Rothkaehl, H., Dabrowski, B., Krankowski, A., Anderson, J., Asgekar, A., Bell, M. E., Bentum, M. J., Best, P., Blaauw, R., Breitling, F., Broderick, J. W., Brouw, W. N., Brüggen, M., Butcher, H. R., Ciardi, B., Geus, E. d., Deller, A., Duscha, S., Eislöffel, J., Garrett, M. A., Grießmeier, J. M., Gunst, A. W., Heald, G., Hoeft, M., Hörandel, J., Iacobelli, M., Juette, E., Karastergiou, A., Leeuwen, J. v., McKay-Bukowski, D., Mulder, H., Munk, H., Nelles, A., Orru, E., Paas, H., Pandey, V. N., Pekal, R., Pizzo, R., Polatidis, A. G., Reich, W., Rowlinson, A., Schwarz, D. J., Shulevski, A., Sluman, J., Smirnov, O., Sobey, C., Soida, M., Thoudam, S., Toribio, M. C., Vermeulen, R., van Weeren, R. J., Wucknitz, O., and Zarka, P. (2018). Shock location and CME 3D reconstruction of a solar type II radio burst with LOFAR. *Astronomy & Astrophysics*, 615:A89. (Cited on pages 67, 104, 105, 115, 119, 125, 143, 156, 160 and 164.)

Zucca, P., Pick, M., Démoulin, P., Kerdraon, A., Lecacheux, A., and Gallagher, P. T. (2014b). Understanding Coronal Mass Ejections and Associated Shocks in the Solar Corona by Merging Multiwavelength Observations. *The Astrophysical Journal*, 795(1):68. (Cited on pages 67 and 115.)